ESTIMATION OF WAVE DIRECTIONAL SPECTRA AND APPLICATIONS TO THE STUDY OF SURFACE GRAVITY WATER WAVES

FRANÇOIS P. BRISSETTE

B.Sc. (Université de Montréal)
B.Eng. (Ecole Polytechnique)
M.Sc. (Université de Montréal)

A Thesis submitted in conformity with
the requirements for the degree of

DOCTOR OF PHILOSOPHY

McMaster University

Department of Civil Engineering
McMaster University

1992

ESTIMATION OF WAVE DIRECTIONAL SPECTRA

DOCTOR OF PHILOSOPHY (1992) McMASTER UNIVERSITY
(Civil Engineering) Hamilton, Ontario

TITLE: Estimation of Wave Directional Spectra and Applications to the Study of Surface Gravity Water Waves

AUTHOR: François P. Brissette
B.Sc. (Université de Montréal)
B.Eng. (Ecole Polytechnique)
M.Sc. (Université de Montréal)

SUPERVISOR: Professor I.K. Tsanis

NUMBER OF PAGES: xxvii, 333

ABSTRACT

This thesis deals with the estimation of wave directional spectra and applications to the study of surface gravity water waves. Theoretical foundations and testing procedures are established to evaluate and compare different methods of extracting the wave directional spectrum from a wave record. An integrated software package for the analysis of directional seas is developed and used to test all methods, and to identify their properties, characteristics and biases. As a result, guidelines for the use of these methods are drawn. The findings indicate that all of the methods currently used for wave directional spectrum estimation have drawbacks. As a result, three new methods are proposed and tested against current methods. Test results indicate that a proposed closed-form of the Maximum Likelihood Method is the best choice, from both a theoretical and computational point of view. The new method was shown to outperform all other estimates for both heave-pitch-roll and wavestaff data. Field data from the Atlantic Ocean, Lake Ontario and Lake St.Clair (spanning two orders of magnitude in size) is investigated in an attempt to demonstrate the resolution potential of the newly developed method of estimating the wave directional spectra. As a result, completely decoupled spectra are observed for the first time in rapidly turning winds, and a clear relationship between the wave relaxation parameter and the wave age is established. Directional spreading parameter values are found to be higher than the established values in previous studies, for both Lake Ontario and Atlantic Ocean data. In addition, the Atlantic Ocean directional spectra are found to be narrower than their Lake Ontario counterpart. Finally, wave measurements in Lake St.Clair indicate that the structure of directional spectra can be very complicated, even in small lakes, and that a strong shear current can cause not only the refraction of an incoming wavefield, but can also inhibit the generation of waves propagating directly against it.

ACKNOWLEDGEMENTS

It would be impossible to complete any work of this magnitude without the help of many people. Several people have contributed to this work in one way or another. It is somewhat easier to remember the persons who directly contributed to the thesis, but one should realize that often, a smile or a listening ear can go a long way in helping to solve problems. For this reason, it is impossible to thank every person who contributed in his own way to the completion of this dissertation. To all of you who are not specifically mentioned below, you have not been forgotten and I sincerely thank you.

First and foremost, I would like to thank my supervisor, Ioannis K. Tsanis for his constant support and encouragement. At all stages of the thesis, he has shown continuous interest and he has worked tirelessly to help solve all problems of technical and non-technical nature encountered in the course of this work. His honesty, integrity and work ethics have been a great source of motivation at all times. He has been everything a graduate student could ask for in a supervisor, and he has also been a friend. For all of that, I thank him greatly.

Many people from the Canada Centre for Inland Waters (CCIW) and other institutions played an important role in laying out the work and by providing easy access to facilities and field data. First of all, Mark Donelan gave helpful suggestions throughout the course of this work, and thoughtfully reviewed many aspects of the dissertation. M.Donelan, M.Skafel (CCIW), S.Venkatesh (Atmospheric Environment Service) P.Liu and D.Schwab (Great Lakes Environmental Research Laboratory) kindly gave permission to use the Lake St.Clair data. G. Terray (Woods Hole Institute of Oceanography) provided a few data analysis MATLAB routines which proved to be instrumental in the development of a full package for the analysis of directional seas. F. Anctil (CSSA consultants) gave invaluable insights on the processing and

data correction of pitch-roll buoys. Also, in various ways, W. Drennan (CCIW), D. Beesley (CCIW) and K. Khama (Finnish Institute of Marine Research) provided appreciated help, and Jian Wu (Civil Eng.) kindly allowed results from his work on hydrodynamic modelling of Lake St.Clair to be used. Contributions by M. Shoukri (Mechanical Eng.) and F. Mirza (Civil Eng.), members of my supervising committee are also greatly acknowledged. I would also like to thank Debbie, Gail and Grace from the Civil Engineering Departmental office, who were always helpful and made the task of dealing with administrative issues a very pleasurable one.

It would have been impossible to successfully complete this work without the help of the Computer Information System (CIS) people who were always there to solve all possible software, hardware and network problems. Because of them, my fear of "dumped cores, segmentation faults and transceiver cable problems" are a thing of the past. To John Benjamins, Todd Pfaff and especially Patricia Monger, I "e-mail" a thousand thanks. I must nevertheless point out that they still have not explained to me why things always go wrong at the worst possible time...

The process of doing scientific research and especially the task of writing a thesis involve a lot of work and dedication, which brings feelings of fulfilment and accomplishment, but also good doses of frustration and discouragement. It would be extremely difficult, if not impossible to go through that process without the support and help of friends and family. I have always been a strong believer in the importance of having a full life outside the working office and I would go as far as saying that the enjoyment and satisfaction one gets out of his work, as well as the quality and efficiency which make up work ethics, can only be as good as your life outside the workplace. In that respect, friends and family play a part as important and vital to the completion of the work, than people directly related to the research project.

There are several people who contributed in making my stay in Hamilton a most enjoyable one. I would like to thank all my co-players of the "Aureoles" softball team for making all those late-day games (and post-game analysis at the Phoenix) so relaxing and so much fun. Our 51-9 record over the past three

years stands on its own, and those crushing wins over the "Civil Disorder" team certainly gave me major bragging rights around the Civil Engineering department. Many Civil Engineering graduate students deserve sincere thanks for their help and enjoyment provided by all those "non thesis-related" discussions on various esoterical topics. In particular I would like to thank Alison, Euan, Brian, and Terry, and my "co-workers" for the last three years, Wu Jian and Ping Xu. In many aspects, the most important year of my stay in Hamilton was the first one, which I spent in the Geology Department. Through my first real contact with "English Canada", I have met that bunch of crazy, but so much fun graduate students from all corners of Canada, many of them who will remain friends forever. I have so many memories over the past four years that I would need an extra Chapter to the thesis... To Tom, Steven, Randy, Steve, Bruce, and especially to Simon Pattison, Mark Birchard, Stu Miller and Bruce "F" Willmer, I say thanks, it's been great !

I also have to thank my Hamilton training partners: Brian Bishop, Bruce Ainsworth who introduced me to those sickening interval sessions on the ravine trail, and Mark Tarnopolski who put me on the "Tarno training schedule" and introduced me to those "character-forming" 60km bike rides in the rain, cold and gusting winds. Why do we do that Mark ? I guess we have not figured that one out yet...

Finalement, à ma mère Denyse et à mon père Claude, je vous dois mes plus sincères remerciements pour avoir toujours été là pour moi et m'avoir toujours encouragé au cours de toutes ces années. La plus grosse partie de ce travail vous est due. Un énorme merci aussi à mes trois soeurs: Anne-Marie, Isabelle et Hélène, ainsi qu'à tous mes amis du Québec. Je ne vous nommerai pas ici mais vous vous connaissez. Et en tout dernier lieu, je tiens bien spécialement à remercier Julie, avec qui j'ai tout partagé au cours cette folle dernière année.

CONTENT

PART II - APPLICATIONS TO THE STUDY OF SURFACE GRAVITY WATER WAVES

LIST OF FIGURES

LIST OF TABLES

LIST OF SYMBOLS

a	= wave amplitude
a_i, b_i	= Fourier coefficients
c	= wave celerity
c_i	= complex Fourier coefficients
d	= water depth
d_f	= degrees of freedom
dA	= complex amplitude
e	= base of natural logarithms (2.71828...)
f	= frequency
f_p	= peak frequency
$\overline{f}$	= non-dimensional frequency (U_w/c)
g	= gravitational acceleration
i	= $\sqrt{-1}$
k	= wavenumber
m_i	= moments of the directional distribution of energy
n	= Manning coefficient
r	= perturbation parameter
r_i, r_j	= plane coordinates of wave sensor
t	= time
t_r	= length of record
x, y	= plane coordinates
$A(\theta,\omega)$	= complex vector used in the MLM formulation
B	= wave directional relaxation parameter
C	= wave celerity
C_p	= wave celerity at the peak frequency
C_{ij}	= co-spectrum
$C(\omega)$	= cross spectral density matrix
C_b	= bottom friction coefficient

$D(\theta,\omega)$ = directional spreading function

F = fetch length

$F(f)$, $F(\omega)$ = one dimensional frequency spectrum

$H(\theta, \omega)$ = transfer function which relates a wave measurement to the water surface elevation

H_i = transfer function

$H(f)$ = entropy function

L = wave length

$L(\ )$ = Lagrange function

N = matrix of noise

Q_{ij} = quad-spectrum

$R[\ ]$ = real part of [ ]

$R_{ij}(\tau)$ = cross-correlation function

$R(\theta,\omega)$ = true or real directional spectrum

$R(\theta)$ = residuals from a least-square fit

$S(\omega,\theta)$ = directional spectrum

$S(\vec{k},\omega)$ = wavenumber-frequency spectrum

$S(\theta)$ = direction spectrum (at a given frequency)

S^R = reconstructed cross spectral density matrix

T = wave period

U, U_w = wind velocity

U_{12}, U_{10} = wind velocity at 12 meters, 10 meters

U, V = depth averaged water current velocity

V,D = eigenvalues and eigenvectors

W = wave age

$W(\theta)$ = window function

$X(\theta,\omega)$ = array response

β = spreading parameter

α_r = equilibrium range parameter (DHH frequency spectrum)

α = constriction factor (for NMLM estimate)

α_i = proportionality coefficient

β_i = proportionality coefficient

δf = spectral band width

$\delta(x-x_o)$ = Dirac delta function

ε_s = scaling factor (to scale directional spectrum energy to frequency spectrum energy)

ε = perturbation parameter to introduce incoherent noise to a CPSD matrix

η = water surface elevation

γ = peak enhancement factor

μ = Lagrange multiplier

ν = peak width factor

ω = angular frequency

ϕ = phase angle, earth latitude

ϕ_i = weight parameter

$\phi(f)$ = DHH frequency spectrum

ϕ_1, ϕ_2 = percentage of energy carried by each mode of a bimodal distribution of energy

ρ^2 = statistical parameter of Long (1980)

τ = time lag

θ = wave direction

$\bar{\theta}$, θ_m = mean wave direction

θ_p = peak wave direction

θ_w = wind direction

υ = relaxation parameter

ξ = stopping criterion for iterative scheme

ζ = normalization factor (for NMLM estimate)

Ω = angular rotation

Φ_{ij} = cross-spectra ($C_{ij} + i\, Q_{ij}$)

Ξ = matrix of transfer function ($H(\theta,\omega)$)· complex phase lag (for pitch-roll buoys).

∇ = gradient operator

Superscripts

H = Hermitian transpose

$*$ = conjugate

-1 = inverse

$\vec{x}$ = vector quantity

$\hat{x}$ = estimated value

$\bar{x}$ = mean value

Subscripts

x, y = components in the plane direction

m	= mean
p	= peak
in	= input
dis	= dissipation
nl	= nonlinear
mlm	= maximum likelihood method estimate
$\cdot$	= dot product, or element-by-element operation (for square matrices)

Acronyms

CASP	= Canadian Atlantic Storm Project
CCIW	= Canada Centre for Inland Water
CMLM	= Convolutive Maximum Likelihood Method
CPSD	= Cross Power Spectral Density matrix
DFT	= Direct Fourier Transform (method)
DHH	= Donelan Hamilton and Hui (frequency spectrum)
EMLM	= Eigen-Vector Maximum Likelihood Method
FFT	= Fast Fourier Transform
IMLM	= Iterative Maximum Likelihood Method
INMLM	= Iterative Normalized Maximum Likelihood Method
JONSWAP	= Joint North Sea Wave Program
MEM	= Maximum Entropy Method
MLM	= Maximum Likelihood Method
MLMC	= Maximum Likelihood Method Corrected form
NDBC	= National Data Buoy Center
NMLM	= Normalized Maximum Likelihood Method
NOAA	= National Oceanic and Atmospheric Administration
NODC	= National Oceanographic Data Center
NSR	= Noise to Signal Ratio
NWRI	= National Water Research Institute
PRB	= Pitch Roll Buoy
SWADE	= Surface Wave Dynamics Experiment
SWAPP	= Surface Wave Processes Program
WAVES	= Water Air Vertical Exchange Study

CHAPTER 1

INTRODUCTION

The ocean has forever been a source of fascination and mystery to generations of humans who came in contact with its sheer immensity. Throughout the years we have had to learn to live with it, to care for it and to fear it as it is the site of some of the most powerful natural events known on earth. Of all the natural phenomena to occur on large bodies of water, waves are probably the most spectacular. Who has not wondered about those long-crested regular waves that reach the shore in the middle of the night in the absence of winds ? And who has not seen on television and watched in awe those tiny surfers attacking the gigantic spillers of Hawaii or Australia ? Questions on the origin and evolution of waves probably came very early in time as the human mind evolved into a thinking machine with an insatiable need to know, understand and explain. This need grew even larger as humans slowly started to tame the ocean and use it to feed, travel, discover and fight. The last two hundred years have seen an exponential growth of both the earth's population and industrialization rate. The rapid increase of ocean navigation coupled with the concentration of populations along urban coastal areas has sparked renewed interest in predicting waves and their effect on ships, coastal processes and man-made structures.

The word "wave" is generic and even "water wave" remains rather vague, as the disturbing and restoring forces responsible for generating and attenuating waves can be quite

different. Figure 1 presents an approximate distribution of ocean surface wave energy as a function of frequency, period and primary disturbing and restoring forces. Most of the energy is concentrated in the "gravity band" where periods range from about 1 second to about 30 seconds. Waves in the gravity band are fed in energy by the wind-induced shear stress and gravity acts as the primary restoring force. Being omnipresent and carrying most of the energy, surface gravity water waves are by far the most important to coastal engineering applications. This does not indicate by any means that the effect of other wave bands is not important or negligible. In the high frequency range, capillary waves, governed by surface tension, are fundamental to the initial growth of gravity waves, and the effect of low frequency waves or oscillations such as tides need not be discussed. And tsunamis, those long, small amplitude waves caused by the earth's sudden movements, can have a great destructive effect once they reach coastal areas. Still, these constitute a different phenomena, and for most engineering applications the gravity band is the main cause of concern. In this work, unless otherwise specified, the term "wave" will be used as an equivalent to "surface gravity water wave".

Surface gravity water waves are complex and hard to describe mathematically. Their three-dimensionality, apparent randomness and non-linear effects governing their evolution make them a hard challenge from an analytical point of view. An accurate physical representation of waves requires a precise representation and description of both the water surface and the underwater velocity field. Using simplifying assumptions, wave theories have been developed to provide a framework for the many coastal engineering applications. The Airy (linear) and Stokes theories are used for deep water problems and a cnoidal theory can be used in shallow areas. These theories provide the engineering and scientific communities with working relationships between wave period, celerity and wavelength, as well as a description of the velocity field under

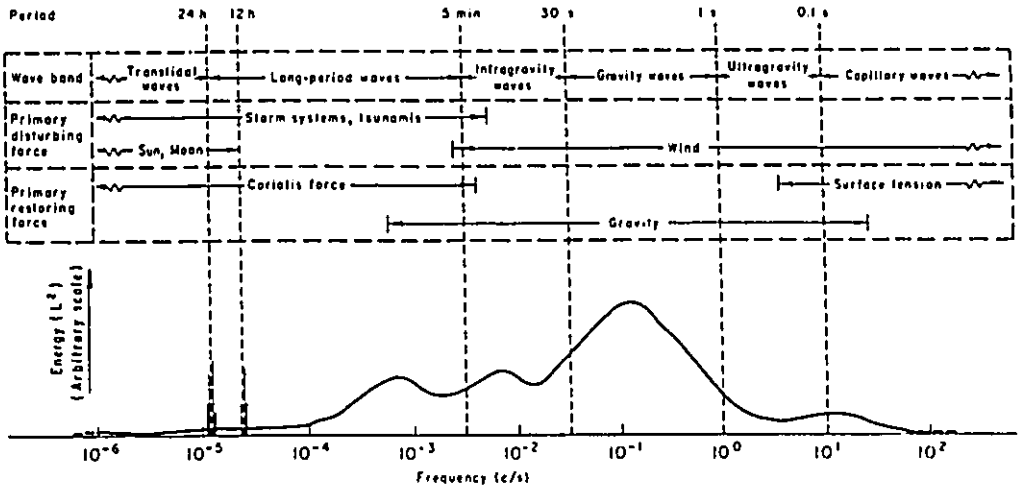

Fig.1.1 Approximate distribution of surface wave energy as a function of frequency, primary disturbing and restoring forces (from the Shore Protection Manual, 1984).

the water surface that give acceptable results for engineering applications. But an accurate description of the water surface is still an area of ongoing research. A representation of the wave energy as a function of frequency, the frequency spectrum, can easily be obtained since it can be extracted from a record of the water surface elevation at one given location. But surface gravity water waves are not long-crested but rather propagate with appreciable angular spreading about their mean direction. The assumption of a single direction of propagation, common to most engineering applications can potentially lead to significant errors, especially in cases of mixed seas where energy peaks can come from different directions. The specification of wave direction of propagation is by no means simple and the physics leading to this angular spread of energy are not well understood, the two main effects being the inherent variability of the source function (i.e. the wind), and non-linear effects between wave components and associated with wave breaking.

A more accurate representation of the wave field in the frequency-direction domain will lead to a better understanding of the wave processes which in turn will help engineers dealing with coastal applications. Waves are fundamental in shaping coastlines, determining the geometry and compositions of beaches, and can have potentially devastating effects on man-made structures both offshore and in coastal areas. Wave climates are important for the design of harbors, waterways, and shore protection measures, where a significant part of the wind energy transmitted to waves is dissipated. The accurate estimation of wave energy and direction of propagation is important for the handling and design of marine vehicles, and has many applications for the offshore industry, particularly the petroleum industry. These applications encompass engineering design, operational efficiency, safety and protection of the environment. A better representation of the surface structure of random seas will also benefit scientists and

limnologists by leading to improved hindcasting and forecasting methods. Finally, a recent area of concern deals with atmospheric pollution. Water occupies roughly 70% of the planet's surface and plays a fundamental role with the atmosphere in regulating the earth's climate. The geological record indicates that the earth's fragile atmosphere is the result of millions of years of complex interaction between air and water. Through breaking, waves mix air and water very efficiently, and account for almost all of the exchange between the atmosphere and water. An accurate description of the ocean surface would be valuable to air-water exchange studies.

Since very little is known about the physical processes leading to the angular spread of energy observed in wave fields, the problem is presently untractable analytically speaking and field observations become the only way of looking at wave directional properties. The problem then becomes part technical, part theoretical. What properties of the water surface should be measured and from these measurements how do we calculate an estimate of the angular spreading of energy and how do we know the estimate is accurate ? Clearly, in this case, the method of estimating the directional properties is as important as the data. A bad estimate, whether or not it was obtained from good data will still be useless, especially when high resolution directional information is needed. The first part of the problem can be dealt with since most wave measuring devices record either the water surface elevation and/or the surface slopes. Other properties of the wave field can also be measured, such as the water surface curvatures and the orbital velocity below the waves, but linear theory allows a direct correspondence to be made between any measured wave properties and the water surface elevation through the use of an appropriate transfer function. The second part of the problem is complex and is the main topic of this work: to establish a basis for selecting an appropriate method of calculating an estimate of the angular spread of energy, and to find a method that will give accurate estimates in various

environmental conditions. If a reliable method of estimation can be formulated, then accurate measurements of wave directional properties can be made which will lead to a better understanding of the growth, evolution and attenuation of wave fields. Ultimately, these will lead to better, safer, and possibly cheaper design criteria for engineering applications.

CHAPTER 2

WATER WAVES: A BRIEF REVIEW

This brief summary is not intended as a complete review of the basics of surface gravity water waves. It is merely an attempt to introduce basic wave notation and lay part of the theoretical foundation relevant to the following chapters. More detailed information can be found in a paper by Bishop and Donelan (1988) or in the books by Phillips (1977), Lighthill (1978), Kinsman (1965) and Dean and Dalrymple (1984). A good introduction on the basics of surface gravity water waves as well as an extensive review of engineering applications is provided by the U.S. Army Corps of Engineers' "Shore Protection Manual" (1984). An effort was made to use notation as consistent as possible with the standard set by the International Association for Hydraulic Research (1987).

For a one-dimensional sinusoidal wave, an expression for the free water surface elevation η is given by:

$$\eta(x,t) = a \cos \theta_x \tag{2.1}$$

where

$$\theta_x = 2\pi \left(\frac{x}{L} - \frac{t}{T}\right) \tag{2.2}$$

a is the wave amplitude defined as half the wave height H (see Figure 2.1), t is the time, x the

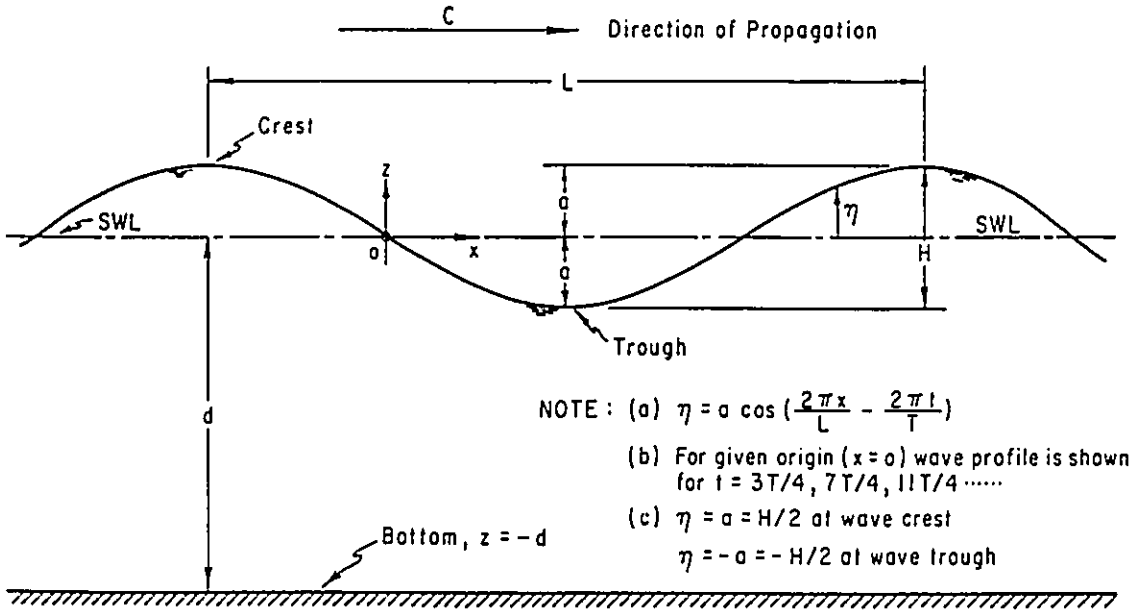

Fig.2.1 One dimensional, sinusoidal, progressive wave - definition of terms (from the Shore Protection Manual, 1984).

position along the x-axis, L the wavelength and T the wave period. Using Eqs. 2.1 and 2.2,

$$\eta(x,t) = a \cos\left[2\pi\left(\frac{x}{L} - \frac{t}{T}\right)\right] = a \cos(kx - \omega t) \tag{2.3}$$

with the wavenumber k and angular frequency ω defined as:

$$k = \frac{2\pi}{L} \qquad \omega = \frac{2\pi}{T} = 2\pi f \tag{2.4}$$

with f the frequency ($f = 1/T$). For convenience and simplicity, complex notation is often used. Using Euler relationships:

$$e^{i\beta} = \cos\beta + i\sin\beta \tag{2.5}$$

$$e^{-i\beta} = \cos\beta - i\sin\beta \tag{2.6}$$

Eq. 2.3 can be rewritten as:

$$\eta(x,t) = R\, a\, e^{i(kx - \omega t)} \tag{2.7}$$

where R denotes the real part. Equations of the form of Eq. 2.7 are often implicitly assumed to be non-imaginary in which case the cipher R is absent.

In the more realistic case of a sinusoidal wave propagating in a two-dimensional space we define the wavenumber vector $\vec{k}$,

$$\vec{k} = (k_x, k_y) = (|\vec{k}| \cos\theta, |\vec{k}| \sin\theta) \tag{2.8}$$

with $|\vec{k}| = k$ and θ is the wave direction of propagation. The subscripts x and y represent orthogonal directions in a Cartesian two-dimensional space. In a complex form, the water surface elevation can then be represented as:

$$\eta(\vec{x},t) = R\, a\, e^{i(\vec{k}\cdot\vec{x} - \omega t + \phi)} \tag{2.9}$$

where $\vec{x} = (x,y)$ is the spatial coordinates vector and ϕ is the phase angle of the sinusoidal wave relative to $\vec{x} = (0,0)$. Eq. 2.9 can be rearranged as:

$$\eta(\vec{x},t) = R\, e^{i(\vec{k}\cdot\vec{x} - \omega t)} dA \tag{2.10}$$

with

$$dA = a\, e^{i\phi} = a\cos\phi + a\, i \sin\phi \tag{2.11}$$

Then,

$$dA\, dA^{*} = a^2 \tag{2.12}$$

and

$$\phi = arg(dA) \tag{2.13}$$

where dA^{*} and arg are respectively the complex conjugate and the argument of dA.

To further generalize the case of one sinusoidal wave in a two-dimensional space, using the assumption that the water surface of a sea state can be represented by the summation of an infinite number of sinusoidal waves with various frequencies ω and wavenumbers $\vec{k}$, we can rewrite Eq. 2.10 as:

$$\eta(\vec{x},t) = R \int_{\omega} \int_{\vec{k}} e^{i(\vec{k}\cdot\vec{x} - \omega t)} dA(\vec{k},\omega) \tag{2.14}$$

which is often referred to as the Fourier-Stieljes representation of the sea surface.

Using time series of the water surface elevation, spectral analysis has been a common tool to characterize the energy of sea states in the frequency domain, in terms of the one-dimensional frequency spectrum $F(\omega)$ or $F(f)$, in which case the energy of each spectral

component or frequency band is related to the square of its amplitude ($a^2/2$). The energy of a sea state can be further characterized by adding information on the direction of travel of each spectral component, to obtain the two-dimensional directional spectrum $S(\omega,\theta)$ where the energy is a function not only of the frequency band but of the direction as well. Using the Fourier-Stieljes representation of the sea surface (Eq. 2.11), we have

$$dA(\vec{k},\omega)\, dA(\vec{k},\omega)^* = a^2(\vec{k},\omega) \tag{2.15}$$

which can then be directly related to the energy spectrum

$$S(\vec{k},\omega)\, d\vec{k}\, d\omega = \frac{1}{2}\overline{dA(\vec{k},\omega)\, dA(\vec{k},\omega)^*} \tag{2.16}$$

where $S(\vec{k},\omega)$ represents the wave vector and frequency spectral density in the interval $[\vec{k};\vec{k}+d\vec{k}]$ and $[\omega,\omega+d\omega]$. The overbar denotes a mean value. The wavenumber-frequency spectrum is a function of k, ω and θ. Using the small amplitude wave theory which assumes linearity of the wave field, ω and k can be related through the linear dispersion relationship

$$\omega^2 = \frac{2\pi g}{L}\tanh\left[\frac{2\pi d}{L}\right] \tag{2.17}$$

where d is the water depth and tanh is the hyperbolic tangent function. For deep water ($d/L > 0.5$), the tanh function asymptotically approaches 1 and the linear dispersion relationship is simply given by $\omega^2 = gk$. With the assumption of linearity of the wave field (see Kinsman for a presentation of the small amplitude wave theory) and using Eq.2.17, the wavenumber-frequency spectrum is then uniquely represented by ω and θ and becomes a directional spectrum so that:

$$S(\theta,\omega)d\theta d\omega = \frac{1}{2}\overline{dA(\theta,\omega)\, dA(\theta,\omega)^*} \tag{2.18}$$

where $S(\theta,\omega)$ represents the directional spectral density in the interval $[\theta,\theta+d\theta]$ and $[\omega,\omega+d\omega]$.

The two-dimensional directional spectrum $S(\theta,\omega)$ is generally expressed as the product of the one-dimensional frequency spectrum $F(\omega)$ and a normalized directional spreading function $D(\theta,\omega)$:

$$S(\theta,\omega) = F(\omega)\, D(\theta,\omega) \tag{2.19}$$

where the function $D(\theta,\omega)$ specifies the directional spreading of energy at each frequency band of the spectrum. The main problem in the determination of the directional spectrum $S(\theta,\omega)$ lies in the evaluation of the normalized spreading function $D(\theta,\omega)$.

CHAPTER 3

ESTIMATION OF DIRECTIONAL SPECTRUM

Many methods to estimate the wave directional spectrum are now available. In this chapter the theory behind most of the currently available methods will be reviewed. The following estimation techniques will be reviewed in an assessment of the current available methods:

Pitch Roll Buoy (PRB): Longuet-Higgins et al.(1963)

Clover-Leaf Buoy (CL): Mitsuyatsu et al.(1975), Tsanis and Brissette (1992)

Maximum Likelihood Method (MLM): Capon (1969), Isobe et al.(1984)

Iterative MLM (IMLM): Pawka (1983), Oltman-Shay and Guza (1984), Krogstad et al.(1987)

Eigenvector MLM (EVMLM): Marsden and Juszko (1986)

Convolutive MLM (CMLM): Tsanis and Brissette (1992a)

Maximum Entropy Method (MEM): Lygre and Krogstad (1986)

The approach of fitting an a priori known function to the data will not be discussed here since the goal of this work is to focus on estimates that yield a "model-free" characterization of the distribution. The only other methods available are the Minimum Nastiness Method of Long and Hasselmann (1979) and Lawson and Long (1983) and a refinement of the same method presented by Herbers and Guza (1990). The former was not implemented because, as pointed out by Marsden and Juszko (1987), it is weakly dependent on an a priori chosen directional distribution, and the latter because it requires time consuming iterations to solve the nonlinear

inverse problem. As pointed out by Herbers and Guza (1990), a simplification of the computational scheme is possible by relaxing the non-negativity constraint of the solution, but this appears to be impractical for routine data analysis of wave data. The implementation of an iterative scheme to solve the non-linear system of equations of Long and Hasselman (1979) or the slightly different scheme of Herbers and Guza (1990) is difficult and the resulting scheme is unstable (Marsden, pers.comm.). Finally, the Bayesian approach of Hashimoto, Kobune and Kameyama (1987) was also not implemented. This approach uses the MLM formulation but also imposes that the solution be the "smoothest" possible. This added constraint severely complicates the problem and makes the implementation of the computational scheme very difficult. The method also requires at least four measurements of the wave field to be stable, making it impossible to use for both pitch-roll-heave buoys and three-wavestaff arrays. These methods all have good potential in resolving directional seas but their limitations make them impractical for routine data analysis of wave data.

The theory behind each reviewed method will be described at length. This is necessary to lay the theoretical background needed for the next chapters and also because there is no currently available review of these techniques in the literature which starts from the basics.

3.1. DIRECT FOURIER TRANSFORM METHODS

3.1.1. Pitch-Roll-Heave Buoy

The Direct Fourier Transform Method (DFT) was first implemented by Longuet-Higgins, Cartwright and Smith (1963) and is still very widely in use today, especially for routine analysis of wave data. The method is generally used for buoy data and was originally designed

for a heave-pitch-roll buoy which records the water surface elevation at its center (heave signal) and the water surface slopes in the east and north directions (angles of pitching and rolling). These three quantities can be denoted as:

$$\eta(t,\vec{x}) \qquad \frac{\partial \eta(t,\vec{x})}{\partial x} \qquad \frac{\partial \eta(t,\vec{x})}{\partial y} \tag{3.1}$$

Using the Fourier-Stieljes representation of the sea surface (Eq. 2.14), the above quantities can be rewritten as:

$$\eta(t,\vec{x}) = R\iint_{\omega\theta} e^{i(\vec{k}\cdot\vec{x}-\omega t)} dA(\theta,\omega) \tag{3.2}$$

$$\frac{\partial \eta(t,\vec{x})}{\partial x} = R\iint_{\omega\theta} i\,k\cos\theta\, e^{i(\vec{k}\cdot\vec{x}-\omega t)} dA(\theta,\omega) \tag{3.3}$$

$$\frac{\partial \eta(t,\vec{x})}{\partial y} = R\iint_{\omega\theta} i\,k\sin\theta\, e^{i(\vec{k}\cdot\vec{x}-\omega t)} dA(\theta,\omega) \tag{3.4}$$

The cross-correlation function between any two quantities (or autocorrelation function if $i = j$) is defined by (where τ is the lag):

$$R_{ij}(\tau) = \frac{1}{T}\int_{t}^{t+T} f_i(t)\, f_j(t+\tau) dt \tag{3.5}$$

Identifying the heave, pitch and roll signals with the subscripts 1, 2 and 3, we have for the case $\vec{x}=(x,y)=(0,0)$:

$$R_{11}(\tau) = \frac{1}{T}\int_{t}^{t+T} \eta(t) \iint_{\omega\theta} e^{-i\omega(t+\tau)} dA(\theta,\omega)\, dt \tag{3.6}$$

which can be rearranged to

$$R_{11}(\tau) = \int_{\omega} \left[\frac{1}{T} \int_{t}^{t+T} \eta(t)\, e^{-i\omega t} dt \right] \int_{\theta} e^{-i\omega\tau} dA(\theta,\omega) \tag{3.7}$$

The brackets contain the expression for the direct Fourier transform of the water surface elevation. The transform is expressed in the positive frequency domain by dA^* (see Eqs. 2.12 to 2.13) and we can rewrite 3.7 as:

$$R_{11}(\tau) = \frac{1}{2} \int_{\omega} dA(\omega)^* \int_{\theta} e^{-i\omega\tau} dA(\theta,\omega) \tag{3.8}$$

Since

$$dA(\omega)^* = \int_{\theta} dA(\theta,\omega)^* \tag{3.9}$$

we can write

$$R_{11}(\tau) = \frac{1}{2} \iint_{\omega\theta} dA(\theta,\omega)^* dA(\theta,\omega)\, e^{-i\omega\tau} = \iint_{\omega\theta} S(\omega,\theta)\, e^{-i\omega\tau}\, d\theta d\omega \tag{3.10}$$

The cross-spectrum of any two quantities Φ_{jk} is given by the Fourier Transform of the cross-correlation function R_{jk}. The cross-spectrum (or power spectrum if $j=k$) is defined by its real (co-spectrum) and imaginary (quad-spectrum) parts such that $\Phi_{jk} = C_{jk} + iQ_{jk}$. The power spectrum of Eq. 3.10 is given by:

$$C_{11} = \frac{1}{T} \int_{t}^{t+\tau} R_{11}(\tau)\, e^{-i\omega\tau} d\tau \tag{3.11}$$

and,

$$C_{11} = \frac{1}{T} \int_{t}^{t+\tau} \int_{\omega} \int_{\theta} S(\omega,\theta)\, e^{i\omega\tau}\, e^{-i\omega\tau}\, d\theta\, d\omega \tag{3.12}$$

which finally gives:

$$C_{11} = \iint_{\omega\theta} S(\omega,\theta)\, d\theta\, d\omega \tag{3.13}$$

Similarly we can find the power spectra and cross spectra of the heave, pitching and rolling signals. At each given frequency they are given by:

$$C_{11}(\omega) = \int_0^{2\pi} S(\omega,\theta) d\theta \tag{3.14}$$

$$C_{22}(\omega) = \int_0^{2\pi} k^2 \cos^2\theta\, S(\omega,\theta) d\theta \tag{3.15}$$

$$C_{33}(\omega) = \int_0^{2\pi} k^2 \sin^2\theta\, S(\omega,\theta) d\theta \tag{3.16}$$

$$Q_{12}(\omega) = \int_0^{2\pi} k \cos\theta\, S(\omega,\theta) d\theta \tag{3.17}$$

$$Q_{13}(\omega) = \int_0^{2\pi} k \sin\theta\, S(\omega,\theta) d\theta \tag{3.18}$$

$$C_{23}(\omega) = \int_0^{2\pi} k^2 \sin\theta \cos\theta\, S(\omega,\theta) d\theta \tag{3.19}$$

The co-spectra C_{12} and C_{13} and quad-spectrum Q_{23} are all equal to zero which indicates a $\pi/2$ phase between the elevation and slope signals and no phase difference between the slope signals.

At any given frequency ω_k, one can express the directional spectrum as a Fourier series:

$$S(\omega_k,\theta) = \frac{1}{2}a_0+a_1\cos\theta+b_1\sin\theta+a_2\cos(2\theta)+b_2\sin(2\theta)+\cdots \tag{3.20}$$

where by definition:

$$a_0 = \frac{1}{\pi}\int_0^{2\pi} S(\omega_k,\theta)\,d\theta \tag{3.21}$$

and

$$a_n+ib_n = \frac{1}{\pi}\int_0^{2\pi} S(\omega_k,\theta)\left[\cos(n\theta)+\sin(n\theta)\right]d\theta = \frac{1}{\pi}\int_0^{2\pi} S(\omega_k,\theta)\,e^{in\theta}\,d\theta \tag{3.22}$$

Rearranging Eqs. 3.14 to 3.22, it can easily be shown that the first five Fourier coefficients are given by:

$$a_0 = \frac{1}{\pi}C_{11} \qquad a_1 = \frac{1}{\pi k}Q_{12} \qquad a_2 = \frac{2}{\pi k^2}(C_{22}-C_{33}) \tag{3.23}$$

$$b_1 = \frac{1}{\pi k}Q_{13} \qquad b_2 = \frac{2}{\pi k^2}C_{23} \tag{3.24}$$

We can compute the power spectra and cross-spectra directly from the time series of the heave, pitch and roll signals and, as a first approximation of the directional spectrum, we can form the partial Fourier series

$$S(\omega_k,\theta) \approx \hat{S}(\omega_k,\theta) = a_0+a_1\cos\theta+b_1\sin\theta+a_2\cos(2\theta)+b_2\sin(2\theta) \tag{3.25}$$

Whether or not Eq. 3.25 is a good approximation of the true directional spectrum depends on the

importance of the neglected higher order terms. To gain some more insights, we can replace Eq. 3.21 and Eq. 3.22 in Eq. 3.25 to give:

$$\hat{S}(\omega_k,\theta) = \frac{1}{2\pi}\int_0^{2\pi} S(\omega_k,\alpha)\left[1+2\cos\alpha\cos\theta+2\sin\alpha\sin\theta+2\cos(2\alpha)\cos(2\theta)+2\sin(2\alpha)\sin(2\theta)\right]d\alpha \quad (3.26)$$

which can be rearranged in the following form

$$\hat{S}(\omega_k,\theta) = \frac{1}{2\pi}\int_0^{2\pi} S(\omega_k,\alpha)\left[1+2\cos(\alpha-\theta)+2\cos\left[2(\alpha-\theta)\right]\right]d\alpha \quad (3.27)$$

Eq. 3.27 indicates that the approximation $\hat{S}(\omega_k,\theta)$ is in fact a smoothed average of the actual function $S(\omega_k,\theta)$ by a weighting function $W(\alpha-\theta)$. Since $W(\alpha-\theta)$ can be negative, so can $\hat{S}(\omega_k,\theta)$ whereas $S(\omega_k,\theta)$ is strictly positive. One of many possible alternative approximations to $S(\omega_k,\theta)$ is given by Longuet-Higgins et al.(1963) as:

$$S(\omega_k,\theta) \approx \hat{S}(\omega_k,\theta) = a_0+\frac{2}{3}(a_1\cos\theta+b_1\sin\theta)+\frac{1}{6}(a_2\cos(2\theta)+b_2\sin(2\theta)) \quad (3.28)$$

The new weighting function

$$W(\alpha-\theta) = \frac{8}{3}\cos^4\left[\frac{1}{2}(\alpha-\theta)\right] \quad (3.29)$$

is a non-negative decreasing function of $|\alpha-\theta|$ and has a RMS (root mean square) width of 51°.

3.1.2. Cloverleaf buoy

The DFT method was extended to cloverleaf buoy measurements by Cartwright and Smith (1964) and Mitsuyasu et al.(1975). In addition to the water surface elevation and surface

slopes, a cloverleaf buoy also measures the curvatures of the water surface. These signals are denoted by:

$$\eta(t,\vec{x}) \quad \frac{\partial\eta(t,\vec{x})}{\partial x} \quad \frac{\partial\eta(t,\vec{x})}{\partial y} \quad \frac{\partial^2\eta(t,\vec{x})}{\partial x^2} \quad \frac{\partial^2\eta(t,\vec{x})}{\partial y^2} \quad \frac{\partial^2\eta(t,\vec{x})}{\partial x\partial y} \tag{3.30}$$

Using the curvature signals and a similar approach to the one previously described, the angular harmonics of order 3 and 4 can be calculated and are found to be given by:

$$\begin{aligned} a_3 &= \frac{1}{\pi k^3}(4Q_{24}-3k^2Q_{12}) \qquad a_4 = \frac{1}{\pi k^4}(8C_{44}-8k^2C_{22}+k^4C_{11}) \\ b_3 &= \frac{1}{\pi k^3}(3k^2Q_{13}-4Q_{35}) \qquad b_4 = \frac{1}{\pi k^4}(4k^2C_{23}-8C_{56}) \end{aligned} \tag{3.31}$$

The approximation to the true directional spectrum then becomes

$$S(\omega_k,\theta) \approx \hat{S}(\omega_k,\theta) = a_0 + \sum_{n=1}^{4}(a_n\cos(n\theta) + b_n\sin(n\theta)) \tag{3.32}$$

Again, it can be shown that the estimate $\hat{S}(\omega_k,\theta)$ is equal to the real spectrum $S(\omega_k,\theta)$ averaged by a weighting function $W(\alpha-\theta)$. In order to make $\hat{S}(\omega_k,\theta)$ non-negative, an alternative approximation is given by:

$$S(\omega_k,\theta) \approx \hat{S}(\omega_k,\theta) = a_0 + \sum_{n=1}^{4}\left[W_n(a_n\cos(n\theta) + b_n\sin(n\theta))\right] \tag{3.33}$$

with

$$W_n = \begin{bmatrix} \frac{8}{9} & \frac{28}{45} & \frac{56}{165} & \frac{14}{99} \end{bmatrix} \tag{3.34}$$

The weighting function is approximately proportional to $\cos^{16}(\frac{\pi}{2})$ and has a RMS width of 29°.

3.2. MAXIMUM LIKELIHOOD METHODS

3.2.1. Maximum Likelihood Method (MLM)

The use of the Maximum Likelihood Method as a way to reconstruct two-dimensional energy spectra has its origin in the field of seismic waves. Capon (1969) used the method to obtain high-resolution wavenumber spectra from an array of sensors. The straight extension to the study of wave data from an array of sensors was done by Oakley and Lozow (1977), Davis and Regier (1977) and Jefferys et al.(1981).

The cross power spectral density (CPSD) matrix obtained from an array of sensors for a frequency ω_k is defined as:

$$\hat{C}_{ij}(\omega_k) = \left[\overline{\frac{f_i(\omega_k)}{|f_i(\omega_k)|} \quad \frac{f_j^*(\omega_k)}{|f_j(\omega_k)|}} \right] \tag{3.35}$$

where $f_i(\omega_k)$ and $f_j(\omega_k)$ are the Fourier transform of the signals from the ith and jth sensors (at frequency ω_k). The overbar indicates that some averaging (over frequency bands or within different blocks at a given frequency) is necessary to achieve a statistically reliable estimate of the true CPSD. The averaging is a standard practice in spectral analysis. The lack of sufficient averaging leads to high coherencies, even between incoherent signals. Averaging a number of blocks at least equal to the number of sensors should insure reliability of the spectral estimates while normalization by the moduli of the Fourier transforms avoids errors caused by unequal sensor calibrations (Jefferys et al., 1981). The normalization can also be done directly on the

signal to ensure similar RMS spread of the signal from each sensor. If a sea state can be represented by the summation of a number of monochromatic waves of power $S(\theta_j,\omega_k)$ coming from directions θ_j , with $j=1,...,N$, then the true CPSD that should be measured (for a given frequency or frequency band ω_k) is:

$$C(\omega_k) = \sum_{j=1}^{N} X(\theta_j,\omega_k)\, X^H(\theta_j,\omega_k)\, S(\theta_j,\omega_k) \tag{3.36}$$

where the superscript H denotes the complex transpose (Hermitian transpose) and $X(\theta_j,\omega_k)$ is the column vector of size M (where M is equal to the number of sensors) with

$$X_p(\theta_j,\omega_k) = e^{ik(\cos\theta_j r_{xp}+\sin\theta_j r_{yp})} = e^{\vec{ik}\cdot\vec{r_p}} \tag{3.37}$$

where $\vec{r_p}=(r_{xp},r_{yp})$ are the x,y coordinates of the pth sensor. One can see that $k(\cos\theta_i r_{xp}+\sin\theta_i r_{yp})$ is the phase difference (in radians) between the pth sensor and the origin ($\vec{x}=(0,0)$), and consequently $e^{\vec{ik}\cdot\vec{r_p}}$ is the complex phase lag between the same sensor and the origin (see also Eqs. 2.10 to 2.13). Often the notation is seen to be $e^{-\vec{ik}\cdot\vec{r_j}}$ which changes the sign of the phase lag (complex phase lag between the origin and the pth sensor). One should note that the CPSD's are not equal depending on the notation (one being the complex conjugate of the other) and that a 180° lag will exist between the respective directional spectra. Assuming the case of a unit energy monochromatic wave from direction θ_j, Eq. 3.36 becomes:

$$C(\omega_k) = X(\theta_j,\omega_k)\, X^H(\theta_j,\omega_k) \tag{3.38}$$

then, X can also be considered as being the array response to a plane wave of unit amplitude. The problem is, having an estimate $\hat{C}(\omega_k)$ of the true CPSD, to find an inverse of Eq. 3.36 that

will yield an estimate of $S(\theta,\omega_k)$. From Eq. 3.36, since the CPSD is formed by the linear combination of the array transfer function in every direction, it is natural to seek an estimate of $S(\theta_j,\omega_k)$ which is a linear combination of the available data $C(\omega_k)$. The chosen estimate has the form:

$$\hat{S}(\theta_j,\omega_k) = A^H(\theta_j,\omega_k)\, C(\omega_k)\, A(\theta_j,\omega_k) \tag{3.39}$$

where A is a complex column vector of size M. Eq. 3.39 can be rewritten after dropping the frequency dependence notation (ω_k) for simplicity,

$$\hat{S}(\theta_j) = A^H(\theta_j)\left[\sum_{i=1}^{N} X(\theta_i)\, X^H(\theta_i)\, S(\theta_i)\right] A(\theta_j) \tag{3.40}$$

which is rearranged to:

$$\hat{S}(\theta_j) = \sum_{i=1}^{N}\left[A^H(\theta_j)\,(X(\theta_i)\, X^H(\theta_i))\, A(\theta_j)\, S(\theta_i)\right] \tag{3.41}$$

Since for two column matrices P and Q, we have $P^H(QQ^H)P = (P^HQ)^2 = (Q^HP)^2$, we can rewrite Eq. 3.41 as:

$$\hat{S}(\theta_j) = \sum_{i=1}^{N}\left[|A^H(\theta_j)\, X(\theta_i)|^2\, S(\theta_i)\right] \tag{3.42}$$

where the absolute value sign simply emphasizes the positiveness of the system. Finally, rearranging 3.42 we find

$$\hat{S}(\theta_j) = |A^H(\theta_j)\, X(\theta_j)|^2 S(\theta_j) + \sum_{i\neq j}\left[|A^H(\theta_j)\, X(\theta_i)|^2 S(\theta_i)\right] \tag{3.43}$$

Eq. 3.43 outlines the facts that the MLM estimate will always be positive and greater than its true value. We want to select the complex vector $A(\theta_j)$ which will correctly estimate the energy from direction θ_j while minimizing the contribution from other directions θ_i. It then becomes an optimization problem under a constraint, which consists in minimizing Eq. 3.43 with respect to $A(\theta_j)$ under the constraint

$$|A^H(\theta_j)\, X(\theta_j)|^2 = 1 \quad or \quad A^H(\theta_j)\, X(\theta_j) = 1 \tag{3.44}$$

A simple analogy to the constraint problem is presented in Appendix 1. The optimization problem can be solved using Lagrange multiplier theory (Lacoss (1971); Jefferys et al., (1981)) which gives the function to be minimized as:

$$L(A(\theta_j),\mu) = A^H(\theta_j)\, C\, A(\theta_j) + \mu\, (A^H(\theta_j)\, X(\theta_j) - 1) \tag{3.45}$$

where μ is a Lagrange multiplier which is determined in the course of solution. Lagrange multiplier theory tells us that the constrained optimization problem is equal to finding the stationary values of the unconstrained function presented in Eq. 3.45. A demonstration of that, following Gottfried and Weisman (1973) is presented in Appendix 2. The minimization of the unconstrained Lagrangian function will be presented in a subsequent chapter. The solution of the problem will be shown in Chapter 7 to give an estimat of the energy of the form

$$\hat{S}(\theta_i,\omega_k) = \frac{\varepsilon_s}{X^H(\theta_i,\omega_k)\, C^{-1}(\omega_k)\, X(\theta_i,\omega_k)} \tag{3.46}$$

where $C^{-1}(\omega_k)$ denotes the inverse of the CPSD and ε_s is a scaling factor which equates the total energy at frequency ω_k to the power in the point spectrum (one dimensional power spectrum). The scaling is needed since, as shown in Eq. 3.43, the MLM estimate of the energy is always

greater than its true value. To avoid singularity of the CPSD matrix, it is advisable to induce a perturbation following a technique suggested by Capon (1969)

$$C(\omega_k) = (1-r)\, C(\omega_k) + r\, I \qquad 0< r \ll 1 \tag{3.47}$$

where I is an identity matrix. This perturbation is equivalent to adding incoherent noise to the sensors which decreases the resolution of the MLM (Jefferys et al., 1981). For this reason it is advisable to use as small as possible a value of r. Typically, and depending on the computational tool accuracy available, r will be $O(10^{-5})$ to $O(10^{-9})$. The effect of the perturbation will be discussed in a subsequent chapter.

This original derivation of the MLM was intended for the analysis of wavestaff data (multiple water elevation data in space) and was extended to mixed instruments array by Isobe et al.(1984). They found that a general form of the MLM was given by:

$$\hat{S}(\theta_i,\omega_k) = \frac{\varepsilon_s}{\sum_m \sum_n C^{-1}_{mn}(\omega_k)\, H^*_m(\theta_i,\omega_k)\, H_n(\theta_i,\omega_k)\, e^{i\vec{k}(\vec{x}_n-\vec{x}_m)}} \tag{3.48}$$

where $H_j(\theta_i,\omega_k)$ is the transfer function which linearly relates any mixed array measurement to the water elevation. In the case of an array of wavestaffs, all the transfer functions H_j are equal to 1 and Eq. 3.48 reverts to Eq. 3.46. Eq. 3.48 can be rewritten as:

$$\hat{S}(\theta_i,\omega_k) = \frac{\varepsilon_s}{\Xi^H(\theta_i,\omega_k)\, C^{-1}(\omega_k)\, \Xi(\theta_i,\omega_k)} \tag{3.49}$$

with

$$\Xi = \begin{bmatrix} H_1 e^{i\vec{k}\cdot\vec{x}_1} \\ H_2 e^{i\vec{k}\cdot\vec{x}_2} \\ \cdot \\ \cdot \\ H_n e^{i\vec{k}\cdot\vec{x}_n} \end{bmatrix} \tag{3.50}$$

and:

$$\Xi^H = \begin{bmatrix} H_1^* e^{-i\vec{k}\cdot\vec{x}_1} \\ H_2^* e^{-i\vec{k}\cdot\vec{x}_2} \\ \cdot \\ \cdot \\ H_n^* e^{-i\vec{k}\cdot\vec{x}_n} \end{bmatrix}^T \tag{3.51}$$

In the case of a pitch-roll-heave signal, Eq. 3.50 becomes:

$$\Xi = \begin{bmatrix} 1 \\ ik\cos\theta \\ ik\sin\theta \end{bmatrix} \tag{3.52}$$

where k is the wavenumber which can be obtained from the linear theory, or more appropriately directly from the CPSD estimates (see Eqs. 3.14 to 3.19):

$$k = \left[\frac{C_{22} + C_{33}}{C_{11}} \right]^{1/2} \tag{3.53}$$

where the subscripts 11, 22, and 33 respectively represent the heave, pitch and roll signals.

3.2.2. Iterative Maximum Likelihood Method (IMLM)

One of the problem of the MLM is that if one reconstructs the CPSD from the energy estimate $S(\theta,\omega_k)$, the reconstructed CPSD, $C^R(\omega_k)$, will be in most cases different from the

original CPSD, $C(\omega_k)$. In an attempt to correct this inconsistency, Pawka (1983) and Oltman-Shay and Guza (1984) used an iterative scheme to force the directional estimate to be consistent with the measured CPSD. This insures that the estimate is indeed one (of the many) possible solution of the directional spectrum. Many such schemes can be used, one of the simplest (Krogstad et al.(1988)) being

$$S_{(n+1)} = S_n + \upsilon \left[S_{MLM} - S^R_{MLM} \right] \tag{3.54}$$

where S_{MLM} is the MLM estimate and S^R_{MLM} is the MLM estimate obtained from the reconstructed CPSD matrix, $C^R(\omega_k)$ using S_n ($S_0=S_{MLM}$). S denotes the directional spectrum $S(\theta,\omega_k)$. A value of υ of 1.2 insured convergence and gave satisfactory results in an average of about 5 iterations (Krogstad et al.(1988)). It should be noted that the iterative scheme presented in Eq. 3.48 involves only the directional estimate and not the CPSD matrix itself. Generally a threshold criterion of the form

$$\xi = \frac{\max |S_{n+1} - S_n|}{S_n} \tag{3.55}$$

is used, so that the iterations may stop once the value of ξ drops below a predetermined threshold.

3.2.3. Eigen-Vector Maximum Likelihood Method (EVMLM)

The eigenvector method has its origin in acoustic wave detection. The rationale behind the technique is that the measured cross-spectral density matrix can be partitioned into noise and signal components (frequency dependence is assumed for simplicity of notation):

$$\hat{C} = C+N \tag{3.56}$$

where $\hat{C}$ is the estimate of the CPSD, C is the underlying real CPSD and N is the system noise. An estimate of the system noise $\hat{N}$ is obtained by computing the eigenvectors and corresponding eigenvalues of the CPSD. Since

$$\hat{C}_{ij} = \sum_{k=1}^{n} V_{kk} D_{ik} D_{kj}^{-1} \tag{3.57}$$

n eigenvectors and n the leading dimension of $\hat{C}$, one can assume that the signal is carried by the m largest eigenvalues while the noise is represented by the $n-m$ smaller eigenvalues such that:

$$\hat{C}_{ij} = \sum_{k=1}^{m} V_{kk} D_{ik} D_{kj}^{-1} + \sum_{l=m+1}^{n} V_{ll} D_{il} D_{lj}^{-1} = \hat{S} + \hat{N} \tag{3.58}$$

The spectral estimate is obtained through Lagrangian theory, similarly to the MLM, but, in this case however, only the estimate of the system noise is minimized which gives a function to be minimized of the fo m (from Eq. 3.44):

$$L(A(\theta_j),\mu) = A^H(\theta_j)\, N\, A(\theta_j) + \mu(A^H(\theta_j)\, \Xi(\theta_j) - 1) \tag{3.59}$$

which yields as a result

$$A(\theta) = \frac{\hat{N}^{-1}\Xi}{(\Xi^H \hat{N}^{-1} \Xi)^2} \tag{3.60}$$

which, upon substitution in Eq. 3.39, gives an estimate of the form:

$$\hat{S}(\theta_i,\omega_k) = \varepsilon_s \frac{\Xi_H \hat{N}^{-1}(\hat{S}+\hat{N})\hat{N}^{-1}\Xi}{(\Xi^H \hat{N}^{-1}\Xi)^2} \tag{3.61}$$

One of the problems of the method lies in the determination of m, the number of eigenvectors which carry the signal. In the case of a pitch-roll-heave signal, the two smallest eigenvectors are assumed to span the noise, since the use of one eigenvector leads to spurious peaks in the directional estimate (Marsden and Jusko, 1987). The use of two eigenvectors makes sense since they correspond to the pitch and roll signals which carry less power than the heave signal. Using only 1 eigenvector unbalances the CPSD matrix, leading to unrealistic solutions of the directional spectrum. For similar reasons, the partition between noise and signal becomes very problematic for wavestaff arrays (where the variance of all wavestaffs should be equal), making the EVMLM impractical.

3.2.4. Convolutive Maximum Likelihood Method (CMLM)

Tsanis and Donelan (1989) observed that their implementation of the MLM was returning an estimate which had a frequency dependent induced spreading. In order to correct for this effect, Tsanis and Brissette (1992a) proposed to convolve the MLM estimate by a window function. Let $S(\theta,\omega_k)$ be the directional spectrum obtained by the Maximum Likelihood Method at a given frequency or frequency band ω_k, and let $R(\theta,\omega_k)$ be the underlying real spectrum. Then,

$$S(\theta,\omega_k) = \int_{-\pi}^{\pi} R(\alpha,\omega_k)\, W(\theta-\alpha,\omega_k) d\alpha \tag{3.62}$$

where $W(\theta)$ is the window (transfer) function of the array and,

$$\int_{-\pi}^{\pi} W(\theta,\omega_k)\, d\theta = 1 \tag{3.63}$$

In computational form,

$$S(j,\omega_k) = \sum_{i=1}^{N} R(i,\omega_k)\, W(j-i,\omega_k) \tag{3.64}$$

where i and j are direction bin indices (for $d\theta=5°, N=72$). For a given frequency, the following system (using a simplified notation) is found:

$$\begin{array}{rcl} S_1 &=& R_1W_N + R_2W_{N-1} + R_3W_{N-2} + \ldots\ldots + R_NW_1 \\ S_2 &=& R_1W_1 + R_2W_N + R_3W_{N-1} + \ldots\ldots + R_NW_2 \\ \vdots & & \vdots \\ S_N &=& R_1W_{N-1} + R_2W_{N-2} + R_3W_{N-3} + \ldots\ldots + R_NW_N \end{array} \tag{3.65}$$

With a known window function, we have a set of N linear equations with N unknowns which can be easily solved using standard techniques. The window function is determined by using an input monochromatic wave to the MLM. For such a case, the real spectrum $R(\theta,\omega_k)$ can be represented by a Dirac delta function defined as

$$\delta(x-x_0) = 0 \qquad \text{for } x \neq x_0 \tag{3.66}$$

with

$$\int_{-\infty}^{\infty} \delta(x-x_0)\, dx = 1 \tag{3.67}$$

It follows that

$$R(\theta,\omega_k) = \delta(\theta-\theta_{max}) \tag{3.68}$$

which means that the spectrum is equal to zero except at $\theta=\theta_{max}$, and

$$S(j,\omega_k) = \sum_{i=1}^{N} \delta(i-i_{max}) W(j-i,\omega_k) = W(j-i_{max},\omega_k) \tag{3.69}$$

from which the window function $W(\theta,\omega_k)$ is determined.

3.3. MAXIMUM ENTROPY METHOD

The Maximum Entropy Method, which has its origin in spectral analysis (Burg, 1967; Lacoss, 1971), was simultaneously developed to calculate an estimate of the directional spectrum by Lygre and Krogstad (1986) and Kobune and Hashimoto (1986). Both derivations have significant differences.

Lygre and Krogstad (1986) formulation directly uses the Fourier coefficients computed in Eqs. 3.23 and 3.24. Normalizing all the coefficients to a_0 and rewriting them to a complex form, we define $f(\theta)$ as a positive function with integral equal to 1 and a Fourier series:

$$f(\theta) = \frac{1}{2\pi} \sum_{n=-\infty}^{\infty} c_n e^{in\theta} \quad , \qquad c_0 = 1, \qquad c_{-n} = c_n^* \tag{3.70}$$

The entropy of f, following Lygre and Krogstad (1986) is defined by:

$$H(f) = -\int_{-\pi}^{\pi} log\,(f(\theta))\, d\theta \tag{3.71}$$

and is maximized $H(f)$ subject to the constraint (in complex form)

$$\int_{-\pi}^{\pi} f(\theta)\, e^{-ik\theta}\, d\theta = c_n \tag{3.72}$$

which can be derived easily from Eqs. 3.14 to 3.23 and which simply states that the Fourier

coefficients of the maximizing function be equal to the input Fourier coefficients. The maximizing function can be shown to be equal to (Ulrych and Bishop, 1975; Lygre and Krogstad, 1986):

$$S(\theta) = \frac{1}{2\pi}(1 - \phi_1 c_1^* - \ldots - \phi_N c_N^*)/|1 - \phi_1 e^{-i\theta} - \ldots - \phi_N e^{-iN\theta}|^2 \tag{3.73}$$

which is the spectral density of the autoregressive system

$$\begin{bmatrix} 1 & c_1^* & . & . & c_{N-1}^* \\ c_1 & 1 & . & . & . \\ . & . & . & . & . \\ . & . & . & . & c_1^* \\ c_{N-1} & . & . & c_1 & 1 \end{bmatrix} \begin{bmatrix} \phi_1 \\ \phi_2 \\ . \\ . \\ \phi_N \end{bmatrix} = \begin{bmatrix} c_1 \\ c_2 \\ . \\ . \\ c_N \end{bmatrix} \tag{3.74}$$

In the pitch-roll-heave case, the first 2 "c" coefficients are known, from which ϕ_1 and ϕ_2 are found to be:

$$\phi_1 = (c_1 - c_2 c_1^*)/(1 - |c_1|^2) \tag{3.75a}$$

$$\phi_2 = c_2 - c_1 \phi_1 \tag{3.75b}$$

The directional spectrum estimate is then obtained directly from Eq. 3.73. In the case of data from a cloverleaf buoy, the first four c coefficients are known and Eq. 3.74 needs to be solved for the ϕ_i coefficients.

Kobune and Hashimoto (1986) derived a more general formulation for mixed-instruments arrays and used the more common definition of the entropy (also called Shannon's entropy) of:

$$H(f) = -\int_{-\pi}^{\pi} f(\theta)\, ln(f(\theta))\, d\theta \tag{3.76}$$

which is also maximized under the constraint given in Eq. 3.72. Using Lagrange multiplier theory, the maximization gives rise to a system of non-linear equations (Eqs. 9 to 12 of Kobune and Hashimoto, 1986) which can be solved using an iterative scheme only if the number of element measurements is less than four. According to Hashimoto et al. (1987), with four or more elements, the iteration fails to converge and the non-linear problem can't be solved. Nwogu (1989) was able to successfully solve the problem for arrays of wave gauges, at the expense of using a complex iterative scheme. Still the method will not converge for narrow distribution functions (Nwogu et al., 1987).

The Entropy definitions in Eqs. 3.71 and 3.76 are different. It can be seen that the entropy given by Eq. 3.71 is maximum for a narrow distribution function, whereas the entropy given by Eq. 3.76 is maximum for a uniform distribution. Essentially, amongst all the functions that satisfy Eq. 3.73, one approach chooses the function closest to uniform distribution, and the other the function closest to a Dirac Delta function. The two approaches seem contradictory, but it should be kept in mind that even though the number of functions satisfying the constraint given by Eq. 3.73 is in theory infinite, the functions themselves should not be too dissimilar in most cases.

CHAPTER 4

MODEL TESTS AND ANALYSIS OF DIRECTIONAL SEAS

As presented in the preceding chapter, a number of methods can be used to obtain an estimate of the wave directional spectrum. The problem lies in the selection of a best method which will yield the most accurate estimate of the true directional spectrum. Since the different methods can hardly be compared from a theoretical point of view, empirical testing will have to be used in order to provide an adequate answer to the above problem. Clearly, for that purpose, comparison of the different methods using field data is not adequate. This approach could help identify recurring differences between the various estimates and probably detect some biases of certain estimates, but since the true underlying directional distribution is unknown, it would prove impossible to draw definite conclusions. The only other alternative is to construct artificial data which is derived using known directional distributions. The simulated wave data can then be used to calculate estimates of the angular spreading of the sea which can then be tested against the known input directional distribution.

4.1. SIMULATION OF WAVE DATA

Having established the need and importance of simulating wave data, it is now necessary to identify the best approach for the simulations. Two avenues are possible. The first one involves the computation of artificial time series of the water surface elevation, from which a

Cross-Power-Spectral-Density (CPSD) matrix can be calculated, whereas the second one directly computes the artificial CPSD's and therefore foregoes the step of transforming the data from the time domain to the frequency domain. Both methods are described below with their respective advantages and disadvantages.

4.1.1. Simulation of time series of water surface elevation

Techniques for the simulation of the water surface elevation of directional seas have been developed for other applications than testing models of directional spectrum. Simulated time series of directional seas are needed to drive segmented wave generators used to perform hydraulic model tests and for any other application that needs a realistic representation of a wave field, such as the calculation of wave loads under various environmental conditions. Only the water surface elevation can be reconstructed using these techniques, but accurate time series of the water surface slopes can be indirectly obtained by using neighboring time series of the water surface elevation to compute the slopes.

Generating time series of the water surface elevation for monochromatic waves is a first step to test some characteristics of directional spectrum estimates, or the geometric properties of wavestaff arrays. The phase lag between each wave (in the case where more than one monochromatic wave is considered) and each wave staff is first computed:

$$\phi_i = k_j(x_i\cos\theta_j + y_i\sin\theta_j) \tag{4.1}$$

where ϕ_i is the phase difference for the i^{th} wave staff, k_j is the wavenumber of the j^{th} monochromatic wave considered, $\vec{x_i} = (x_i, y_i)$ is the position of the i^{th} wave staff and θ_j is the direction of propagation of the j^{th} wave. The Fourier coefficients (a + ib) for each wave

components of amplitude a are given by:

$$dA = \left(\frac{a}{2}\cos\phi + i\,\frac{a}{2}\sin\phi \right) \tag{4.2}$$

The energy of each monochromatic wave is given by:

$$dA^{*}dA = \frac{1}{2}a^{2} \tag{4.3}$$

Having computed the Fourier coefficients of all the monochromatic waves considered, the water surface elevation time series can be readily obtained from the inverse Fourier Transform of the frequency domain. The various individual signals can then be added up. Although tests with a number of monochromatic waves can prove informative, more realistic directional spectra (than the delta functions corresponding to the monochromatic case) need to be simulated. Two approaches can be used: the single summation model and the double summation model.

4.1.1.a The single summation model

In this model, each frequency component is characterized by one and only one single direction of propagation. Each basic frequency increment Δf (equal or smaller to the frequency resolution of the directional spectrum analysis program) is further subdivided into M sub-frequencies, each associated with one direction of propagation θ_i . Within each frequency increment, the complete spectrum of directions is then covered. The total number of frequencies considered N is then equal to the number of basic frequency increments multiplied by M. The model is expressed as:

$$\eta(x,y,t) = \sum_{i=1}^{N} a_i \cos\left[\vec{k}_i\vec{x} - \omega_i t + \phi_i\right] \tag{4.4}$$

with

$$\vec{k_i} = (k_x, k_y) = (k\cos\theta, k\sin\theta) \quad \text{and} \quad k = |\vec{k_i}| \tag{4.5a}$$

$$\vec{x} = (x, y) \tag{4.5b}$$

$$\omega_i = 2\pi i \Delta f / M \tag{4.5c}$$

$$a_i = \sqrt{2F(f_i)\, D(f_i, \theta_i)\, \Delta f \Delta\theta} \tag{4.5d}$$

$$\Delta\theta = \frac{2\pi}{M} \tag{4.5e}$$

$$\phi_i = 2\pi\, U[0,1] \tag{4.5f}$$

which indicates that the phase is selected randomly from a uniform deviate. Other alternatives for the phase or amplitude selection are available (see Miles, 1989) but are essentially equivalent. The wavenumber k is obtained from ω_i using the linear dispersion relationship $\omega_i^2 = kg\tanh(kd)$ with the water depth d. Since only one direction is associated with each frequency, the most efficient way to produce the water elevation time series is through an inverse Fourier Transform.

4.1.1.b The double summation model

The double summation model is expressed as:

$$\eta(x,y,t) = \sum_{i=1}^{N}\sum_{j=1}^{M} a_{ij}\cos\left[k_i(x\cos\theta_j + y\sin\theta_j) - \omega_i t + \phi_{ij}\right] \tag{4.6}$$

Where N is the number of frequency and M the number of directions. The double summation

model is simply a discrete version of a sea state that can be represented by adding up an infinite number of monochromatic wave trains propagating at all frequencies and directions with an amplitude compatible with a given directional spectrum. The biggest difference between the single and the double summation models is that the latter accepts waves coming from different directions at any given frequency.

4.1.1.c Results and comparison

For the purpose of testing spectral estimators, the best technique should give, for a long-enough time series, a good estimate of the CPSD matrix which will in turn give good, high-resolution directional spectrum estimates. The directional spectrum estimates should be able to reproduce the essential features of the input spectrum for a model to be considered adequate. A number of time series were computed using both summation models with various number of frequencies and directions. Figures 4.1 and 4.2 outline the results. In all of the tests, a given directional spectrum was used as an input, times series were computed, Fast-Fourier-Transformed, and a Maximum Likelihood Estimate was calculated from the cross-spectra between the wave signals. For all the tests, sampling rate was 20 Hz and 6 times series were computed in order to match the settings of the 6 wave-staffs array on the National Water Research Institute (NWRI) research tower (details given in a subsequent chapter). Figure 4.1 presents the MLM estimate for three different simulations using the single summation method. The left-hand-side (LHS) plots are the directional spectra (frequency-direction) and the RHS plots are the same, but multiplied by the frequency in order to emphasize details at higher frequencies. The first test uses 256 frequency increments with 64 directions, giving a 27 minute long time series of 32768 points. The second test uses 128 directions for a 55 minute long time series and 65536 data points. Finally, the last

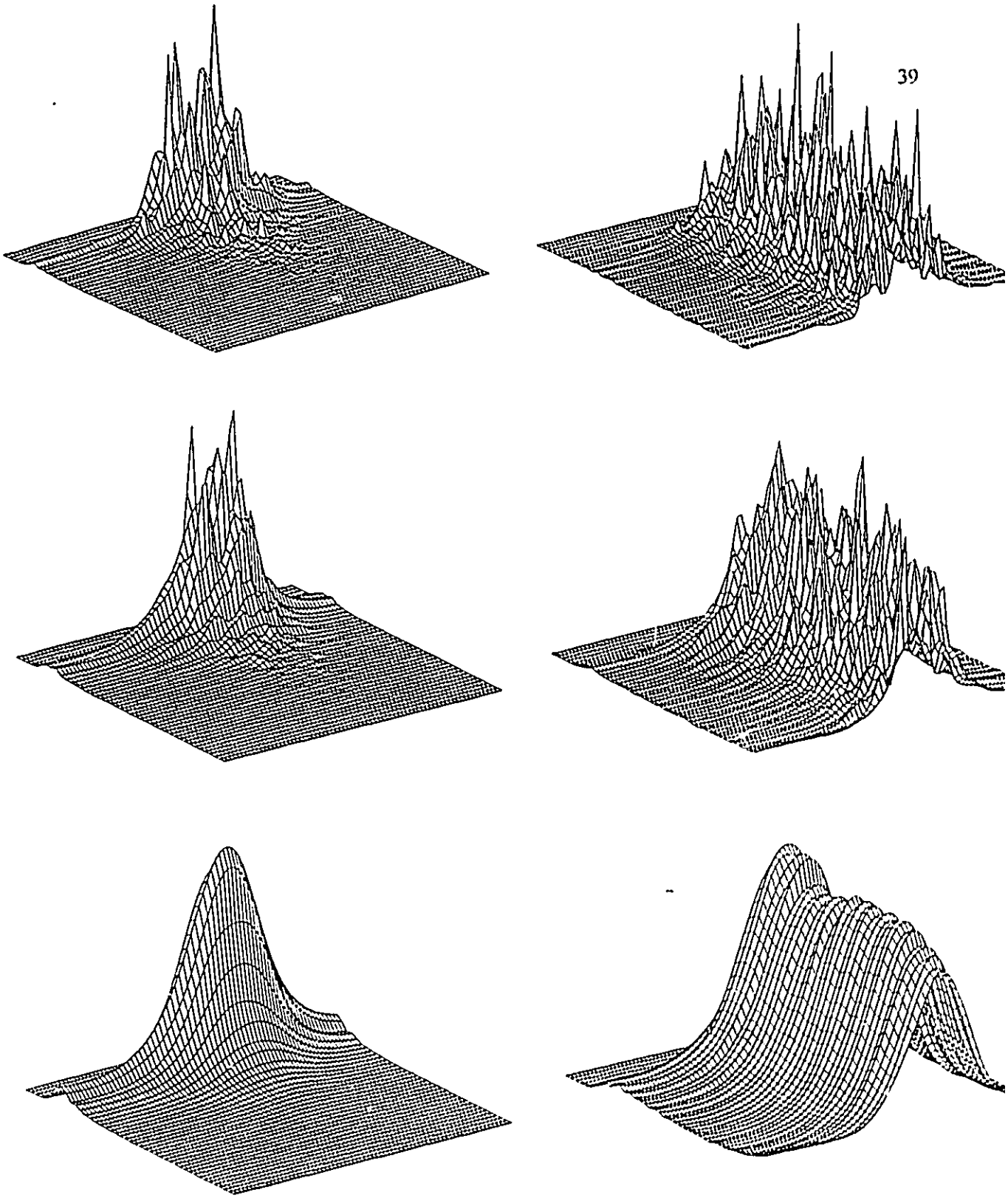

Fig.4.1 Wave directional spectrum (MLM estimate) from a six-wavestaff array signal obtained using a single summation model ($f = 0\text{–}1\ Hz$). The RHS plots are the same as the LHS but multiplied by f^3 in order to emphasize high-frequency features. Simulation parameters: Top- 256 frequencies, 64 directions for 32768 points, Middle- 256 frequencies, 128 directions for 65536 points , Bottom- 2048 frequencies, 256 directions for 1048576 data points.

test uses 2048 frequencies with 256 directions for a 14 hour long time series. Clearly, the first two simulations are not adequate for the purpose of comparing fine details in the resolution of directional spectrum estimates. The third test provides an estimate which is smooth and free of the random peaks characterizing shorter simulations. From these tests, predictably, it can be concluded that the more frequencies and directions are used, the better the cross-spectral estimates will be, giving smoother directional spectrum estimates. The problem is that to achieve a smooth spectral estimate, unreasonably long time series are needed. The third simulation had in excess of 1 million data points and the file generated with the 6 signals was 97 Megabytes long. Considering the amount of data generated and the high number of tests needed, this approach is impractical.

Figure 4.2 presents results from two simulations using the double-summation model, with 2048 frequency increments and 64 directions each. The first one was 10 minutes long (12000 data points) and the second one 50 minutes long. In both cases, it can be seen that the variability is still too high for these simulations to be considered acceptable. As noted by Miles and Funke (1987), the problem with double summation models is that wave components traveling in different directions at the same frequency are "phase-locked" together, resulting in a wave field which is neither ergodic or stationary. They also noted that in any frequency band, the energy will vary from 0 to 4 times its average value, independently of the number of wave directions used. Another problem with the model is the length of time needed to calculate the time series. In the two simulations presented in Figure 4.2, it was necessary to keep track of 131000 wave components at each sampling time which proved to be too slow, even on a fast Sun Sparcstation, to be reasonably used for many tests.

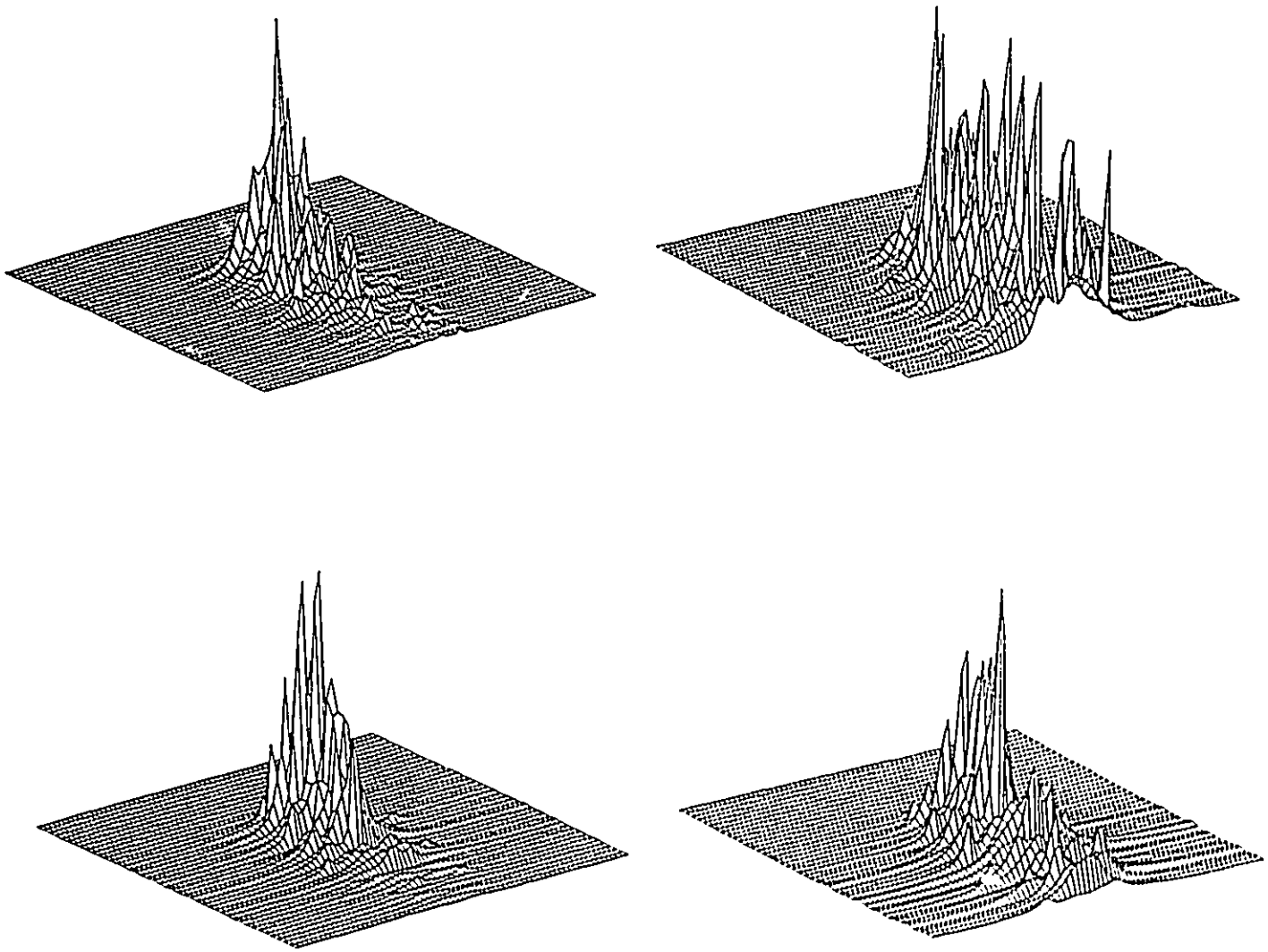

Fig.4.2 Wave directional spectrum (MLM estimate) from a six-wavestaff array signal obtained using a double summation model ($f = 0$–1 Hz). The RHS plots are the same as the LHS but multiplied by f^4 in order to emphasize high-frequency features. For both simulations 130000 wave components were used. Top- 12000 points, Bottom- 50000 points.

4.1.2. Simulation of cross-power-spectral-density matrix

The other option is to directly calculate the CPSD using equation (3.36):

$$C(\omega_k) = \sum_{j=1}^{N} X(\theta_j,\omega_k)\, X^H(\theta_j,\omega_k)\, S(\theta_j,\omega_k) \tag{4.7}$$

where $S(\theta_j,\omega_k)$ is a given directional spectrum. The main advantage in this approach lies in its simplicity. It also foregoes the computationally expensive steps of simulating time series of the water surface elevation and transforming the data from the time domain to the frequency domain. The full simulation from a time series may seem more complete since it includes the effect of windowing and averaging the initial data through the use of a FFT, but it should be noted that even though these effects can be significant, it might in fact be advisable to compare the different methods of estimating the directional spectrum without these effects, in order to observe the true behavior of the estimates. The effect of windowing and spectral smoothing are well documented in textbooks on spectral analysis and analysis of time series. And since simulated time series are not necessarily a good representation of sea states, these effects would better be investigated with field data. For these reasons, in all of the test cases, CPSD's were directly simulated using Eq. 4.7.

4.2. SOFTWARE FOR THE ANALYSIS OF DIRECTIONAL SEAS

Directional analysis of sea states is overall a relatively new, specialized and still under development field, and as such no software is available commercially. Work for this thesis will make extensive use of simulated and field data to calculate directional spectrum estimates and statistical parameters. Modules will also have to be provided for transforming the data

(windowing, FFT, smoothing...) and producing output results in the form of graphs and datafiles. To accomplish this task two programs were developed, with acronyms DIRSPEC and MIDSAP.

4.2.1. Program DIRSPEC

The DIRectional SPECtrum analysis program DIRSPEC was originally developed at the NWRI for use on their CYBER system. The original 4000 lines FORTRAN code was essentially geared toward the analysis of data from the six wave-staffs array on the Lake Ontario Research Tower. The source code was imported to McMaster University where it was extended to 6000 lines and adapted to work on both Workstations and PC based machines. The program is fully described in Tsanis and Brissette (1991) and the program structure is outlined in Figure 4.3. DIRSPEC calculates the wave directional spectra from a wavestaff array using five different methods. In addition, higher order statistics based on these methods can be evaluated. The program permits the analysis of three different types of data: monochromatic waves (up to 30 wave fronts), predetermined distributions ($sech^2$) and field data (3 to 6 wavestaffs). As illustrated in Figure 4.3, DIRSPEC requires two input files (one if no field data), the water surface elevation data and a setup datafile which contains the information for a given analysis such as sampling rate, position of wavestaffs etc. DIRSPEC handles and generates a large amount of data which have to be treated accordingly. The results are included in two datafiles. DATAFILE1 is an ASCII file containing all the results in a comprehensive form. Results for each method and associated statistics are outlined at each frequency. DATAFILE2 is a stripped down version which contains the results in a numbers-only form, ready to be imported in other commercially available software for plotting of the results. A complete description of the program structure can be found in Tsanis and Brissette (1991).

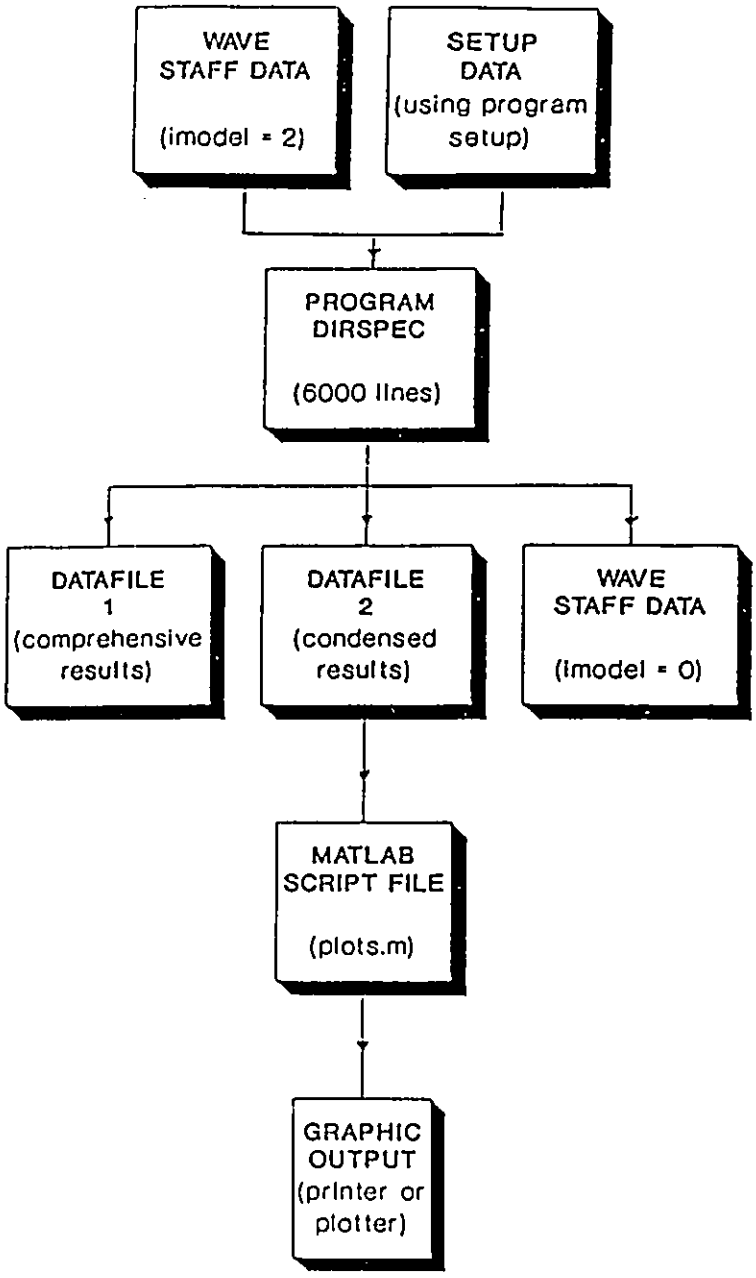

Fig.4.3 Input-Output structure of program DIRSPEC.

DIRSPEC is an efficient program for the analysis of wave-staff data but the length of the source code makes it difficult to modify, change or add segments of codes to the main program. The work in this thesis will require adding up routines to handle heave-pitch-roll data and many new routines for new methods of estimating the wave directional spectrum. Testing will require intensive work on only parts of the total code. For these reasons, it was judged impractical to further modify the structure of DIRSPEC and it was decided to implement a new code, more modular and using a more efficient programming language.

4.2.2. Program MIDSAP

The Multi-Instruments Directional Spectrum Analysis Program (MIDSAP) consists of a number of routines which perform different tasks. The approach of linking multiple routines provides flexibility and has the distinct advantage of allowing easy modifications of the linkage to better suit specific needs. The common platform for the different routines is the high-level MATLAB software package (The MathWorks, Inc.) for scientific and engineering numerical computation. MATLAB is derived from the matrix software developed by the LINPACK and the EISPACK project which represent the state-of-the-art in software for matrix computation. Versions of the MATLAB software package are available for most systems (DOS based PC, Macintosh, VAX and UNIX based machine) making the program very versatile. Computations within MATLAB are highly vectorized, insuring maximum performance. This is of primary importance since directional analysis of time series of wave data can be expensive from a computational viewpoint.

MIDSAP is subdivided into four main modules (Figure 4.4) which handle the different steps of the directional analysis. The first module deals with input data and handles both field

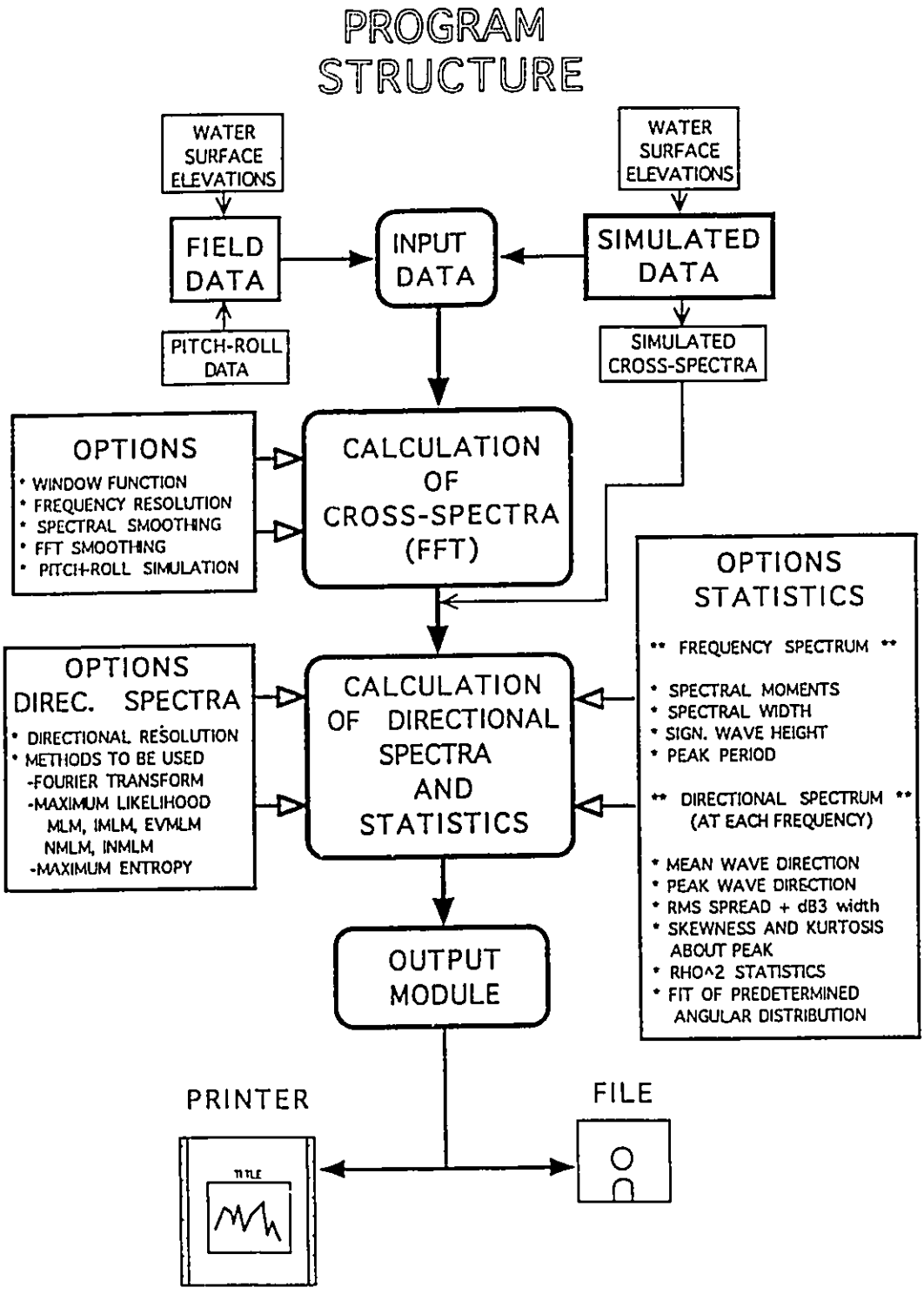

Fig.4.4 Program structure of the Multi-Instruments Directional Spectrum Analysis Program (MIDSAP).

and simulated data. The second module transforms the data from the time domain to the frequency domain and calculates the cross-spectra between the different input signals. The third (and most important) module uses the cross-spectra computed in the previous step to obtain the different directional spectrum estimates from which different statistics are calculated. Finally, the fourth module handles the results and redirects them to the printer/plotter or data files. The four modules are described below.

4.2.2.a Module 1- Generation of wave data

Even though in most cases MIDSAP will probably be used for field data analysis, there are still many applications which might require simulated data. Time series of any length can be produced within MIDSAP which uses a single-summation random Fourier coefficients method. The single-summation method was chosen because it produces homogeneous wave fields over a finite period of time (Miles, 1989). Simulated Cross-Power-Spectral-Density matrices (CPSD) can also be reconstructed, an important option when testing a new wave-gauge array geometry or when trying to select the best spectral estimation method for a particular application. The program comes with the Donelan, Hamilton and Hui (1985) representation for the frequency spectrum and two spreading functions, the $sech^2$ and the $\cos^2$. MIDSAP also allows for a user-specified directional spectrum.

Field data to be used by MIDSAP should already be in a corrected form but the program nevertheless performs a basic quality check. Initially, any linear trend in the data is removed. For wave gauge data, the variance of the signals is computed and a warning is issued if differences greater than 5% are observed. For heave-pitch-roll data, MIDSAP compares the calculated wavenumber to the theoretical one using linear theory and verifies that the phase shifts

between the heave and slope signals are close to $\pi/2$ leading to imaginary only cross-spectra. These tests assume a linear wave field and failure to meet these criteria does not necessarily indicate faulty data. Faulty data will almost invariably lead to spurious peaks in the sensitive non-linear directional spectrum estimates and this can also be used to assess data quality.

4.2.2.b Module 2- Spectrum analysis

All methods used to calculate wave directional spectrum estimates make use of the cross-spectra between the various wave signals. An important part of a directional analysis consists of transforming the time series to the frequency domain. The MATLAB Fast-Fourier-Transform (FFT) routine is used for that task. If the time series length is not a power a two, a slower algorithm is used. MIDSAP options allows for variable windowing and smoothing schemes. Windowing and smoothing are important topics since they both can affect the results of the directional analysis. Seven different windows (most of them included in the MATLAB package) can be used within MIDSAP. The choice of a window can be important for high resolution directional spectrum analysis since it can influence the ability of the FFT to recognize small secondary peaks or peaks of similar energy near the same frequency (in the frequency spectrum). See Harris (1978) for a discussion on the characteristics of windows in harmonic analysis. The initial frequency resolution is given by Sr/N_l where Sr is the sampling rate and N_l the length of a block of data. The time series is divided into a number a blocks (overlapping each other or not) which are separately windowed FFT'ed and averaged. The block size can be chosen so as to directly obtain the wanted frequency resolution, or directional spectrum estimates can be computed using a finer frequency resolution and subsequently averaged. The former technique (FFT smoothing) gives smoother estimates but could potentially hide fine details of the

directional spectrum. The technique to be used should be a function of the quality of the data and on the amount of information needed.

4.2.2.c Module 3- Directional parameters

MIDSAP provides the option of using most of the methods available to estimate the wave directional spectrum and to test these methods in order to select the most appropriate one for a given application. Basic parameters such as significant wave height, peak and average period are calculated from the frequency spectrum. In addition to basic directional parameters such as mean wave and peak wave direction, directional parameters are also calculated using the first moments (m_1 m_4) of the directional distribution at each frequency:

$$m_n = \frac{\int_{-\pi}^{\pi} (\theta-\bar{\theta})^n \hat{S}(\theta,\omega_k)\, d\theta}{\int_{-\pi}^{\pi} \hat{S}(\theta,\omega_k)\, d\theta} \tag{4.8}$$

The rms spread, skewness and kurtosis are then respectively given by:

$$\sqrt{m_1} \qquad \frac{m_3}{m_2^{1.5}} \qquad \frac{m_4}{m_2^2} \tag{4.9}$$

The ρ^2 statistics of Long (1980) which gives an estimate on how well a directional estimate accounts for the data is calculated (see Appendix 3 for details). Finally, MIDSAP allows known spreading functions ($sech^2$ and $\cos^2$) to be fitted to all directional estimates.

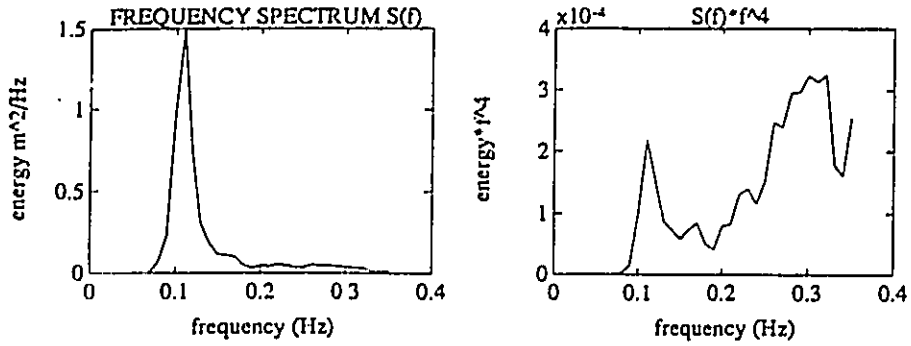

Fig.4.5 Sample output of MIDSAP (Frequency spectrum).

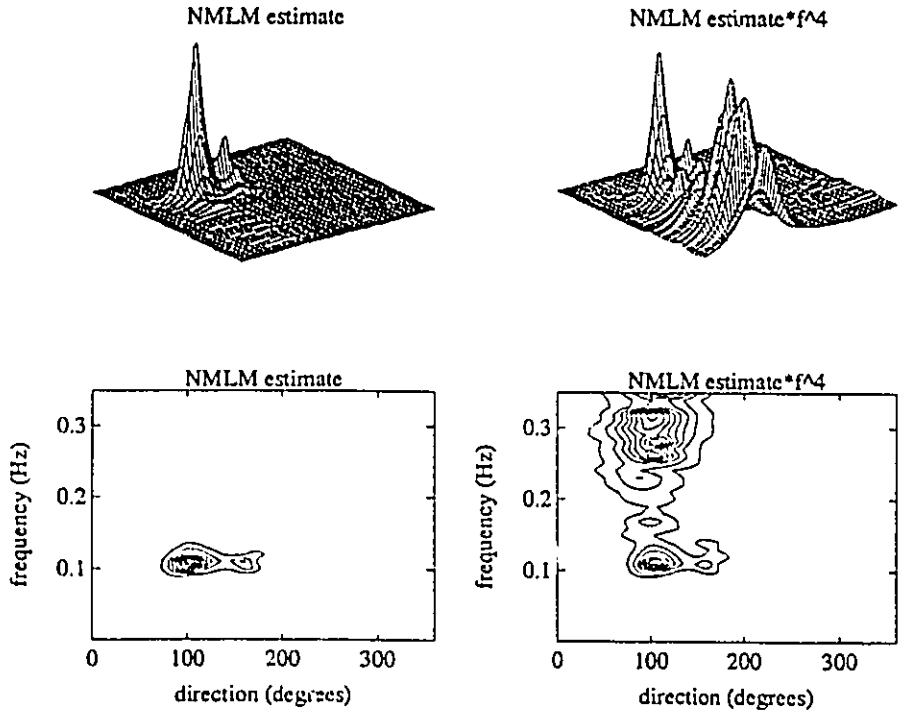

Fig.4.6 Sample output of MIDSAP (Directional spectrum estimates).

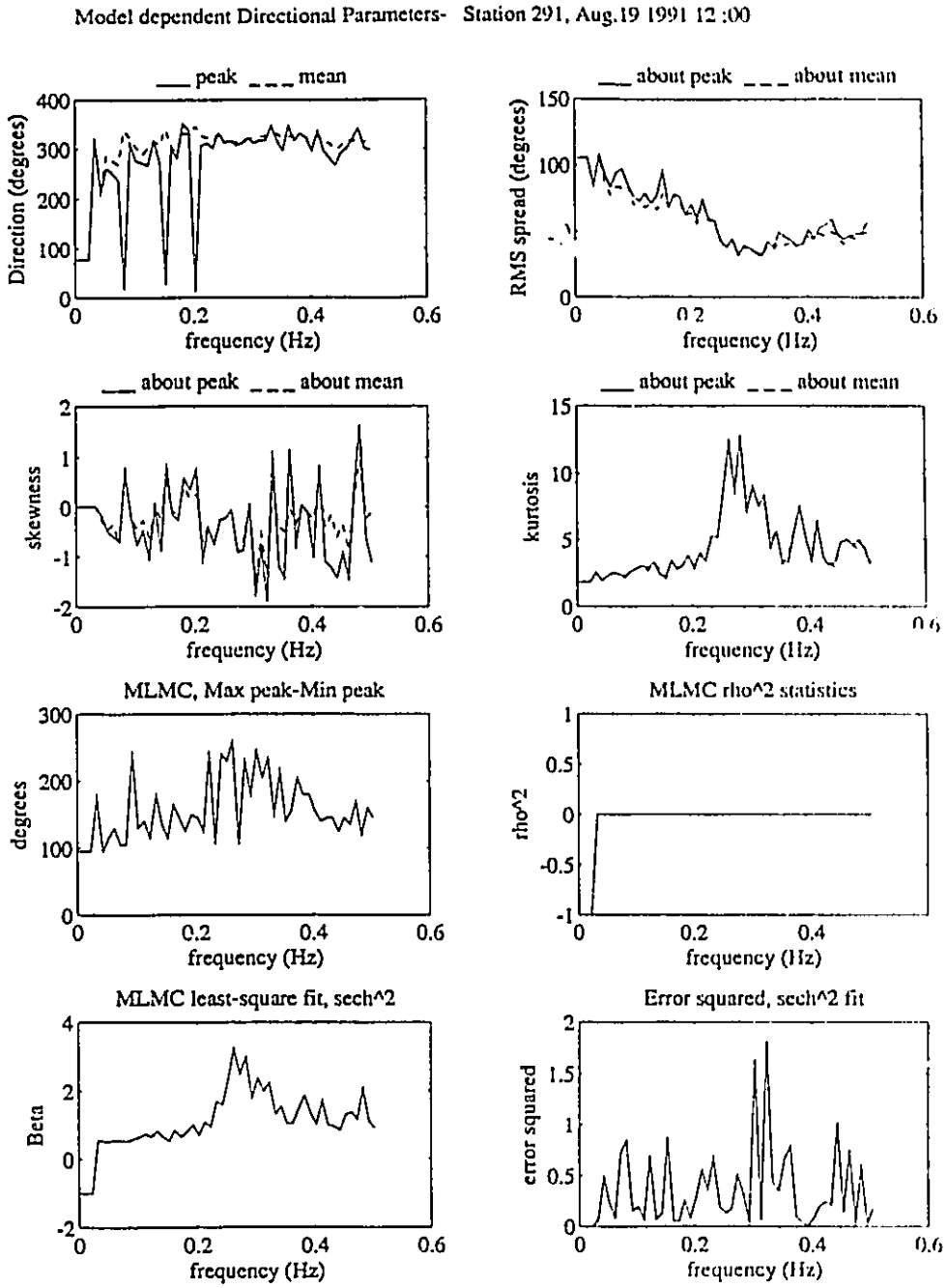

Fig.4.7 Sample output of MIDSAP (Directional parameters and statistics).

4.2.2.d Module 4- Output

MIDSAP automatically generates up to 86 three-dimensional, contour and X-Y plots that illustrate the results of the directional analysis. The graph file can be redirected to most available plotters and printers from within the MATLAB environment. Results can also be saved in ASCII format for use by other software packages. Figures 4.5, 4.6 and 4.7 show part of a typical output. Energy plots are always shown in normal units and multiplied by frequency to the fourth power in order to outline features at higher frequency (Figures 4.5 and 4.6).

4.2.2.e Program performance

Most of the routines being vectorized, the efficiency of the program is very high. For a 20 minutes long heave-pitch-roll data set sampled at 4 Hz (4800 data points), runtime for a full directional analysis (all directional estimates computed) was 8 minutes on a Sun Sparcstation and about 18 minutes on a 33 MHz 486-PC. Comparative results using DIRSPEC were around 15 and 33 minutes respectively.

CHAPTER 5

HEAVE-PITCH-ROLL DATA: COMPARISON OF EXISTING METHODS

In this chapter, the most common methods of estimating the wave directional spectrum will be evaluated. These are, the Direct Fourier Transform or pitch-roll-heave parametric method (herein noted as PRB), the Maximum Likelihood Method (MLM) and its iterative (IMLM) and eigen-vector (EVMLM) forms, and the Maximum Entropy Method (MEM). The tests performed will help identify the strong and weak points of each methods and as a result will help tc focus on the needs of better-performing methods.

5.1. TEST PROCEDURE

The comparison of the different directional spectrum estimators is based on different tests. In order to identify the inherent characteristics and biases of the different techniques, noise free CPSD were constructed using Eq. 4.7 and used as an input to the different spectral estimators. In the test cases where a frequency spectrum was needed, a DHH spectrum (Donelan, Hamilton and Hui, 1985) was used:

$$\phi(f) = \frac{\alpha_r g^2 (2\pi f)^{-4}}{f_p} \exp\left[-\left(\frac{f_p}{f}\right)^4\right] \gamma^{\exp\left[\frac{-(f-f_p)^2}{2\nu^2 f_p^2}\right]} \tag{5.1}$$

where

$$\alpha_r = 0.006W^{-0.55} \tag{5.2a}$$

$$\nu = 0.08(1+4W^3) \tag{5.2b}$$

$$\gamma = \begin{cases} 1.7-\log W\,; & 0.2 < W \le 1 \\ 1.7\,; & 1 < W < 1.2 \end{cases} \tag{5.2c}$$

and f_p is the peak frequency. The spectral parameters α_r (equilibrium range parameter), ν (peak width factor) and γ (peak enhancement factor) are functions of the wave age W only (W is the ratio of wave celerity at the spectral peak to the wind speed component in the direction of travel of the peak wave). The chosen spreading function is the hyperbolic secant squared function which yields a directional spectrum of the form:

$$S(f,\theta) = \frac{1}{2}\phi(f)\,\beta\,sech^2\left\{\beta\left[\theta-\bar{\theta}(f)\right]\right\} \tag{5.3}$$

where $\bar{\theta}(f)$ is the mean wave direction and β the spreading parameter given by:

$$\beta = \begin{cases} 2.61(f/f_p)^{+1.3} & ;\ 0.56 < \dfrac{f}{f_p} \le 0.95 \\ 2.28(f/f_p)^{-1.3} & ;\ 0.95 < \dfrac{f}{f_p} \le 1.6 \\ 1.24 & ;\ \textit{otherwise} \end{cases} \tag{5.4}$$

Then, isotropic noise was added in order to investigate the ability of the different estimators to pick a signal in the presence of noise. The signal to noise ratio (NSR) is defined as in Oltman-Shay and Guza (1984) and Marsden and Juszko (1987):

$$NSR = \frac{\int_0^{f} \int_0^{2\pi} N(f,\theta)\, d\theta\, df}{\int_0^{f} \int_0^{2\pi} S(f,\theta)\, d\theta\, df} \tag{5.5}$$

where $N(f,\theta)$ represents the noise function.

It should be noted that this definition of noise is not exactly commensurable with the true noise expected in the cases of field data. The use of isotropic noise such as defined in Eq. 5.5 will help test the ability of the differents methods to pick up a signal out of a system with a net DC component. The addition of noise should diminish the ability of some methods to pick the directional peak but, the input spectrum is still well defined. In the case of field data, incoherent noise will be embedded within the CPSD matrix and will tend to degrade the computed spectra, sometimes by creating spurious peaks. Since the incoherent noise can come from many different sources, the effect is extremely hard to simulate properly for test cases.

A final test was done by simulating a bimodal sea over a full range of frequencies. Using the $sech^2$ spreading with variable spreading over frequency, the test allowed multiple bimodal distributions to be investigated within a single test. Finally, the tests results were compared to one case of field data. These data come from the Surface Wave Dynamics Experiment (SWADE) which took place from October 1990 to April 1991 (Weller et al., 1991). This analysis of SWADE data is concerned with the Discus-N buoy. The Discus-N buoy was located at $73^{\circ}48.9'W$ longitude and $38^{\circ}11.6'N$ latitude, at the edge of the continental shelf offshore of Virginia. The water depth at these coordinates is 120 m. The Discus-N buoy was a heave-pitch-roll NDBC/SWADE 3 meters discus directional buoy. Details on instrumentation, data processing methods and quality control can be found in Anctil et al. (1992) and in a

subsequent chapter. Segments of data 34 minutes in length and sampled at 1 Hz were analyzed. Consecutive blocks of data were Fourier transformed and averaged, giving spectral estimates with bandwidth 0.0078 Hz and 32 degrees of freedom. Tables 5.1 and 5.2 provide a list of the simulation tests and field data presented in this thesis. In all of the test cases, the frequency range considered will be up to 0.5 Hz with a frequency bandwidth of 0.0078 Hz. This corresponds to a 1 Hz sampling rate and block size of 128 data points used in the analysis of SWADE field data.

5.2. TEST RESULTS

In a first step, the response of the different methods to unimodal distributions was investigated. Forty-one $sech^2$ distribution functions were generated with values of the spreading parameter β ranging from 1 to 5 and NSR values ranging from 0 to 0.25 giving a total of 164 simulated unimodal angular distributions. Figure 5.1 presents values of the ratio of the maximum peak of each estimate to the maximum peak of the input distribution for all the simulated cases. Figure 5.2 presents results in a similar format for the rms spread while Figures 5.3 and 5.4 display typical results of the angular distribution of energy at different frequencies, NSR and values of the spreading parameter β.

From these results, it can be seen that both the PRB parametric method and MLM consistently underpredict the maximum peak and overpredicts the spreading. The performance of the PRB parametric method degrades rapidly as the spreading function becomes narrower (higher β) while the performance of the MLM degrades with higher NSR. At low levels of isotropic noise (low NSR), which should be expected for normal-quality data, the MLM estimate

TABLE 5.1. Model Tests

TEST TYPE	noise to signal ratio	ϕ (f)	β values $sech^2$	0	f_p	W
unimodal distribution	0 to 0.25	-	1 to 5	180	-	-
unimodal sea	0.1	DHH	$\beta = function\,(f/f_p)$	180	0.15	1.2
bimodal sea	0.05	DHH	$\beta = function\,(f/f_p)$	100, 240	0.11, 0.2	1.2, 1.0

TABLE 5.2. Field Data

Run	segment	Julian date	GMT time	length (min)	Wind dir deg	U (m/s)
F68	150 to 184 min.	319	16.41	34.0	106	9.4

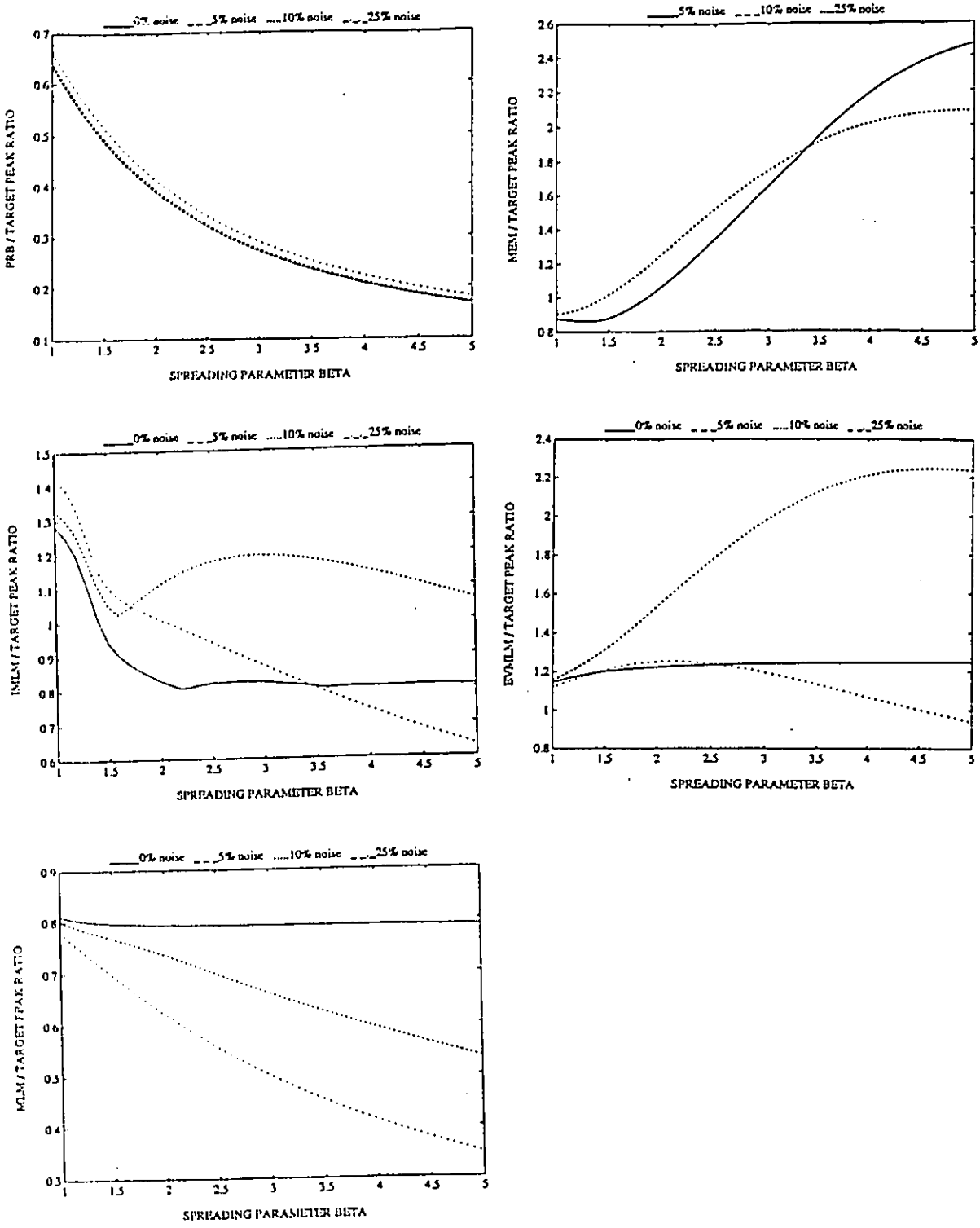

Fig.5.1 Ratio of Maximum Peak to Target Peak for each estimate as a function of the spreading parameter β and noise to signal ratio (NSR). MEM curve at 0% noise is omitted because estimates are bimodal.

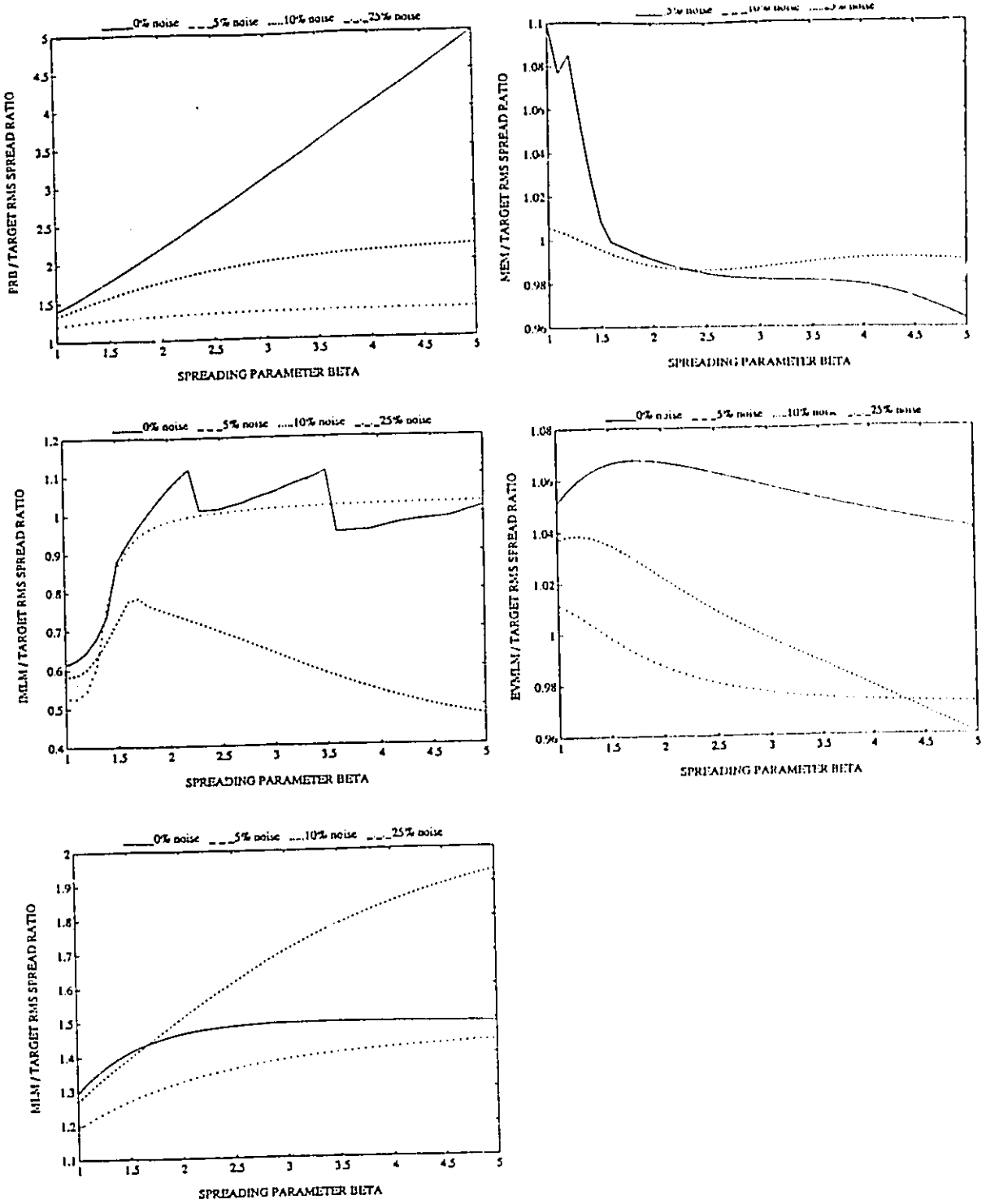

Fig.5.2 Ratio of RMS spread to Target RMS spread for each estimate as a function of the spreading parameter β and noise to signal ratio (NSR). MEM curve at 0% noise is omitted because estimates are bimodal.

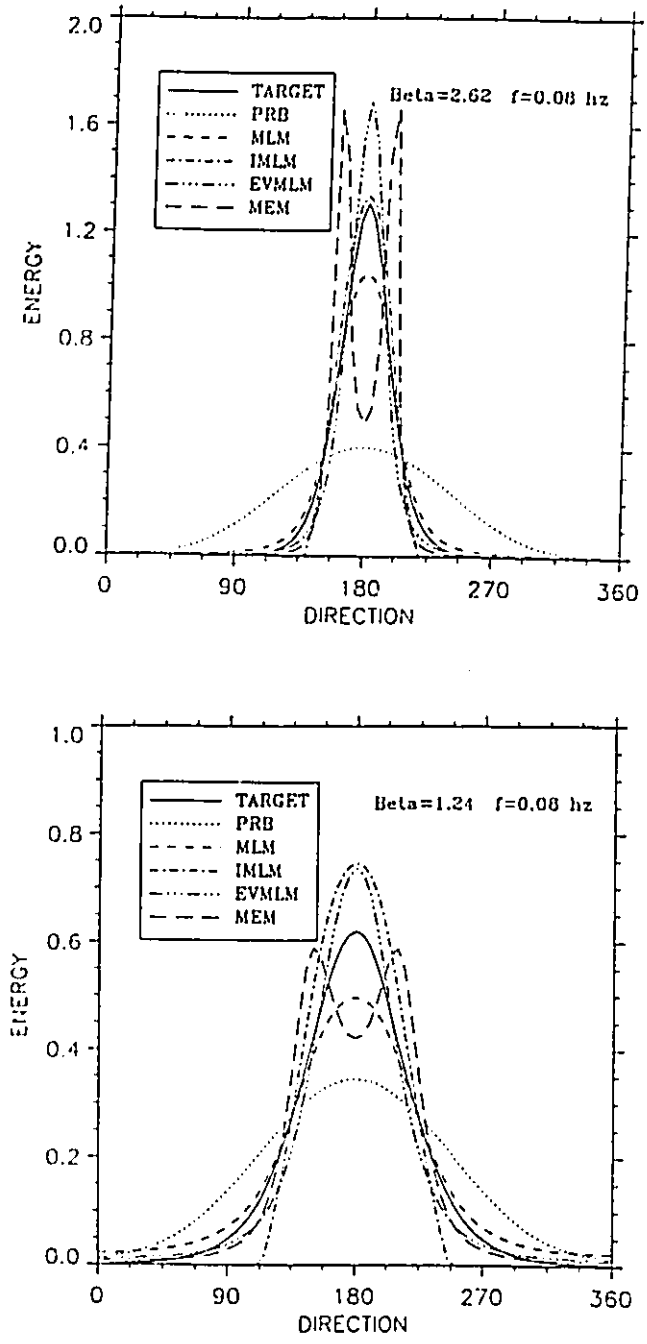

Fig.5.3 Directional spectrum estimates for a $sech^2$ spreading function. Top- β=2.62, f =0.08Hz, Bottom- β=1.24, f =0.08Hz.

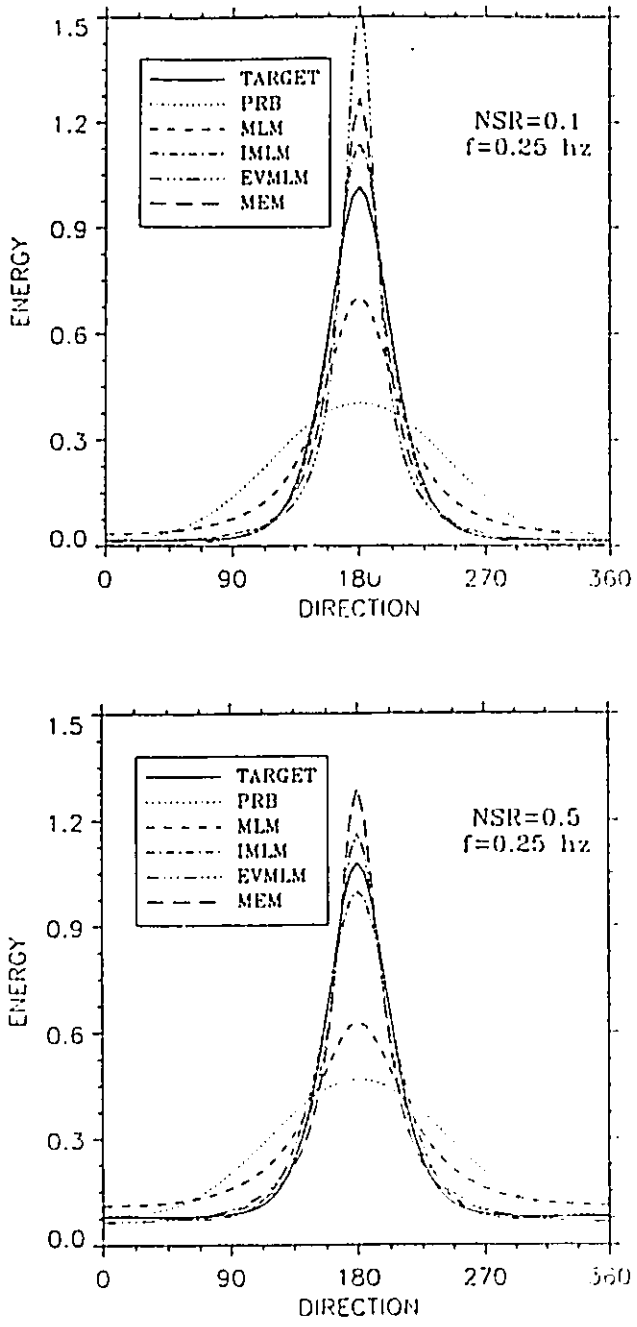

Fig.5.4 Directional spectrum estimates for a $sech^2$ spreading function. β=2.0, f =0.25Hz. Top- NSR = 0.1 Bottom- NSR = 0.5.

shows little dependence with values of the spreading parameter β. The MEM predicts the RMS spread very accurately in most cases but severely overpredicts the maximum peak. These two facts indicate that the MEM returns an estimate which does not preserve the shape of the input function. In addition, the MEM returns a bimodal estimate (Figure 5.3) at low NSR. Both the IMLM and EVMLM estimate characteristics are a function of the spreading of the input distribution functions, especially so at β values lower than 2.5. General trends are hard to isolate for those two methods but both estimates are found to improve at higher NSR. The IMLM generally gets better at higher frequencies while the performance of the EVMLM generally decreases slightly with increasing frequency.

It should be noted that the results were found to be independent of the frequency for the PRB parametric method, MLM and MEM. Results are wavenumber dependent for the IMLM and EVMLM, as shown in Figures 5.5a and 5.5b. The IMLM behavior with frequency is similar to the case of a wave gauge array as observed by Tsanis and Brissette (1992). For high signal to noise ratios, at low frequencies, the solution was rapidly found to oscillate resulting in impossible non-positive values of the directional spectrum. Setting negative values to zero was found to hinder convergence of the iterative scheme. In such cases, it was found that 3 iterations was a good compromise, insuring convergence to a reasonable accuracy while avoiding oscillations in all of the test cases. The EVMLM estimate becomes narrower at higher frequencies. This is a direct consequence of the way the input CPSD is partitioned between noise and signal and will be further discussed later.

In a next step, a unimodal sea was simulated using a DHH frequency spectrum with a peak frequency f_p=0.15 Hz, centered at 180° and with a NSR value of 0.1. The spreading function was the $sech^2$ with values of the spreading parameter β varying with frequency

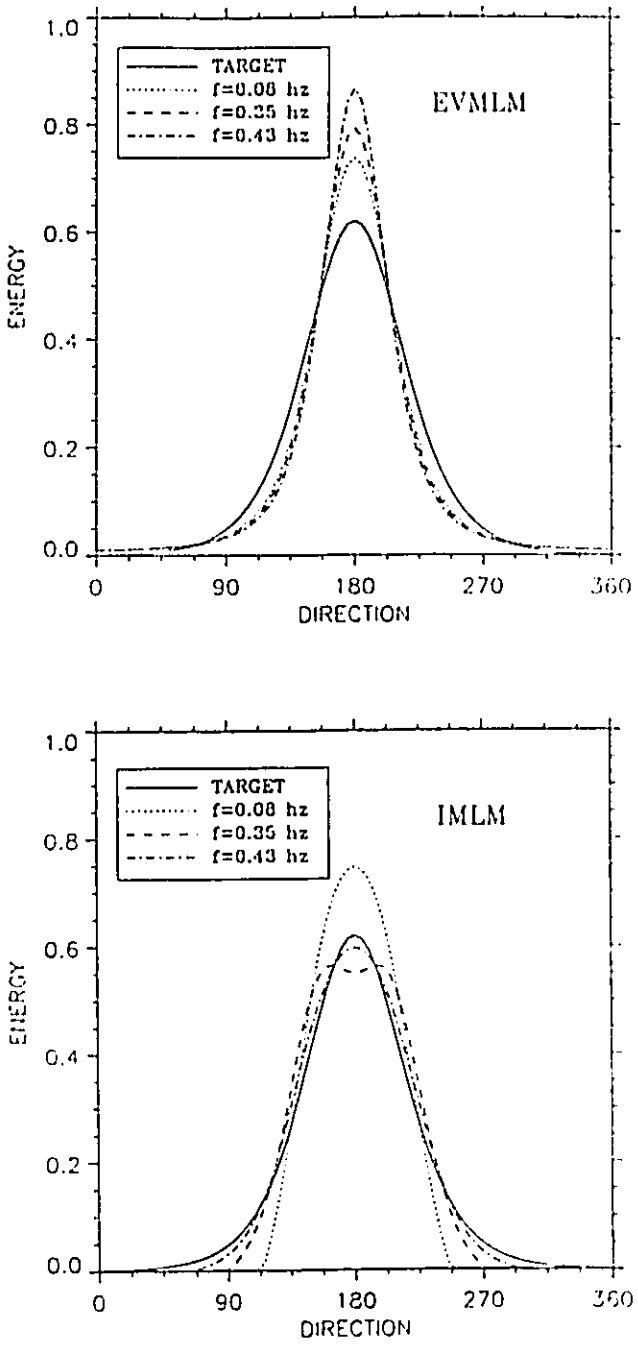

Fig.5.5 Frequency dependence of the results for the Top- EVMLM estimate and, Bottom- IMLM estimate. The other estimates are frequency independent.

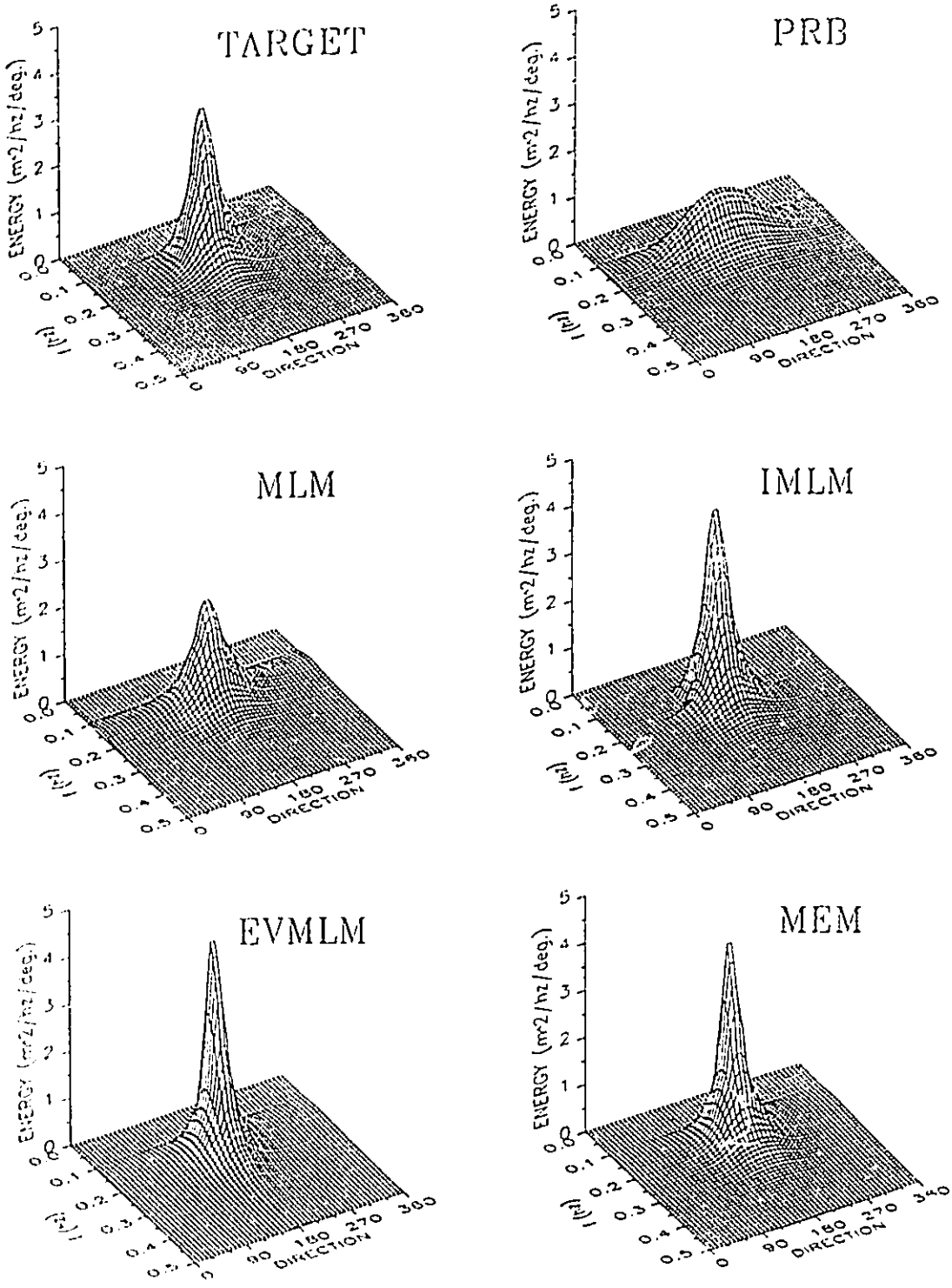

Fig.5.6 Surface plots of directional estimates for unimodal sea test case. DHH input spectrum with $sech^2$ spreading function, $f_p = 0.15Hz$, $W = 1.2$.

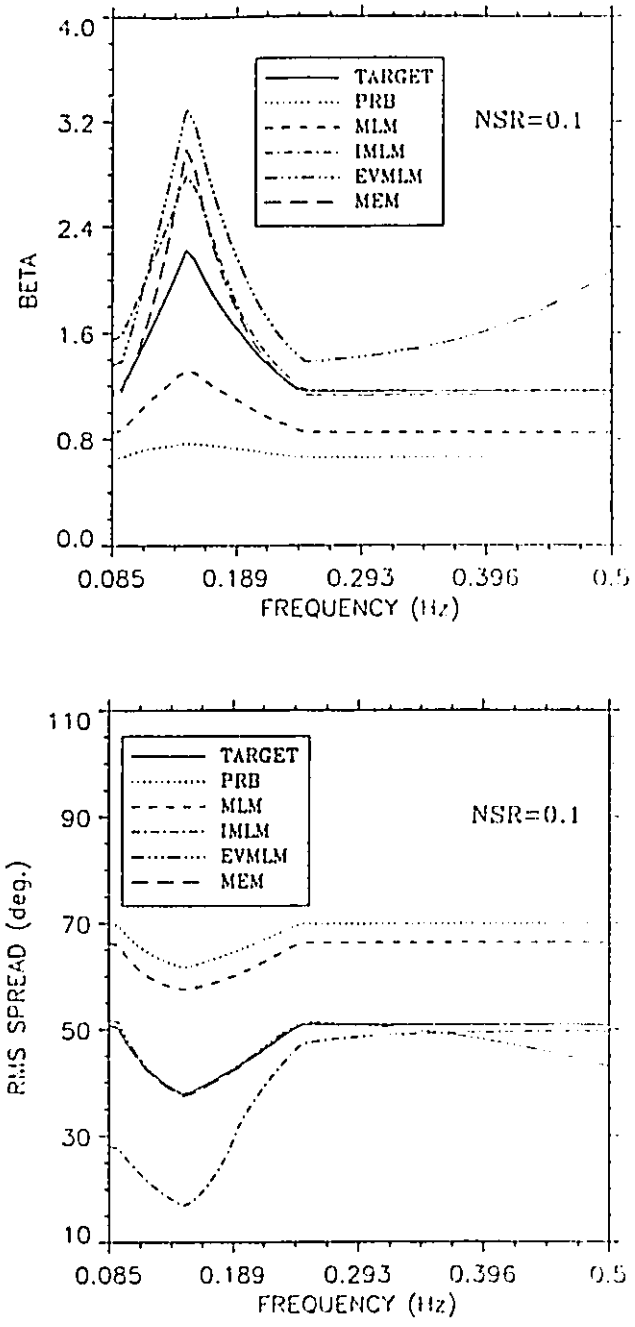

Fig.5.7 Top- β parameter best-fit for each spectrum estimates, Bottom- rms spread (The MEM curve very nearly coincides with the TARGET curve).

following Eq. 5.4. Figure 5.6 illustrates the results in the form of 3D plots. Figures 5.7a and 5.7b summarize the results by presenting a least square fit of a $sech^2$ distribution using the spreading parameter β as a free parameter, and the root mean square spreading (RMS spread) for each technique. Similarly to the unimodal distribution function tests, the PRB parametric method and MLM techniques consistently overpredict the spreading over the entire range of frequencies while the IMLM overpredicts at low frequencies but behaves quite nicely in the upper half of the frequency range. The PRB estimate shows little variation of its characteristics compared to the target spectrum. A 25% variation in the RMS spread of the input function translates into a 10% variation for the PRB estimate, and β values only display a 13% variation compared to 50% for the input functions. The MEM and EVMLM exhibit a similar behavior in the low frequency end as they both predict the RMS spread very accurately despite overshooting the maximum peak as shown by the higher values of the spreading parameter β (Fig 5.7a). These two observations indicate that those two methods are unable to preserve the shape of the spreading function. In this regard, at higher frequencies and wider spreading, both methods give results more consistent with the shape of the input spreading function.

The final step was an attempt at simulating a bimodal sea. The input spectra consist of one fully developed spectrum ($W=1.2$) with peak frequency $f_p=0.11\ Hz$ coming from 100°, and a second spectrum ($W=1.0$) with peak frequency $f_p=0.2\ Hz$ at 140°. The spreading functions were $sech^2$ with variable values of the spreading parameter as defined in Donelan et al.(1985). Because of the variable spreading, this simulation allows multiple bimodal distributions to be looked at. In both cases, the noise to signal ratio was set at 0.05. Figure 5.8 presents the results in the form of 3D plots, and Figures 5.9a and 5.9b present the results at two discrete frequencies. The PRB parametric method is the only one unable to resolve any

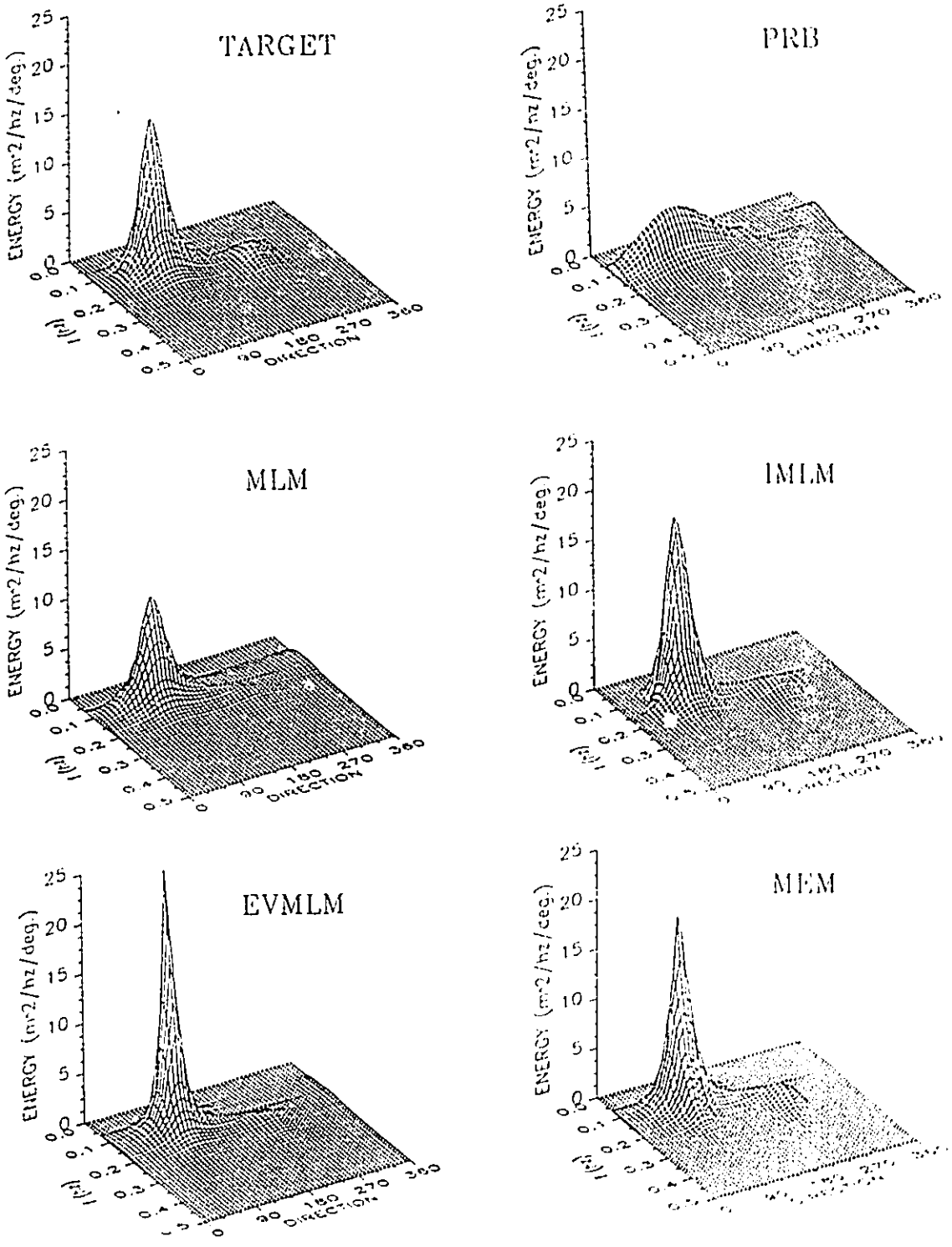

Fig.5.8 Surface plots of directional estimates for bimodal sea test case. Swell: DHH spectrum with $sech^2$ spreading function, f_p=0.11Hz, W=1.2, θ=100. Wind sea: DHH spectrum with $sech^2$ spreading function, f_p=0.2Hz, W=1, θ=240.

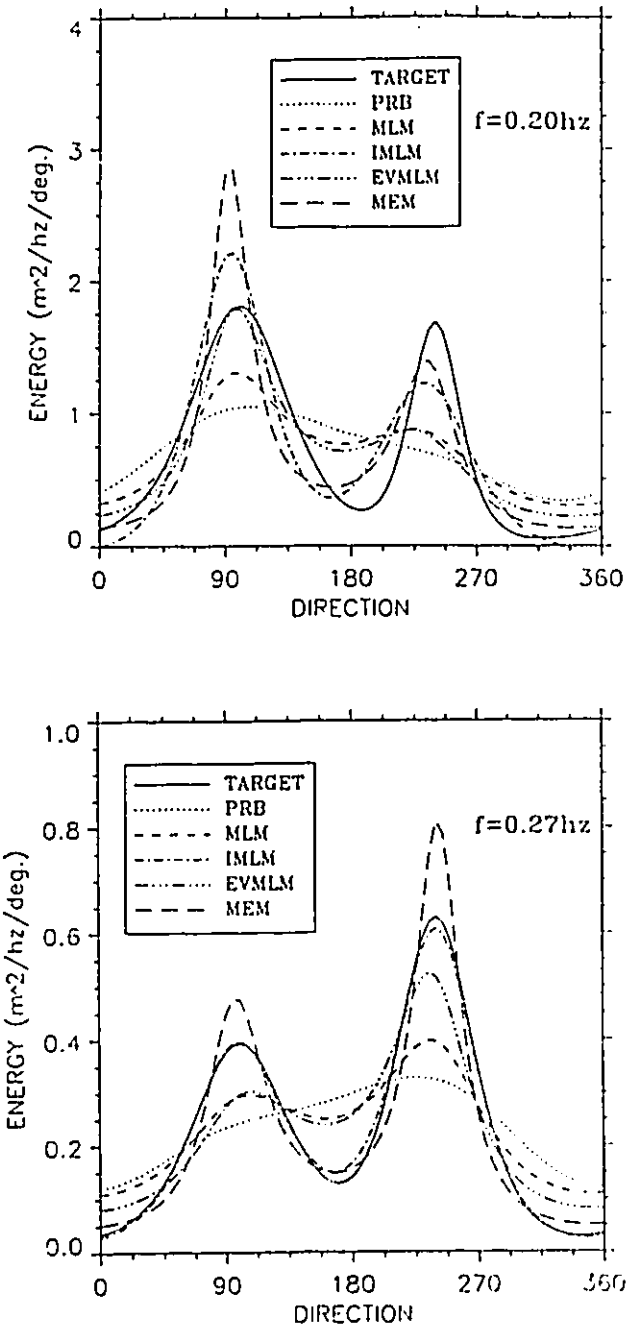

Fig.5.9 Directional spectrum estimates for bimodal sea test case, at frequencies of: Top- 0.20 Hz, Bottom- 0.27 Hz.

bimodality at any of these frequencies. Results from this technique are strongly skewed unimodal distributions. Figure 5.9a presents a case (f =0.2 Hz) with two peaks of equal magnitude but different spreading. All techniques favored the wider peak, overpredicting its relative magnitude compared to the narrower one. These results outline the tendency of every technique to return a bimodal estimate in which both distributions have similar spreading. Figure 5.9b illustrates the inverse case, two peaks of unequal energy both with similar spreading. Results are better as most techniques conserve the correct energy ratio between each peaks. In this case the IMLM resolves almost perfectly the input distribution.

5.3 FIELD DATA

One SWADE field case was examined in order to see if the observations made from synthetic data test cases could be extended to field data. The segment of data analyzed was 34 minutes long during which wind conditions were stable (9.4 m/sec from 106°). 3D plots are presented in Figure 5.10. In these plots the direction of propagation is about the mean wind direction of 106°. All techniques resolved a unimodal spectrum with peak frequency at 0.085 Hz. At this frequency the wave propagate at a 35° angle to the wind direction. The difference between wind and wave direction decreases gradually at increasing frequencies and above 0.17 Hz the waves essentially travel with the wind. Figure 5.10 presents 3D plots for all estimates while Figure 5.11a is a plot of the RMS spread with frequency. The IMLM is seen to produce the estimate with the lowest RMS spread at low frequencies (<0.25 Hz) and joins the MEM RMS spread at higher frequencies. Both the MEM and EVMLM techniques give similar estimates of the RMS spread at frequencies lower than 0.3 Hz, at which point the EVMLM departs and becomes progressively narrower. The MLM and PRB parametric methods give higher estimates

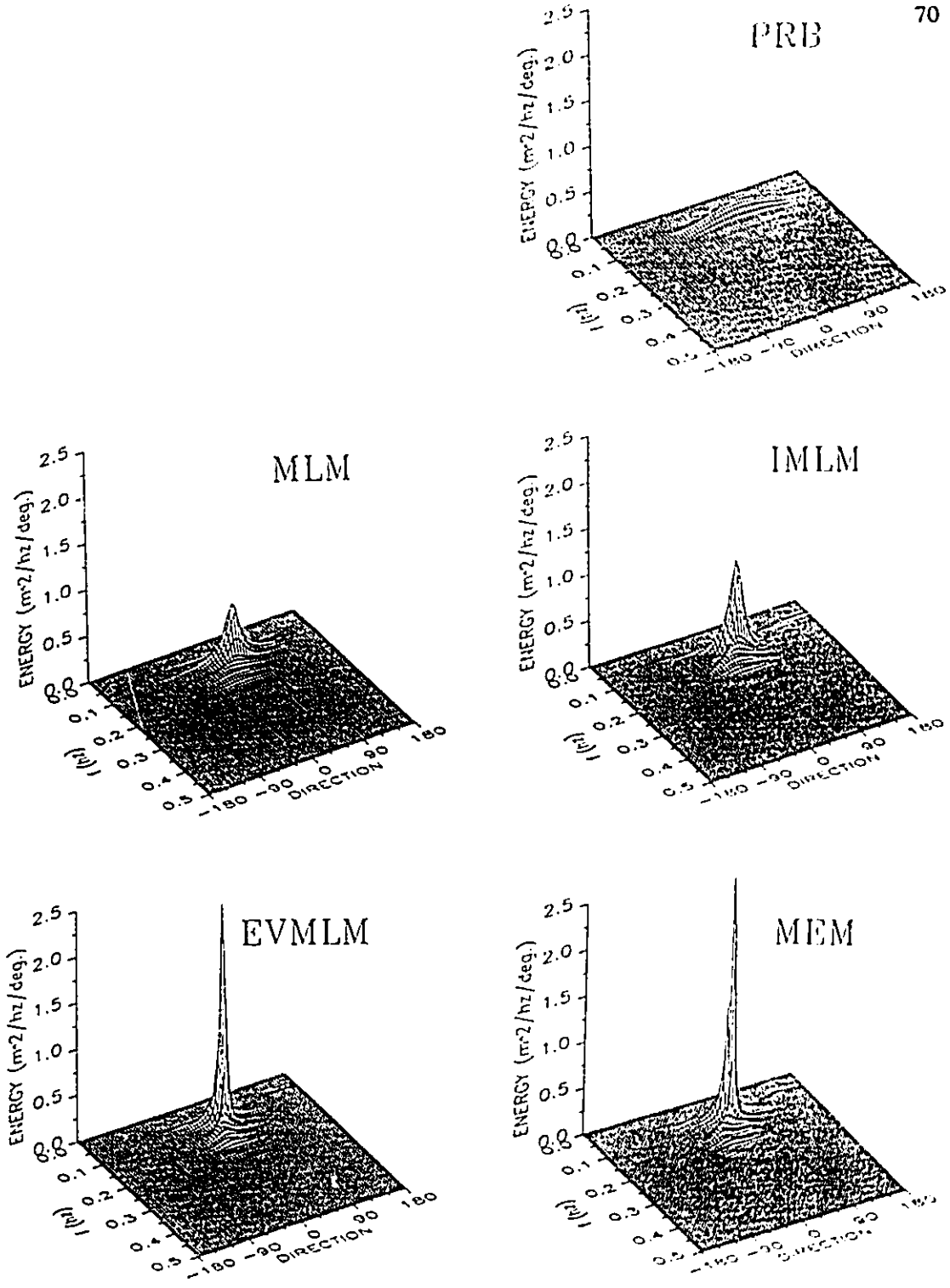

Fig.5.10 Directional spectrum estimates for SWADE field data. Wave direction is about mean wind direction (105°).

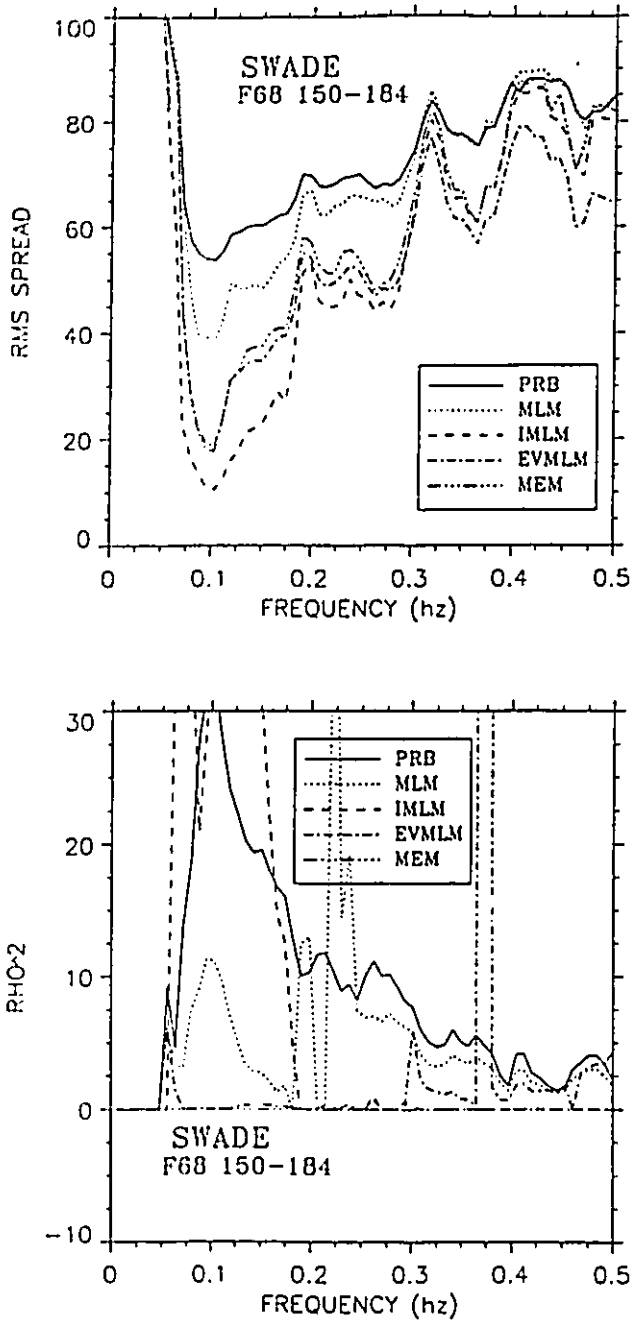

Fig.5.11 Top- rms spread and, Bottom- ρ^2 statistics for all directional estimates (SWADE run F68).

of the spreading than the other three methods. These results are almost identical to the one obtained in the model tests (see Figure 5.7b). Finally, Figure 5.11b is a plot of the ρ^2 statistics of Long (1980) as implemented by Marsden and Juszko (1987). Details on the ρ^2 statistics are given in Appendix 3. This statistical test assumes that the directional spectrum estimate is in fact the true spectrum and that the error between the measured CPSD and the CPSD reconstructed from the estimate is the result of statistical variability. As emphasized by Long (1980), statistical validity should be considered a necessary but not sufficient condition to attest the "goodness" of an estimate. In a sense, the ρ^2 value is more indicative of a bad estimate, than of a good one. For seven degrees of freedom (Marsden and Juszko, 1987), any value of ρ^2 below 9.8 satisfies the 80% interval of confidence. Essentially, the lower the value, the better the estimate accounts for the data. The PRB parametric method estimate is rejected at lower frequencies but gets progressively better at higher frequencies where the spreading is predictably wider. The IMLM estimate is also rejected at low frequencies due to convergence problems in the iterative scheme but quickly rejoins the MEM at $\rho^2=0$ at $f > 0.19$ where both estimates are fully consistent with the data. This characteristic is intrinsic to the MEM and a result of a convergent iterative scheme for the IMLM. Both MLM and EVMLM are generally "statistically valid" estimates, the latter accounting for a better fit with the data.

5.4. DISCUSSION

For comparison purposes, Table 5.3 and 5.4 present parameters calculated for each spectral estimates, for the tests presented in Figures 5.3 to 5.9. Values of the spreading (RMS spread), kurtosis and a least-square fit of the spreading parameter β are presented. In addition, two "error parameters" Err1 and Err2 are computed:

$$Err1 = \frac{1}{2}\frac{\int_0^{f}\int_0^{2\pi} |S(f,\theta)-\hat{S}(f,\theta)|\, d\theta\, df}{\int_0^{f}\int_0^{2\pi} S(f,\theta)\, d\theta\, df} \qquad Err2 = \left[\frac{\int_0^{f}\int_0^{2\pi} \left[S(f,\theta)-\hat{S}(f,\theta)\right]^2 d\theta\, df}{\int_0^{f}\int_0^{2\pi} S(f,\theta)\, d\theta\, df}\right]^{1/2} \tag{5.6}$$

The first parameter Err1 is essentially the ratio of the volume (area) of the summation of the errors over the total energy. The second parameter Err2, while more difficult to interpret physically, quantifies more specifically the behavior of the different techniques to over and underpredict the energy around the spectral peak, where the largest deviations between the true spectrum and the estimate are usually encountered.

Data in Tables 5.3 and 5.4 reveal that no technique performs well in all test cases. The traditional direct Fourier transform technique (PRB) gives an estimate which displays little variation with regard to the input spectrum. The calculated angular spreading is consistently too high, and predictably gets better as the input function becomes wider and closer to the PRB parametric method weighting function. Examination of the error parameters *Err* 1 and *Err* 2 in Table 5.3 indicate that the MLM and EVMLM estimates are the best in noise-free tests. In tests with noise, the IMLM, EVMLM and MEM estimates rise above the other two. The error parameter *Err* 2 is more favorable to the IMLM estimate reflecting the tendency of the other two estimates to more severely overpredict the energy at the peak of the distribution.

The tendency of the Maximum Entropy Method to yield bimodal estimates (Figure 5.3) at low NSR is a characteristic of the method and not a numerical artifact. For the low NSR test cases, a sensitivity analysis of the system of Eqs. 3.73 and 3.74 was performed, and the system was found to always be well conditioned. The bimodal MEM estimates in such cases are an

TABLE 5.3. Test Results for Unimodal Distributions

β = 1.24 NSR = 0.0 f=0.08 hz						
	Target	PRB	MLM	IMLM	EVMLM	MEM
Err1	0.0	0.49	0.19	0.31	0.18	0.27
Err2	0.0	0.077	0.031	0.051	0.030	0.053
β	1.24	0.70	1.02	1.57	1.48	1.11
RMS spread	41.5	65.3	56.6	26.8	43.9	51.5
Kurtosis	3.87	2.80	4.12	2.31	6.0	3.25
β = 2.62 NSR = 0.0 f=0.08 hz						
	Target	PRB	MLM	IMLM	EVMLM	MEM
Err1	0.0	0.96	0.17	0.17	0.23	0.63
Err2	0.0	0.187	0.041	0.036	0.061	0.190
β	2.62	0.83	2.17	2.81	3.41	2.0
RMS spread	19.8	54.7	29.4	15.3	20.6	28.3
Kurtosis	4.20	2.73	9.60	2.40	16.06	3.35
β = 2.00 NSR = 0.1 f=0.25 hz						
	Target	PRB	MLM	IMLM	EVMLM	MEM
Err1	0.0	0.71	0.38	0.09	0.28	0.16
Err2	0.0	0.130	0.066	0.019	0.073	0.038
β	1.85	0.74	1.20	2.05	2.65	2.18
RMS spread	40.4	63.1	58.8	33.0	39.8	39.9
Kurtosis	8.29	2.98	4.36	8.03	8.64	7.89
β = 2.00 NSR = 0.5 f=0.25 hz						
	Target	PRB	MLM	IMLM	EVMLM	MEM
Err1	0.0	0.52	0.39	0.06	0.08	0.09
Err2	0.0	0.094	0.068	0.011	0.013	0.023
β	1.39	0.60	0.71	1.32	1.38	1.53
RMS spread	64.6	76.8	78.7	63.7	62.6	64.6
Kurtosis	4.34	2.71	2.89	4.47	4.35	4.32

TABLE 5.4. Test Results Unimodal and Bimodal Seas

TEST # 3 DHH spectrum Unimodal sea					
	PRB	MLM	IMLM	EVMLM	MEM
Err1	0.64	0.34	0.16	0.24	0.12
Err2	0.0273	0.0140	0.0088	0.0148	0.0093
TEST # 4 DHH spectrum Bimodal sea					
	PRB	MLM	IMLM	EVMLM	MEM
Err1	0.63	0.35	0.22	0.28	0.17
Err2	0.0279	0.0131	0.0101	0.0168	0.0075

exact ($\rho^2 = 0$) but incorrect solution of the spectrum. This outlines the fact that statistical validity of an estimate is not a sufficient condition for its goodness. The tendency of the EVMLM to give narrower estimates at high frequencies (Figure 5.7a) is also intrinsic to the method. The higher the frequency, the stronger the pitch and roll signals will be compared to the heave signal yielding relatively greater values of the smaller eigenvalues of the CPSD matrix. The noise being associated with the two smaller eigenvectors, the resulting estimate will be narrower (smaller angular spread) since the "signal" part of the CPSD will now be heavily weighted toward the heave signal. In fact, the EVMLM estimate obtained by minimizing the system noise is very nearly identical to a Maximum Likelihood Method estimate obtained from the "signal" partition of the original CPSD.

Obtaining a statistically valid estimate is important to assess the quality of the models. Figure 5.11b indicates that the estimates are generally valid, except the PRB parametric method estimate and the IMLM estimate at frequencies lower than 0.19 Hz, due to convergence problems. The IMLM estimate is accurate at higher frequencies and in cases of bimodal distributions. The IMLM iterative scheme will converge at low frequencies for wide spreading functions or sufficiently high NSR. In such cases, negative values resulting from the iterative scheme are avoided.

Which of these techniques should be used for routine data analysis still remains a difficult question to answer. Clearly the PRB parametric method is inadequate if any detailed directional information is needed. Its estimate performs poorly in the case of narrow spreading function and does not account for the data very well, as shown by high ρ^2 values. If the only directional information needed is the mean direction of wave propagation, then the method could be adequate, but only in cases of unimodal seas. Significant errors should be expected for the

RMS spread and in cases of bimodal distributions. All four other techniques give reasonably good estimates but all have problems. Based on the tests presented in this chapter, the following points can be emphasized: The EVMLM estimate overpredicts peak energy and its estimate is wavenumber dependent. The MEM estimate also overpredicts peak energy and could give questionable bimodal distributions in some cases. The IMLM does not converge well at low frequencies and the MLM systematically overpredicts the spreading. The MLM is not the best estimate in any of the test cases but its performance is steady, the estimate being robust, statistically valid in most cases and very unlikely to give spurious results.

5.5. CONCLUSIONS

The direct Fourier transform (PRB) method is easy to implement and does not require lengthy computations such as matrix inversions or eigenvector calculations common to other methods. The drawback is that the truncated Fourier series gives an estimate which is in most cases non statistically valid and systematically overpredicts the angular spreading. The Maximum Likelihood Method gives a very robust estimate with very stable characteristics with frequency and spreading. Its performance diminishes in the presence of noise although it is not a problem for realistic noise levels. The estimate is statistically valid in most cases although it always overpredicts the RMS spread. The Iterative Maximum Likelihood Method is the best estimate at frequencies higher than 0.2 Hz, where it gives very accurate results. At lower frequencies, problems with the iterative scheme were encountered leading to statistically "non-valid" estimates. The iterative scheme also makes this method a lot more "expensive" than the others from a computational point of view. The Eigen-Vector Maximum Likelihood Method gives results which accounts for the data better than its MLM counterpart. The estimate

generally overpredicts peak energy and is dependent on the wave number especially at higher frequencies where it increasingly underpredicts the wave field angular spreading. The Maximum Entropy Method gives good results in cases where background noise is present. Its tendency to choose bimodal distributions at low NSR is an unwanted characteristic but in the analysis of field data presented in this paper (and other cases) this did not seem to create any problems. The MEM gives an estimate which is fully consistent with the data but it consistently overpredicts the energy at the distribution peaks, especially in the case of narrow distributions.

The main conclusion is that no estimate performs well in all cases. The Maximum Likelihood Estimate is robust, computationally efficient and statistically valid in most cases. It consistently overpredicts the spreading but its characteristics are only weakly dependent on the spreading of the input function or the wavenumber. These are valuable assets for routine data analysis and the MLM is the only estimate that carries these advantages. The MLM should then probably be favored over the other methods. The MEM, IMLM and EVMLM could give better estimates in some cases but because of their unwanted characteristics, care should be used in their interpretation. This make them less attractive for day-to-day analysis of wave data. More work needs to be done in this area to improve our ability to measure directional spectra with accuracy and reliability.

CHAPTER 6

WAVE-STAFF DATA: COMPARISON OF EXISTING METHODS

The use of wavestaff arrays, which give multiple measurements of the water surface elevation in both time and space are another way of obtaining directional information. Wavestaff arrays are not as widely used as pitch-roll-heave buoys, essentially because a fixed platform is needed for mounting the array. This makes the approach a lot less versatile, costly and nearly impossible to implement in deep water. On the other hand, wavestaff arrays, by measuring more information than heave-pitch-roll buoys, are highly susceptible to give higher resolution directional estimates, especially when more than three-wavestaff are used.

One of the primary problems associated with wavestaff arrays is to settle on a particular array spacing and design. The spacing should be essentially designed with the wavelengths of interest in mind. The rule should simply be that the quantization error for each wavestaff be significantly lower then the difference in water elevation expected between the wavestaffs. The shortest wavelength of interest should also be significantly longer (say 3 or 4 times) than the array spacing in order to avoid spatial aliasing. As an example, an array spacing of 0.25 meters should be adequate for wave periods of 0.6 to 8 seconds (Tsanis and Donelan, 1989). The array design and its directional properties are a different problem. In this work, four array configurations with three, four, five and six-wavestaff respectively, will be investigated as shown in Figure 6.1. The emphasis will be put on the three and six-wavestaff arrays of Figure 6.1, which

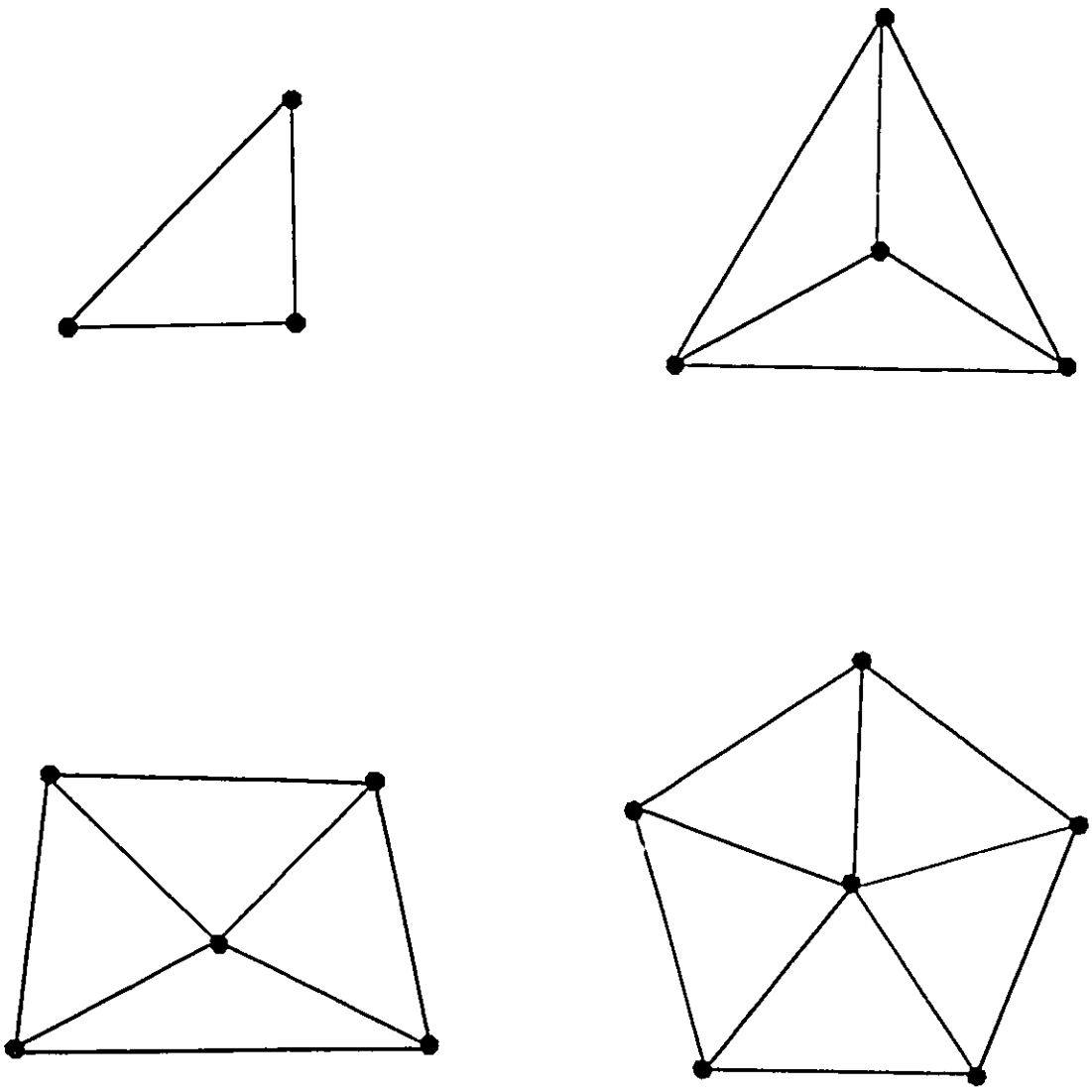

Fig.6.1 Geometry of the various wavestaff arrays tested.

correspond to the arrays used by the National Water Research Institute (NWRI) in Lake St.Clair (Venkatesh et al., 1987) and Lake Ontario (Tsanis and Donelan, 1987), and which data will be used in subsequent chapters. Discussion on the directional properties of these arrays will be postponed till chapter 7. As will be discussed, the generality of the results presented in this chapter will not be affected by this omission.

6.1. METHODS TO BE USED

When using multiple water elevation data to compute an estimate of the wave directional spectrum, two different approaches can be applied. The first one directly uses the water elevation signals, whereas the second one uses those signals to calculate approximations of the water surface slopes, then allowing pitch-roll-heave equivalent methods to be used. The two approaches are briefly described.

6.1.1. Direct methods

The two methods that will be reviewed in this chapter are the Maximum Likelihood Method (MLM) and its iterative form (IMLM). As mentioned in chapter 3, the Eigen-Vector MLM (EVMLM) and Maximum Entropy Methods can hardly be used for wavestaff data. The EVMLM because of the difficult task of selecting the eigenvectors which carry the noise, and because of the associated lack of symmetry, the MEM because its estimates are unstable and the computational algorithm is very hard to implement, making both of these methods unsuitable for routine data analysis. The Convolutive MLM (CMLM) as described in chapter 3 will also not be reviewed here for reasons outlined in chapter 7.

6.1.2. Simulation of heave-pitch-roll signal

Using the different water surface elevation signals, it is possible to compute approximations of the slope signals from which one can use the methods outlined in the previous chapters. In doing so, one essentially uses N signals from the N available wavestaffs and reduces the available amount of information to three signals. Intuitively, this might not seem to be a very wise approach but it has a few advantages. First, methods which can only be used for heave-pitch-roll signals, such as the MEM and EVMLM can also be extended to wavestaff array measurements. Second, assuming the reconstructed slope signals are accurate, it allows for a direct comparison of the methods for both types of measurements. Better insights can then be gained on the advantages of using a N-wavestaff array compared to the more traditional pitch-roll buoy. Obviously, for a high number of wavestaffs, the advantage is there, but questions such as whether or not a four-wavestaff array is better performing than a pitch-roll buoy are unanswered.

Using the linearity property of the Fourier Transform, it is possible to calculate the cross-spectra of any signal obtained from a linear combination of the water surface elevations η_i from the N-wavestaff array. Using the water elevation from one wavestaff as the heave signal and approximating the slopes as a linear combination of the water elevations we can write:

$$\eta(t,\vec{x}) = \eta_i \tag{6.1a}$$

$$\frac{\partial \eta(t,\vec{x})}{\partial x} = \alpha_1\eta_1 + \alpha_2\eta_2 + \alpha_3\eta_3 + ... + \alpha_N\eta_N \tag{6.1b}$$

$$\frac{\partial \eta(t,\vec{x})}{\partial y} = \beta_1\eta_1 + \beta_2\eta_2 + \beta_3\eta_3 + ... + \beta_N\eta_N \tag{6.1c}$$

from which we can find that the heave, pitch and roll cross-spectra (see Appendix 4) are given

by:

$$C_{\eta\eta} = C_{ii} \tag{6.2a}$$

$$C_{xx} = \sum_{i=1}^{N} \alpha_i^2 C_{ii} + 2\sum_{i=1}^{N}\sum_{j=i+1}^{N} \alpha_i \alpha_j C_{ij} \tag{6.2b}$$

$$C_{yy} = \sum_{i=1}^{N} \beta_i^2 C_{ii} + 2\sum_{i=1}^{N}\sum_{j=i+1}^{N} \beta_i \beta_j C_{ij} \tag{6.2c}$$

$$C_{\eta x} = \sum_{j=1}^{N} \alpha_j C_{ij} \tag{6.2d}$$

$$C_{\eta y} = \sum_{j=1}^{N} \beta_j C_{ij} \tag{6.2e}$$

$$C_{xy} = \sum_{i=1}^{N}\sum_{j=1}^{N} \alpha_i \beta_j C_{ij} \tag{6.2f}$$

with the subscripts η , x and y referring respectively to the heave, pitch and roll signals and the subscripts i and j to the wavestaffs. Appendix 4 also gives the form of Eqs. 6.2a to f for both the three and six-wavestaff arrays presented in Figure 6.1.

Before using the reconstructed slope signals to calculate directional spectrum estimates, it is important to verify if the array configuration is such that our slopes will be accurate. A test on the theoretical behavior of the arrays can be performed in the following fashion. Using Eqs. 3.14 to 3.16, it can be shown that the wavenumber k is given by:

$$k = \left[\frac{C_{xx} + C_{yy}}{C_{\eta\eta}} \right]^{1/2} \tag{6.3}$$

Using any realistic directional spectrum, it is possible to calculate the cross-spectra between the different wavestaff signals from which, using equations 6.2a-6.2f, we can compute the cross-spectra between the heave-pitch-roll signals. It is then possible to compare k to the true

wavenumber k_t directly obtained from the deep water linear dispersion relationship:

$$k_t = \frac{\omega^2}{g} \tag{6.4}$$

Figure 6.2 presents the results of such a test for the three and six-wavestaff arrays of Lake St.Clair and Lake Ontario respectively. For these arrays, the slopes are calculated as follow:

$$\eta(t,\vec{x}) = \eta_2 \tag{6.5a}$$

$$\frac{\partial \eta(t,\vec{x})}{\partial x} = (\eta_1 - \eta_2)/0.25 \tag{6.5b}$$

$$\frac{\partial \eta(t,\vec{x})}{\partial y} = (\eta_2 - \eta_3)/0.25 \tag{6.5c}$$

for the Lake St.Clair array, with the angular (degrees) and radial (meters) coordinates of the wavestaffs given by:

$$R = [\,0.25 \quad 0 \quad 0.25\,] \qquad A = [\,180 \quad 0 \quad 90\,] \tag{6.6}$$

and:

$$\eta(t,\vec{x}) = \eta_3 \tag{6.7a}$$

$$\frac{\partial \eta(t,\vec{x})}{\partial x} = 0.5\left[\frac{\eta_1-\eta_3}{0.25} + \frac{2\eta_3-(\eta_5+\eta_6)}{2 * 0.2023}\right] \tag{6.7b}$$

$$\frac{\partial \eta(t,\vec{x})}{\partial y} = 0.5\left[\frac{\eta_2-\eta_4}{2 * 0.2378} + \frac{\eta_5-\eta_6}{2 * 0.1469}\right] \tag{6.7c}$$

for the Lake Ontario array, with angular and radial coordinates:

$$R = [\,0.25 \quad 0.25 \quad 0 \quad 0.25 \quad 0.25 \quad 0.25\,] \qquad A = [\,0 \quad 72 \quad 0 \quad 288 \quad 144 \quad 216\,] \tag{6.8}$$

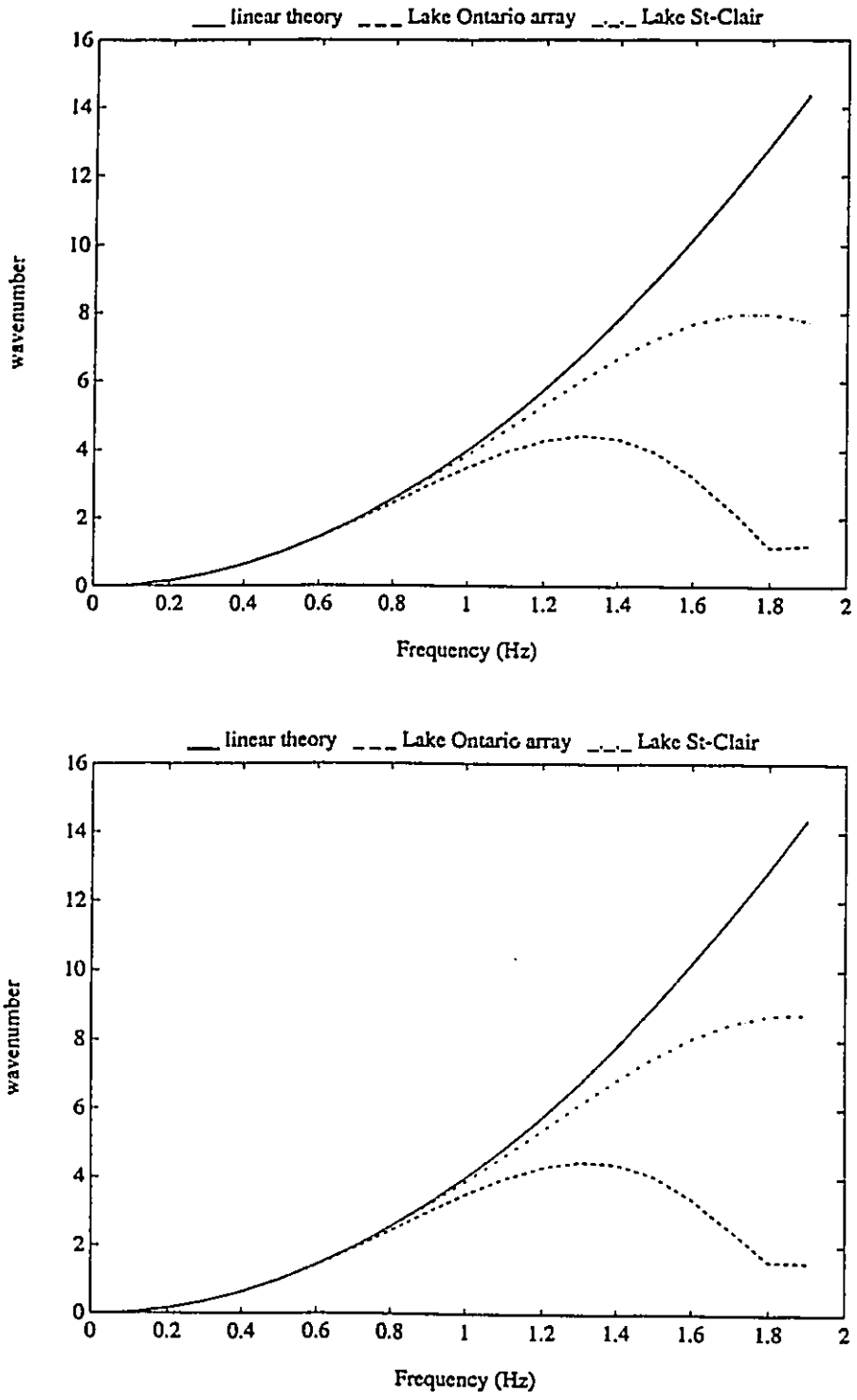

Fig.6.2 Theoretical and measured response of wavestaff array with respect to calculation of water surface slopes. Solid line is linear theory, dashed line is theoretical response for Lake Ontario array and dash-dotted line is for Lake St.Clair array. Top: using monochromatic wave input, Bottom: using $sech^2$ spreading function with $\beta = 2$.

Figure 6.2a was computed using as an input for each frequency, a monochromatic wave of unit amplitude, and for Figure 6.2b, a $sech^2$ spreading function with a value of the spreading parameter β of 2.62. The two figures are nearly identical indicating that the slope response of both arrays is largely independent of the wave field. It can be seen that the slopes approximation are better for the three-wavestaff array of Lake St.Clair than for the six-wavestaff array used in Lake Ontario. The approximations become poorer at higher frequencies, when the array spacing becomes more comparable with the wavelength. The Lake Ontario slope calculations make use of more wavestaffs over a larger area and are therefore more imprecise then their St.Clair counterparts. Figure 6.2 nevertheless shows that the calculated slopes are accurate to within 5% up to 1.25 Hz for the Lake St.Clair array and up to 0.7 Hz for the Lake Ontario array. These values should be considered maximum frequencies, when using pitch-roll-heave equivalent methods for these particular arrays.

6.2. TEST PROCEDURE

The comparison of the different directional spectrum estimators is based on the same tests performed in the previous chapter in the evaluation of the estimates dealing with heave-pitch-roll data. The nature of the tests is outlined in Table 6.1. Only the results for the direct methods are presented, namely the MLM and IMLM. The results for the pitch-roll-heave equivalent methods were found to be essentially identical to the ones presented in the previous chapter and Figures were omitted to avoid unnecessary duplication of results.

TABLE 6.1. Model Tests

TEST TYPE	noise to signal ratio	ϕ (f)	β values $sech^2$	θ	f_p	W
unimodal sea	0.1	DHH	$\beta = function\ (f/f_p)$	180	0.15	1.2
bimodal sea	0.05	DHH	$\beta = function\ (f/f_p)$	100, 240	0.11, 0.2	1.2, 1.0

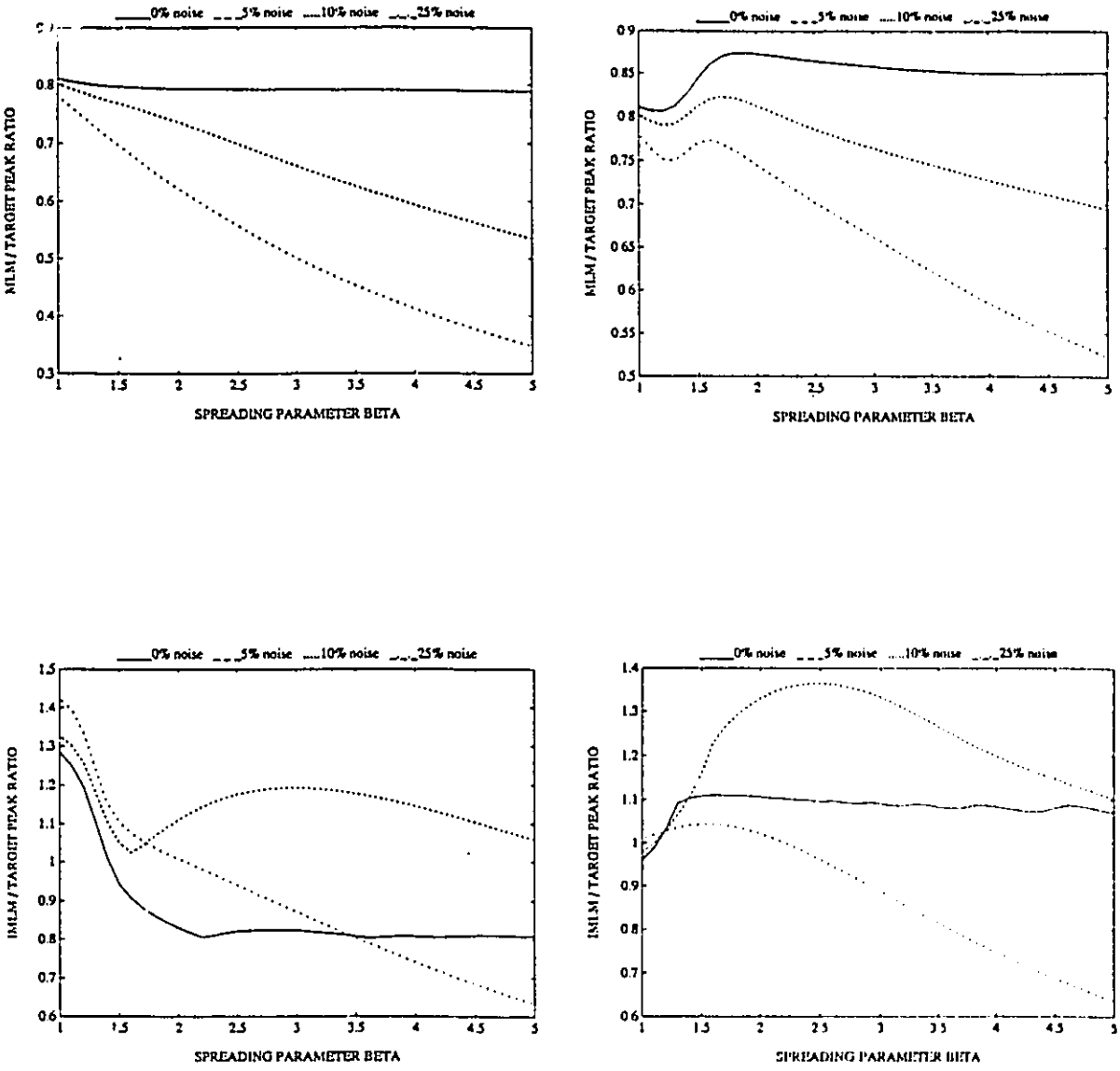

Fig.6.3 Ratio of Maximum Peak to Target Peak for MLM and IMLM estimates as a function of the spreading parameter β and noise to signal ratio (NSR). Top left: MLM estimate, 3-wavestaff array, Top right: MLM estimate, 6-wavestaff array, Bottom left: IMLM estimate, 3-wavestaff array, Bottom right: IMLM estimate, 6-wavestaff array.

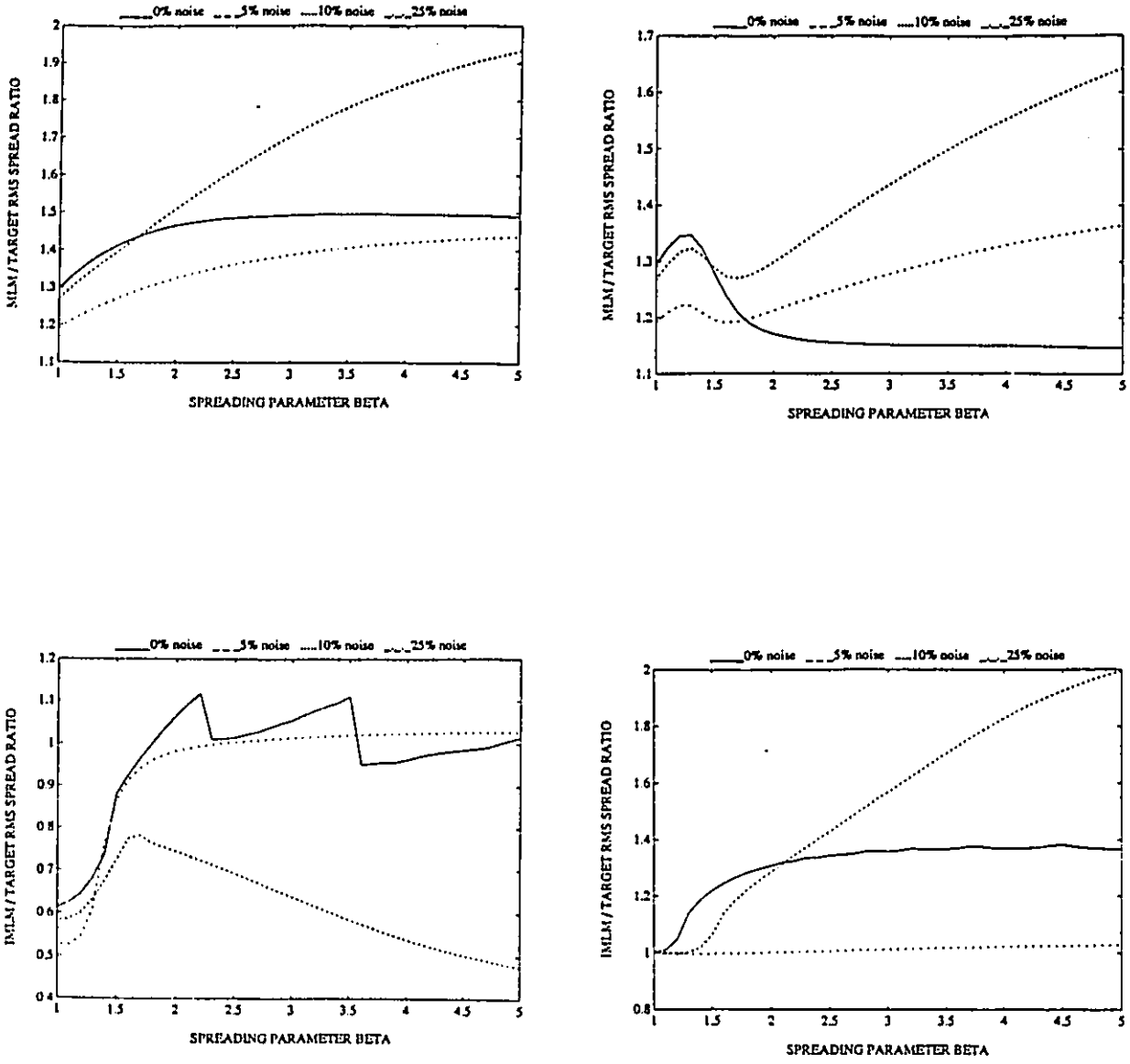

Fig.6.4 Ratio of RMS spread to Target RMS spread for MLM and IMLM estimates as a function of the spreading parameter β and noise to signal ratio (NSR). Top left: MLM estimate, 3-wavestaff array, Top right: MLM estimate, 6-wavestaff array, Bottom left: IMLM estimate, 3-wavestaff array, Bottom right: IMLM estimate, 6-wavestaff array.

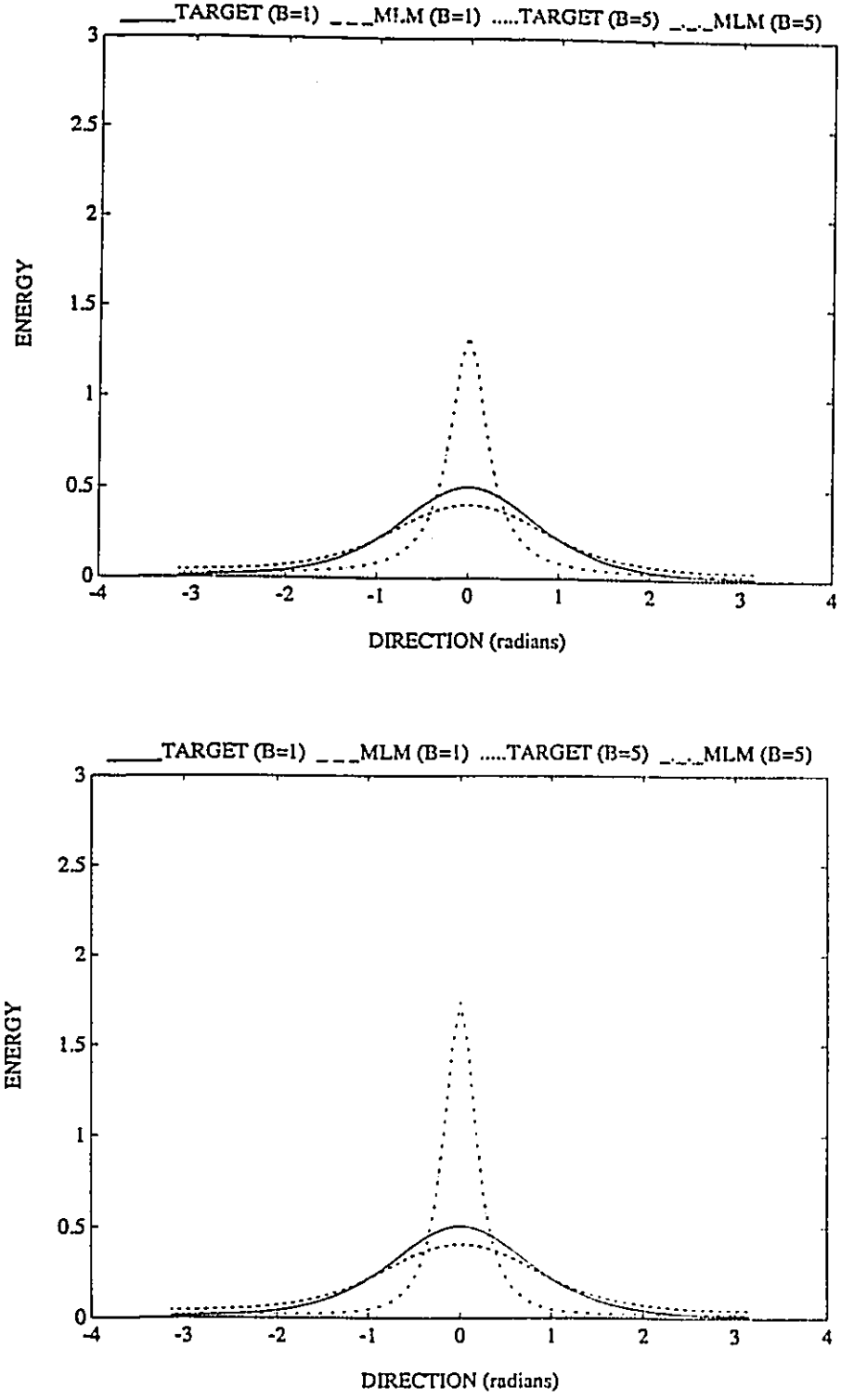

Fig.6.5 MLM estimate for $sech^2$ spreading functions with β values of 5 and 1 and noise to signal ratio of 5%. Top: 3-wavestaff array, Bottom: 6-wavestaff array.

6.3. TEST RESULTS

The first test was intended to test the response of the different methods to unimodal spreading functions. Forty-one $sech^2$ spreading functions with values of the spreading parameter β ranging from 1 to 5 and NSR values ranging from 0 to 0.25 were used, giving a total of 164 simulated unimodal angular distributions. Figure 6.3 presents values of the ratio of the maximum peak of each estimate to the maximum peak of the input distribution for all the simulated cases. Figure 6.4 presents results in a similar format for the RMS spread while Figures 6.5 and 6.6 display typical results from these tests. These four Figures display MLM and IMLM estimates for both the three and six-wavestaff array of Figure 6.1. Results for the equivalent pitch-roll-heave methods are essentially identical to the ones presented in Figures 5.1 to 5.4.

From these Figures, it can be seen that the MLM main characteristics of underpredicting the maximum peak and overpredicting the spreading are conserved from the three wavestaff array to the six wavestaff array, although the values of maximum peak and spreading are more accurate for the six-wavestaff array. In both types of arrays, the performance of the MLM decreases with increasing noise and again, similarly to the heave-pitch-roll cases presented in Chapter 5, at low levels of isotropic noise (low NSR), the MLM estimates show little dependence with values of the spreading parameter β. Figure 6.5 shows that the improvement of performance obtained by increasing the number of wavestaffs is especially noticeable for narrow spreading functions (β=5). The improvement is marginal for β values smaller than about 1.25.

For the IMLM, trends are harder to isolate from Figures 6.3 and Figure 6.4. Results from Figure 6.6 indicates that these are at least partly due to the fact that the iterative scheme

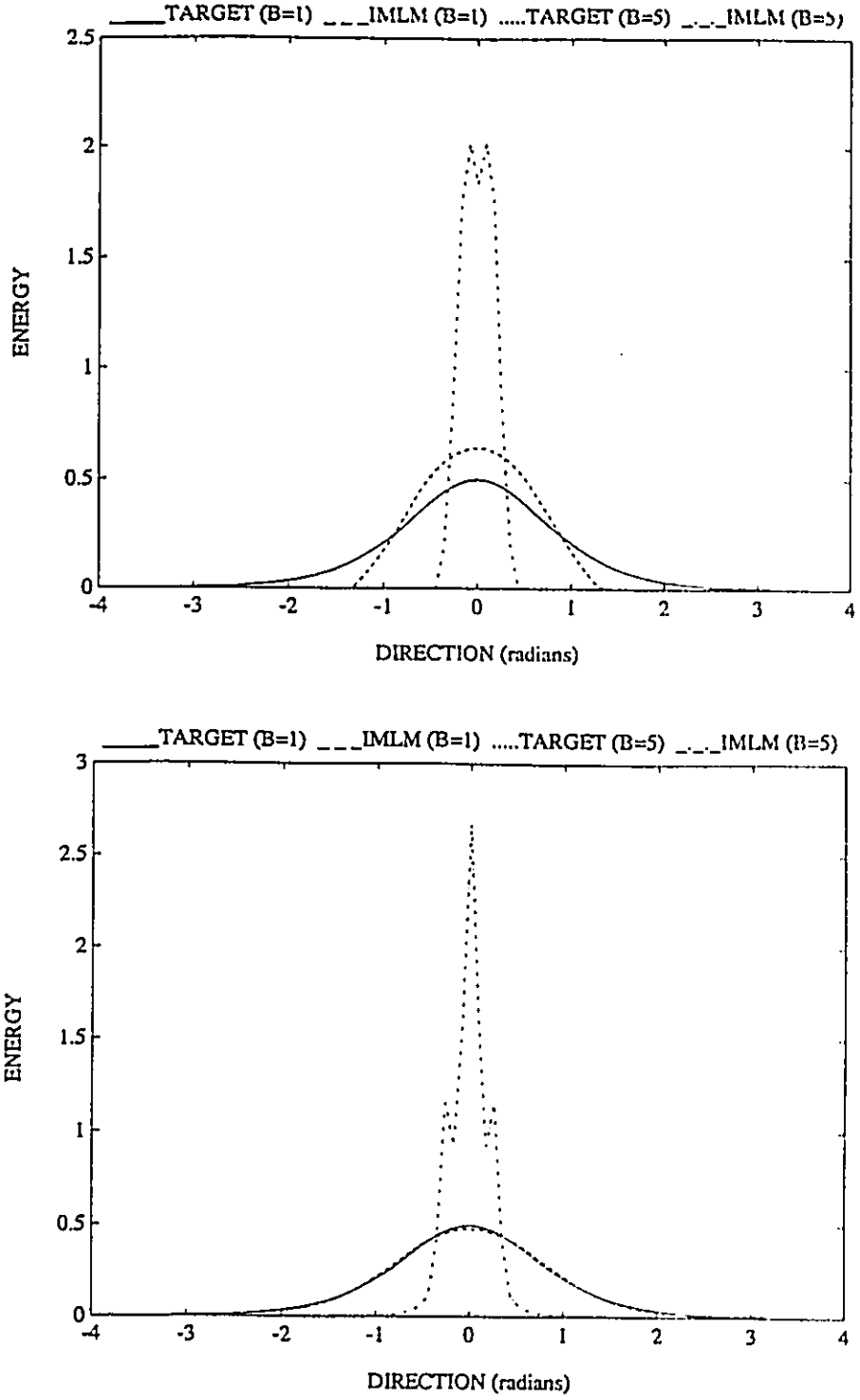

Fig.6.6 IMLM estimate for $sech^2$ spreading functions with β values of 5 and 1 and noise to signal ratio of 0%. Top: 3-wavestaff array, Bottom: 6-wavestaff array.

converges to a more complex bimodal or even trimodal solution of the directional spectrum. Similarly to what was observed in the previous chapter, the iterative scheme was found to either yield impossible negative values of the directional spectrum for the three-wavestaff array or to converge toward a possible but wrong bimodal solution of the same directional spectrum. Again, limiting the number of iterations to three was found to be a good compromise, insuring convergence to a reasonable accuracy while avoiding unwanted oscillations and wrong bimodal solutions of the directional spectrum.

Finally, from Figures 5.1, 5.2, 6.3 and 6.4, it can be seen that the results from the model tests for the three-wavestaff array are identical to those obtained from a pitch-roll-heave buoy.

The next two tests are attempts at simulating realistic cases of unimodal and bimodal seas. Similarly to the previous chapter, DHH frequency spectra were used with the $sech^2$ spreading functions. Table 6.1 defines the parameters used for both simulations. Figure 6.7 and 6.8 respectively present the results in the form of 3D plots for both simulations for the MLM and IMLM, and for the four wavestaff arrays shown in Figure 6.1. The main feature of Figures 6.7 and 6.8 is the failure of the four-wavestaff array to return a correct estimate at higher frequencies for both the MLM and IMLM. Results at two discrete frequencies of 0.15 and 0.4 Hz are shown for the MLM and IMLM for both of the test cases in Figures 6.9 to 6.12. In those four Figures the curve for the four-wavestaff array was ommited because of its failure to return a proper estimate. For the MLM estimate there is a significant improvement going to five-wavestaff from three. Going to six by adding one wavestaff does not bring out any improvement for both unimodal and bimodal distributions. The additional wavestaff comes into play when using the IMLM, and the six-wavestaff array becomes clearly superior. For all the distributions in the unimodal and bimodal sea test cases, the IMLM is closer to target than the MLM. The additional

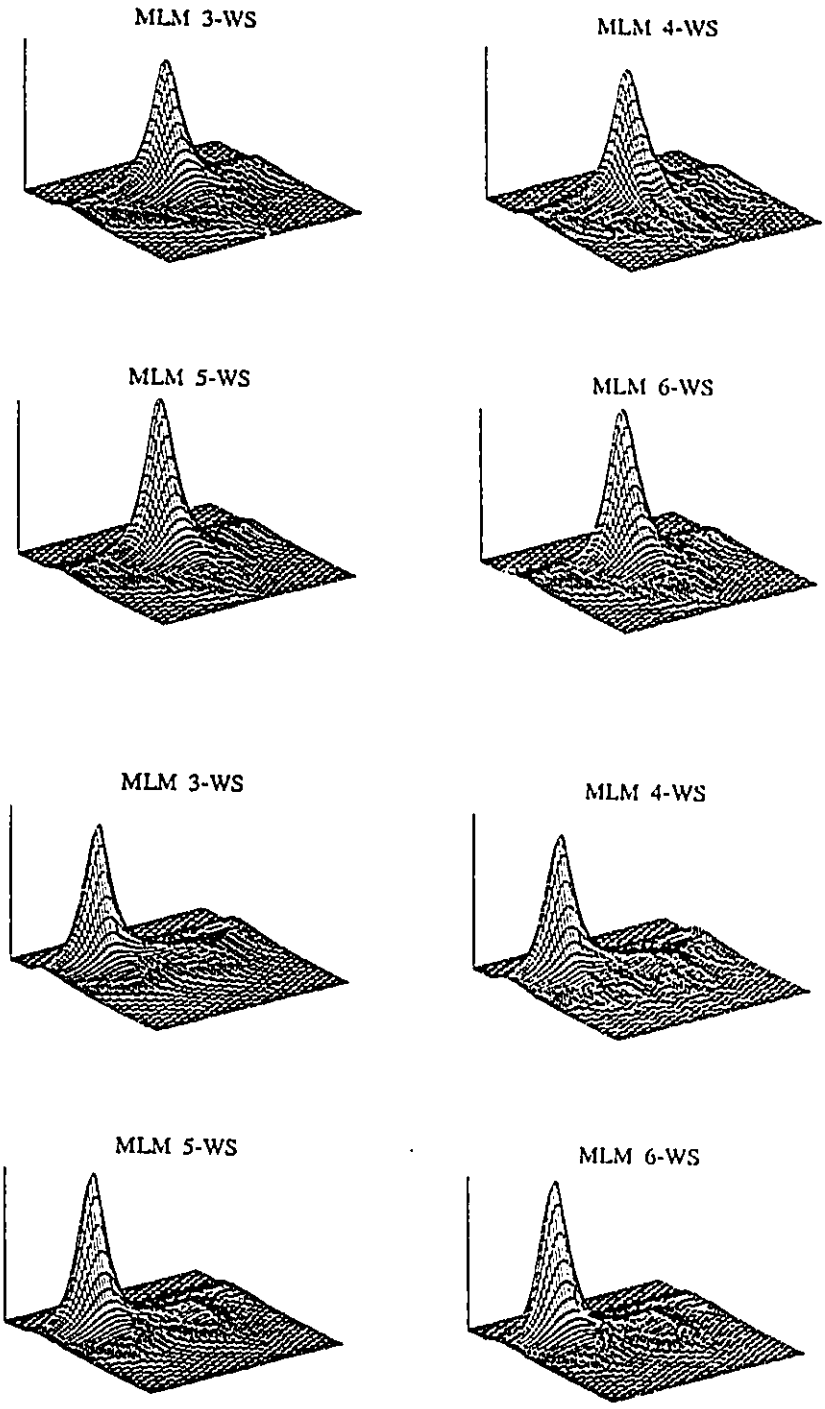

Fig.6.7 MLM estimates for the four-wavestaff arrays of Figure 6.1 for unimodal and bimodal sea test cases. Top four plots: unimodal sea test case. Bottom four plots: bimodal sea test case. For all plots, frequency is up to 0.5 Hz.

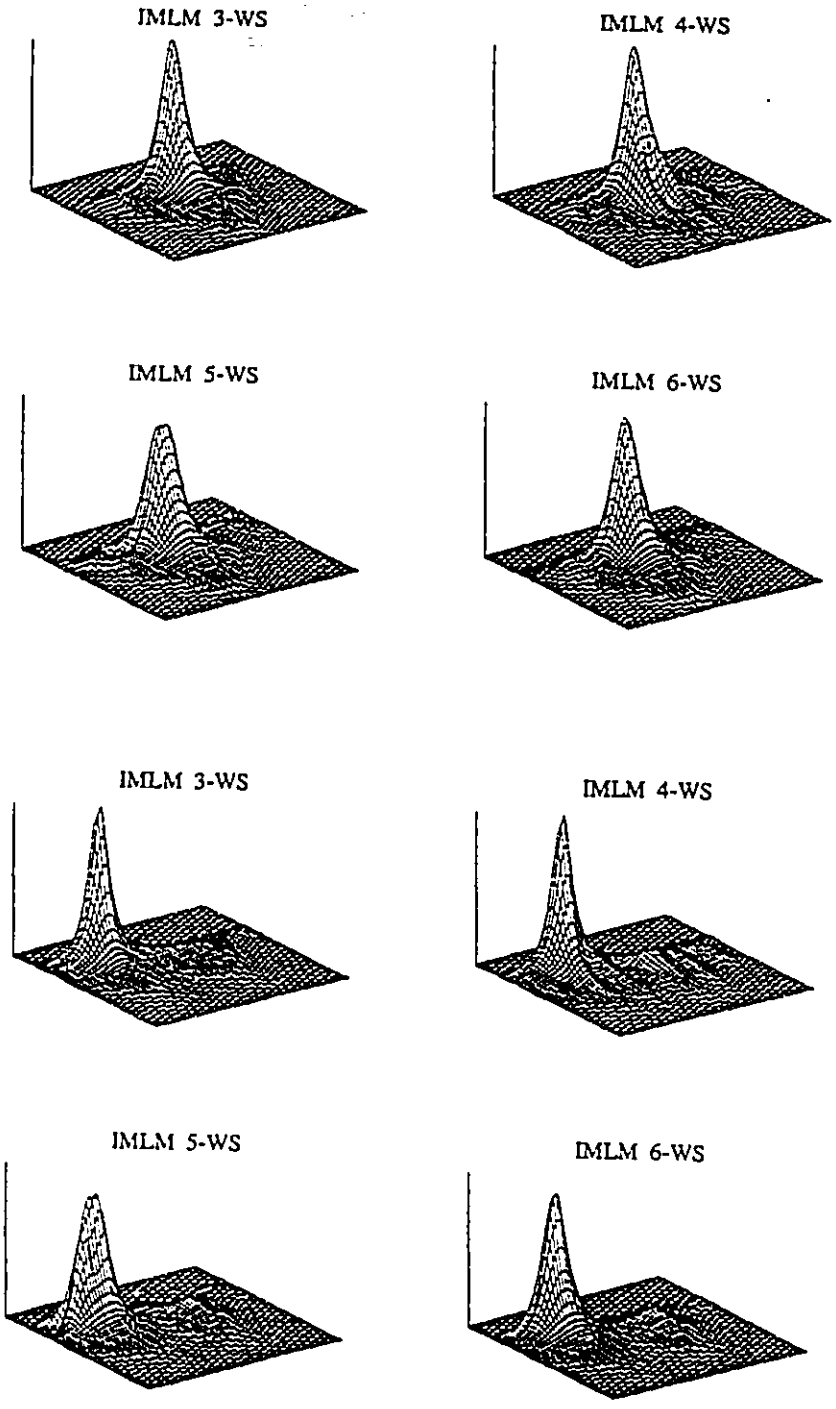

Fig.6.8 IMLM estimates for the four-wavestaff arrays of Figure 6.1 for unimodal and bimodal sea test cases. Top four plots: unimodal sea test case, Bottom four plots: bimodal sea test case. For all plots, frequency is up to 0.5 Hz.

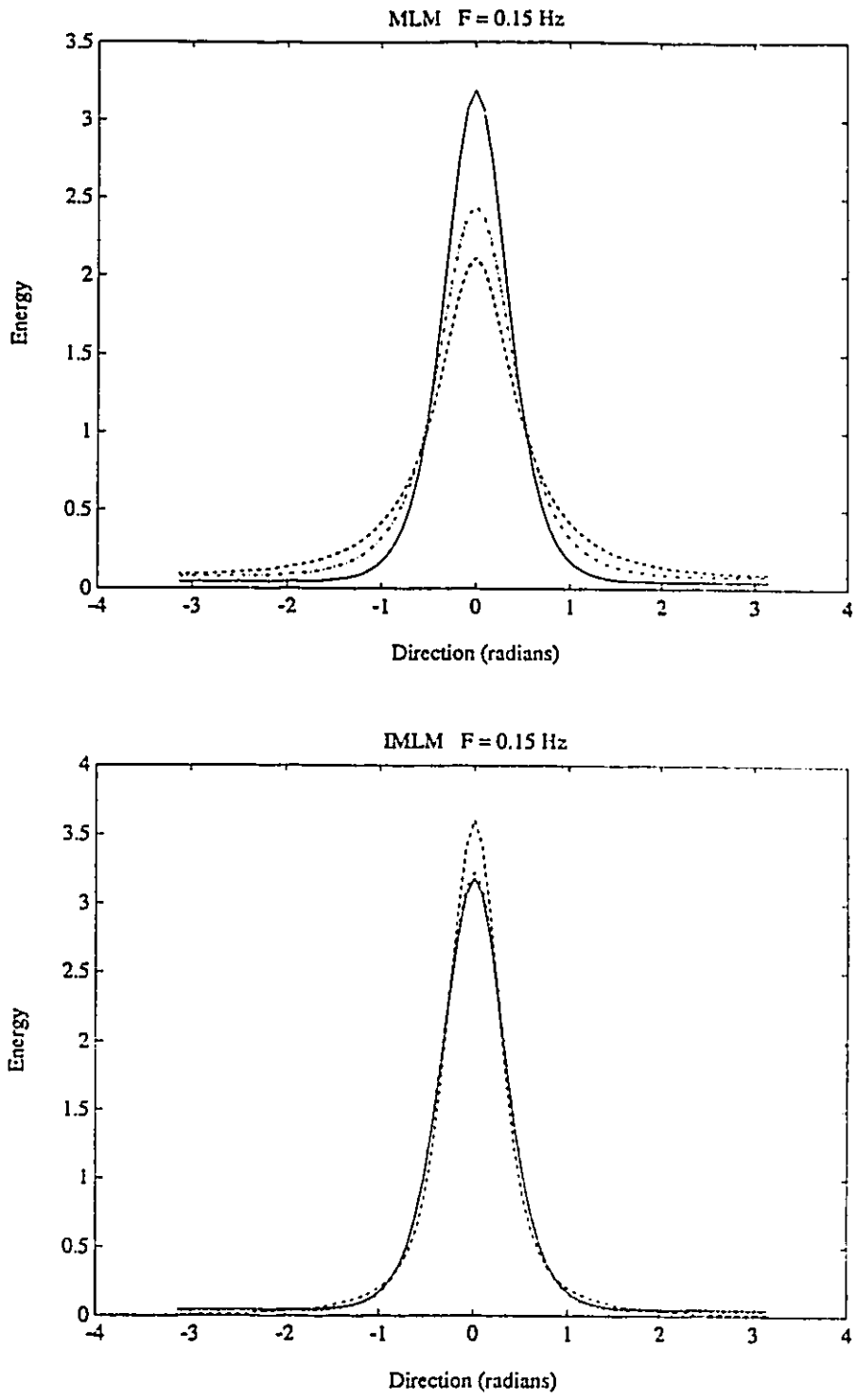

Fig.6.9 Unimodal sea test case results at $f = 0.15\ Hz$. Solid line = target, dashed line = 3-wavestaff array, dotted line = 5-wavestaff array, dash-dotted line = 6-wavestaff array (the 4-wavestaff array results are omitted). Top: MLM estimate, Bottom: IMLM estimate.

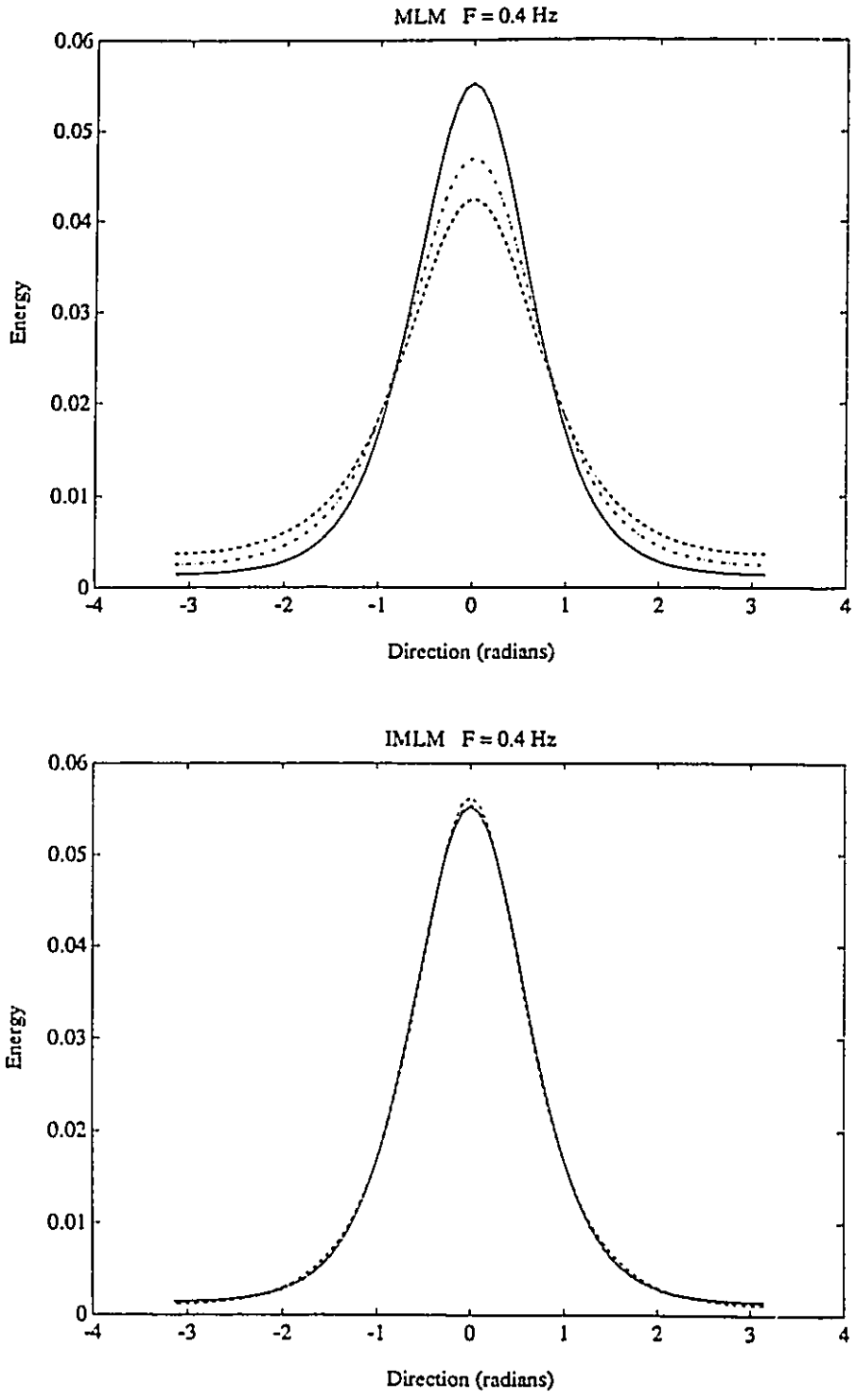

Fig.6.10 Unimodal sea test case results at $f = 0.4\,Hz$. Solid line = target, dashed line = 3-wavestaff array, dotted line = 5-wavestaff array, dash-dotted line = 6-wavestaff array (the 4-wavestaff array results are omitted). Top: MLM estimate, Bottom: IMLM estimate.

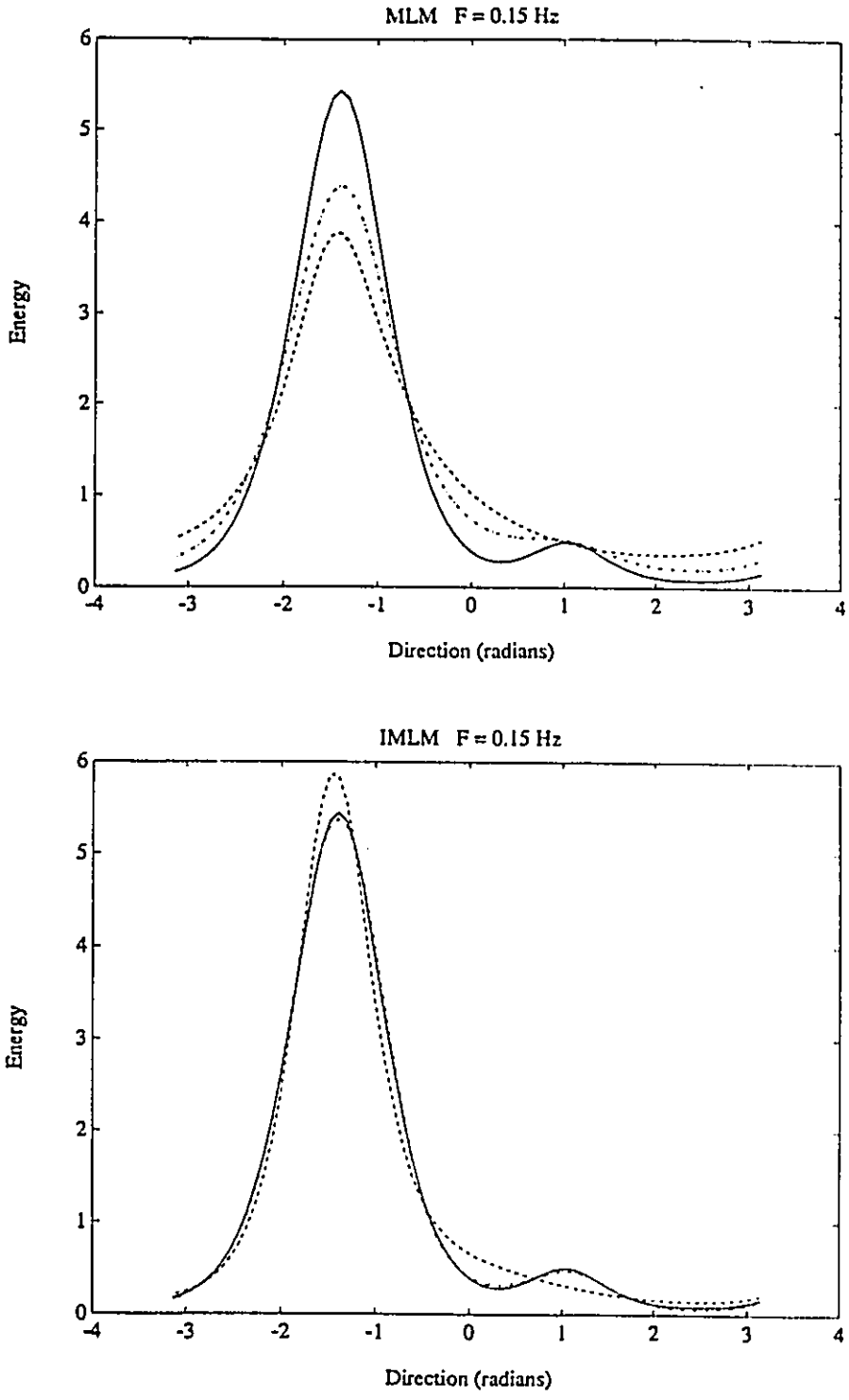

Fig.6.11 Bimodal sea test case results at $f = 0.15\,Hz$. Solid line = target, dashed line = 3-wavestaff array, dotted line = 5-wavestaff array, dash-dotted line = 6-wavestaff array (the 4-wavestaff array results are omitted). Top: MLM estimate, Bottom: IMLM estimate.

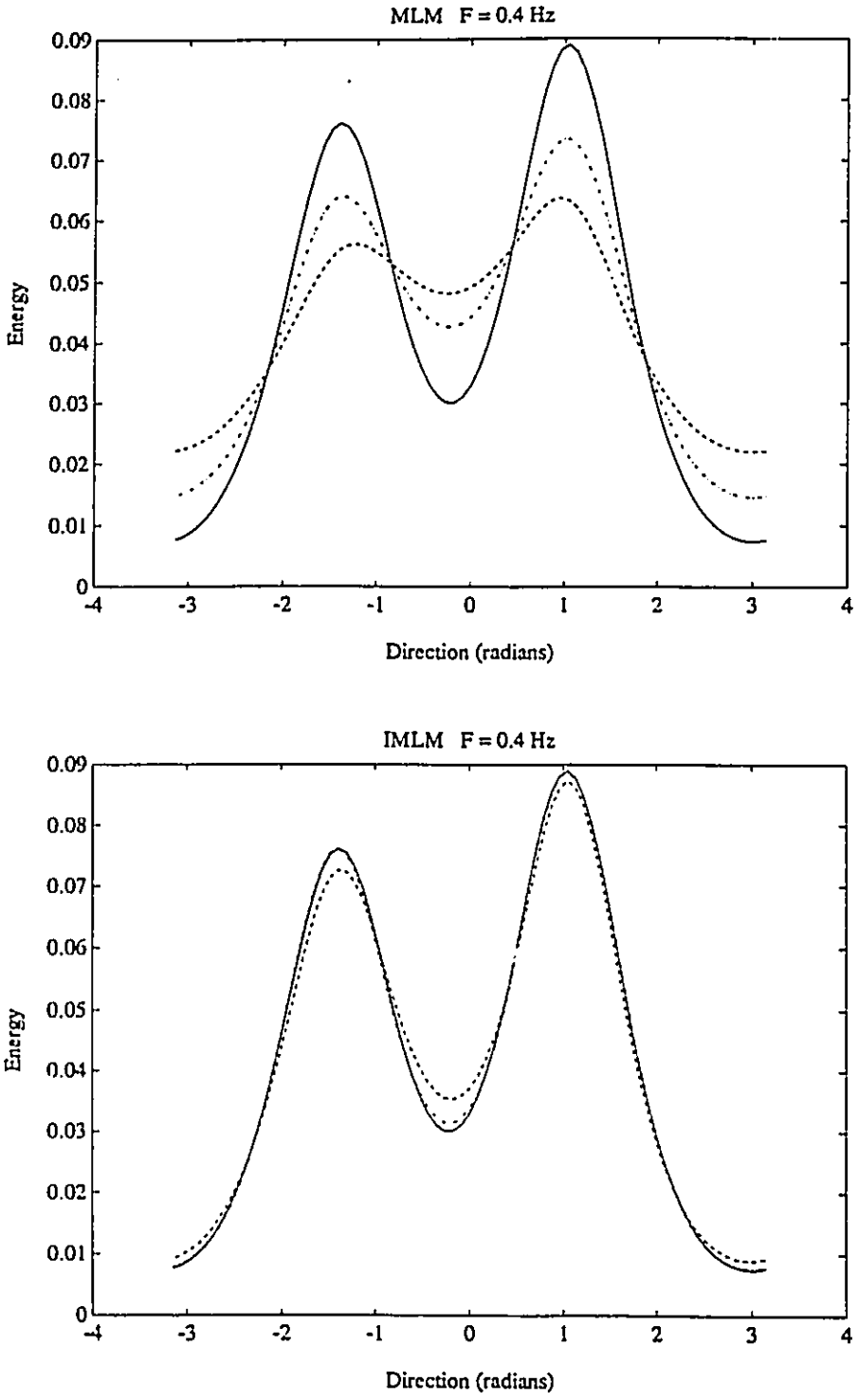

Fig.6.12 Bimodal sea test case results at $f = 0.4\,Hz$. Solid line = target, dashed line = 3-wavestaff array, dotted line = 5-wavestaff array, dash-dotted line = 6-wavestaff array (the 4-wavestaff array results are omitted). Top: MLM estimate, Bottom: IMLM estimate.

resolution potential given by additional wavestaffs is particularly evident from Figure 6.11, where the three-wavestaff array fails to detect the secondary peak.

6.4. DISCUSSION

Results between the pitch-roll-heave equivalent methods and true pitch-roll-heave methods are found to be essentially equivalent for all of the tests cases. This fact should not be considered surprising as long as the theoretical slope response (calculated as in 6.1.2) of the arrays is good. Also, the equivalence of the three-wavestaff array to the pitch-roll-heave buoy, demonstrated from the model tests, should not be interpreted as meaning that the use of a heave-pitch-roll buoy will give identical results to those from a three-wavestaff array. The equivalence is there in theory, since in both cases we have three measurements of the wave field, but from a practical viewpoint, there are differences. The digitization and data correction as well as calibration errors for wavestaff arrays should be smaller than for a heave-pitch-roll buoy. The reasons for that are numerous. First, the accuracy of a wavestaff in measuring the water surface elevation is very good, the digitization error being of the order of 1mm. The directional properties of the arrays are also well known since its position is fixed in space. The potential for errors is far greater when using heave-pitch-roll buoys. Buoys are never perfect wave followers, they are free to drift and rotate around their axis and their response can be affected by their mooring line. In addition to that, slopes are more difficult to measure than the straight water elevation. It should nevertheless be noted that an exact measurement of the slopes is not needed, that is the oscillation of the buoy does not need to exactly coincide with the water surface slope as long as this effect is the same in every direction. In these conditions, the shape of the spectrum will be preserved as long as the wavenumber k is calculated using Eq. 6.3 and not using the linear

dispersion relationship (Eq.6.4). If the buoy data is carefully corrected, results should be close to the results from a wavestaff array. Such a comparison is presented by Anctil et al. (1992) for a three-meter Discus buoy used in the SWADE experiment. Further discussion on the corrections of buoy data will be presented in Chapter 10.

Error parameters were calculated for both the unimodal and bimodal sea test cases using Equation 5.6. Results for those tests are outlined in Tables 6.2 and 6.3. Results from the equivalent heave-pitch-roll methods are also included in these Tables for comparison purposes. From these Tables, a few points should be raised. First, the IMLM scheme works better for wavestaffs arrays than for the pitch-roll-heave signal. This can be seen by comparing the error parameters for both the three-wavestaff array and the buoy data. Even though the MLM estimates are identical in both cases, the IMLM performs better for the wavestaff array. Also, it can be seen that at least 5 wavestaffs are needed to notice a significant improvement over the estimate obtained from a pitch-roll-heave buoy. It should nevertheless be noted that arrays with four-wavestaff with a different geometry than the one presented in Figure 6.1 could possibly give better results. The failure of the four wavestaffs array to return a good estimate is not well understood. It is not a directional effect since both the unimodal and bimodal sea test cases present the same features. It can only be hypothesized that the symmetry of the array (the three and five-wavestaff arrays are not) for a low number of wavestaffs might be an unwanted characteristic. Finally, when using arrays of wavestaffs, the IMLM should be used to reach the full resolution potential of the arrays. Simply using the MLM might not be worthwhile since similar and even better resolution could be obtained using the IMLM (and even the MEM) on a good quality heave-pitch-roll dataset. On the other hand, the IMLM should not be considered an answer to all of the problems. Problems with convergence of the iterative scheme are always

TABLE 6.2. Test Results Unimodal Sea

METHOD	Err1	Err2
MLM (buoy)	0.17	0.0140
MLM (3 ws.)	0.17	0.0160
MLM (4 ws.)	0.18	0.0161
MLM (5 ws.)	0.10	0.0099
MLM (6 ws.)	0.10	0.0101
IMLM (buoy)	0.08	0.0088
IMLM (3 ws.)	0.04	0.0048
IMLM (4 ws.)	0.09	0.0070
IMLM (5 ws.)	0.04	0.0058
IMLM (6 ws.)	0.01	0.0011
PRB (buoy)	0.32	0.0273
EVMLM (buoy)	0.12	0.0148
MEM (buoy)	0.06	0.0093

TABLE 6.3. Test Results Bimodal Sea

METHOD	Err1	Err2
MLM (buoy)	0.17	0.0131
MLM (3 ws.)	0.18	0.0150
MLM (4 ws.)	0.17	0.0149
MLM (5 ws.)	0.11	0.0098
MLM (6 ws.)	0.10	0.0093
IMLM (buoy)	0.11	0.0101
IMLM (3 ws.)	0.07	0.0072
IMLM (4 ws.)	0.09	0.0078
IMLM (5 ws.)	0.07	0.0084
IMLM (6 ws.)	0.03	0.0032
PRB (buoy)	0.32	0.0279
EVMLM (buoy)	0.14	0.0168
MEM (buoy)	0.09	0.0075

possible and the method should always be used with care and IMLM bimodal estimates looked at with a critical eye. Overall, depending on the method to be used for estimating the wave directional spectrum, results from Figures 6.9 to 6.12 as well as Tables 6.2 and 6.3 show that additional wavestaffs might not necessarily improve the directional resolution, depending on the method of estimating the directional spectrum that is used. These results outline the importance of carefully designing the arrays and testing them before putting them to use.

6.5. CONCLUSION

Results presented in this chapter outline that in general, the more wavestaffs used, the better the potential for high-resolution of directional seas will be. But, the choice of a method to calculate the directional spectrum is fundamental to the choice of instrumentation, as some methods of estimating the wave directional spectrum will still be better on pitch-roll-heave data than others on wavestaff arrays data, despite the added resolution potential. For the wavestaff array configurations tested, the IMLM (with a stopping criterion of three iterations) proved to be the better performing method.

Finally, wavestaff arrays should be designed not only for the wave periods of interest, but also as a function of the method of estimating the wave directional spectrum, as the array geometry and number of wavestaffs will have an effect on the quality of the directional estimates.

CHAPTER 7

PROPOSED NEW METHODS

Results from the previous two chapters indicate that the spectral estimates obtained from most methods have characteristics which are a function of the frequency considered and of the spreading of the input distribution. One of the most interesting results from the previous chapter was the fact that the properties of the MLM estimate were found to be essentially independent of the spreading of the energy distribution. This property was used as a focusing point in trying to improve on the current methods of estimating the wave directional spectrum. In a first step, the properties of the MLM are further investigated.

7.1. THE EFFECT OF NOISE PERTURBATION

In Chapter 3, in the presentation of the Maximum Likelihood Method, it was advised to perturb the Cross-Power-Spectral-Density matrix estimate in order to avoid singularity. This is done by perturbing the CPSD using (3.47):

$$C = (1-\varepsilon)\, C + I\varepsilon \qquad 0<\varepsilon \ll 1 \tag{7.1}$$

where I is the Identity matrix. This perturbation is equivalent to adding incoherent noise to the system and should therefore decrease the resolution of the method. Therefore, it is important to evaluate the effect (if any) of the perturbation on the stability of the system to solve, and on the

estimate itself.

7.1.1. MLM estimate and directional properties of arrays

The sensitivity of the MLM to a perturbation was investigated using monochromatic waves as an input at different frequencies. In a same way, the directional response of wavestaff arrays was also investigated by looking at monochromating waves coming from different directions. For that purpose, the three and six-wavestaff arrays of Figure 6.1 were used. For the three-wavestaff array used in Lake St.Clair, wave directions of 0° and 45° (mathematical convention) were compared, whereas for the six-wavestaff array used in Lake Ontario, directions of 0° and 20° were used. These directions were chosen in order to try to maximize the difference in the array configuration from the viewpoint of the mean wave direction of propagation. For example, the six-wavestaff array has a 36° symmetry, and the chosen directions of 0° (in the axis of symmetry) and 20° (approximately in between two axis of symmetry) should maximize any present directional effects. Results for the Lake St.Clair array are presented in Figures 7.1 and 7.2. Figure 7.1 presents MLM estimates for two monochromatic waves coming from 0° at respective frequencies of 0.1 and 0.5 Hz. Four MLM estimates are computed at each frequency with four values of the perturbation parameter "ε" : 10^{-7}, 10^{-6}, 10^{-5} and 10^{-4}. Results indicate that the perturbation induces smearing of the MLM estimate. The effect is especially noticeable at low frequencies. At a frequency of 0.1 Hz, the peak energy is only at 20% of its true value when $\varepsilon = 10^{-4}$. Figure 7.2 essentially displays the same results but also superposes the results for a second monochromatic wave coming from 45°. The results indicate that the perturbation not only induces artificial smearing of the MLM estimate, but also creates directional discrepancies within the array. Table 7.1 displays values of the inverse condition number for all test cases and

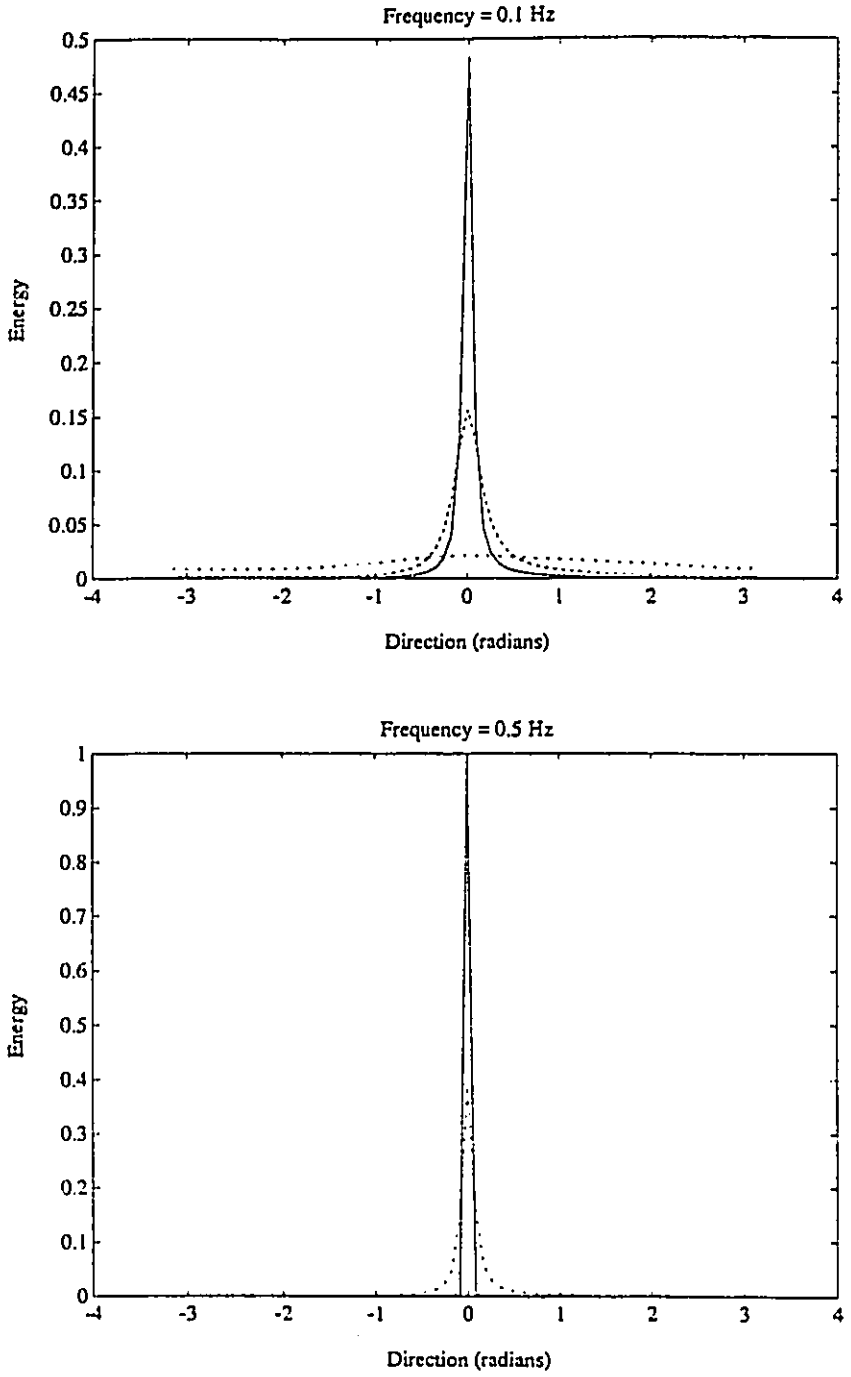

Fig.7.1 MLM estimate (3-wavestaff array) for a monochromatic wave input coming from 0°. Value of perturbation parameter ε : solid line 10^{-7}, dashed line 10^{-6}, dotted line 10^{-5}, dash-dotted line 10^{-4}. Top: $f = 0.1\ Hz$, Bottom: $f = 0.5\ Hz$.

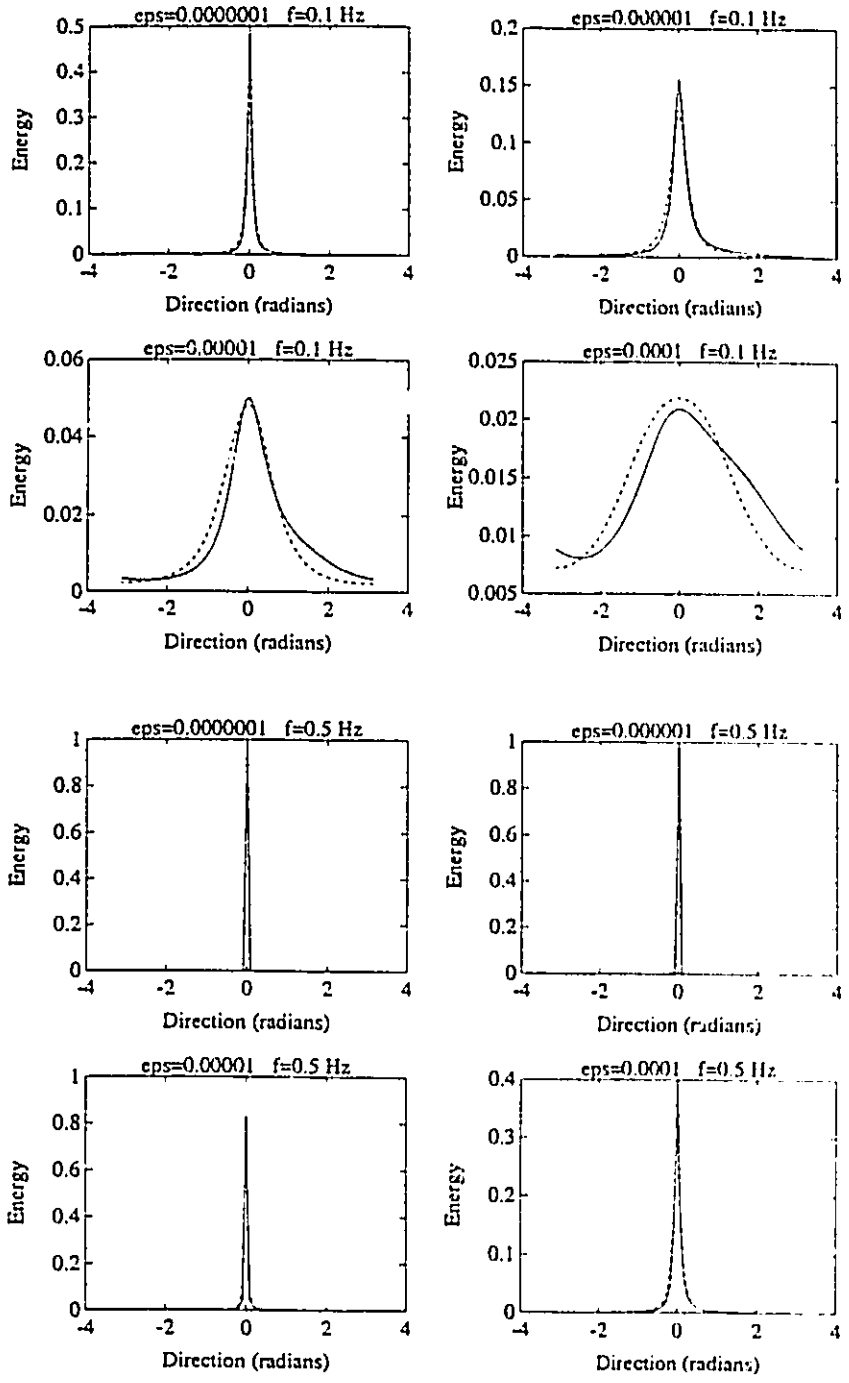

Fig.7.2 MLM estimate (3-wavestaff array) for monochromatic wave inputs coming from 0^{o} (solid line) and 45° (dashed line), at four different values of the perturbation parameter ε. Top four plots: $f = 0.1\ Hz$, Bottom four plots: $f = 0.5\ Hz$.

TABLE 7.1. Inverse Condition Number of CPSD for Monochromatic Wave Input Before and After Perturbation

Lake Ontario Array, Wave direction = 0°				
	$\varepsilon = 10^{-7}$	$\varepsilon = 10^{-6}$	$\varepsilon = 10^{-5}$	$\varepsilon = 10^{-4}$
before	$2.9 \cdot 10^{-19}$	$2.9 \cdot 10^{-19}$	$2.9 \cdot 10^{-19}$	$2.9 \cdot 10^{-19}$
after	$3.3 \cdot 10^{-8}$	$3.3 \cdot 10^{-7}$	$3.3 \cdot 10^{-6}$	$3.3 \cdot 10^{-5}$
Lake Ontario Array, Wave direction = 20°				
	$\varepsilon = 10^{-7}$	$\varepsilon = 10^{-6}$	$\varepsilon = 10^{-5}$	$\varepsilon = 10^{-4}$
before	$2.1 \cdot 10^{-18}$	$2.1 \cdot 10^{-18}$	$2.1 \cdot 10^{-18}$	$2.1 \cdot 10^{-18}$
after	$2.8 \cdot 10^{-8}$	$2.8 \cdot 10^{-7}$	$2.8 \cdot 10^{-6}$	$2.8 \cdot 10^{-5}$
Lake St.Clair Array, Wave direction = 0°				
	$\varepsilon = 10^{-7}$	$\varepsilon = 10^{-6}$	$\varepsilon = 10^{-5}$	$\varepsilon = 10^{-4}$
before	$2.5 \cdot 10^{-37}$	$2.5 \cdot 10^{-37}$	$2.5 \cdot 10^{-37}$	$2.5 \cdot 10^{-37}$
after	$6.6 \cdot 10^{-8}$	$6.6 \cdot 10^{-7}$	$6.6 \cdot 10^{-6}$	$6.6 \cdot 10^{-5}$
Lake St.Clair Array, Wave direction = 45°				
	$\varepsilon = 10^{-7}$	$\varepsilon = 10^{-6}$	$\varepsilon = 10^{-5}$	$\varepsilon = 10^{-4}$
before	$2.0 \cdot 10^{-17}$	$2.0 \cdot 10^{-17}$	$2.0 \cdot 10^{-17}$	$2.0 \cdot 10^{-17}$
after	$5.8 \cdot 10^{-8}$	$5.8 \cdot 10^{-7}$	$5.8 \cdot 10^{-6}$	$5.8 \cdot 10^{-5}$

both arrays. From the data in the Table, it can be seen that the perturbation effectively removes the singularity problem and creates a system with the inverse condition number being of the order of the perturbation. Using a small enough perturbation seems to effectively removes the singularity without adverse effects such as smearing of the estimate, or directional effects for wavestaff arrays. Results for the six-wavestaff array used in Lake Ontario are presented in Figures 7.3 and 7.4 and indicate that there is also a "perturbation-dependent" smearing of the MLM estimate, although not as severe as in the case of the Lake St.Clair array (for a given perturbation). Directional effects (Figure 7.4) are also noticeably absent, more than likely due to the greater symmetry of the array.

From the results, it is found that the artificial smearing of the MLM estimate, as observed by Tsanis and Donelan (1989), is a numerical artifact and not a characteristic of the MLM itself. This is also emphasized by the fact that the MLM is derived under the constraint:

$$X(\theta_i)^H A(\theta_i)=1 \tag{7.2}$$

which imposes that a monochromatic wave be passed with unit gain.

7.1.2. Discussion and conclusion

The perturbation of the CPSD through Eq. 7.1 has a definite effect on the resolution of the MLM. In order to avoid any artificial perturbation-induced smearing of the directional spectrum, or directional effects for wavestaff arrays with few wavestaffs or little symmetry, the value of the perturbation parameter ε should be smaller than at least 10^{-6} and preferably 10^{-7}. This should insure that the CPSD is invertible without any adverse effect on the MLM resolution. The smearing effects due to such a small value indicate that truncation and rounding errors might

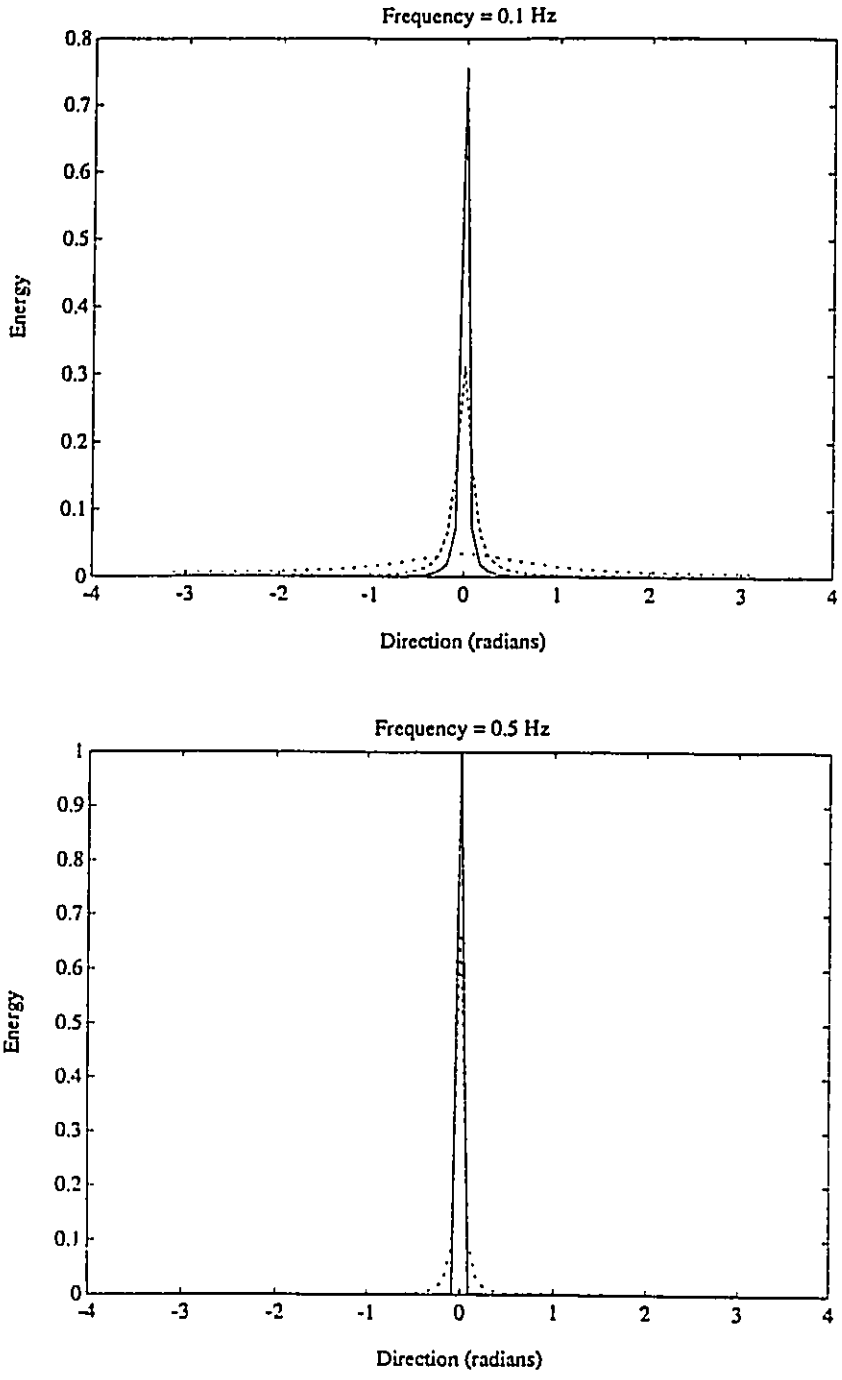

Fig.7.3 MLM estimate (6-wavestaff array) for a monochromatic wave input coming from 0°. Value of perturbation parameter ε : solid line 10^{-7}, dashed line 10^{-6}, dotted line 10^{-5}, dash-dotted line 10^{-4}. Top: $f = 0.1\ Hz$, Bottom: $f = 0.5\ Hz$.

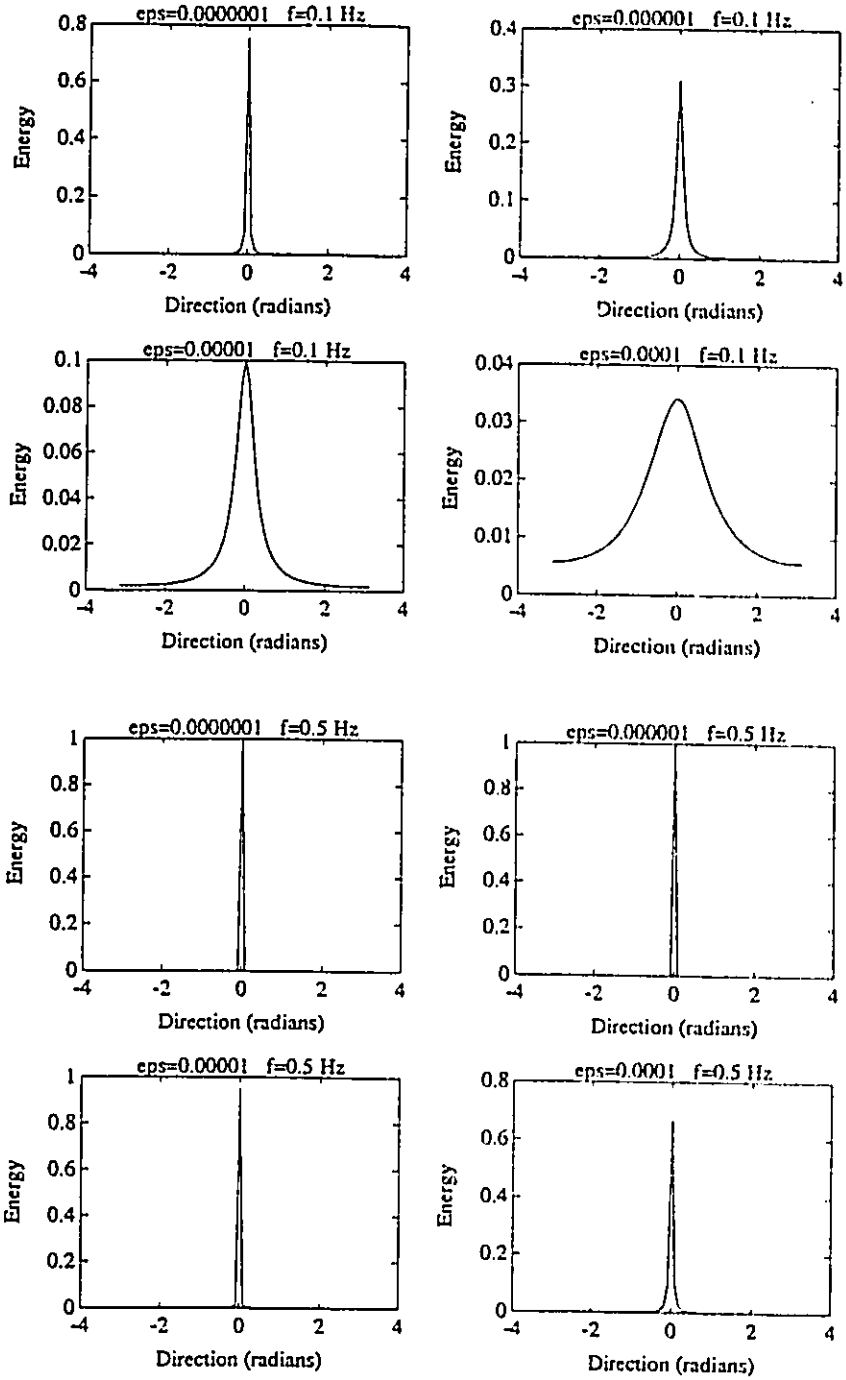

Fig.7.4 MLM estimate (6-wavestaff array) for monochromatic wave inputs coming from 0^{o} (solid line) and 22.5^{o} (dashed line), at four different values of the perturbation parameter ε. Top four plots: $f = 0.1\ Hz$, Bottom four plots: $f = 0.5\ Hz$.

also possibly induce artificial smearing of the MLM estimate. For this reason, the use of double-precision in computer codes is strongly recommended at the level of the Fourier Transform and calculation of the MLM estimate procedures. It should be noted that the Fortran program DIRSPEC presented in Chapter 4 operates in single precision whereas the program MIDSAP (also presented in Chapter 4) operates within the MATLAB platform which uses double precision (14 significant digits) as a default.

A few words should be said about the singularity of CPSD matrices. As mentioned by Jefferys et al. (1981), singularity will naturally occur when less wave frequencies fall within a FFT window width than there are wave properties measured. From Eq. 3.36, it can be seen that the CPSD can be expressed as the sum of N products of two vectors. The matrix obtained from the simple product of two vectors is a dyadic form and is necessarily singular. If the size of the matrix is "n", it naturally follows that at least "n" dyadic forms need to be added up to remove the singularity. For the analysis of field data, it is very unlikely that fewer wave frequencies will be present than the number of measured wave properties, and the perturbation should not be necessary. Also, as pointed out by Jefferys et al.(1981), small perturbations due to noise, quantization errors and leakage from neighboring frequencies could make an otherwise singular system appropriately conditioned. But, for test cases using Eq.3.36, or for simulations in directional wave tanks, the problem is very likely to be present. For these reasons, it is recommended that the CPSD be nevertheless perturbed for all cases, using a value of ε small enough so as to not produce any artificial smearing of the wave directional spectrum or produce directional effects for wavestaff arrays. Examination of field data (see future chapters) indicated that effectively, in most cases, the added perturbation was not necessary as the system was already well conditioned due to naturally occurring noise.

7.2. A MODIFIED FORM OF THE CONVOLUTIVE MLM

The results presented in the previous section clearly outline that the basis for the Convolutive MLM scheme of Tsanis and Brissette (1992), presented in Chapter 3, is not general in the sense that it corrected mainly for a numerical artifact introduced due to a lack of precision and not an intrinsic property of the MLM. Nevertheless, the scheme can still be used by choosing a different convolution window.

The window function used by Tsanis and Brissette (1992) for the convolution was calculated using a monochromatic wave as an input to the MLM. As a result, the convolution scheme had a significant effect for narrow spreading functions and a somewhat less significant effect for distributions with a larger spreading. Instead of using a monochromatic wave as the input to the MLM (since it is now known that the output will be unchanged for a good estimate) the idea is to use a function with a known spreading, compute the MLM estimate and then find the window function which, once convolved with the MLM estimate, will give back the input function. From the constraint 7.1, we should expect the MLM estimate to be close to target for narrow spreading functions, and to become a more and more smeared estimate as the spreading increases. The problem then becomes to select the spreading parameter β from which to calculate the window function. An aspect of the convolution process is that the wider the function (in terms of spreading), the more complex the window function will be. Window functions with negative values must be avoided since they might potentially result in impossible negative values of the directional spectrum. The procedure that was used was to select a $sech^2$ spreading function with a high value of the spreading parameter β, compute the MLM estimate, calculate the window function, and then lower the β value until the window starts to oscillate and give negative values. The procedure is presented in Fig. 7.5 which displays the shape of the

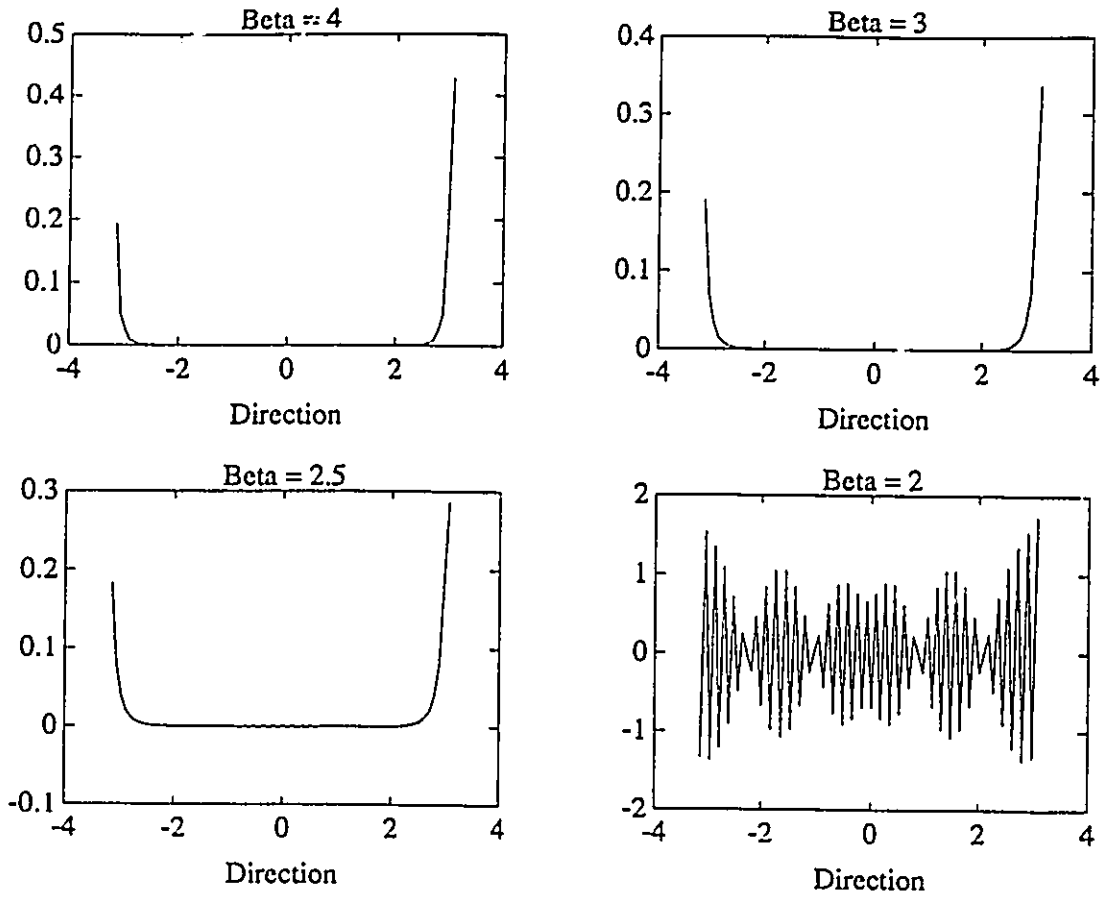

Fig.7.5 Shape of the convolution window for the Convolutive Maximum Likelihood Method as a function of the value of the spreading parameter β used in the target $sech^2$ spreading function.

window function for different values of the spreading parameter β. It can be seen that at a value of β = 2.5, the window starts to give negative values. As a result, the window function that was chosen was computed using as an input a $sech^2$ spreading function with β = 3.

The convolution process was also performed in a slightly different manner than presented in Chapter 3, where the convolution scheme was based on the assumption that the MLM estimate $\hat{S}(\theta)$ was equal to the true underlying spectrum $S(\theta)$ convolved by the window function W of the MLM process:

$$\hat{S}(\theta) = \int_{-\pi}^{\pi} S(\alpha)\, W(\theta-\alpha) d\alpha \tag{7.3}$$

The present formulation reverses the assumption and simply states that the true spectrum is equal to the MLM estimate convoluted by a window function:

$$S(\theta) = \int_{-\pi}^{\pi} \hat{S}(\alpha) W(\theta-\alpha) d\alpha \tag{7.4}$$

The two approaches are equivalent but the advantage of the present formulation is that Eq. 7.4 can be expressed as the system of equations

$$\begin{aligned}
S_1 &= \hat{S}_1 W_N + \hat{S}_2 W_{N-1} + \hat{S}_3 W_{N-2} + \ldots\ldots + \hat{S}_N W_1 \\
S_2 &= \hat{S}_1 W_1 + \hat{S}_2 W_N + \hat{S}_3 W_{N-1} + \ldots\ldots + \hat{S}_N W_2 \\
&\cdots \\
S_N &= \hat{S}_1 W_{N-1} + \hat{S}_2 W_{N-2} + \hat{S}_3 W_{N-3} + \ldots\ldots + \hat{S}_N W_N
\end{aligned} \tag{7.5}$$

The system of equations given in 7.5 is similar to the one presented in 3.65 but has the distinct advantage of not requiring any matrix inversion for the calculation of $S(0)$. In the present formulation, the window function is determined by rearranging 7.5 and solving for W, knowing

$S(\theta)$ and $\hat{S}(\theta)$.

7.3. A NORMALIZED FORM OF THE MLM

The convolutive MLM aims at correcting the artificial angular spreading imposed by the MLM. The convolution window was chosen so that a distribution function with a spreading parameter $\beta = 3$ be perfectly convoluted to its correct form. The window function is then constant and the results of the CMLM should be dependent on the spreading of the function to be convoluted. This is an unwanted characteristic and a method which could correct the artificial angular spread of the MLM, independently of the spreading, should, in theory, be superior. The Normalized MLM (MLM) is an attempt at this task.

7.3.1. Unimodal Distributions

In order to investigate the response of the MLM toward distributions of variable spreading, a series of 50 $sech^2$ distribution functions given by:

$$S(\theta) = \frac{1}{2}\,\beta\, sech^2\left[\beta(\theta)\right] \tag{7.6}$$

were generated, using values of the spreading parameter β ranging from 1 to 6 which encompass the normal range of 1.24 to 2.62 found in wind waves as defined by Donelan, Hamilton and Hui (1985). Using each distribution function, a CPSD matrix was reconstructed from which a MLM estimate was computed. Finally a $sech^2$ spreading function was fitted to each MLM estimate using a least-square criterion. Figure 7.6a shows a plot of the β values fitted to the MLM estimate (for heave-pitch-roll data) as a function of the input β values. Figure 7.6b shows the

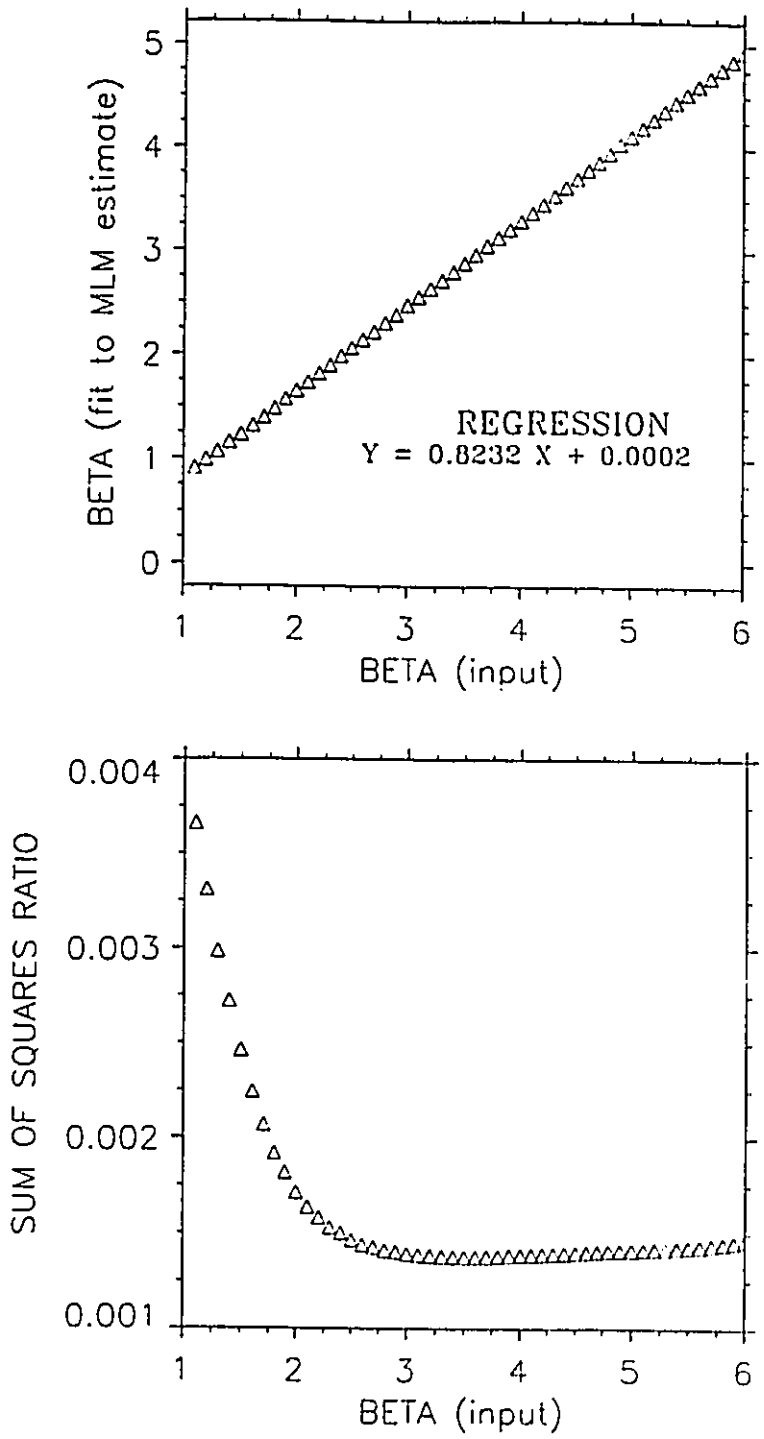

Fig.7.6 Least-square fits of $sech^2$ spreading functions to the MLM estimates (heave-pitch-roll data) obtained using as a target $sech^2$ spreading functions with β values ranging from 1 to 6. Top: comparison of β values between input and fitted populations, Bottom: Sum of squares ratio of least-square fit.

values of a "sum of squares ratio" defined as:

$$\frac{\sum_{i}^{N} \left[S(\theta_i) - \hat{S}_{mlm}(\theta_i)\right]^2}{\sum_{i}^{N} S(\theta_i)^2} \tag{7.7}$$

Figure 7.6a shows that the MLM estimate overpredicts the spreading, but interestingly, this overprediction is constant over the entire range of values of the spreading parameter β. The fit of the $sech^2$ spreading functions to the MLM estimates was excellent in every case as expressed in Figure 7.6b.

This inherent characteristic of the MLM suggests that since the artificial angular spreading induced by the method can be reduced to a constant, it should then be possible to account for it by forcing the MLM estimate of the angular energy distribution to a narrower form. There are different ways of accomplishing this task, one of the simplest being to normalize the energy in each direction according to a factor ζ_i defined as:

$$\zeta_i = \alpha \frac{sech^2(\alpha \beta \theta_i)}{sech^2(\beta \theta_i)} \tag{7.8}$$

where β is the spreading parameter of the $sech^2$ distribution function fitted to the MLM estimate and α is a "constriction" factor whose value is fixed at 0.82 accordingly to the linear least-square fit performed in Figure 1. Essentially, the normalization factor ζ_i simply rescales the energy in every direction according to a ratio of $sech^2$ spreading functions chosen as to exactly account for the MLM induced angular spreading.

The same test was also performed for the three and six-wavestaff arrays of Figure 6.1.

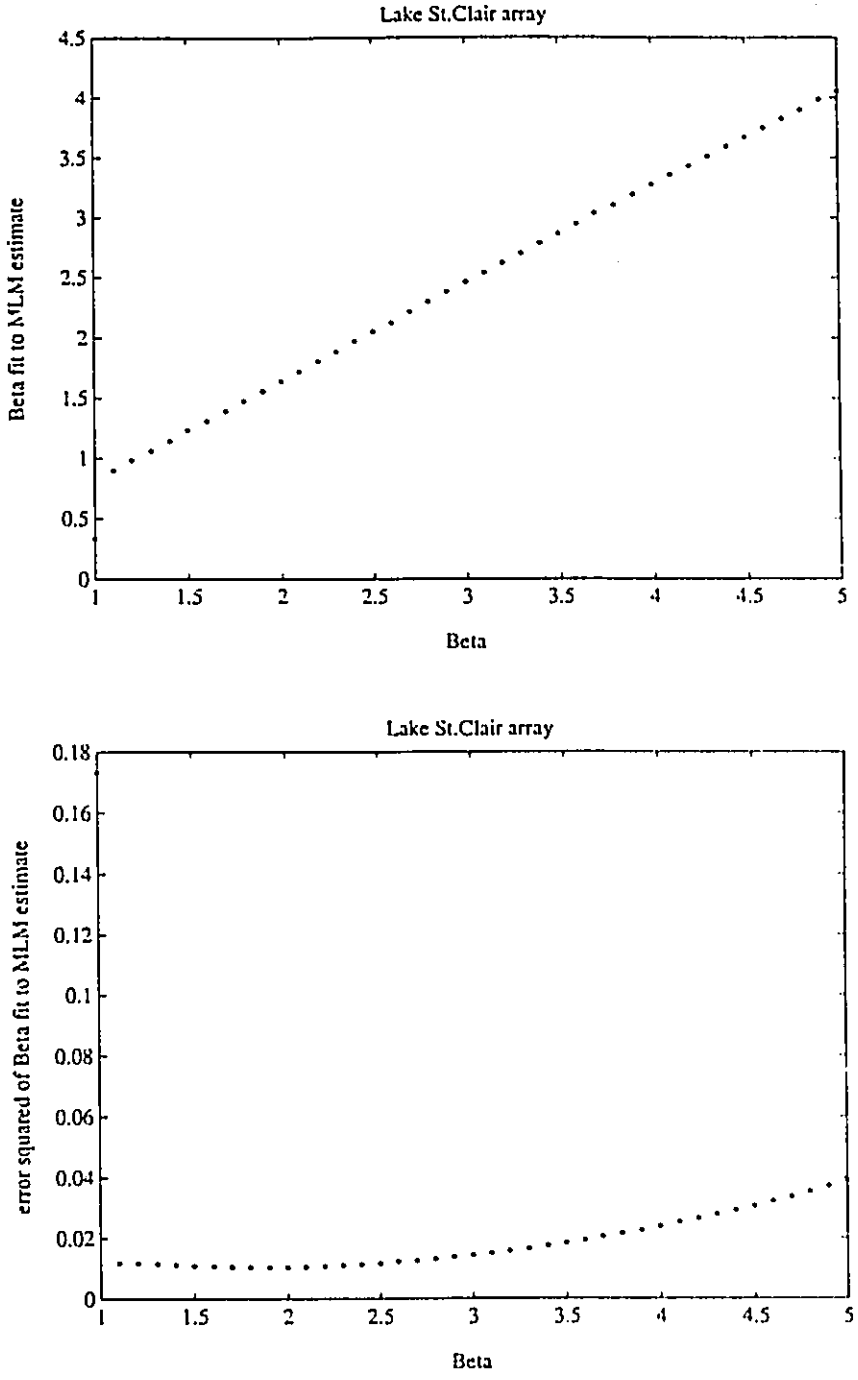

Fig.7.7 Least-square fits of $sech^2$ spreading functions to the MLM estimates (3-wavestaff array data) obtained using as a target $sech^2$ spreading functions with β values ranging from 1 to 6. Top: comparison of β values between input and fitted populations. Bottom: Sum of squares ratio of least-square fit.

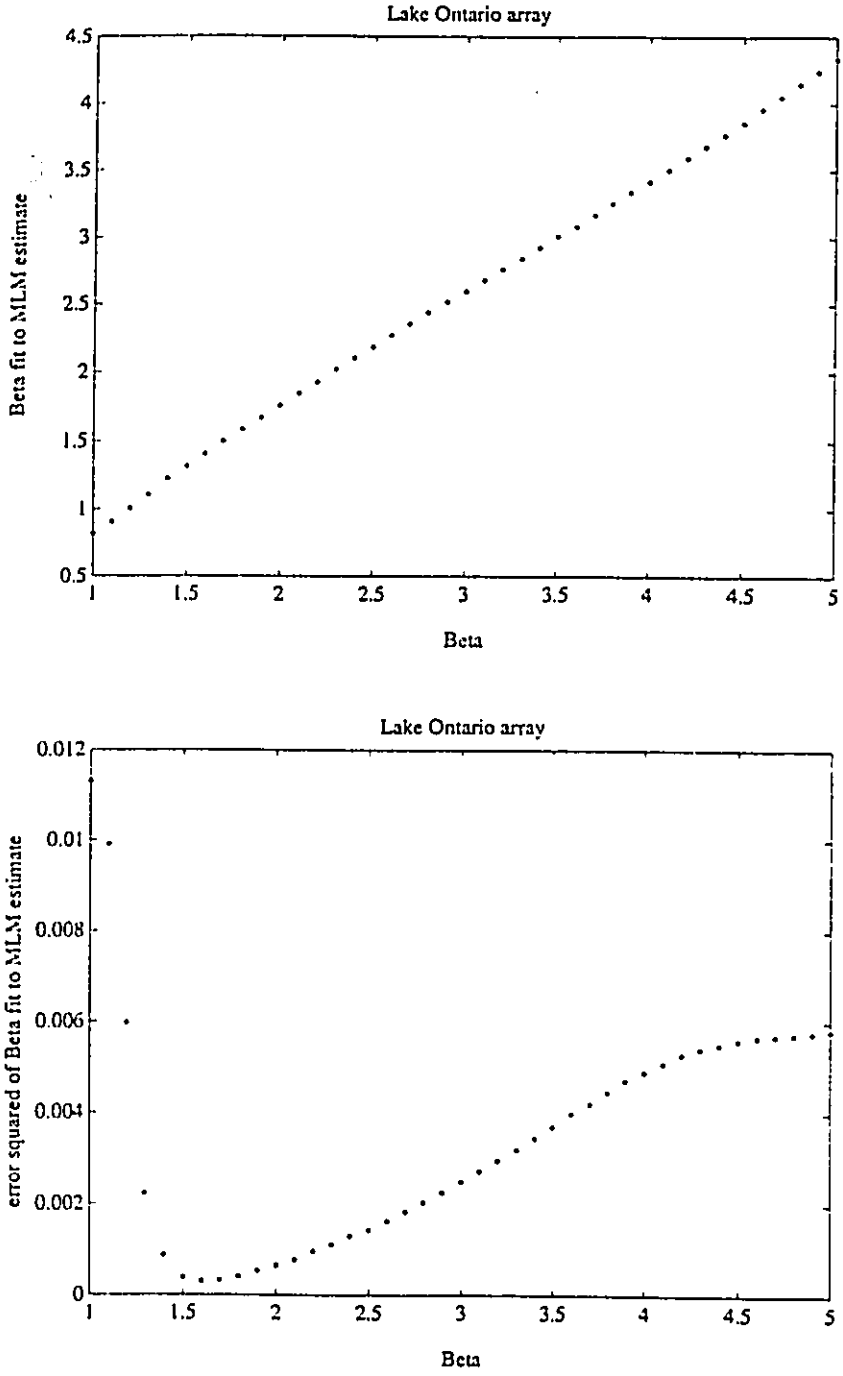

Fig.7.8 Least-square fits of $sech^2$ spreading functions to the MLM estimates (6-wavestaff array data) obtained using as a target $sech^{\beta}$ spreading functions with β values ranging from 1 to 6. Top: comparison of β values between input and fitted populations. Bottom: Sum of squares ratio of least-square fit.

Figures 7.7 and 7.8 indicate that the constant overprediction of the MLM is inherent to the method and not a function of the instrumentation. On the other hand, the value of the constriction factor α will be a function of the number of wave properties measured (and not of the instrumentation). The α parameters for the three and six-wavestaff arrays are respectively 0.82 and 0.87. The equivalence of the parameter for the three-wavestaff array and the pitch-roll-heave buoy was predictable from the results presented in Chapter 6 since both systems behave identically.

7.3.2. Bimodal Distributions

Since the normalization scheme works on the basis of a unimodal distribution, it is necessary in a first step to extract the unimodal distributions buried in the angular distribution of energy, and then carry individual normalizations on each of these unimodal distributions. Although a seemingly simple task for the human eye, the procedure of separating distributions with an automated computer routine is a deceptively complicated one.

7.3.2.a Separating bimodal distributions into unimodal components

Any angular distribution of energy $S(\theta)$ can be expressed as

$$S(\theta) = \frac{1}{2}\,\phi_1\,\beta_1\,sech^2\left[\beta_1\left[\theta-\bar{\theta}_1\right]\right] + \frac{1}{2}\,\phi_2\,\beta_2\,sech^2\left[\beta_2\left[\theta-\bar{\theta}_2\right]\right] + R(\theta) \qquad (7.9)$$

the sum of two $sech^2$ distribution functions and a residual $R(\theta)$. In order to fit two $sech^2$ functions to the angular distribution of energy, 6 parameters have to be fixed, the position of the distributions (θ_1 θ_2), their spreading (β_1 β_2) and scaling (ϕ_1 ϕ_2). The best-fit criterion should

minimize the summation of the square of the errors between the target and fitted distribution; the usual least-square fit criterion. A least-square fit involving 6 free parameters is a very delicate operation very likely to be slow and to converge on an unwanted local minimum. In order to improve the efficiency of the least-square fit, it is necessary to reduce the number of free parameters, preferably below 5. Normalizing $S(\theta)$ to unity, it can be shown that

$$\phi_1 = 1 - \phi_2 \tag{7.10}$$

and by fixing $\bar{\theta}_1$ to the peak of the angular distribution of energy, we can reduce the number of free parameters to four. Carefully choosing initial values for the free parameters will insure maximum efficiency of the iterative scheme. Following the least-square fit, the value of the residuals $R(\theta)$ will give an indication on the goodness of the fit and the validity of the approach. The multivariate function minimization routine of MATLAB uses the Nelder-Meade simplex algorithm which is very robust (Press et al., 1986). Figure 7.9 shows a typical example of a least-square fit performed on a distribution consisting of two $\cos^2$ distributions functions. Despite the fact that the target distributions are different in nature than the fitted one, the residual is small. As mentioned previously, the quality of the fit is not that fundamental to the method since the fitted parameters are used only in order to calculate the normalization factors, which are themselves only weakly dependent on the finer details of the fit.

7.3.2.b Normalization properties of bimodal distributions

In the case of unimodal distributions, the value of the constriction parameter α was constant. In cases where two unimodal distributions are intertwined, it is necessary to verify that the MLM characteristic of overpredicting the spreading stays constant. Figure 7.10 shows the heave-

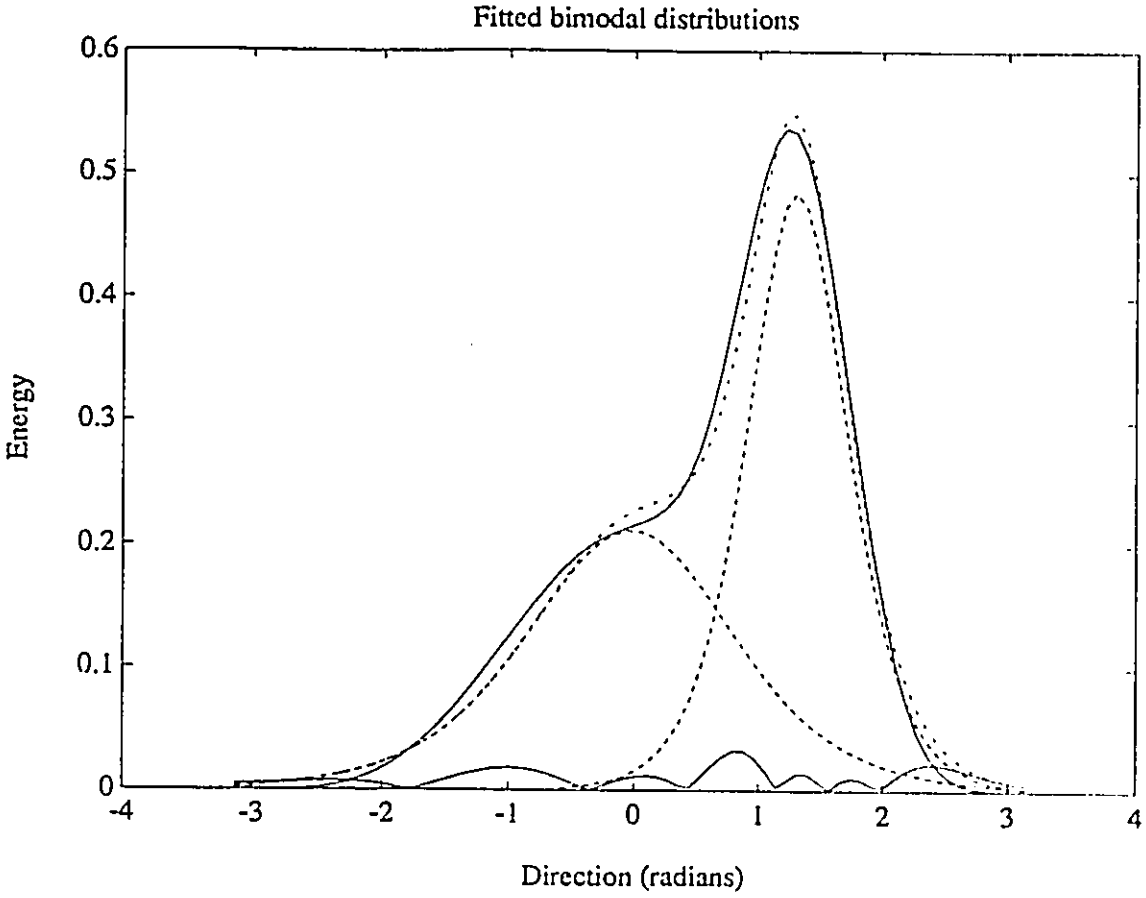

Fig.7.9 Example of results obtained from the fitting of two $sech^2$ spreading functions to an observed angular distribution of energy. Main solid line: observed distribution, dashed lines: fitted populations, solid line: residuals obtained from the least-square fit.

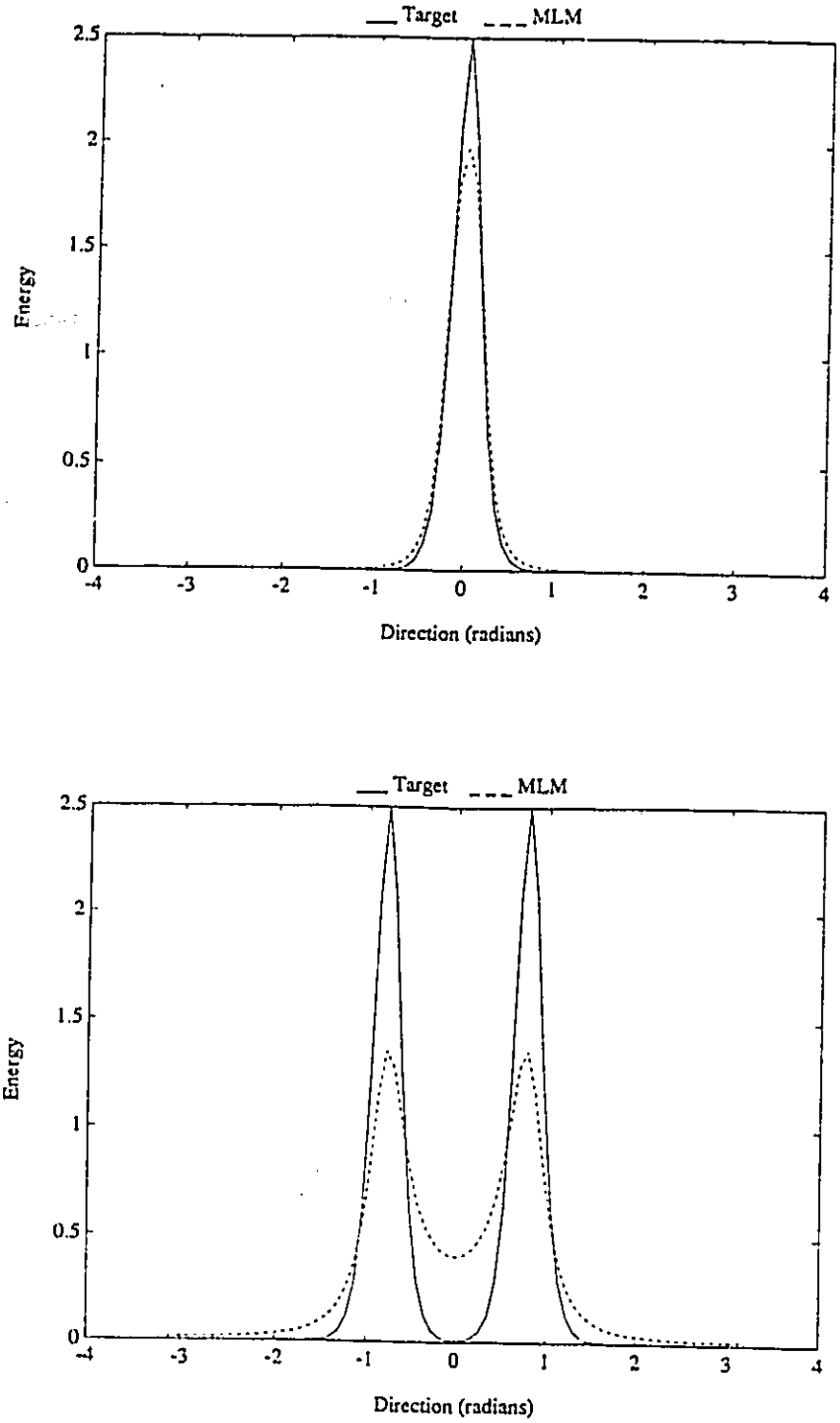

Fig.7.10 MLM estimates (pitch-roll data) for unimodal (top) $sech^2$ function ($\beta = 2$), and bimodal (bottom) distribution composed of two identical $sech^2$ functions ($\beta = 2$). Solid line: target, dashed line: MLM estimate.

pitch-roll MLM estimates for both a unimodal and bimodal distributions consisting of $sech^2$ spreading functions with $\beta = 5$. It can be seen that the MLM induced smearing is greater for the bimodal distribution, indicating non-linearity of the Method in that respect. This means that in order to obtain a good estimate, the two distributions can be separated into unimodal components but can't be normalized using the same value of α previously used. It should be expected that the normalization parameters might possibly be a function of the spacing between the distributions, their spreading and the energy ratio between the distributions. Of those three, only the energy ratio has an effect. It is known because from Figure 7.10, it was seen that the MLM smearing was larger for equal energy bimodal distributions than for the equivalent unimodal distribution, whereas at the other hand of the spectrum, for bimodal distributions with a large energy ratio (one distribution containing most of the energy) it should be expected that the Normalization will tend toward its unimodal form.

In order to establish a correcting scheme for bimodal distributions, a series of bimodal distributions with different spacing, spreading and energy ratios were used, from which MLM estimates were computed. In order to simplify the task, only bimodal distributions with equal spreading of both distributions were used. The MLM estimates were then separated into unimodal components following the procedure outlined in 7.3.2.a. Various parameters were then computed to relate the "target" distributions to the MLM distributions in order to establish a corrective normalizing scheme for bimodal distributions. After testing many different parameters in order to maximize the corrective scheme, it was possible to establish correcting rules based on only two measured values of the MLM fitted populations: The spreading parameter β of the population containing the most energy, and the peak ratio between both populations. Figure 7.11 is a plot of the ratio of the β values fitted to the MLM estimate (for the 6 wavestaff array of Lake

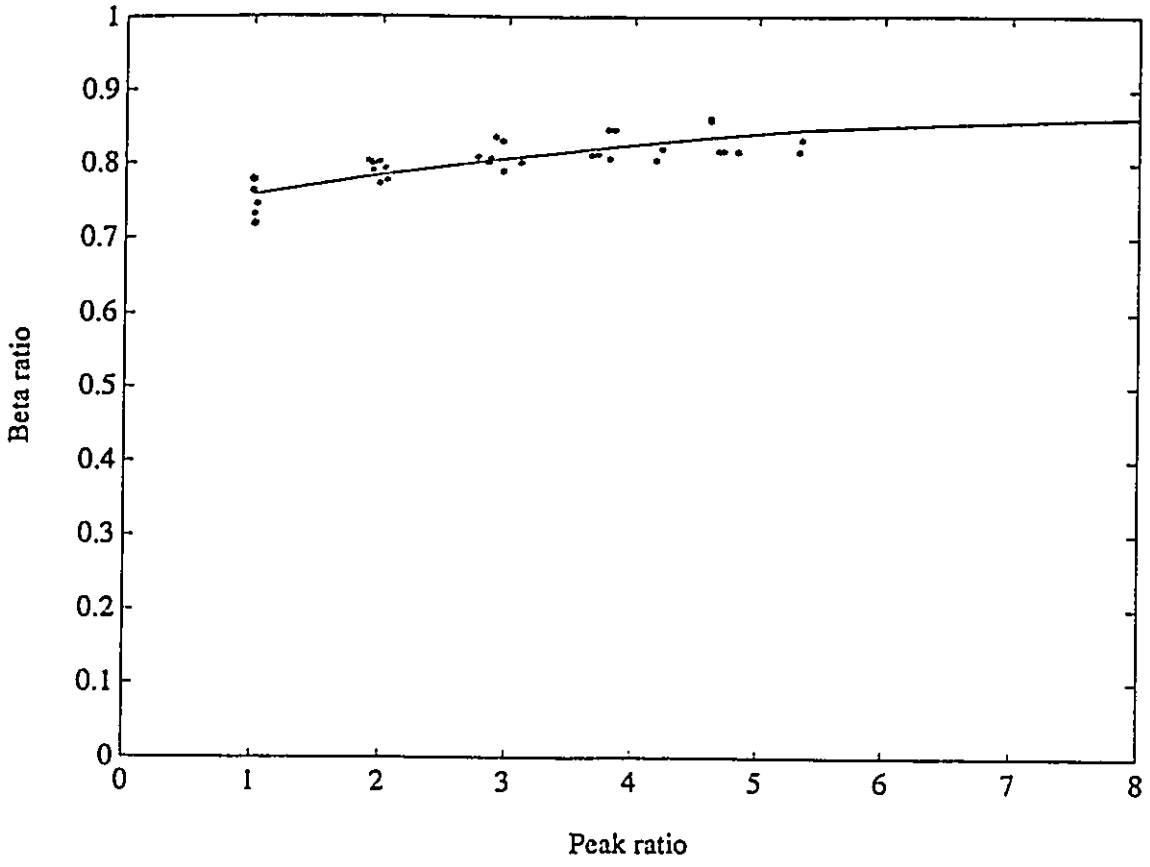

Fig.7.11 Normalization scheme for bimodal distribution (6-wavestaff array data). Established relationship between the spreading parameter β of the population containing the most energy, and the peak ratio between both fitted populations.

Ontario) to the input β values, as well as a least-square fit of the data points. It can be seen that the MLM smearing becomes more important as the energy becomes more evenly distributed between the two distributions. For high peak ratios (meaning that most of the energy is in one distribution), the β ratio tends to 0.87 which is the value determined for unimodal distributions in Figure 7.8a. Using this graph, the distribution containing more energy can be normalized. The next step was to relate the true peak ratio (TPR) to the measured peak ratio (PR) in order to normalize the second distribution. This can be done using the plots shown in Figure 7.12. These plots express the relationship between TPR and PR as a function of the spacing and spreading of the functions. All the relationships are linear and allow the direct normalization of the second distribution. More details are given in Appendix 7.

7.3.3. An Iterative form of the NMLM

The Normalized form of the MLM is an empirical procedure which aims at correcting the artificially induced spreading of the MLM. As such, the NMLM estimate will not be consistent with its input CPSD matrix in most cases. That is, if one reconstructs the CPSD matrix from the NMLM estimate, the resulting matrix will be different from the one originally used in calculating the estimate. Similarly to the MLM case, it is possible to use an iterative scheme to correct for this inconsistency. A similar scheme to the one presented in Eq. 3.54 was used:

$$S_{(n+1)} = S_n + \upsilon \left[S_{MLM} - S^R_{MLM} \right] \tag{7.11}$$

with the difference that the starting point of the scheme was taken as $S_0 = S_{NMLM}$, instead of $S_0 = S_{MLM}$ used in the usual IMLM. It can be seen from Eq. 7.11 that the iterative scheme forces the convergence of the Iterative NMLM using the MLM estimate, and not the NMLM estimate.

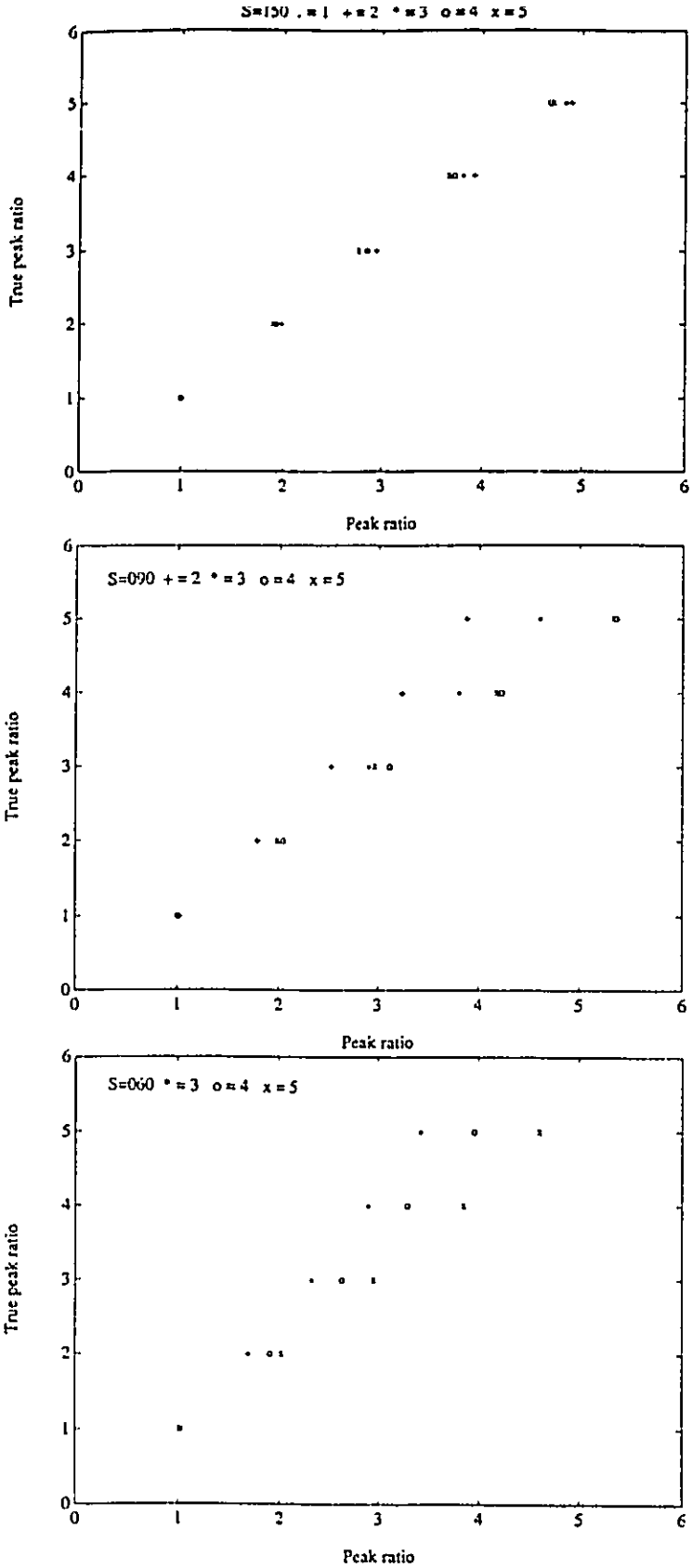

Fig.7.12 Normalization scheme for bimodal distribution (6-wavestaff array data). Established relationship between the true peak ratio (TPR) of the input distribution to the measured peak ratio (PR).

This was done to speed up the convergence since an MLM estimate is faster to compute than another NMLM estimate (see Chapter 9), and also because since the NMLM is an empirically based fitting method, convergence would not necessarily be fully warranted in all cases. In short, the proposed scheme is identical to the one presented in Chapter 3 for the IMLM except that it uses the NMLM estimate as a starting point for the iterations. If the NMLM correcting scheme is effective, its estimate should be closer to the real spectrum than the MLM estimate should, and the iterative scheme should then converge faster and give a better estimate.

7.4. AN EXACT FORM OF THE MLM

The CMLM and NMLM method are both empirical methods, in the sense that they rely on measured properties of the MLM to establish a corrective scheme. As a result these methods can be evaluated solely on their performance. Even if these methods perform extremely well, a sound, logical and theoretical framework for the derivation and use of the methods will be absent. The goal of this work is without a doubt to find a best-performing method, but the strong foundation and elegance of a theoretically sound method is indeed a wanted characteristic.

The derivation of the Maximum Likelihood Method for the estimation was presented in Chapter 3. It was shown that a solution of the form of Eq. 3.29 was sought

$$\hat{S}(\theta_j,\omega_k) = A^H(\theta_j,\omega_k)\, C(\omega_k)\, A(\theta_j,\omega_k) \tag{7.12}$$

which was shown to be equal to (after the frequency dependence notation is dropped for simplicity)

$$\hat{S}(\theta_j) = \sum_{i=1}^{N} \left[|\, A^H(\theta_j)\, X(\theta_i)\,|^2\, S(\theta_i) \right] \tag{7.13}$$

Essentially, Eq. 7.13 indicates that the wave energy at a given direction of propagation θ_j is equal to the sum of the energy in each directional band θ_i multiplied by a weighting factor, function of both the direction of interest θ_j and all the other direction bins θ_i. The weighting function at any direction θ_i is given by:

$$|A^H(\theta_j)\, X(\theta_i)|^2 \tag{7.14}$$

From the optimization constraint (Eq. 3.44), we know that when $i = j$ the weighting factor is equal to unity. At each frequency, the MLM estimate $\hat{S}(\theta_j)$ can be rewritten in the following form for each of the N direction bins:

$$\begin{aligned}
\hat{S}(\theta_1) &= |A^H(\theta_1)X(\theta_1)|^2 S(\theta_1) + |A^H(\theta_1)X(\theta_2)|^2 S(\theta_2) + \ldots\ldots + |A^H(\theta_1)X(\theta_N)|^2 S(\theta_N) \\
\hat{S}(\theta_2) &= |A^H(\theta_2)X(\theta_1)|^2 S(\theta_1) + |A^H(\theta_2)X(\theta_2)|^2 S(\theta_2) + \ldots\ldots + |A^H(\theta_2)X(\theta_N)|^2 S(\theta_N) \\
&\;\;\vdots \qquad\qquad \vdots \qquad\qquad \vdots \qquad\qquad \vdots \\
\hat{S}(\theta_N) &= |A^H(\theta_N)X(\theta_1)|^2 S(\theta_1) + |A^H(\theta_N)X(\theta_2)|^2 S(\theta_2) + \ldots\ldots + |A^H(\theta_N)X(\theta_N)|^2 S(\theta_N)
\end{aligned} \tag{7.15}$$

which can be rewritten under the simple form

$$\underline{\hat{S}} = |\underline{A}\ \underline{X}^T|^{.2}\ \underline{S} \tag{7.16}$$

where the ".2" exponent denotes an element-by-element operation and $\underline{A}$ and $\underline{X}$ are N by M matrices where M is the number of sensors or the number of measured wave properties, and $\underline{\hat{S}}$ and $\underline{S}$ are column vectors of size N. More specifically,

$$\underline{A} = \begin{bmatrix}
[A_1^*(\theta_1) & A_2^*(\theta_1) & \ldots\ldots & A_M^*(\theta_1)] \\
[A_1^*(\theta_2) & A_2^*(\theta_2) & \ldots\ldots & A_M^*(\theta_2)] \\
[A_1^*(\theta_3) & A_2^*(\theta_3) & \ldots\ldots & A_M^*(\theta_3)] \\
 & \ddots & \ddots & \\
[A_1^*(\theta_N) & A_2^*(\theta_N) & \ldots\ldots & A_M^*(\theta_N)]
\end{bmatrix} \tag{7.17}$$

and

$$\underline{X} = \begin{bmatrix} [X_1(\theta_1) & X_2(\theta_1) & \ldots\ldots & X_M(\theta_1)] \\ [X_1(\theta_2) & X_2(\theta_2) & \ldots\ldots & X_M(\theta_2)] \\ [X_1(\theta_3) & X_2(\theta_3) & \ldots\ldots & X_M(\theta_3)] \\ & \cdot\ \cdot\ \cdot & & \\ & \cdot\ \cdot\ \cdot & & \\ [X_1(\theta_N) & X_2(\theta_N) & \ldots\ldots & X_M(\theta_N)] \end{bmatrix} \tag{7.18}$$

From Eq. 7.16, it can be seen that if all the vectors $A(\theta_i)$ are known, and since all the $X(\theta_i)$ are defined, after calculating the MLM estimates $\hat{S}(\theta_i)$ we can define a real algebraic system of N equations with N unknowns: the values of the underlying real directional spectrum. The system can then be solved as:

$$\underline{S} = inv \left\{ |\underline{A}\ \underline{X}^T|^2 \right\}\ \underline{\hat{S}} \tag{7.19}$$

where *inv* denotes the inverse of the square matrix $|\underline{A}\ \underline{X}^T|^2$ of rank N. In order to find an expression for the $A(\theta_i)$ vectors it is necessary to carry the optimization of the Lagrangian function given in chapter 3 as:

$$L(A(\theta_i),\mu) = A^H(\theta_i)\, C\, A(\theta_i) + \mu\,(A^H(\theta_i)\, X(\theta_i) - 1) \tag{7.20}$$

For three measurements of the wave field, Eq. 7.20 can be rewritten at length as:

$$A_1(A_1^* C_{11} + A_2^* C_{21} + A_3^* C_{31}) + A_2(A_1^* C_{12} + A_2^* C_{22} + A_3^* C_{32}) + A_3(A_1^* C_{13} + A_2^* C_{23} + A_3^* C_{33}) - \mu(A_1 X_1 + A_2 X_2 + A_3 X_3 - 1) \tag{7.21}$$

Carrying the minimization requires taking the partial derivatives $\partial l/\partial A_1$, $\partial l/\partial A_2$, $\partial l/\partial A_3$. In matrix form the result can be show to be equal to:

$$CA(\theta_i) = \frac{\mu}{2} X(\theta_i) \tag{7.22}$$

or

$$A(\theta_i) = \frac{\mu}{2} C^{-1} X(\theta_i) \tag{7.23}$$

Using the minimization constraint $X(\theta_i)^H A(\theta_i)=1$ (Eq. 3.44) within Eq. 7.23 and rearranging, we find:

$$\frac{\mu}{2} = \frac{1}{X(\theta_i)^H C^{-1} X(\theta_i)} \tag{7.24}$$

from which we find, combining Eqs. 7.23 and 7.24:

$$A(\theta_i) = \frac{C^{-1} X(\theta_i)}{X(\theta_i)^H C^{-1} X(\theta_i)} \tag{7.25}$$

With the general form of $A(\theta_i)$ known and given by Eq. 7.14, the system to solve to obtain an exact form of the MLM (Eq. 7.8) is given by:

$$\underline{S} = inv \left[\left| \left[\frac{C^{-1} X(\theta_i)}{X(\theta_i)^H C^{-1} X(\theta_i)} \right] \underline{X}^T \right|^2 \right] \hat{\underline{S}} \tag{7.26}$$

The general form of the MLM estimate was given in Eq.3.39 as:

$$\hat{S} = A(\theta_i)^H C A(\theta_i) \tag{7.27}$$

Using the following relationship,

$$(C^{-1} X(\theta_i))^H = X(\theta_i)^H C^{-1} \tag{7.28}$$

and combining Eq.7.25 and Eq.7.27, it is possible to retrieve the MLM estimate as expressed in

Eq.3.46:

$$\frac{1}{X(\theta_1)^H C^{-1} X(\theta_i)} \tag{7.29}$$

We can finally rewrite Eq. 7.19 (or Eq. 7.26) as follows:

$$\underline{S} = \frac{inv\left[\left|\left[\frac{C^{-1} X(\theta_i)}{X(\theta_i)^H C^{-1} X(\theta_i)}\right] \underline{X}^T\right|^2\right]}{\underline{X(\theta_i)^H C^{-1} X(\theta_i)}} \tag{7.30}$$

which is in theory, an exact solution of the wave directional spectrum using the Maximum Likelihood Method. This solution, contrarily to the MLM estimate, should be fully consistent with the input CPSD and be a true estimate of the directional spectrum.

An infinite number of directional spectrum can be consistent with the CPSD matrix and thus give the same MLM estimate, but only one can be consistent with Eq. 7.28. The new method will be referred to with the acronym MLMC which stands for either MLM Corrected method and MLM Closed-form.

CHAPTER 8

COMPARISON OF ALL METHODS

In Chapters 5 and 6, a comparison of existing methods was presented, based on a few test cases involving both unimodal and bimodal distributions. The number of tests was limited (especially in the bimodal range) as the aim was essentially to identify the strong and weak attributes of each method, in order to establish the needs for better performing methods and to help focusing additional work in estimating wave directional spectra. Following that, three new methods of estimating the wave directional spectrum were presented, all based on the Maximum Likelihood principle. For the purpose of this work, we now have nine different methods and variants for estimating the wave-directional spectrum for heave-pitch-roll data, and fourteen different methods and variants for wavestaff data. All the methods reviewed in this chapter and appropriate references are listed in Table 8.1 for heave-pitch-roll data and Table 8.2 for wavestaff data. Before drawing any definite conclusion on the choice of a best performing method, it is necessary to thoroughly test all methods for a large number of both unimodal and bimodal distributions. A large enough number of tests will insure validity and warrant generality of the conclusions drawn on the results. Following the synthetic test cases, field data needs to be looked at in order to try to confirm the validity of the results obtained from the test cases, and to insure that all methods (with a special emphasis on the methods presented in Chapter 7) can be applied to the analysis of field data.

TABLE 8.1. Methods Used for Heave-Pitch-Roll Data

METHOD	ACRONYM	REFERENCES
Direct Fourier Transform Method	DFT	Longuet-Higgins et al.(1963)
Maximum Entropy Method	MEM	Lygre and Krogstad (1986)
Maximum Likelihood Method	MLM	Jefferys et al.(1981)
Iterative MLM	IMLM	Krogstad et al.(1988)
Eigen-Vector MLM	EVMLM	Marsden and Juszko (1987)
Convoluted MLM	CMLM	This work
Normalized MLM	NMLM	This work
Iterative NMLM	INMLM	This work
MLM Corrected	MLMC	This work

TABLE 8.2. Methods Used for Wavestaff Data

METHOD	ACRONYM	REFERENCES
Maximum Likelihood Method	MLM	Jefferys et al.(1981)
Iterative MLM	IMLM	Krogstad et al.(1988)
Normalized MLM	NMLM	This work
Iterative NMLM	INMLM	This work
MLM Corrected	MLMC	This work
Equivalent Pitch-Roll-Heave Methods		
Direct Fourier Transform Method	DFT	Longuet-Higgins et al.(1963)
Maximum Entropy Method	MEM	Lygre and Krogstad (1986)
Maximum Likelihood Method	MLM2	Jefferys et al.(1981)
Iterative MLM	IMLM2	Krogstad et al.(1988)
Eigen-Vector MLM	EVMLM	Marsden and Juszko (1987)
Convoluted MLM	CMLM	This work
Normalized MLM	NMLM2	This work
Iterative NMLM	INMLM2	This work
MLM Corrected	MLMC2	This work

8.1. TEST PROCEDURE

The procedure for the unimodal and bimodal synthetic test cases will be the same for both heave-pitch-roll and wavestaff data.

8.1.1. Unimodal Distributions

In order to examine the response of the different methods to unimodal distributions, two spreading functions will be used, the $sech^2$ of Donelan et al. (1985) and $\cos^2$ introduced by Longuet-Higgins et al. (1963), and with angular distributions respectively given by:

$$S(\theta) = \frac{1}{2}\beta sech^2\left[\beta(\theta-\bar{\theta})\right] \tag{8.1}$$

$$S(\theta) = \cos^{2s}\left[\frac{1}{2}(\theta-\bar{\theta})\right] \tag{8.2}$$

The use of two different spreading functions will allow comparisons to be made to insure that the different methods return estimates which are not dependent on the form of the angular spreading of energy. This is especially critical in the case of the Normalized form of the MLM (NMLM) which has to use a given spreading function in its normalization scheme.

In total, 8 distributions were generated for both spreading functions, giving a total of 16 unimodal test cases. Values of the spreading parameters ranged from 1 to 4.5 for β and from 2 to 35 for the "s" parameter of the $\cos^2$ spreading function. The target spreading functions for all 16 tests are displayed in Appendix 5. Similarly to the procedure used in the test cases presented in Chapter 5 and 6, CPSD matrices were directly obtained using the target spectra, and from which directional spectrum estimates were computed. The estimates were all computed at a frequency

of 0.5 Hz. The choice of frequency is not critical since most methods return estimates which are frequency independent, and also because all computations were done using the accuracy guidelines set in section 7.1, thus reducing to a minimum most frequency-dependent (or wavenumber-dependent) effects. All the unimodal distributions chosen for the 16 tests are symmetrical. Since skewed unimodal (one peak) distributions can be seen as the sum of two closely spaced symmetrical unimodal distributions, they will be considered as bimodal distributions.

8.1.2. Bimodal Distributions

In the ocean, the wavefield at any given location is affected not only by the local wind conditions, but also potentially by any other meteorological system on the same ocean. Low frequency swell components dissipate very little energy and can propagate far away from their generation area and interact with waves being actively generated by another meteorological system. For this reason, bimodal seas are more the norm than the exception in the open ocean and there is a particular interest in being able to resolve such bimodalities. For all bodies of water smaller than a typical meteorological system, roughly 500 km across, one should expect to observe unimodal directional spectra. This should be true most of the time, at least around the spectral peak, but even then, mixed seas have been observed in Lake Ontario (see Tsanis and Donelan, 1989) which is only about 300 km long in its long fetch direction. Bimodal sea states can also be created by rapidly turning winds (Van Vledder and Holthuijsen, 1988) or due to refraction or reflection effects around islands or alongshore. Evidence from this work (next chapters) also indicate that bimodal sea states can be the result of wave-current interaction, fetch-length effect, and that bimodal distributions might be the norm in the higher frequency

range. In short, any wave study involving the directional spectrum is extremely likely to deal with bimodal spectra and many of the most interesting aspects of the evolution of wavefields involve such bimodalities. For these reasons, it is fundamental that methods of estimating the wave-directional spectrum be able to resolve bimodalities of the wavefield.

In order to investigate different methods response to bimodal seas, a number of bimodal distributions were created using three $sech^2$ spreading function with respective values of the spreading parameter β of 1, 3 and 5. All 6 possible combinations of these spreading functions were used with spacings of 30°, 90° and 150°, and energy ratios between the spreading functions ranging from 1 to 4 with intervals of 1. The combination of all possibilities gives a total of $6 \cdot 3 \cdot 4 = 72$ generated bimodal distributions. The target spreading functions for all 72 tests are displayed in Appendix 6. These 72 cases are though to cover most realistic possible cases of bimodal distributions.

8.2. HEAVE-PITCH-ROLL DATA

As listed in Table 8.1, nine differents methods of estimating the wave directional spectrum from heave-pitch-roll data are considered. All in all, in the course of this 3 years study, in excess of 200 different test cases have been performed and over 600 field data cases have been analyzed. To appropriately summarize the results is a formidable task. Only a few test cases can be shown in this dissertation and a particular effort was made to select tests representative of the general characteristics of the different methods of estimating the wave directional spectrum.

8.2.1. Test Results

As the comparison of the various estimates is based on tests using unimodal distributions, and then bimodal distributions, both cases will be discussed separately.

8.2.1.a Unimodal test cases

Figure 8.1 presents comparative histograms of the average errors Err1 and Err2 defined in Eq.5.6. Remembering that Err1 is the ratio of the summation of the errors between model and estimate over the total energy, it can be seen that the performance of the various estimates is generally good, with 5 methods giving estimates with less than 10% error. For both error parameters, clearly, the MEM and DFT methods are by far the worst estimates, and the NMLM, the best. The behavior of the various methods is usually predictable for unimodal distributions, and as such, the results of only one test case will be presented, that of a $sech^2$ spreading function with $\beta = 1.5$ (Figure 8.2). Similarly to the observations made in Chapter 5, the DFT and MLM methods return an estimate which is too wide, whereas the EVMLM is too narrow. The IMLM estimate, obtained using three iterations is pretty close over much of the spectrum but the tails can be observed to cut quite abruptly, which indicates the onset of instability. Because of that, the IMLM estimate will generally not be consistent with its CPSD matrix, as indicated by the high ρ^2 values in Figure 8.3. The CMLM estimate is nearly identical to the MLM indicating that the convolution has had little effect at that spreading. Finally, both the MEM and MLMC estimates are close to the model distribution away from the peak but the MEM fails at the peak by returning a bimodal estimate, whereas the MLMC is too flat. This characteristic was shown for the MEM to be the result of using perfectly symmetrical distributions with no noise, conditions never encountered in nature. Such behavior was never encountered in field data for

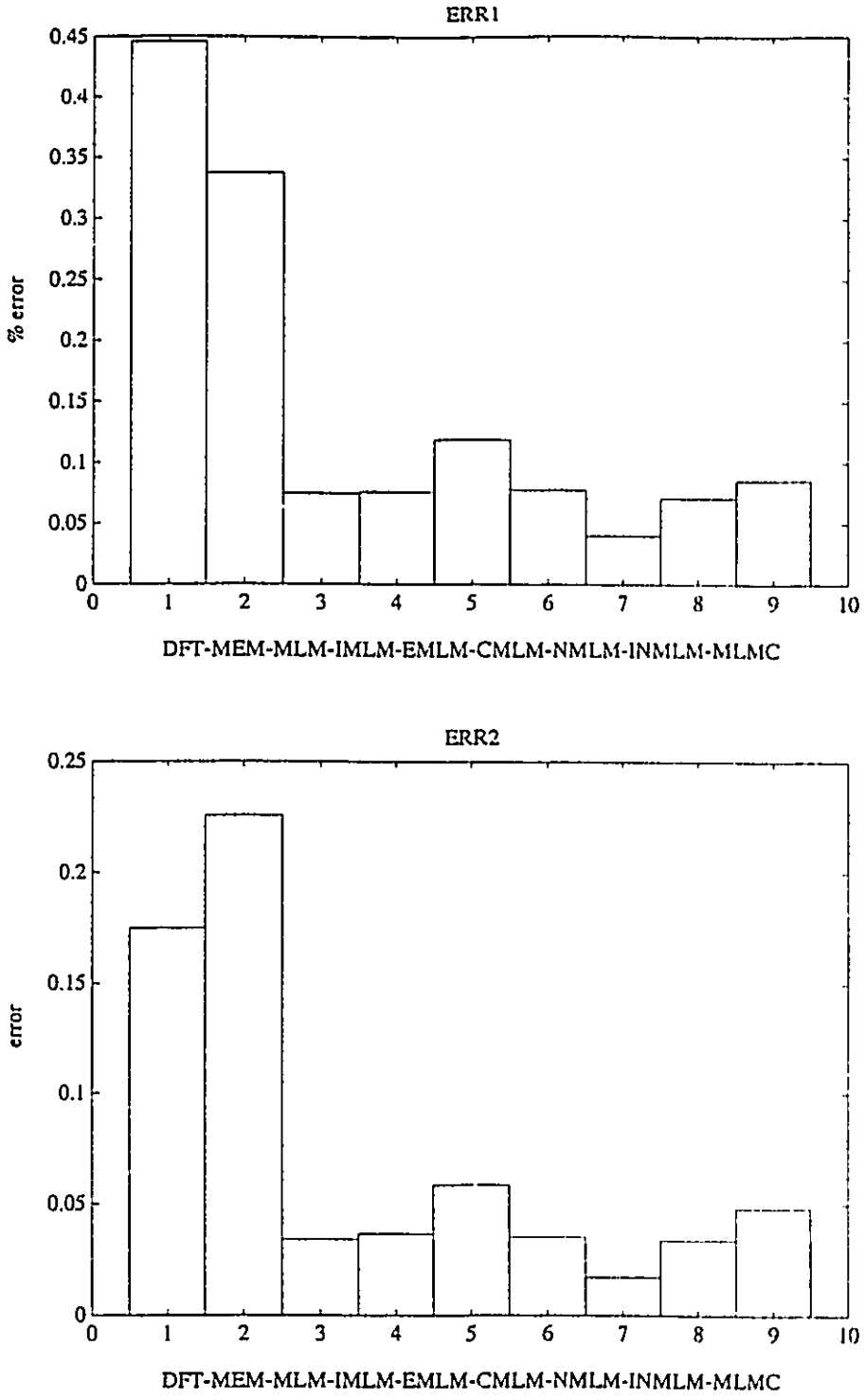

Fig.8.1 Comparative histogram of average error parameters for all directional spectrum estimation methods (pitch-roll data, unimodal test cases).

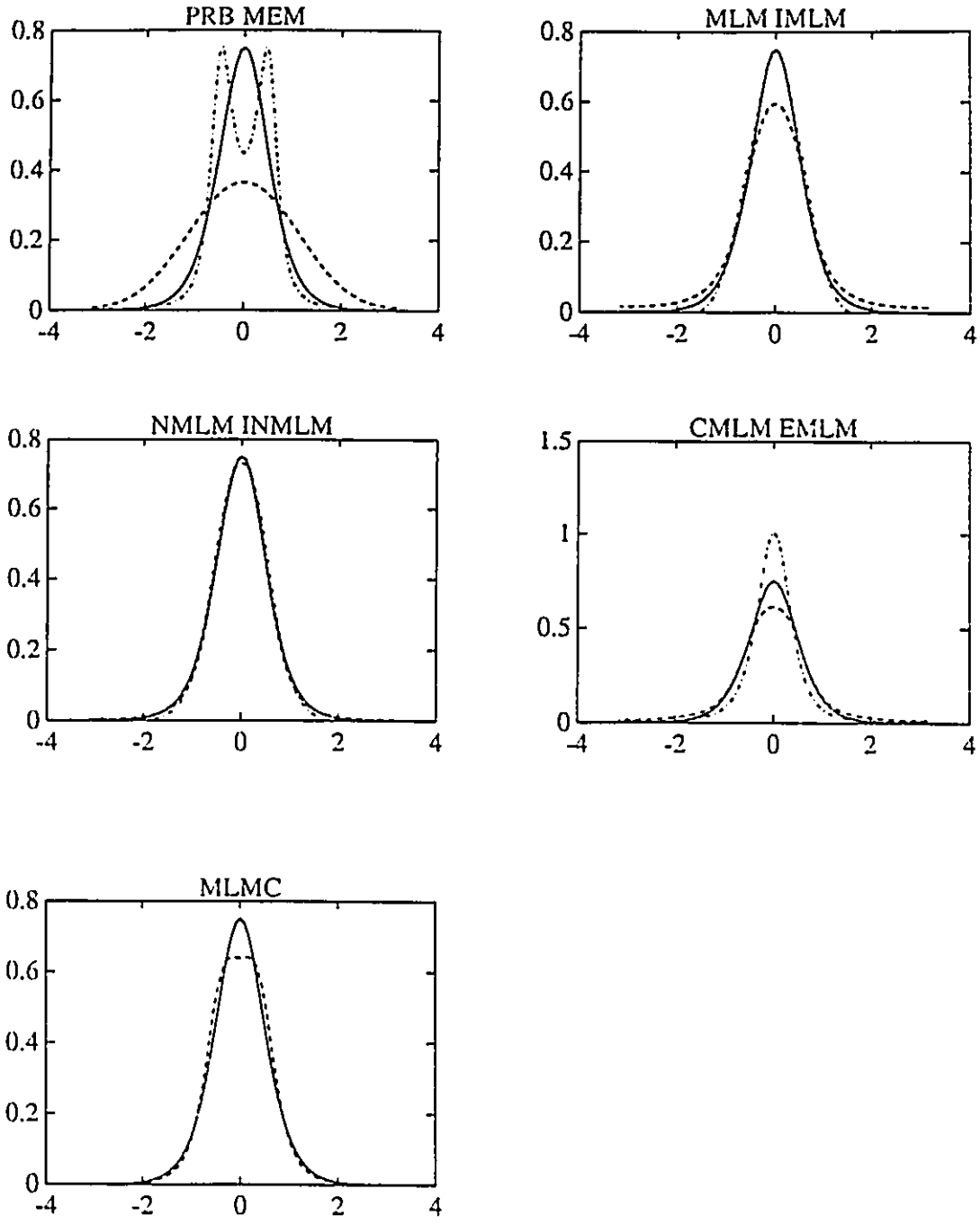

Fig.8.2 Typical directional spectrum estimates for unimodal distribution function ($sech^2$ function with β = 1.5. Solid line is the target distribution, dashed line corresponds to method's name on top left of the graph and dash-dot line to method's name on top right.

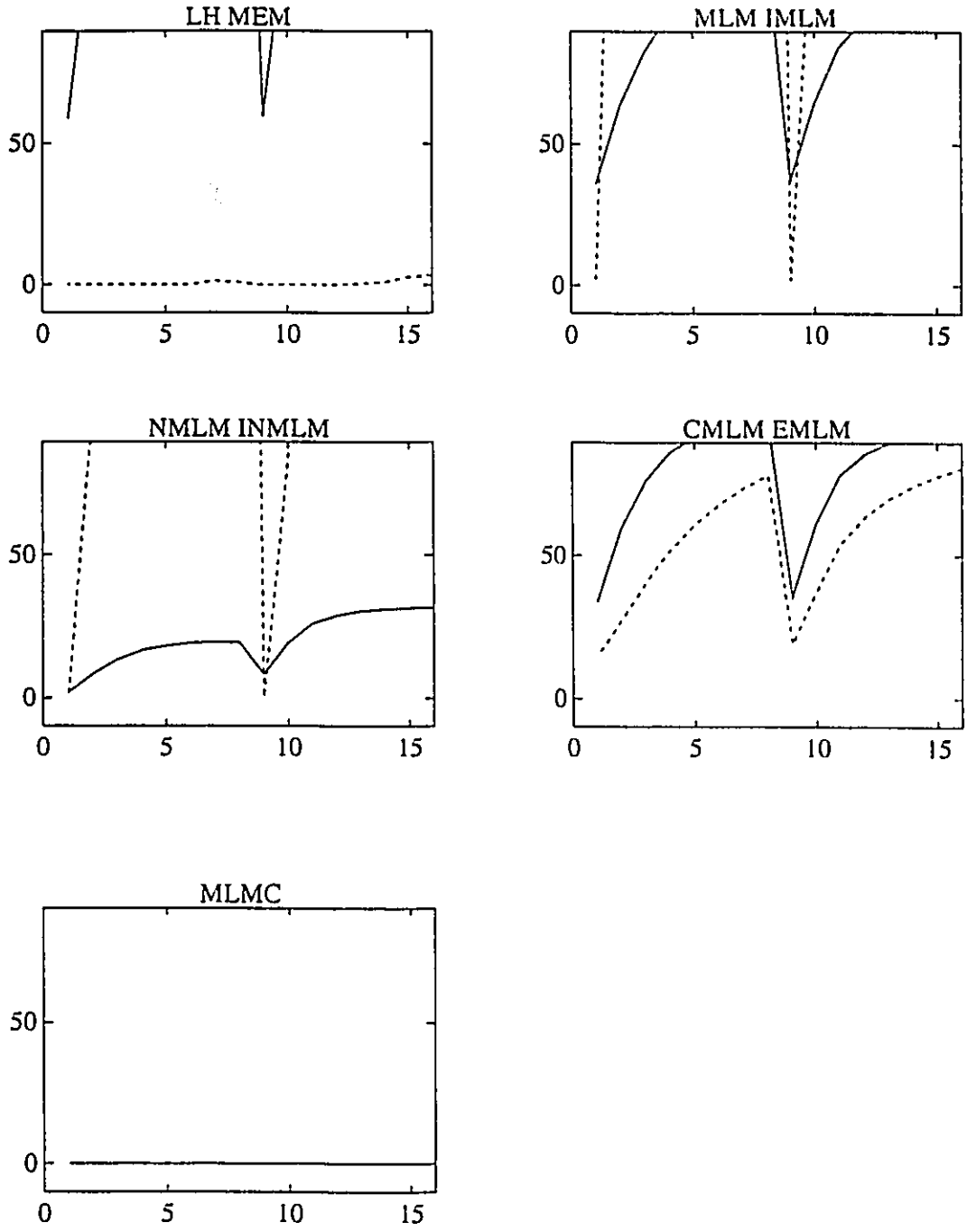

Fig.8.3 ρ^2 statistics for all methods for all unimodal distribution test cases (pitch-roll data).

both the MEM and MLMC as will be discussed later. Finally Figure 8.3 presents the ρ^2 statistic for all estimates and test cases. As previously explained, a value of 9.8 is considered satisfactory at the 80% level. Clearly, only the MEM and MLMC estimates are fully consistent with the data, the other methods failing to meet the 80% level. For the two iterative schemes (IMLM and INMLM) this indicates failure to converge. The NMLM estimate, despite being very close to the model spectrum is also generally not consistent with the data. Nevertheless, it should be noted that from an engineering viewpoint, it does not necessarily mean that the estimate is unacceptable. This point will be addressed in more detail later.

8.2.1.b Bimodal test cases

Figure 8.4 presents comparative histograms for the errors Err1 and Err2 averaged over all of the 72 test cases. Both histograms give comparable results and indicate that two methods, the IMLM and MLMC are superior to the rest. The same observation can also be made in Figure 8.5 which presents for each method, the number of test cases in which its estimate is amongst the best two. Both the IMLM and MLMC are chosen 75% of the time. Six model tests were chosen as representative of the characteristics of most estimates, and the results are presented for each method in Figures 8.6 to 8.14. Basic characteristics for each method are briefly outlined.

DFT- The method essentially fails to recognize bimodalities in most cases and is clearly not adequate to reconstruct the entire directional spectrum.

MLM- The MLM estimate recognizes the main "rough" feature of most model tests but consistently overpredict the spreading.

CMLM- The CMLM estimate is an improvement over the MLM estimate in cases of narrow spreading functions. In other cases, improvement is negligible.

MEM- The MEM estimate is very good at picking the individual unimodal distributions making

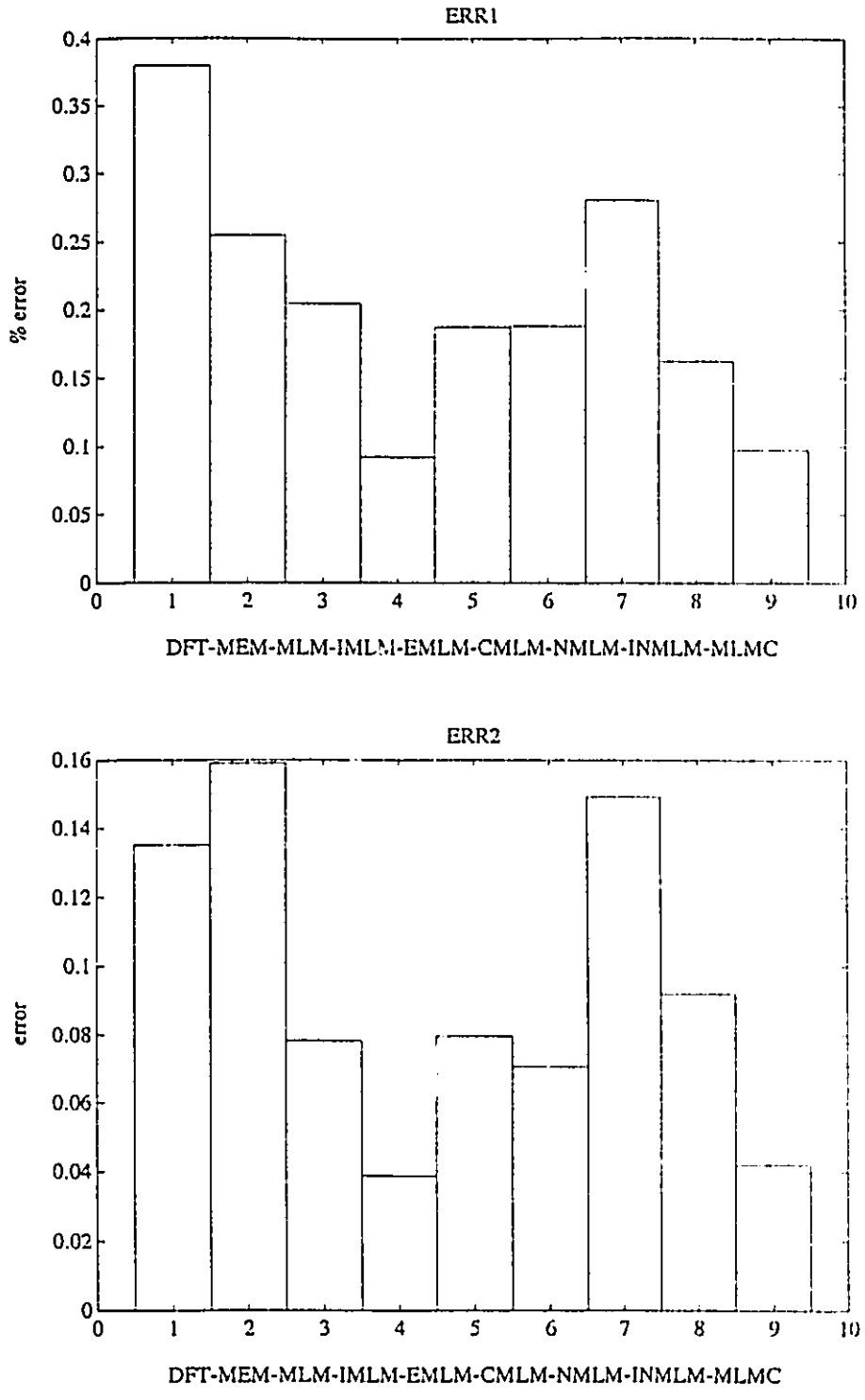

Fig.8.4 Comparative histogram of average error parameters for all directional spectrum estimation methods (pitch-roll data, bimodal test cases).

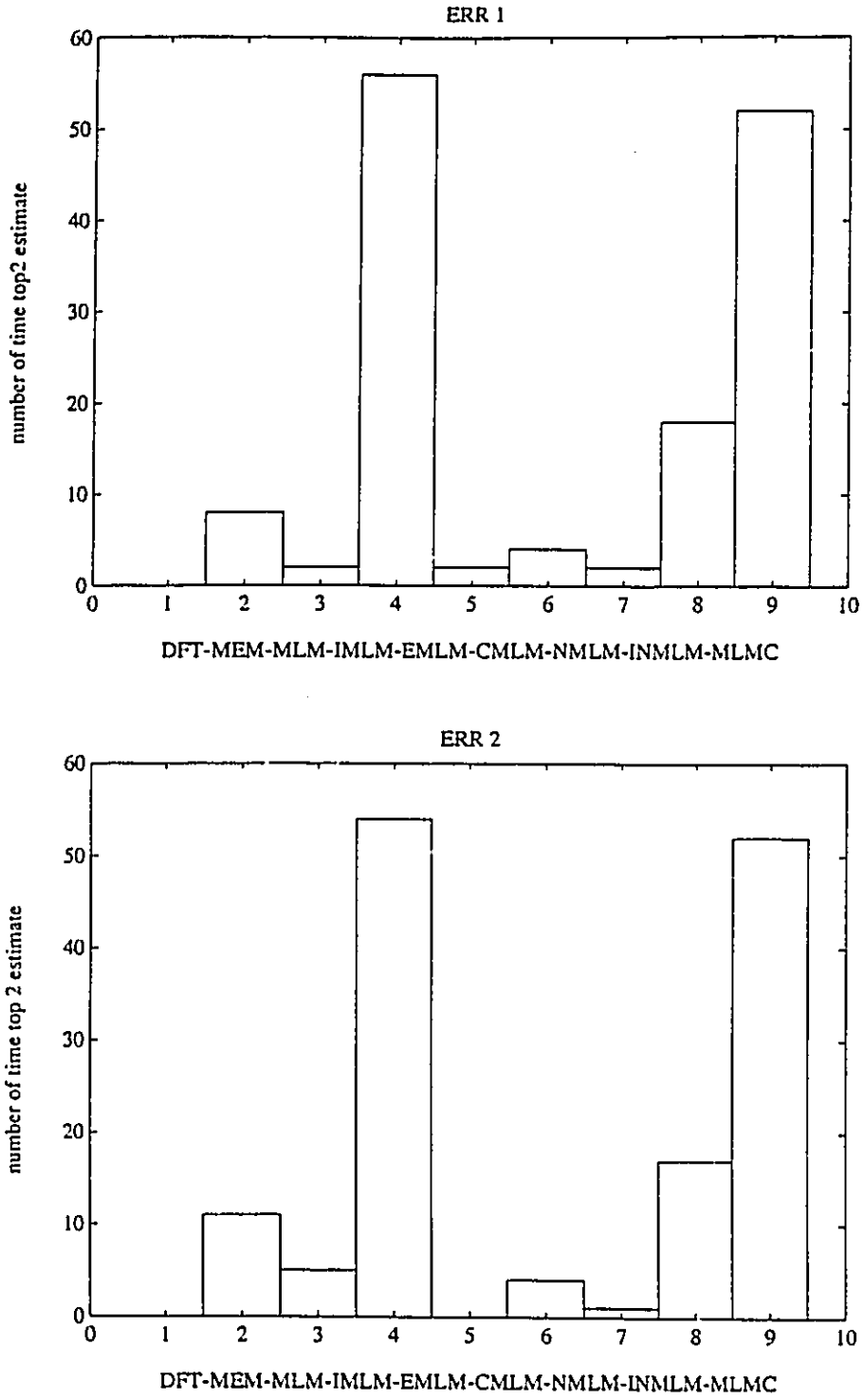

Fig.8.5 Comparative histogram of number of test cases in which a method's estimate ranked amongst the best two according to error parameters Err1 and Err2 (pitch-roll data, bimodal test cases).

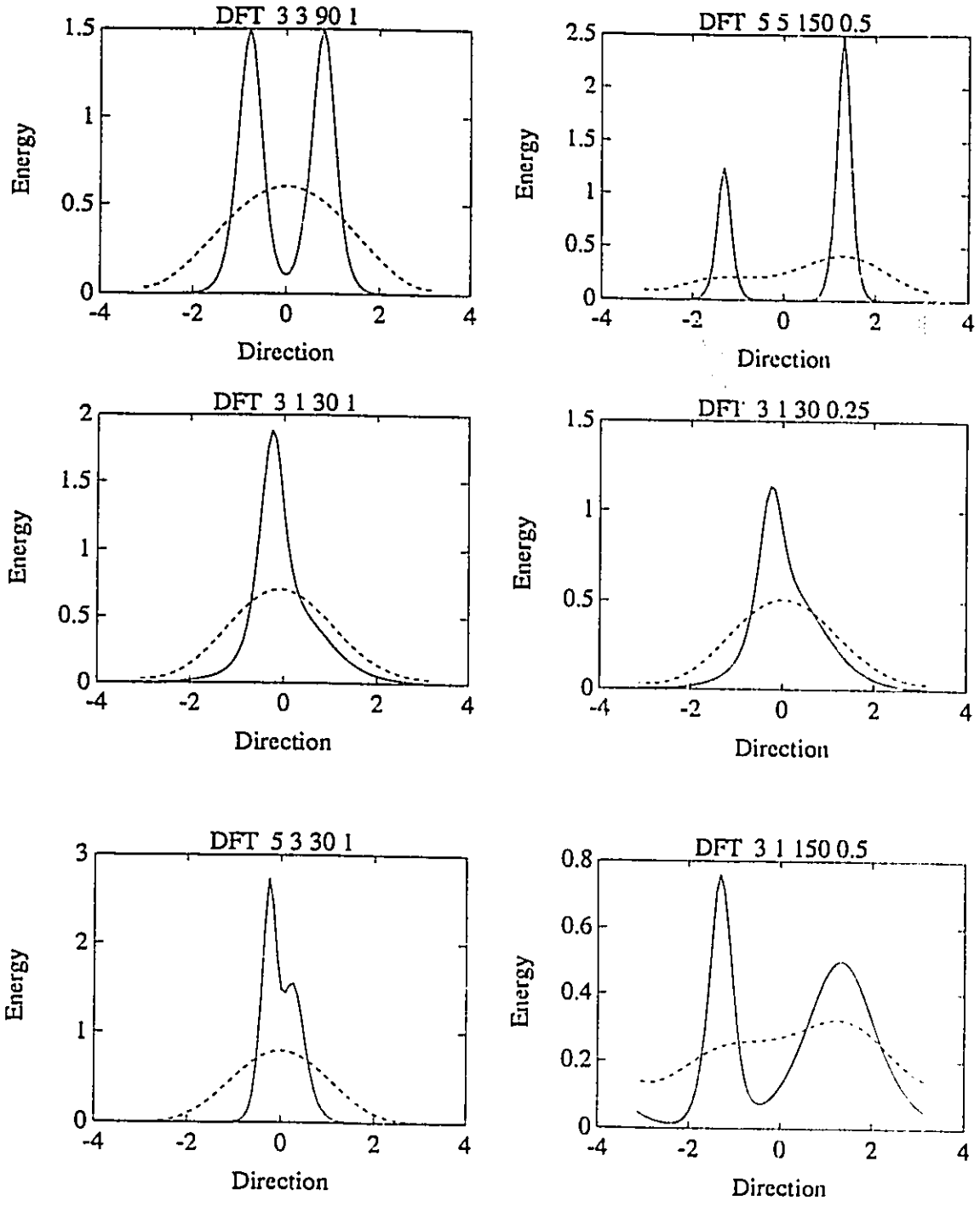

Fig.8.6 Typical results for DFT method as represented by 6 different bimodal test cases. The four numbers on top of each graph define the bimodal distribution as: β values for both modes, spacing and energy ratio. Solid line is the target and dashed line is the estimate (pitch-roll data).

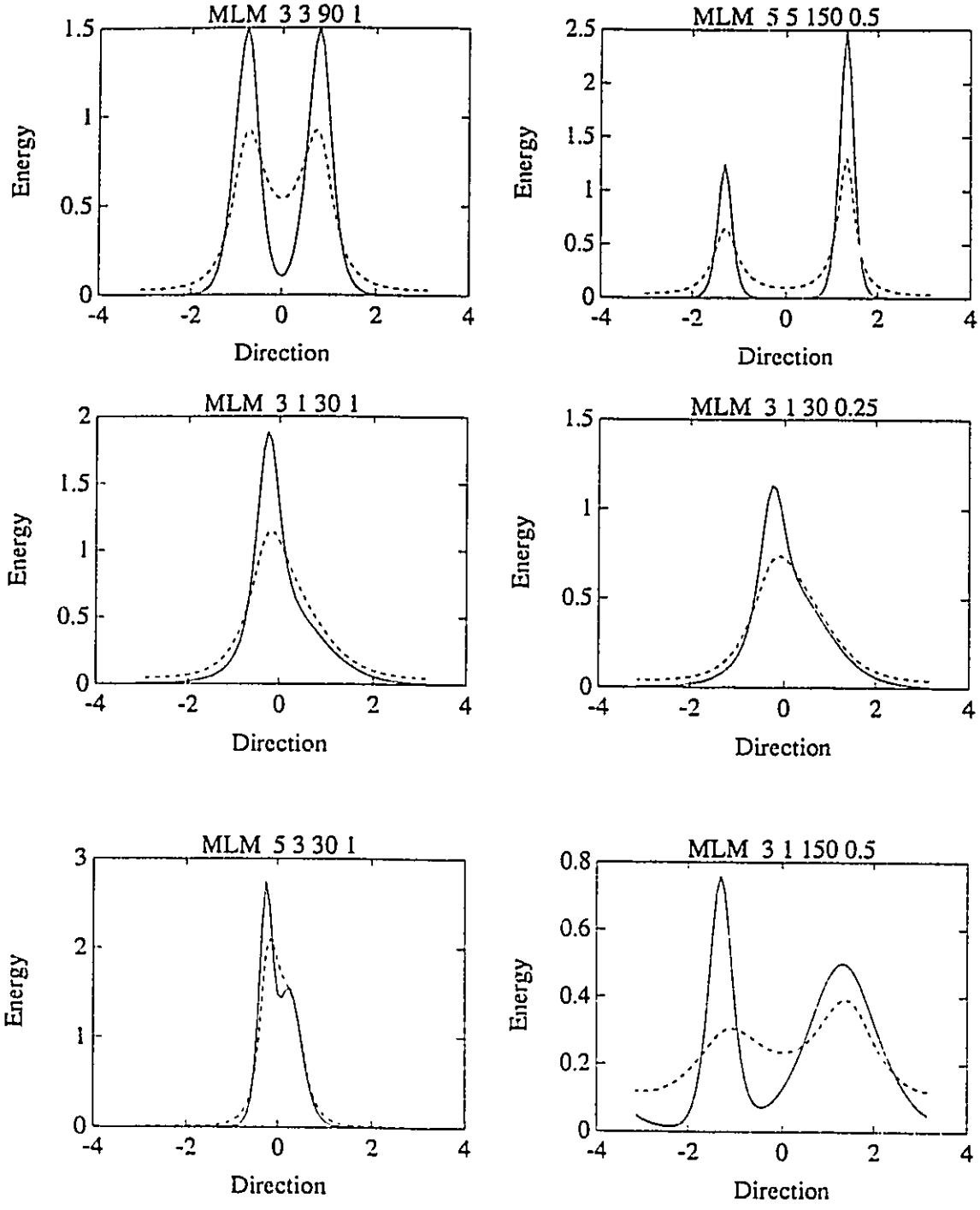

Fig.8.7 Typical results for MLM method as represented by 6 different bimodal test cases. The four numbers on top of each graph define the bimodal distribution as: β values for both modes, spacing and energy ratio. Solid line is the target and dashed line is the estimate (pitch-roll data).

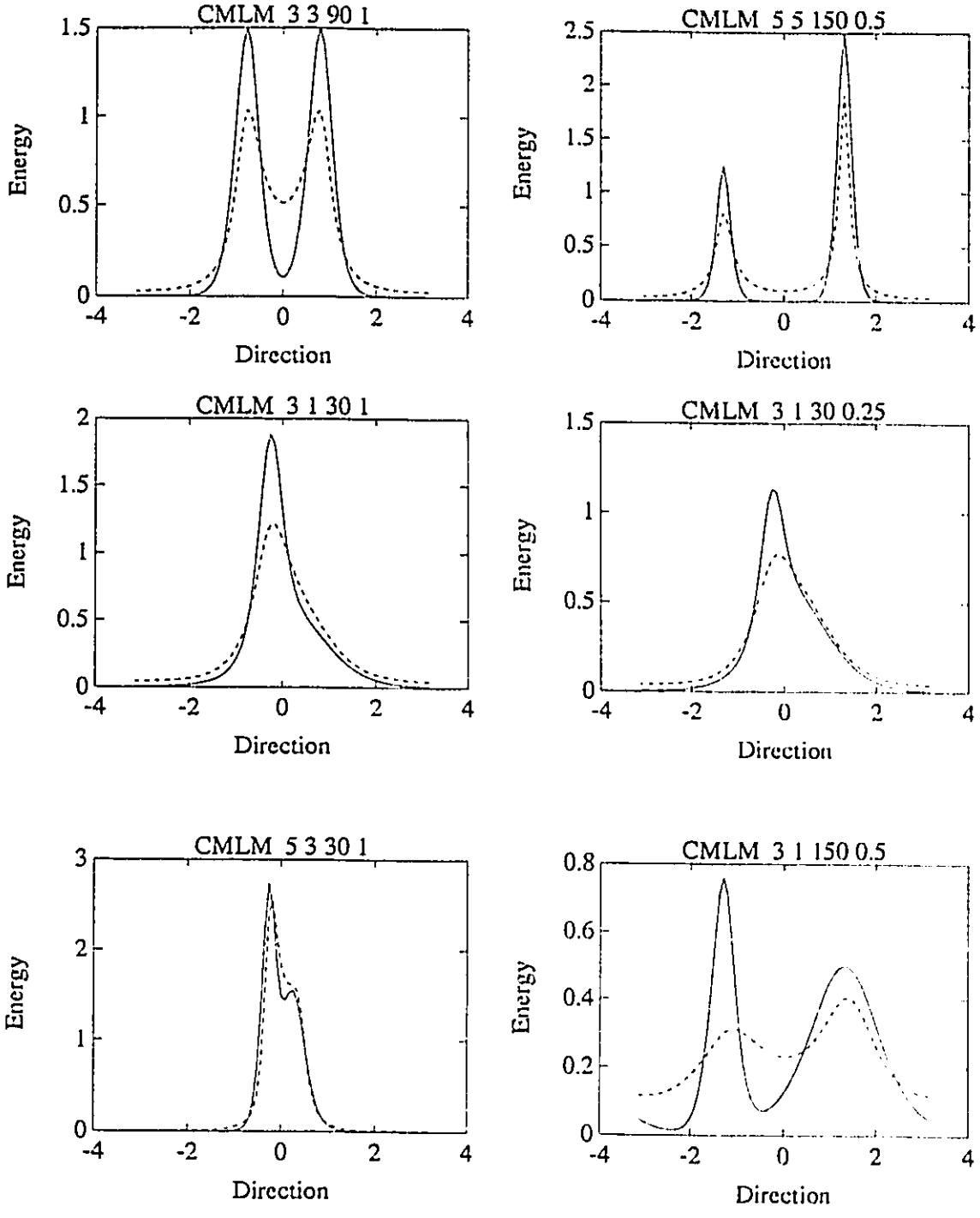

Fig.8.8 Typical results for CMLM method as represented by 6 different bimodal test cases. The four numbers on top of each graph define the bimodal distribution as: β values for both modes, spacing and energy ratio. Solid line is the target and dashed line is the estimate (pitch-roll data).

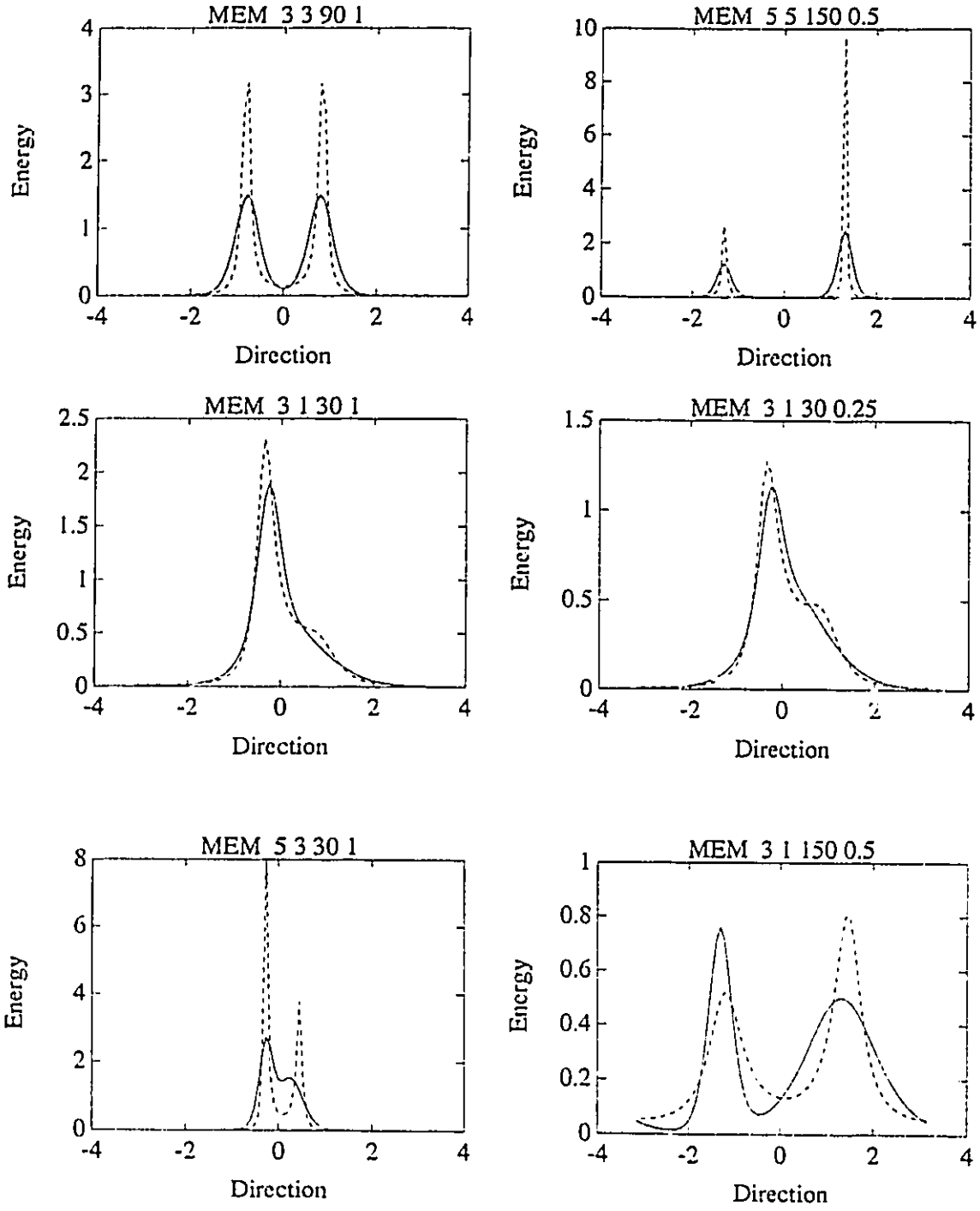

Fig.8.9 Typical results for MEM method as represented by 6 different bimodal test cases. The four numbers on top of each graph define the bimodal distribution as: β values for both modes, spacing and energy ratio. Solid line is the target and dashed line is the estimate (pitch-roll data).

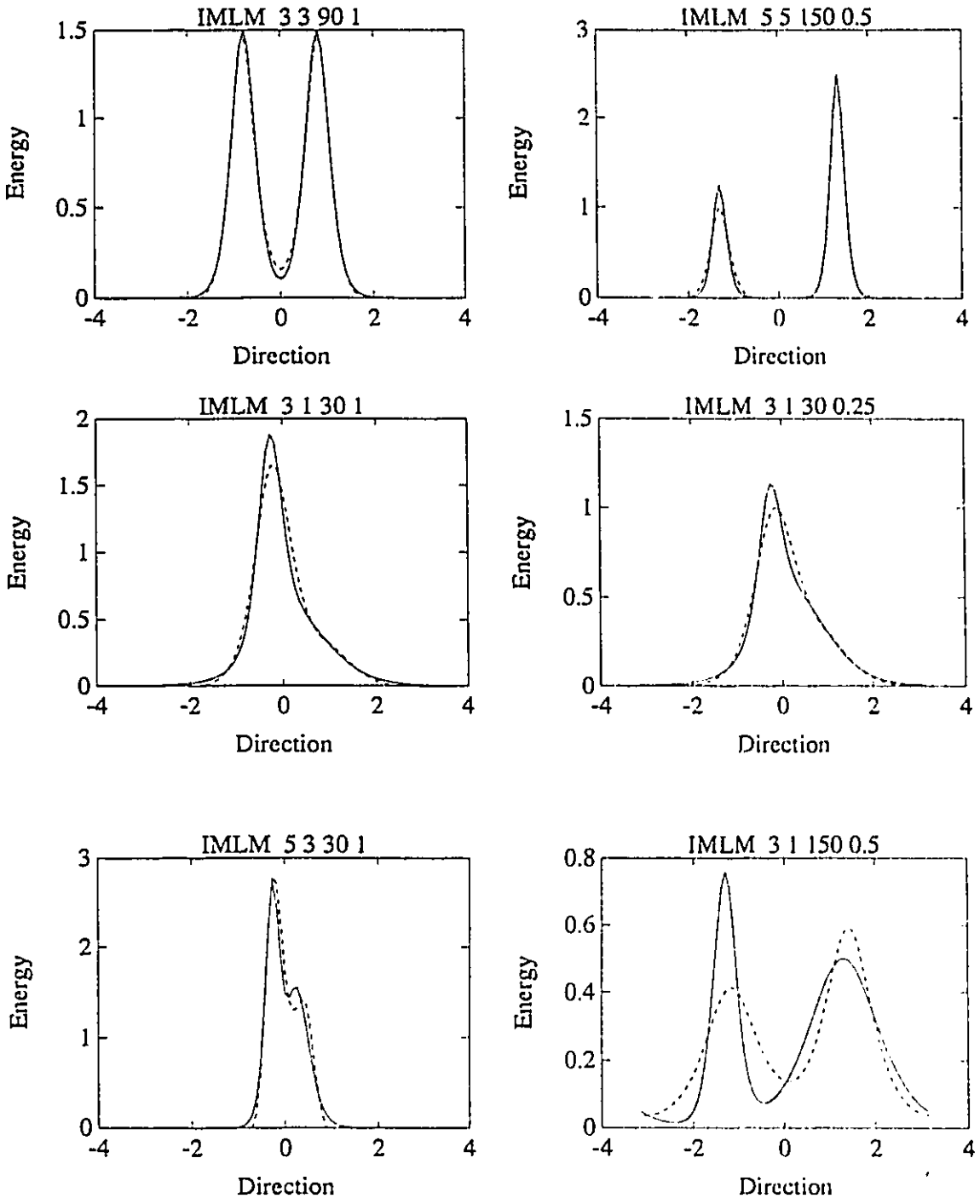

Fig.8.10 Typical results for IMLM method as represented by 6 different bimodal test cases. The four numbers on top of each graph define the bimodal distribution as: β values for both modes, spacing and energy ratio. Solid line is the target and dashed line is the estimate (pitch-roll data).

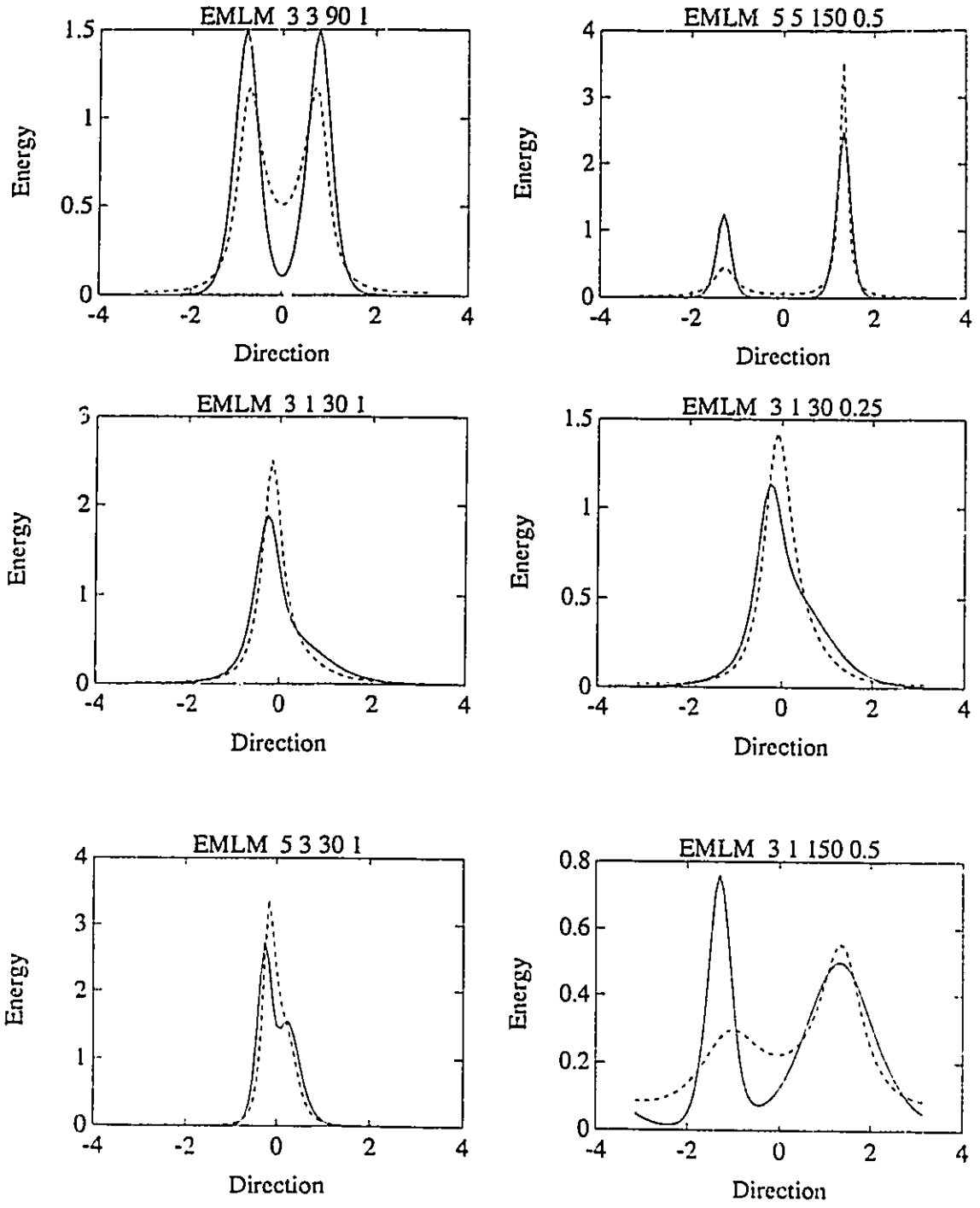

Fig.8.11 Typical results for EMLM method as represented by 6 different bimodal test cases. The four numbers on top of each graph define the bimodal distribution as: β values for both modes, spacing and energy ratio. Solid line is the target and dashed line is the estimate (pitch-roll data).

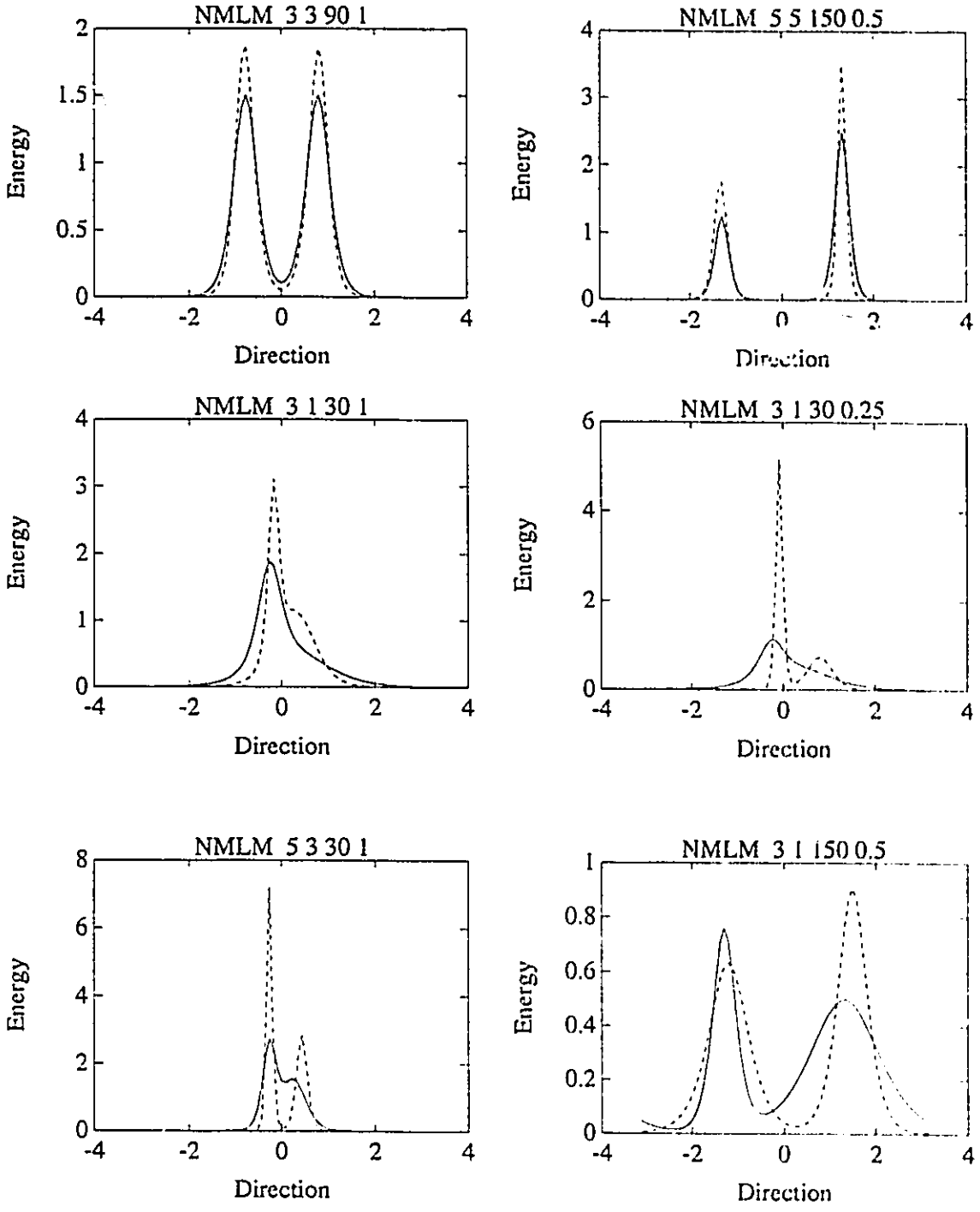

Fig.8.12 Typical results for NMLM method as represented by 6 different bimodal test cases. The four numbers on top of each graph define the bimodal distribution as: β values for both modes, spacing and energy ratio. Solid line is the target and dashed line is the estimate (pitch-roll data).

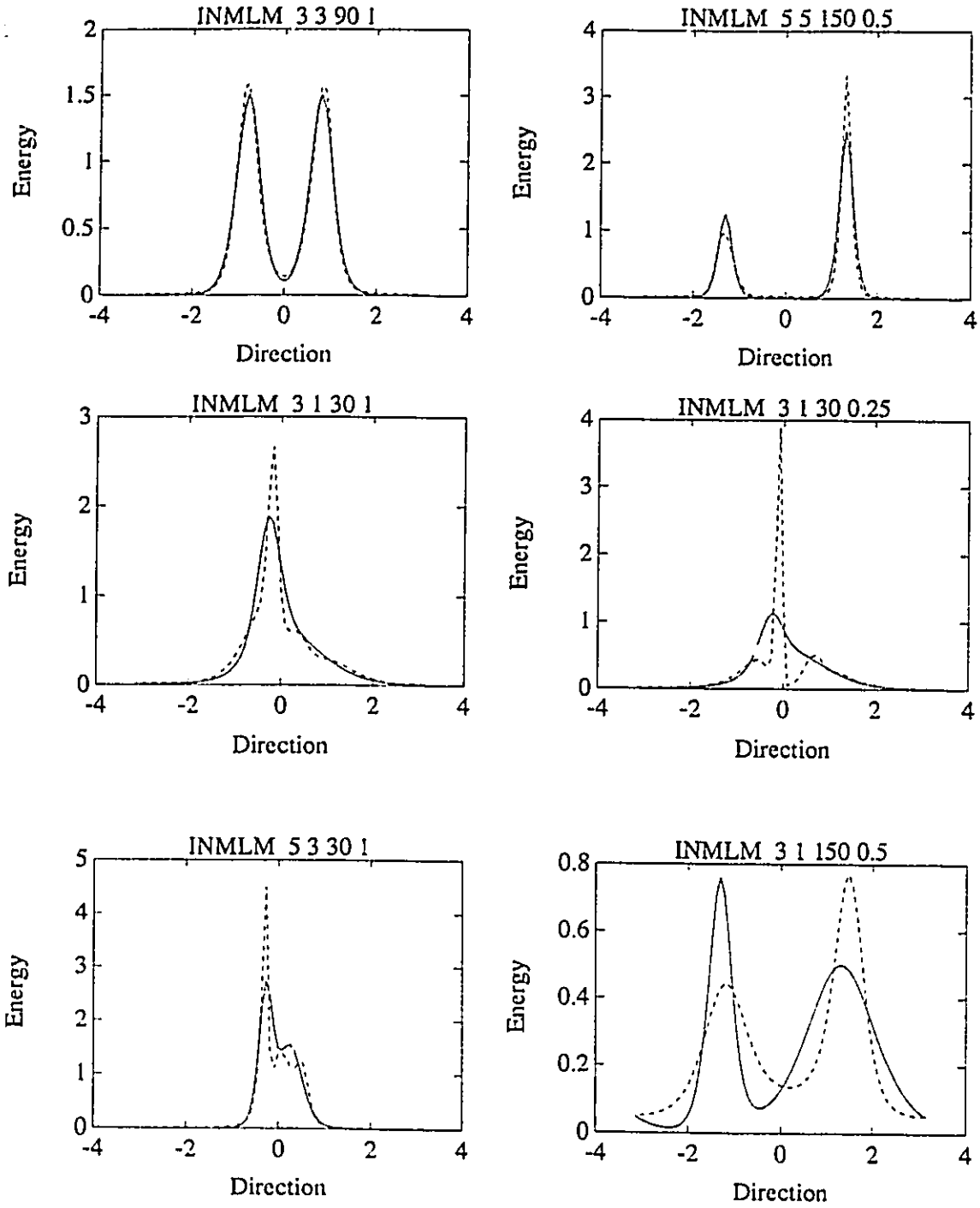

Fig.8.13 Typical results for INMLM method as represented by 6 different bimodal test cases. The four numbers on top of each graph define the bimodal distribution as: β values for both modes, spacing and energy ratio. Solid line is the target and dashed line is the estimate (pitch-roll data).

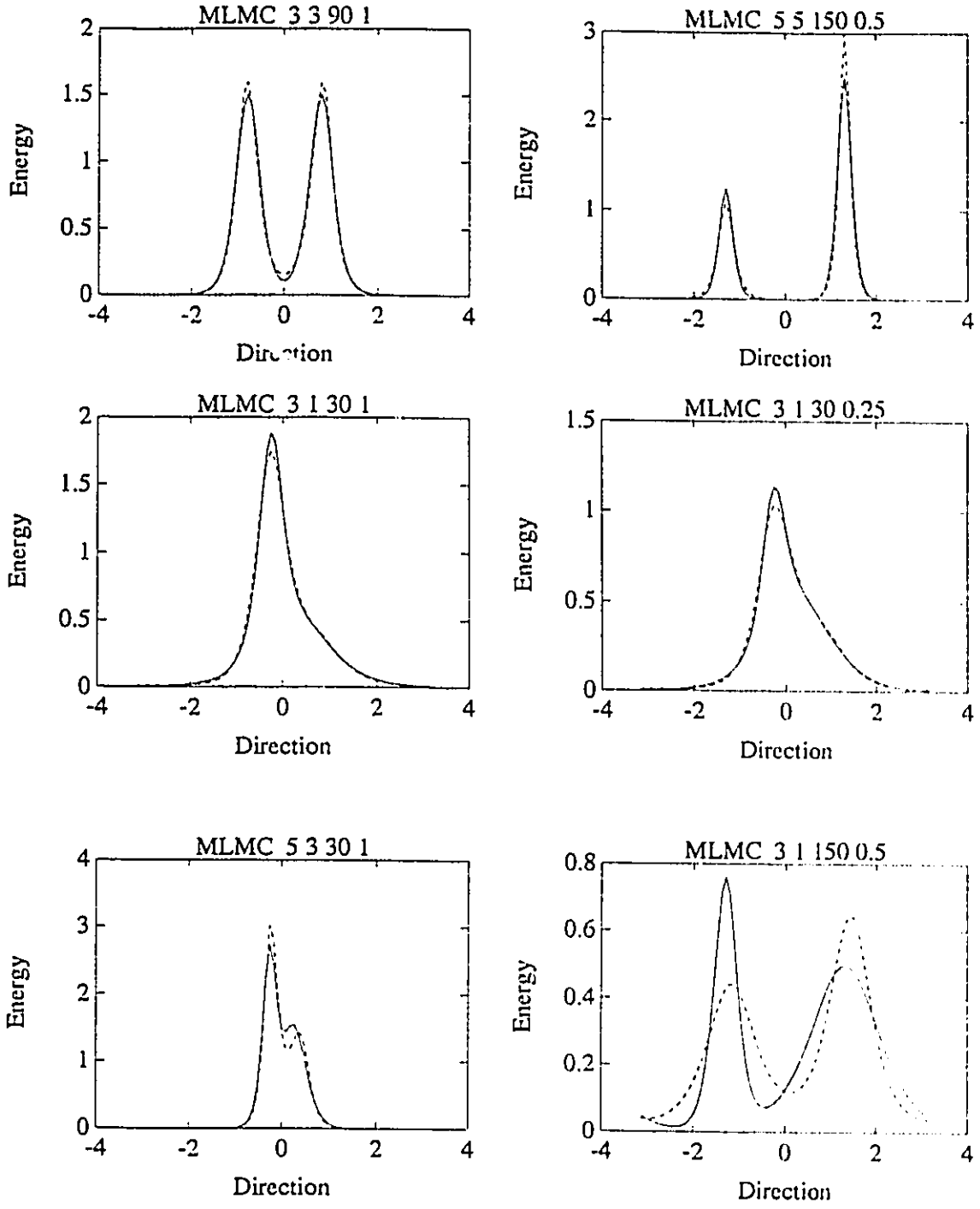

Fig.8.14 Typical results for MLMC method as represented by 6 different bimodal test cases. The four numbers on top of each graph define the bimodal distribution as: β values for both modes, spacing and energy ratio. Solid line is the target and dashed line is the estimate (pitch-roll data).

up the model tests, but as was the case for unimodal tests, the MEM clearly underpredicts the spreading.

IMLM- The performance of the IMLM is quite good for the first 5 model test presented. Its performance is more comparable to the other methods for the last one. The IMLM estimates are consistent with the data (contrarily to unimodal test cases) as shown by the low ρ^2 values presented in Figure 8.15.

EMLM- The EMLM method is inconsistent in the sense that it sometimes overpredicts, sometimes underpredicts the peak energy. On the other hand, from a consistency viewpoint, in all of the test cases, it is consistently off target. From a qualitative point of view, its general performance is comparable to the MLM estimate, although the latter is consistent in all discussed aspects (see Chapter 5).

NMLM- The NMLM estimate is inconsistent as it is reasonably accurate in some cases and off mark in others. Generally it tends to overpredict the peak energy but sometimes underpredicts (not shown). The estimate is more accurate for widely spaced unimodal components.

INMLM- The INMLM is an iterative procedure similar to the IMLM except that it uses a different starting point (NMLM estimate). As such, the results are different. The method, despite producing an estimate consistent with the data (see ρ^2 statistic in Figure 8.15), often converges to a true but wrong estimate of the directional spectrum.

MLMC- In accordance to the results presented in the Figures 8.4 and 8.5 histograms, the MLMC estimate is similar to the IMLM one and is very close to target in all cases except the last one. The MLMC outperforms the IMLM in cases of skewed distributions.

For most of the test cases, the MLMC and IMLM are clearly the best estimates. Their failure to resolve accurately the last model test is also shared by all other methods. All methods

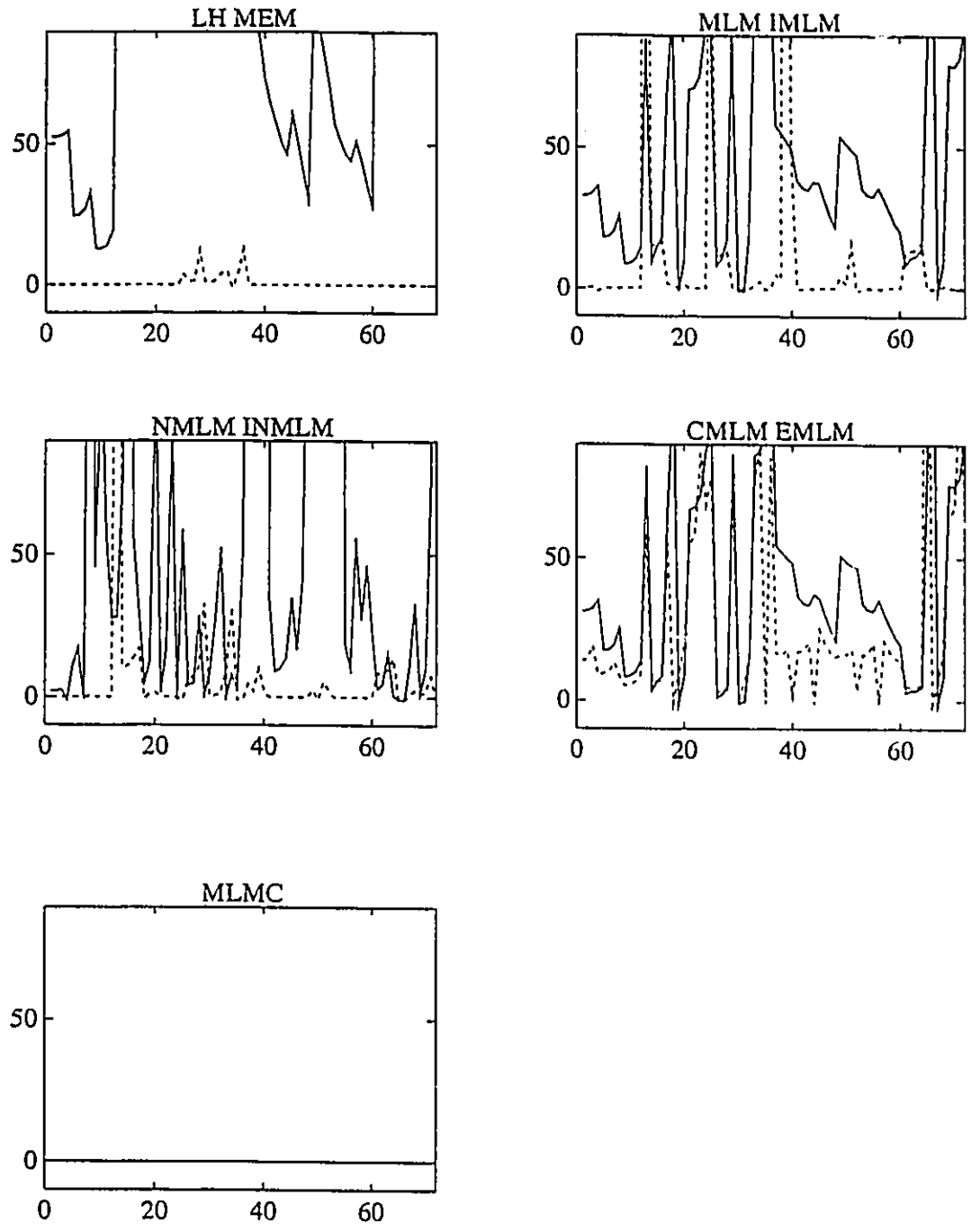

Fig.8.15 ρ^2 statistics for all methods for all bimodal distribution test cases (pitch-roll data).

seem to be unable to resolve to resolve cases of distributions with similar magnitude peaks but different spreading. All methods tend to return two modes with similar spreading. It is in cases like this that the IMLM or MLMC are generally not amongst the best estimates. For most "more realistic" model tests (situations in which two modes with similar magnitude peaks and significantly different energy spreading are probably unlikely), they are systematically the best estimates.

Finally Figure 8.15 presents the ρ^2 statistics for all methods and bimodal test cases performed. Results are similar to the one obtained in the unimodal case, the only difference being that the iterative methods (IMLM and INMLM) successfully converge in most cases. This difference was also noted in Chapter 5.

8.2.2. Field Data

One field data case is presented in Figure 8.16. The data is from the Atlantic Ocean, via the SWADE experiment. Details concerning the field data case selected are not important at this stage, since we are only interested in the basic features of the directional spectra, and whether or not they are consistent with the test results characteristics. Ample details on the SWADE experiment and field data will be given in Chapter 10.

Essentially, and similarly to the results already presented in Chapter 5, Figure 8.16 indicates that all of the main characteristics observed in test cases are preserved. Both the IMLM and MLMC estimates are similar as they resolve the bimodality present at 0.11 Hz. The EMLM and MLM methods return skewed estimates but do not recognize the peaks as separate, whereas the MEM separates the peaks quite nicely but underpredicts their respective energy spread. The CMLM estimate is not significantly different than the MLM estimate, and the Direct Fourier

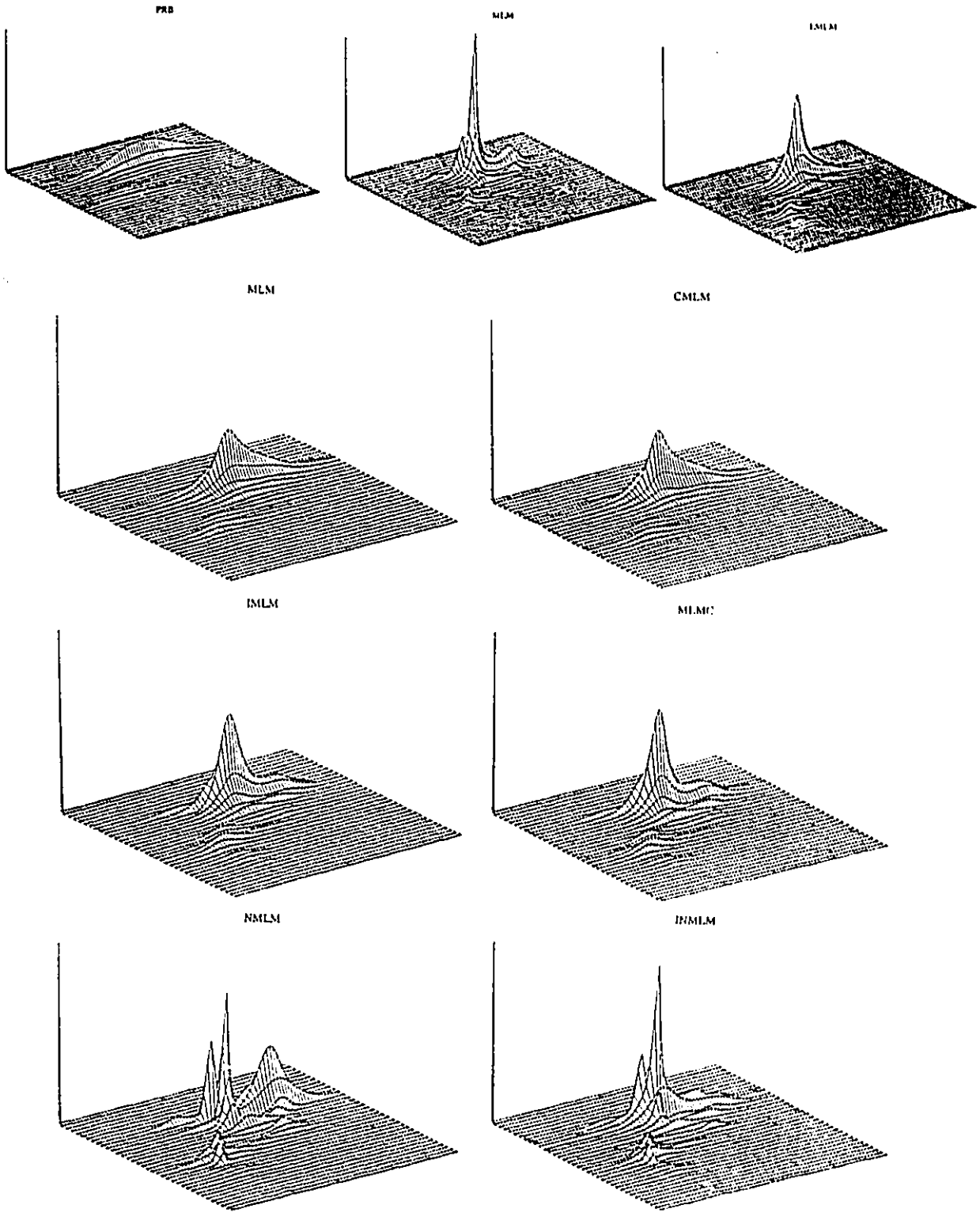

Fig.8.16 Comparative results for Atlantic Ocean Field data (pitch-roll-heave data). Frequency is from 0 to 0.35 Hz.

Transform Method (PRB) returns a unimodal estimate. Finally, it should be noted that the NMLM and INMLM estimates are inconsistent from one frequency band to the other, indicating that small changes in the model (as should be expected from one frequency band to the next) can produce significant differences in the returned estimate. This characteristic is also present in test cases as can be seen by looking at the third and fourth included test cases. These results (also confirmed by numerous other field data cases) indicate that conclusions drawn on test cases can be extrapolated to field data with confidence.

8.3. WAVESTAFF DATA

Many of the differences between different arrays were discussed in Chapter 6 and as a result, in this chapter, only the six-wavestaff array of Figure 6.1 will be discussed. The six-wavestaff array was chosen because it allows a superior resolution of wavefields than the three-wavestaff array whose results can also be closely correlated to the heave-pitch-roll data results, and also because the array configuration is the one used in Lake Ontario by the National Water Research Institute, whose data will be examined in Chapter 11. As listed in Table 8.2, 13 methods of estimating the wave directional spectrum are considered, five direct methods and nine pitch-roll equivalent methods.

8.3.1. Test Results

8.3.1.a Unimodal test cases

Figure 8.17 presents comparative histograms of the average errors Err1 and Err2 defined in Eq.5.6. It can be seen that the performance of the various estimates is generally good, with 10

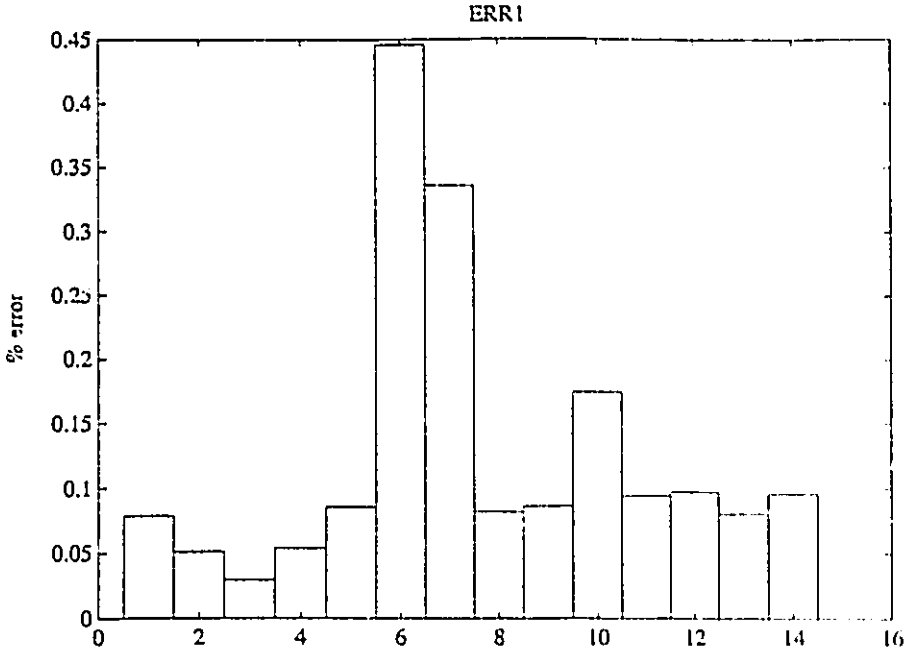

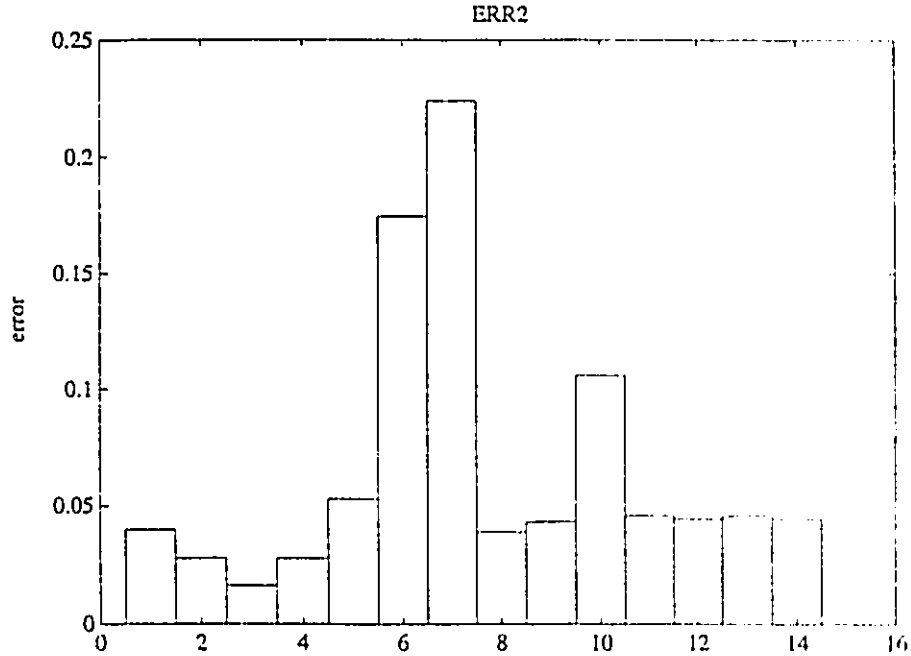

Fig.8.17 Comparative histogram of average error parameters for all directional spectrum estimation methods (wavestaff data: direct and pitch-roll equivalent methods, unimodal test cases).

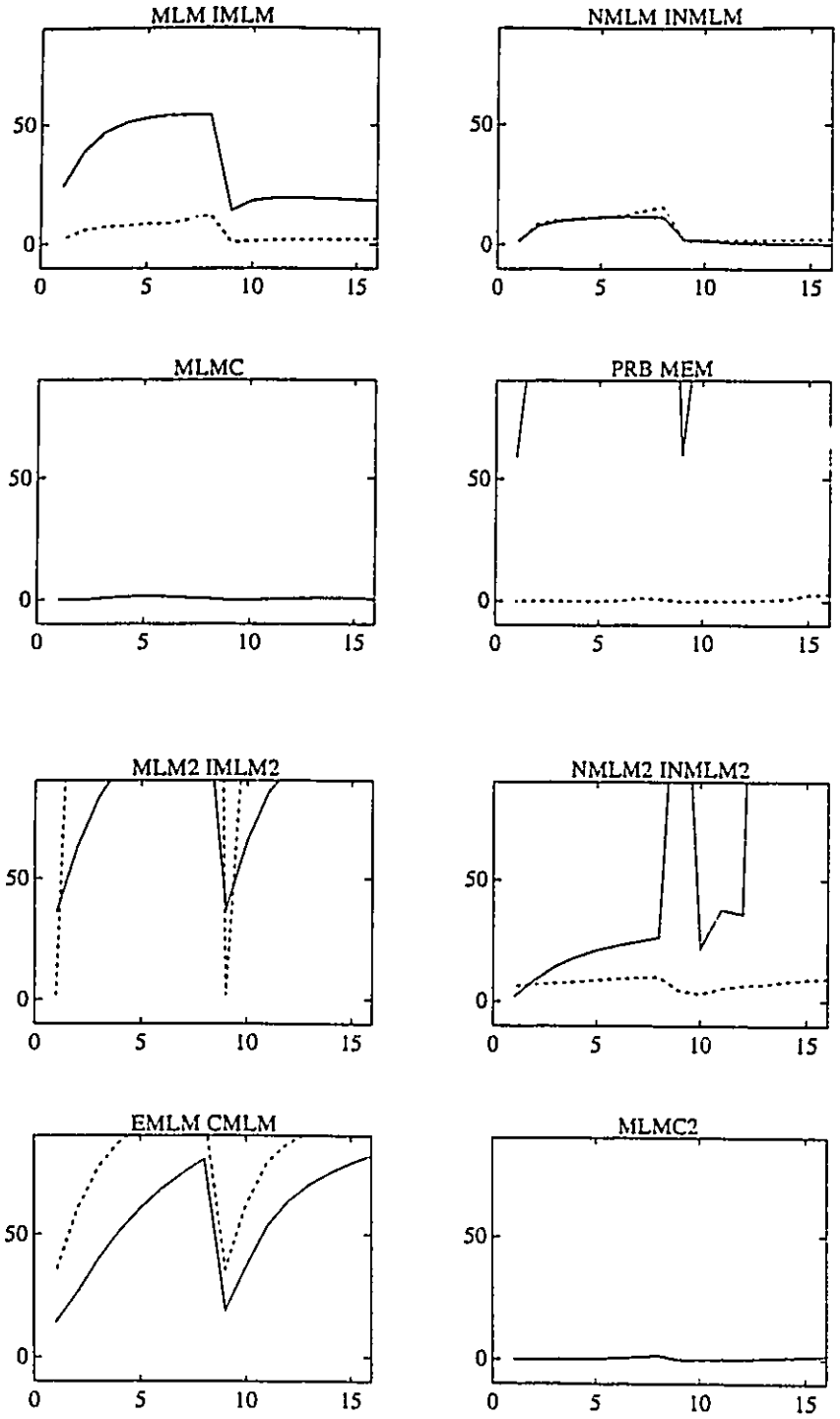

Fig.8.18 ρ^2 statistics for all methods for all unimodal distribution test cases (wavestaff data: direct and pitch-roll equivalent methods).

methods giving estimates with less than 10% error for the first error parameter Err1. Above all, the NMLM estimate is shown to perform the best for symmetrical, unimodal spreading functions. The performance of the pitch-roll equivalent methods is very similar to their performance with buoy data. Since results are not markedly different than the one already presented, no test results will be shown. Figure 8.18 presents the ρ^2 statistics for each tests for all methods. The results indicate that all direct method estimates (except the MLM) are acceptable at the 80% level ($\rho^2 > 9.8$) whereas only the MEM, MLMC and INMLM satisfy this criterion for pitch-roll equivalent methods. These results are similar to the ones reported in the previous section for pitch-roll data.

8.3.1.b Bimodal test cases

Contrary to the unimodal test cases, where no methods was clearly superior, the comparative histograms for the bimodal test cases indicate that the MLMC method gives the best performing estimate, with an average error of less than 4% for the first error parameter Err1. This conclusion is further emphasized in Figure 8.20 which presents for each method, the number of test cases in which its estimate is the best. In 60 test cases out of 72 (83%), the MLMC was the best estimate, the next best method incidentally being the same (MLMC2-equivalent pitch-roll-heave method) with 5 cases. To identify the next best performing methods, Figure 8.21 presents for each method, the number of test cases in which its estimate ranks amongst the top three. From this plot, one can see that only 5 methods achieve a better than 30% success rate for both error parameters. These are in order: MLMC, INMLM, IMLM2, MLMC and IMLM. It is interesting to note that equivalent pitch-roll methods (namely the IMLM2 and MLMC2) perform as well as the direct methods (outside the MLMC) which use twice as much information to reconstruct the angular spreading of energy.

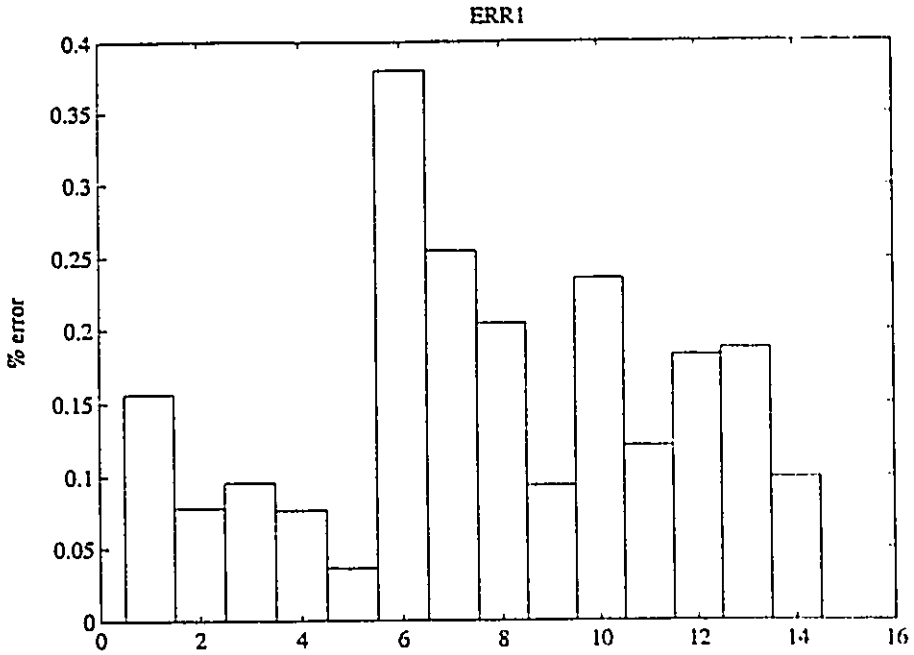

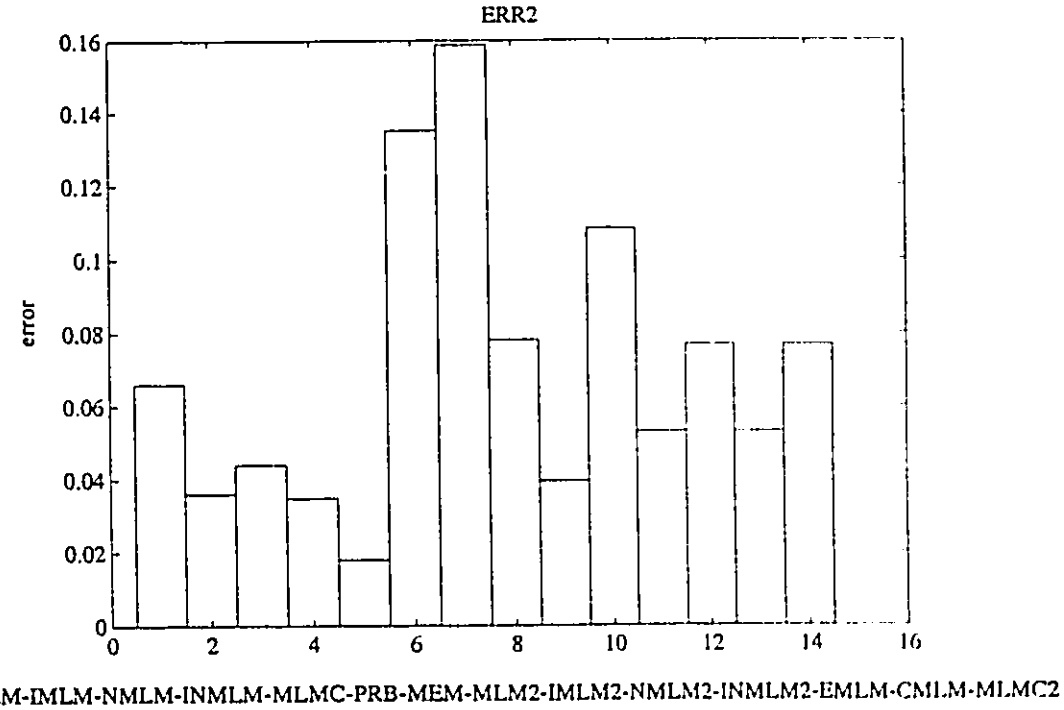

Fig.8.19 Comparative histogram of average error parameters for all directional spectrum estimation methods (wavestaff data: direct and pitch-roll equivalent methods, bimodal test cases).

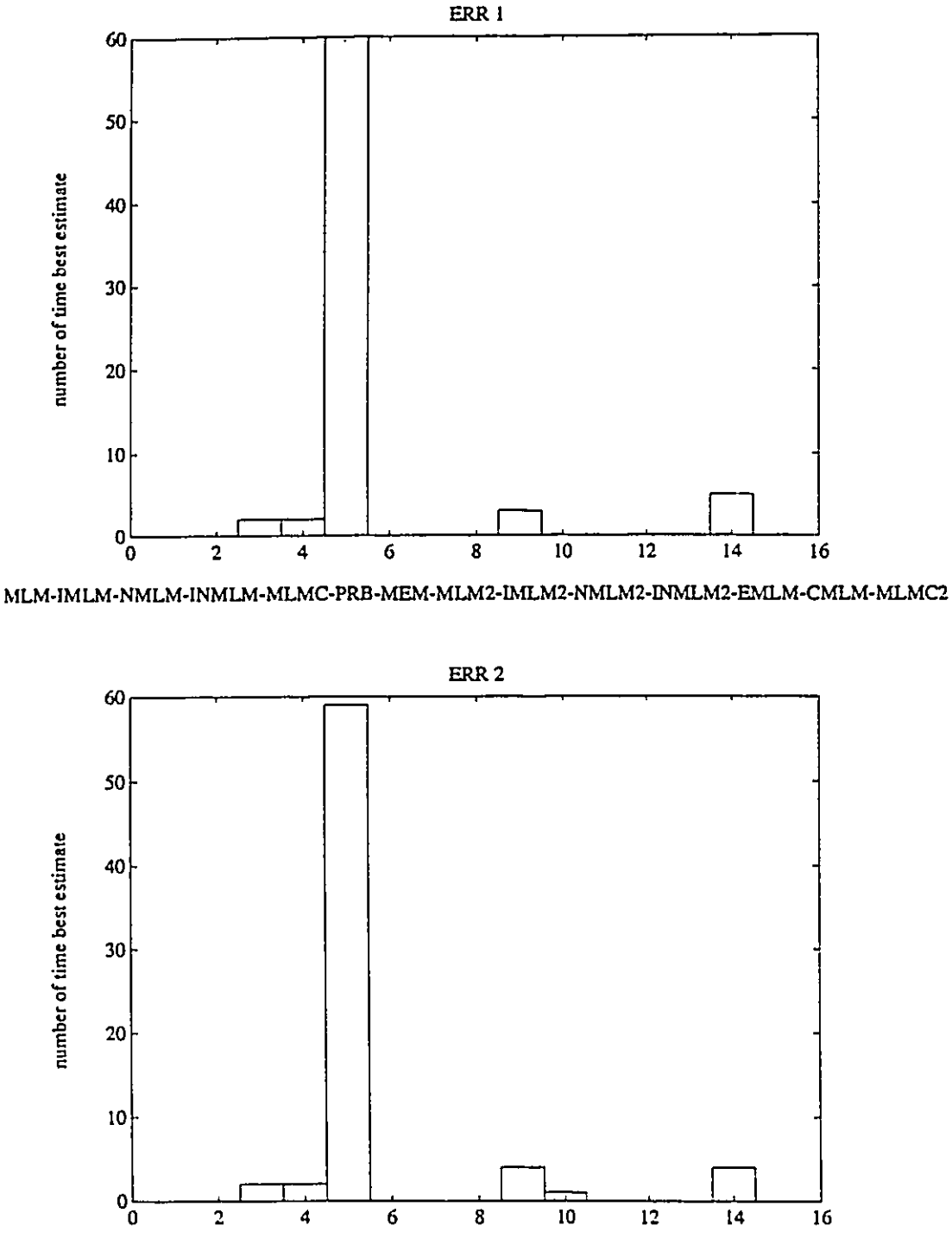

Fig.8.20 Comparative histogram of number of test cases in which a method's estimate ranked as the best according to error parameters Err1 and Err2 (wavestaff data: direct and pitch-roll equivalent methods, bimodal test cases).

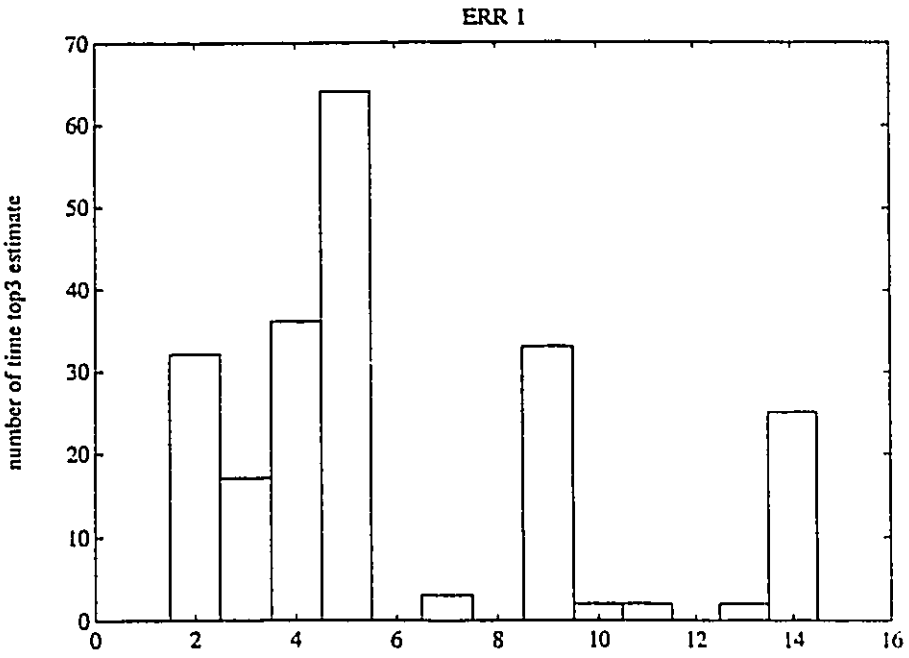

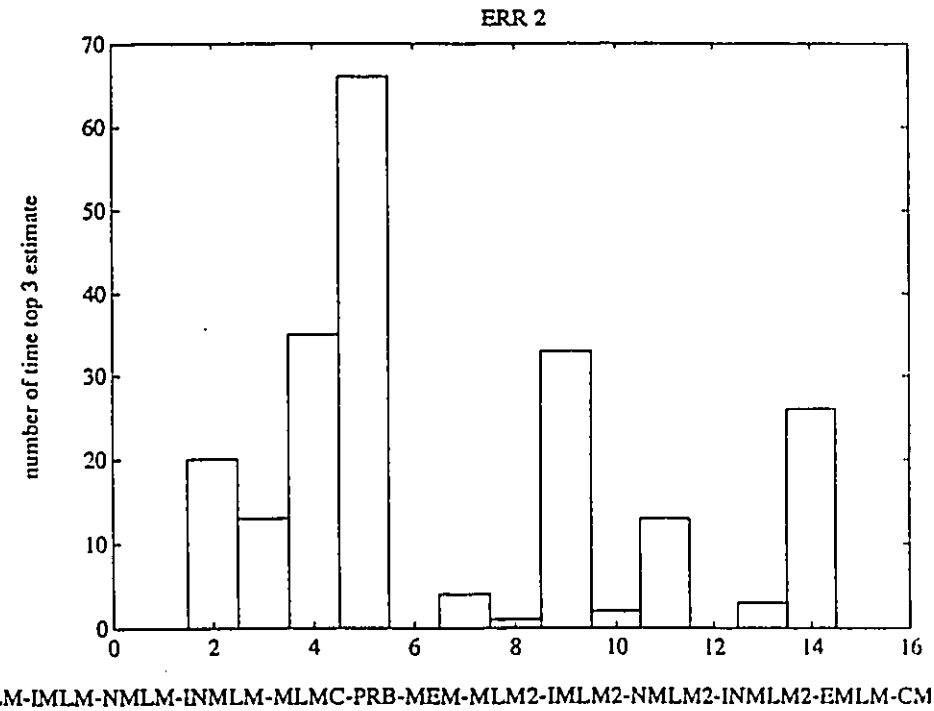

Fig.8.21 Comparative histogram of number of test cases in which a method's estimate ranked amongst the best three according to error parameters Err1 and Err2 (wavestaff data: direct and pitch-roll equivalent methods, bimodal test cases).

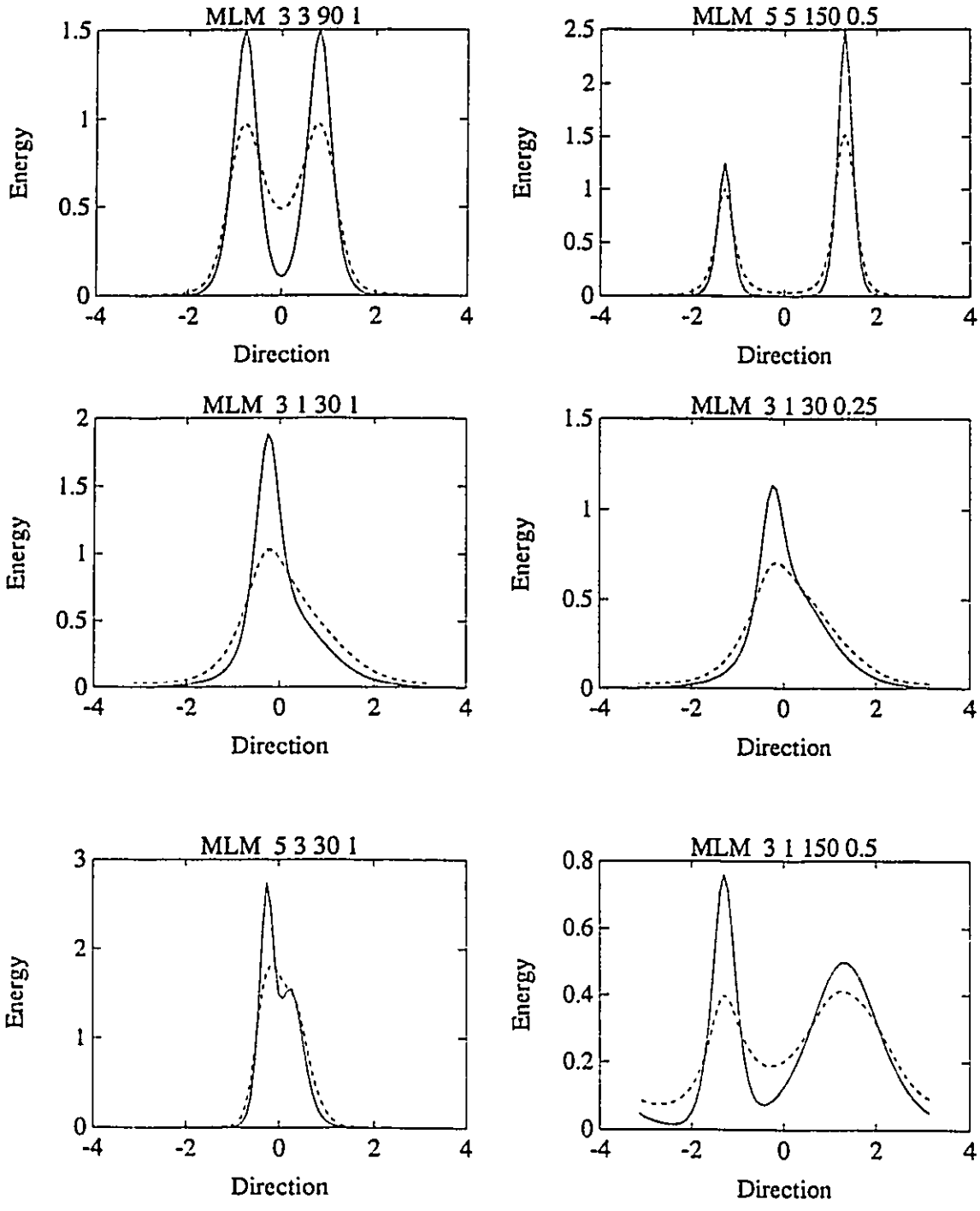

Fig.8.22 Typical results for MLM method as represented by 6 different bimodal test cases. The four numbers on top of each graph define the bimodal distribution as: β values for both modes, spacing and energy ratio. Solid line is the target and dashed line is the estimate (wavestaff data, direct method).

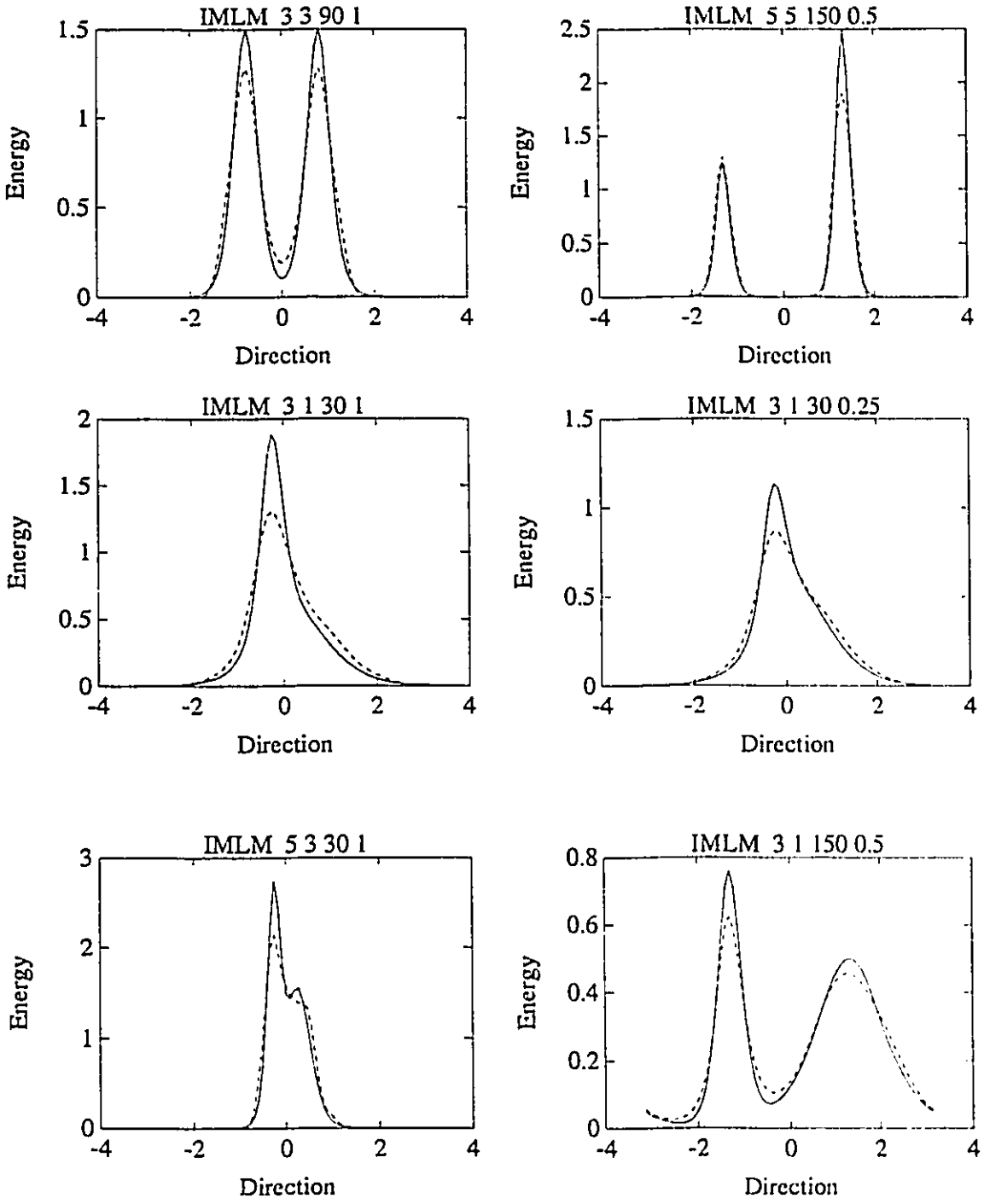

Fig.8.23 Typical results for IMLM method as represented by 6 different bimodal test cases. The four numbers on top of each graph define the bimodal distribution as: β values for both modes, spacing and energy ratio. Solid line is the target and dashed line is the estimate (wavestaff data, direct method).

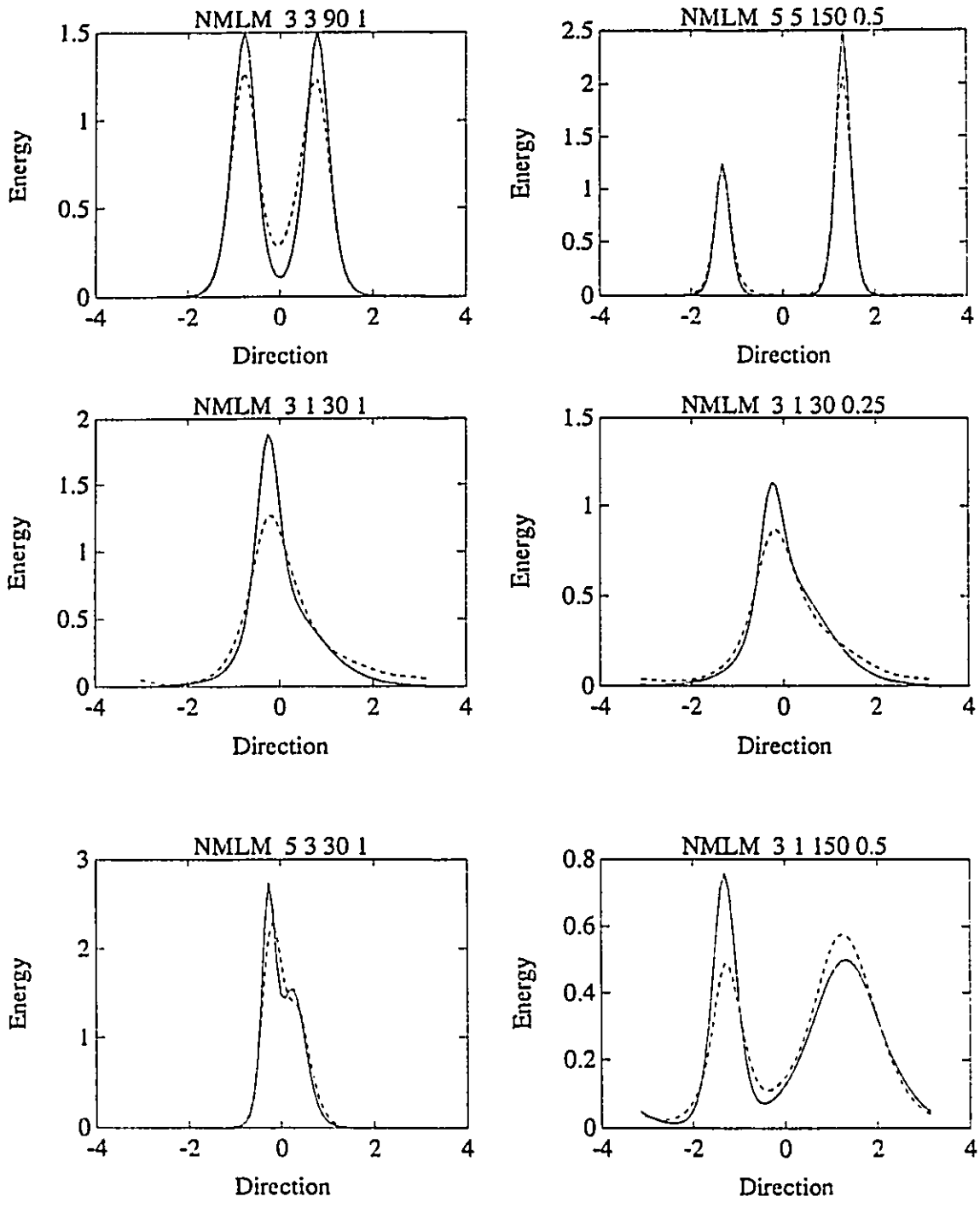

Fig.8.24 Typical results for NMLM method as represented by 6 different bimodal test cases. The four numbers on top of each graph define the bimodal distribution as: β values for both modes, spacing and energy ratio. Solid line is the target and dashed line is the estimate (wavestaff data, direct method).

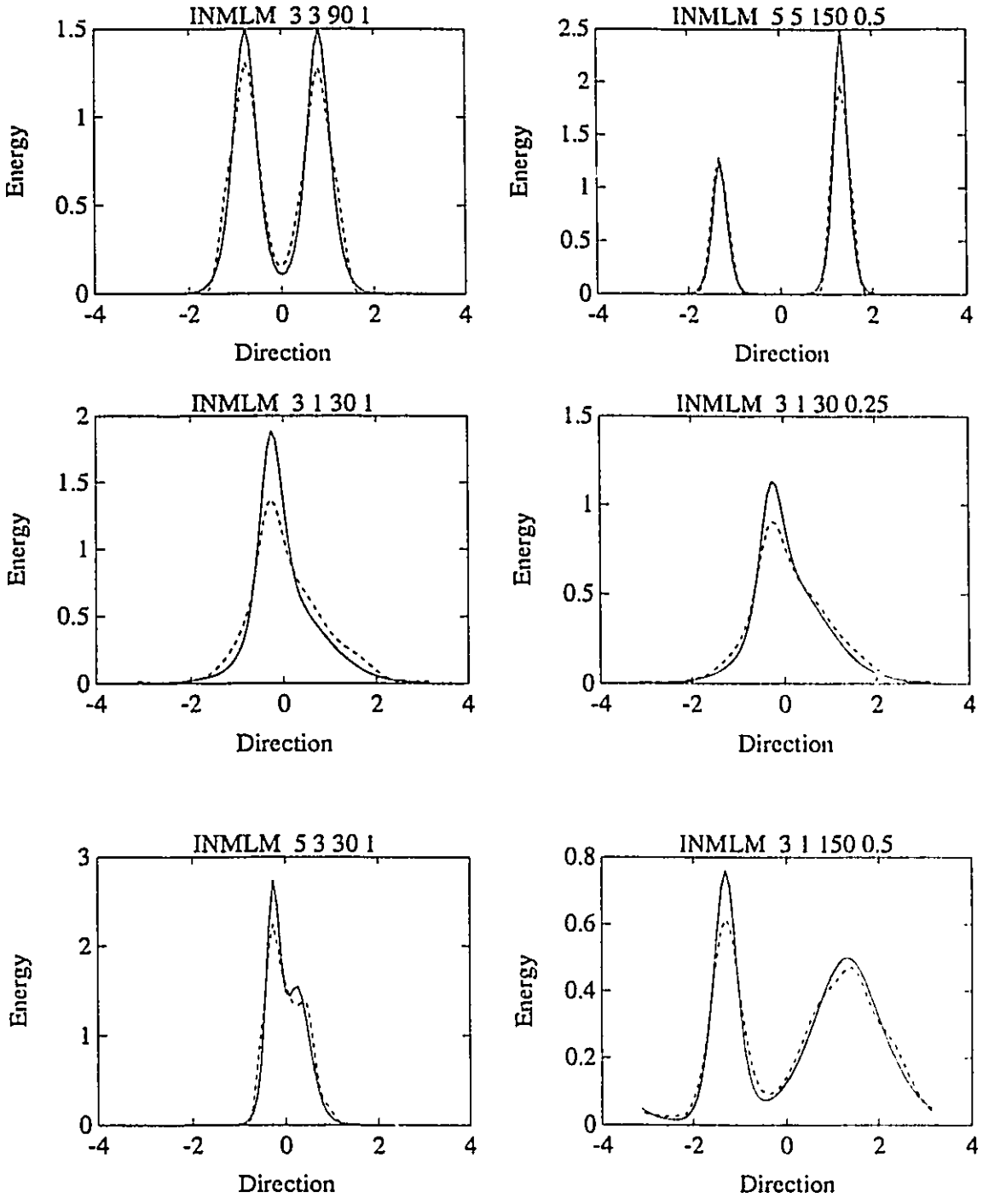

Fig.8.25 Typical results for INMLM method as represented by 6 different bimodal test cases. The four numbers on top of each graph define the bimodal distribution as: β values for both modes, spacing and energy ratio. Solid line is the target and dashed line is the estimate (wavestaff data, direct method).

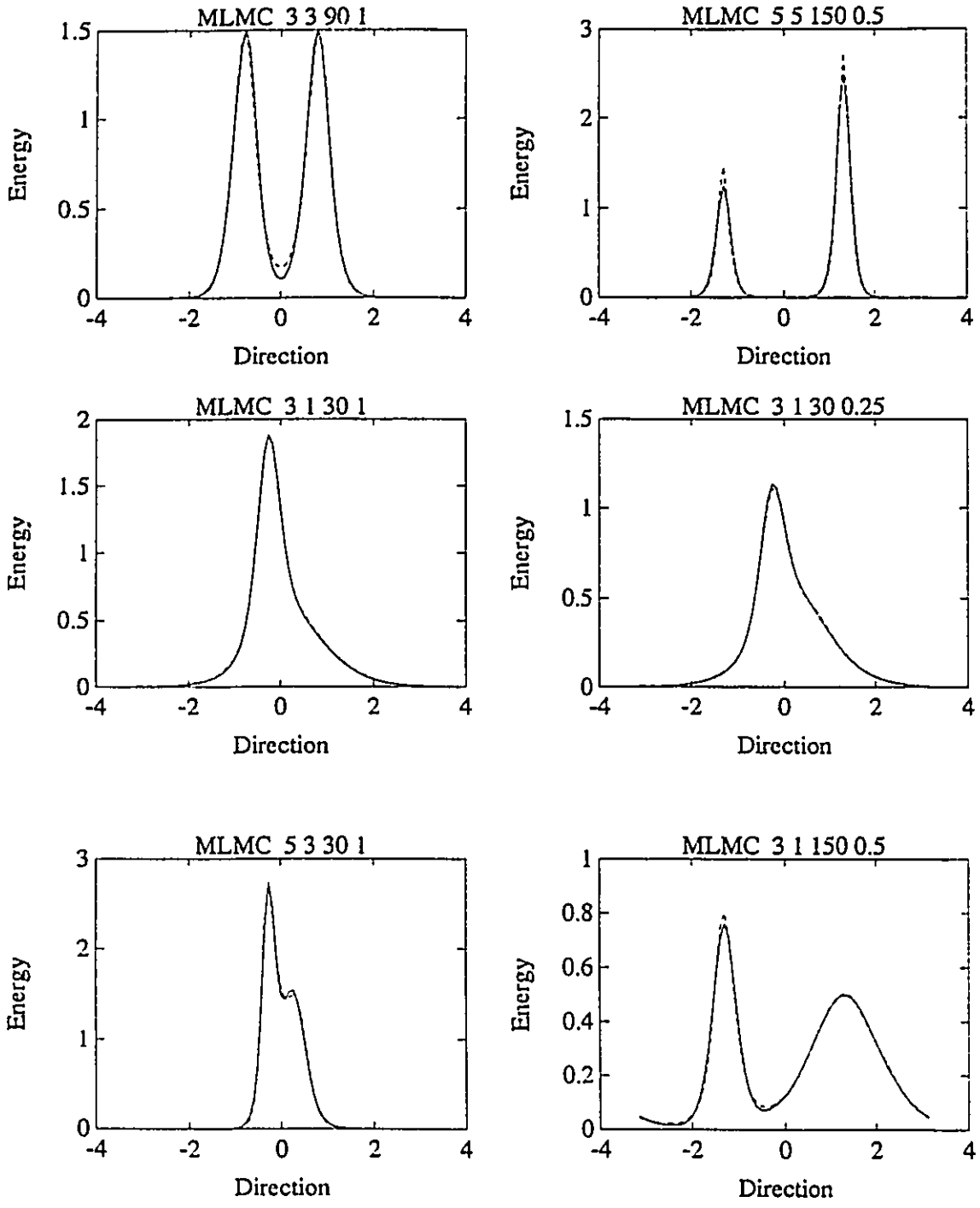

Fig.8.26 Typical results for MLMC method as represented by 6 different bimodal test cases. The four numbers on top of each graph define the bimodal distribution as: β values for both modes, spacing and energy ratio. Solid line is the target and dashed line is the estimate (wavestaff data, direct method).

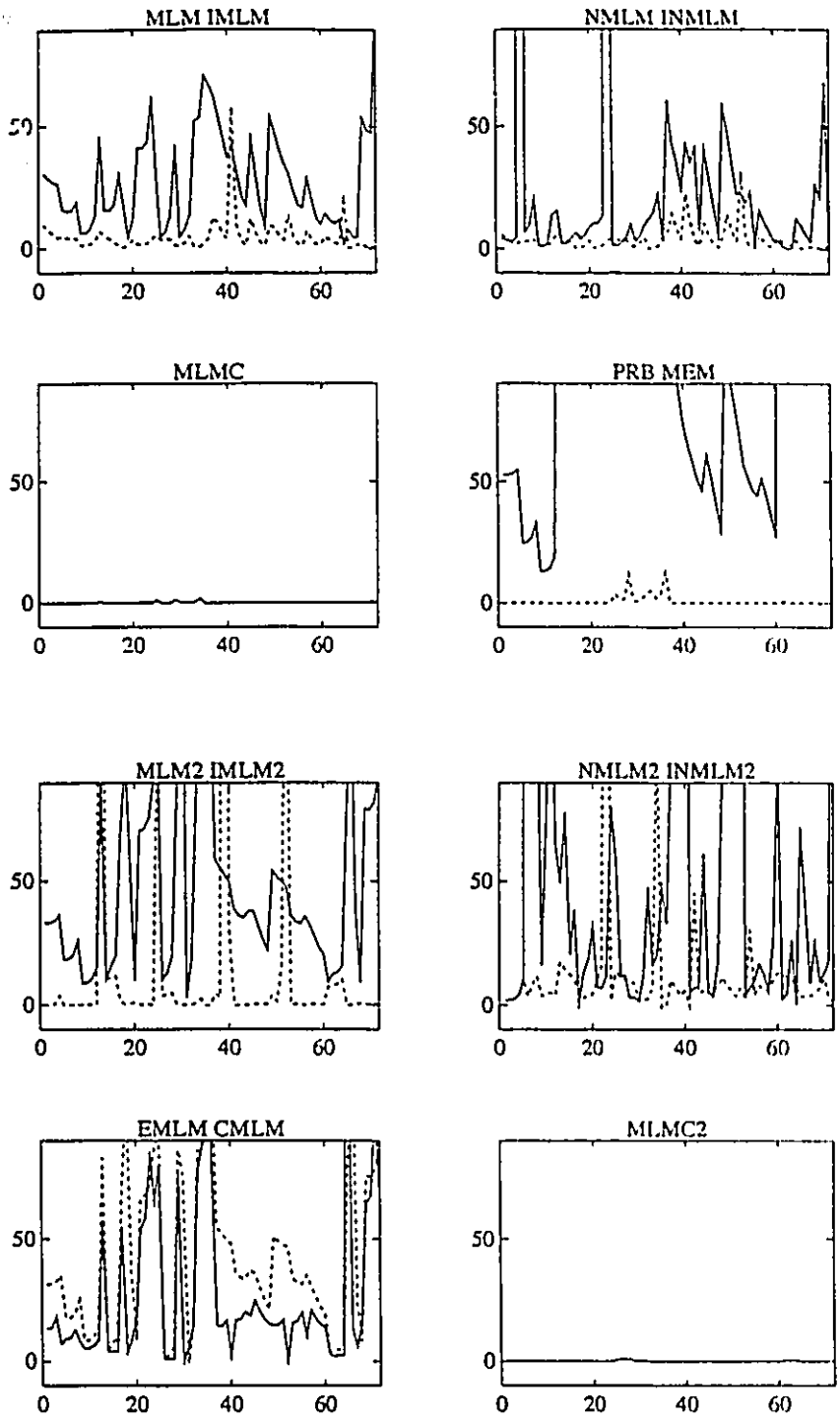

Fig.8.27 ρ^2 statistics for all methods for all bimodal distribution test cases (wavestaff data: direct and pitch-roll equivalent methods).

The results for the same six model tests that were shown for heave-pitch-roll methods are displayed for direct methods in Figure 8.22 to 8.26. The results for pitch-roll equivalent methods were very similar to the ones presented in the preceding section and are not discussed. Basic characteristics for each direct method are briefly outlined.

MLM- The performance of the MLM method is clearly improved compared to the buoy cases (Figure 8.7), but it still gives an estimate which is too wide.

IMLM- The performance of the IMLM estimate is generally good but surprisingly, it is not superior to the IMLM estimate for buoy data (Fig.8.10) except for the last test case which is more accurately reproduced. The convergence of the iterative scheme was excellent, as shown by the low ρ^2 values presented in Figure 8.27.

NMLM- The performance is quite good and is comparable with any method discussed so far besides the MLMC. The performance of the estimate, when compared to the buoy data estimate (Figure 8.12), indicate that the corrective scheme is much more accurate for the six wavestaff data, indicating in turn a more predictable behavior of the MLM estimate.

INMLM- The performance of the INMLM is similar to the IMLM, as both methods use a not too dissimilar starting point (MLM vs. NMLM), and as both schemes converge successfully in most cases as indicated by the ρ^2 values in Figure 8.27.

MLMC- The performance of the MLMC is flawless, as it reproduces almost exactly, even in the finer details, all of the model tests.

In general, clearly, the MLMC is the best estimate for the six-wavestaff array investigated. The other direct methods perform well, but surprisingly enough not any better than the best method for pitch-roll data (MLMC and IMLM), except for test cases with modes having significantly different spreading, as shown in the lower right test case presented in Figures 8.22 to

8.26. In such cases, the added information allows the direct methods to better resolve the model tests.

8.3.2. Field Data

The two field data cases presented herein were selected amongst many others as being representative of the general behavior of the various methods. Not all directional estimates will be shown, as the discussion will focus on the most relevant ones. Data comes from Lake Ontario and the various aspects related to field data acquisition will be discussed in Chapter 11.

Figure 8.28 presents a case of a high frequency, 0.8 *Hz* wind sea. Four direct methods (MLM, IMLM, MLMC, NMLM) and four pitch-roll equivalent methods (MLM2, IMLM2, MEM, MLMC2) estimates are presented. Contrary to what was observed in the test cases, it does not seem that better resolution is achieved from the direct methods. The estimates are not any peakier and less consistent from one frequency band to the other. The IMLM does not converge and oscillates even with the limited number of 3 iterations (it is possible to get rid of the oscillations by perturbing the CPSD with a greater amount of noise as was discussed in Chapter 7, but at the expense of returning a much flatter estimate). The MLMC method also tends to produce oscillations. The sudden peak observed in the NMLM estimate at a higher frequency is the result of a problem within the population fitting algorithm and not linked to the normalizing scheme.

Essentially, it would seem that noise, or a lack of conistency within the cross-spectra adversely affects the resolution of the direct methods and prevent them from reaching their full potential. Since the discussed spectrum had a high frequency and therefore relatively low energy, one should expect a higher signal to noise ratio and so, in order to confirm the previous

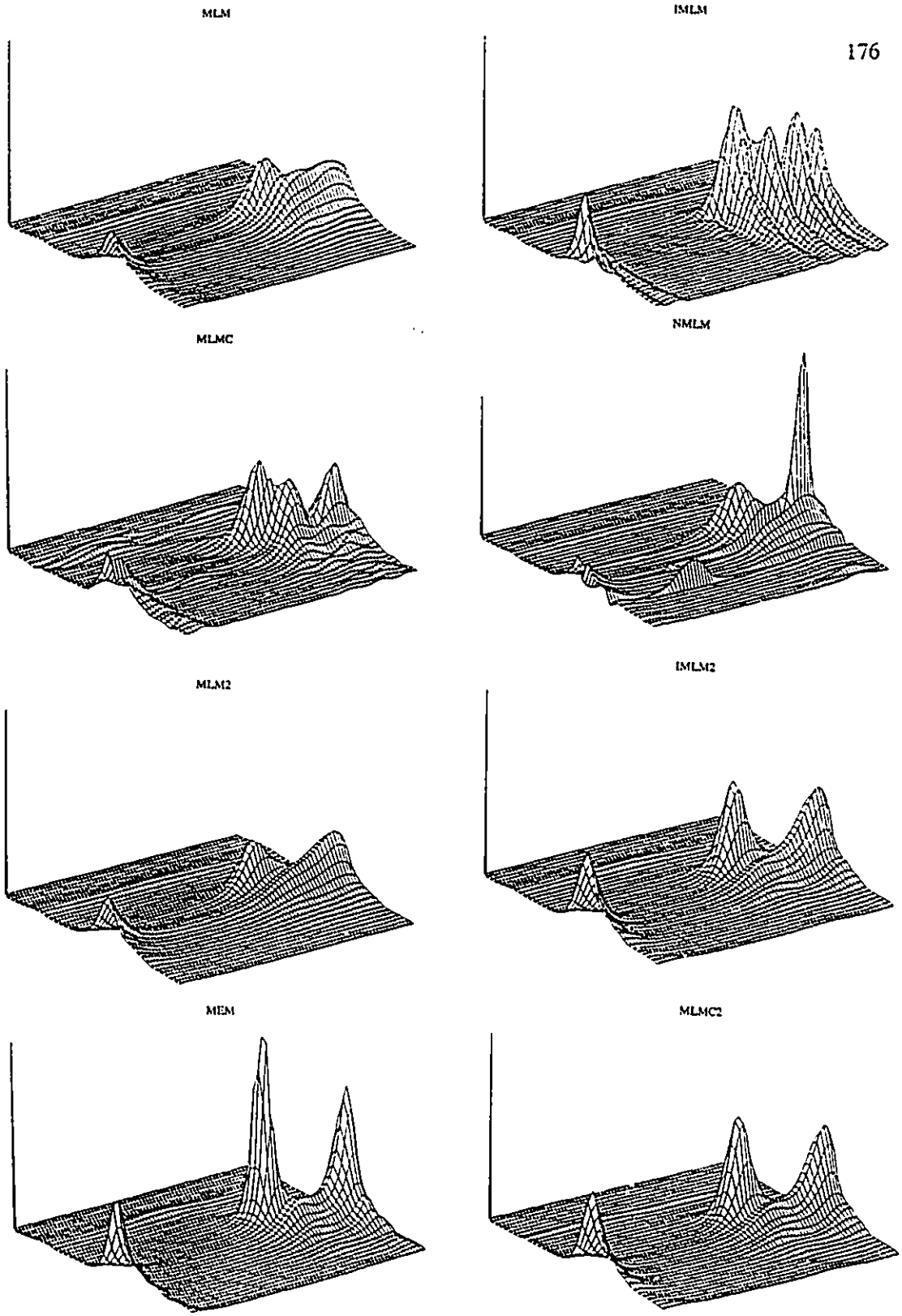

Fig.8.28 Comparative results for Lake Ontario Field data (wavestaff data). Frequency is from 0 to 1.5 Hz ($f_p = 0.8\ Hz$).

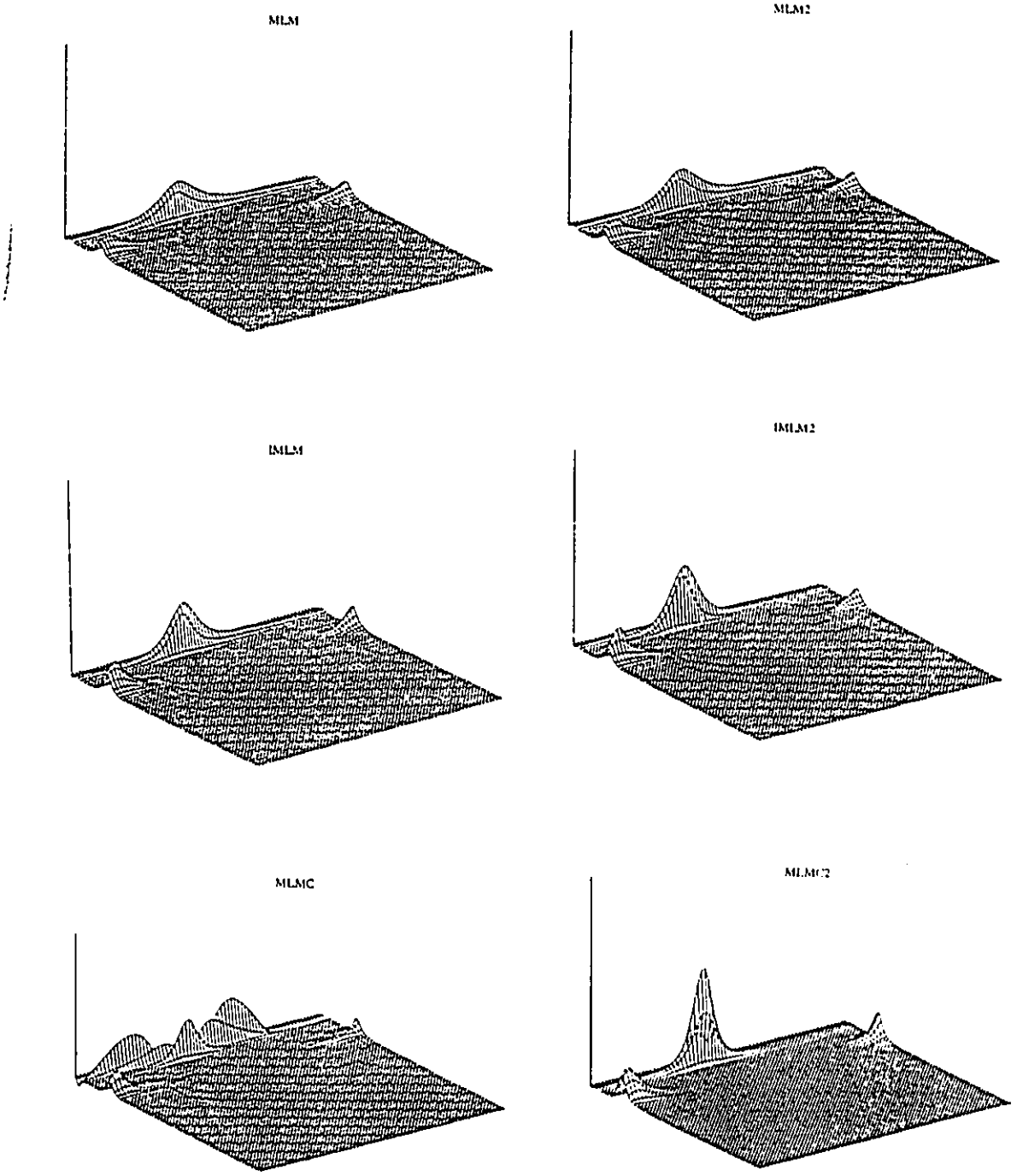

Fig.8.29 Comparative results for Lake Ontario Field data (wavestaff data). Frequency is from 0 to 2.5 Hz ($f_p = 0.11\ Hz$).

results a higher energy field data case was considered. The field data case shown in Figure 8.29 consists of a 0.11 *Hz* swell and a 0.46 *Hz* wind sea. Six estimates are shown in Figure 8.29, three Direct methods (MLM, IMLM, MLMC) and their pitch-roll equivalent methods (MLM2, IMLM2, MLMC2). The direct methods estimates are better than for the previous cases (the IMLM converges) but the pitch-roll equivalent methods produce estimates which are peakier for all three methods considered. This is also shown in Figure 8.30 which presents comparative results at four different frequencies. The pitch-roll equivalent MLM estimate is peakier at frequencies lower that 0.5 Hz. At frequencies greater than 0.5 Hz, the direct method MLM estimate is slightly narrower, but less than should be expected from the test cases. The MLMC estimate is clearly narrower at all frequencies, an observation which is consistent with the test results. The MLMC method fails at frequency smaller than 0.1 Hz (Figure 8.29) probably due to higher sensitivity of the method and increasing relative quantization errors at lower frequencies. Figure 8.31 illustrates the theoretical slope response of the array (when calculating the slopes as in Eq.6.7) plotted against the measured response, following the procedure outlined in Chapter 6 and in Appendix 4. One can see that starting at a frequency of about 0.12 *Hz*, the reconstructed slopes are not accurate anymore (due to quantization errors, as the water elevation difference over two wavestaffs becomes of the same order of magnitude than the digitization errors). This can very well explain the instability in the MLMC estimate which appears to be more sensitive than other estimates.

In order to make sure that the features observed using field data were true and not numerical artifacts of some sort, various testing steps were undertaken. The response of a three-wavestaff array was investigated and it was found that the direct methods estimates were also more prone to instabilities and oscillations than the pitch-roll equivalent. The pitch-roll

equivalent estimates were calculated using the slopes in various directions (same scheme as in Eq.6.7) without any significant differences. Finally, the block averaging scheme used in the FFT was varied using window lengths from 512 to 4096 points. The resulting estimates were averaged to the same frequency bandwidth and the results are displayed in Figure 8.32 for the MLM estimates. It can be seen that the essential features of the spectra are conserved but that the direct method estimates display a lot more variability in the cases of longer FFT windows, where more relative noise should be present.

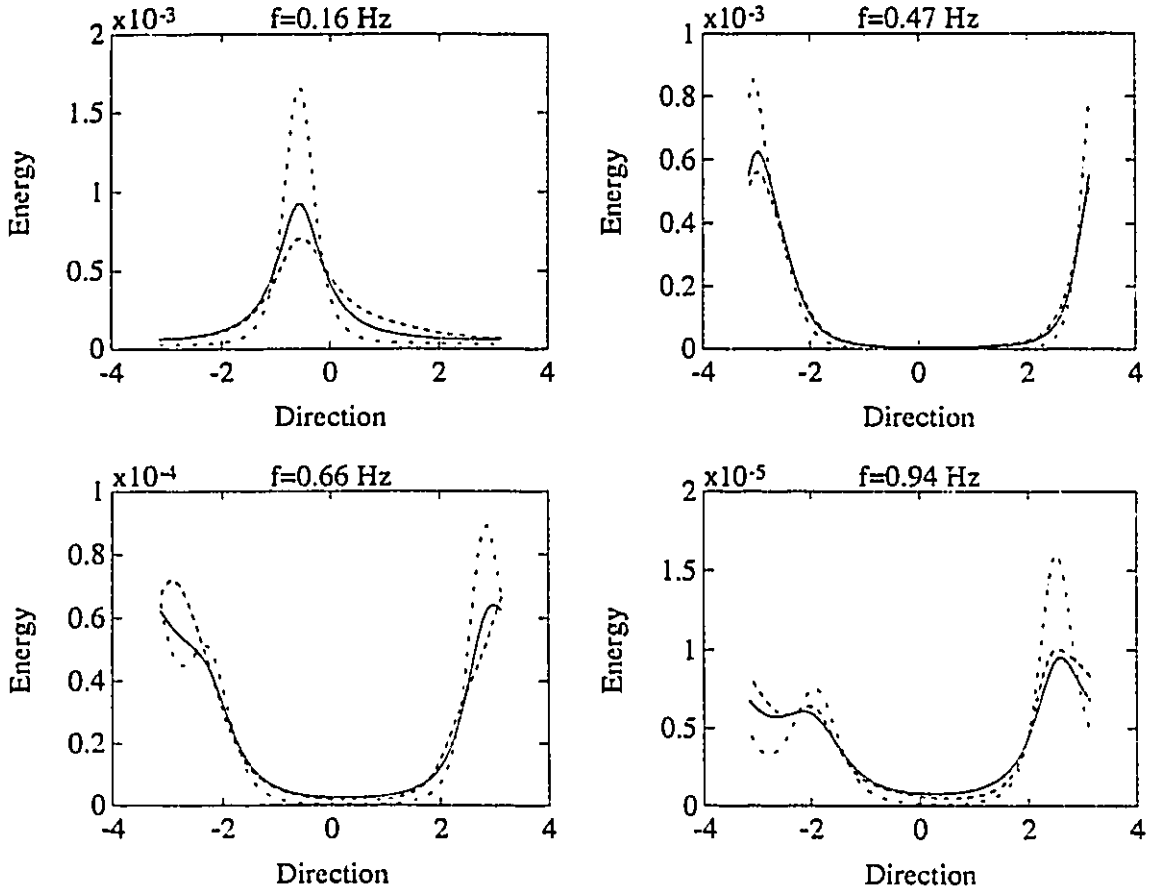

Fig.8.30 Directional spectrum estimates for Lake Ontario Field data (wavestaff data) at various frequencies. Solid line- pitch-roll equivalent MLM estimate, dashed line- MLM estimate, dash-dotted line- pitch-roll equivalent MLMC

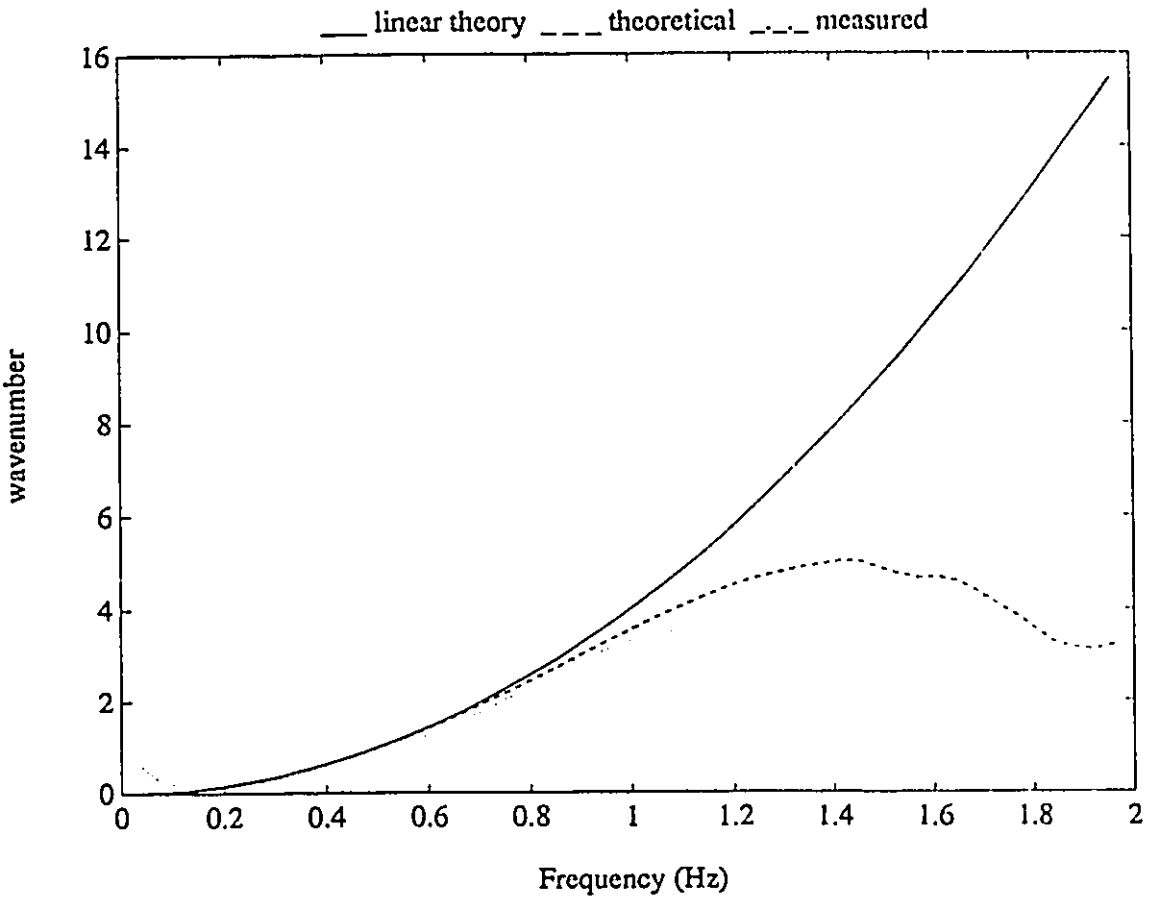

Fig.8.31 Theoretical and measured response of wavestaff array with respect to calculation of water surface slopes. Solid line is linear theory, dashed line is theoretical response and dotted line measured response.

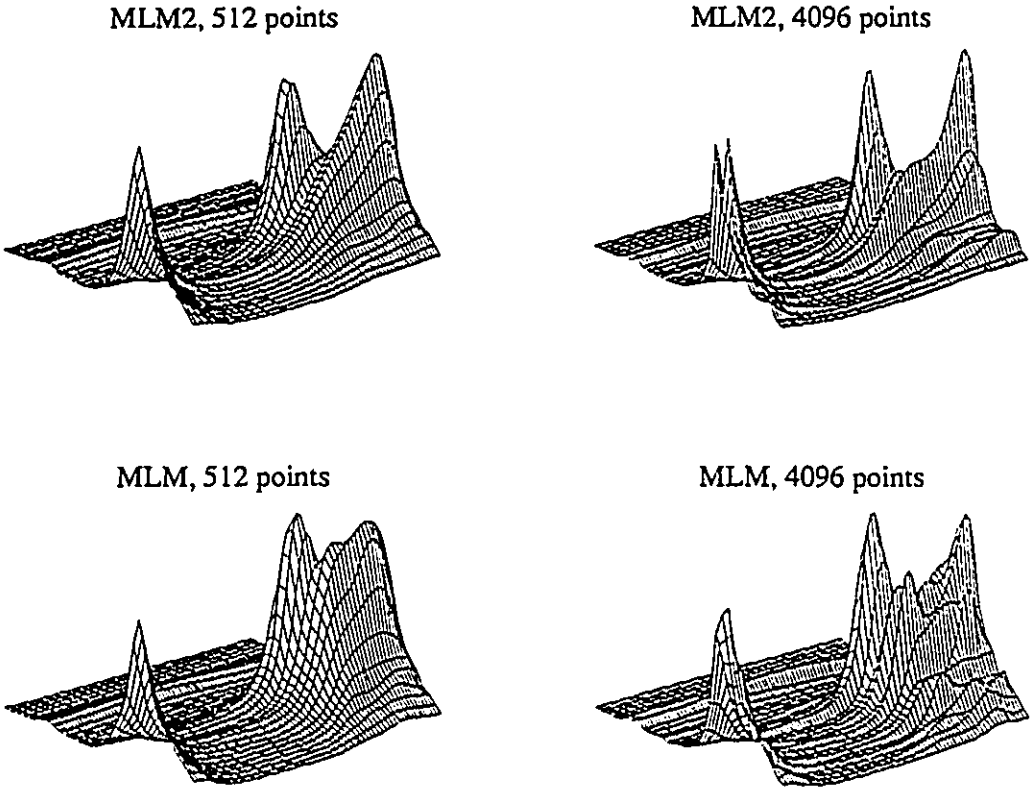

Fig.8.32 Directional spectrum estimates for Lake Ontario Field data (wavestaff data), using FFT window lengths of 512 and 4096 points (estimates are averaged to the same frequency bandwidth). Uppermost plots- pitch-roll equivalent MLM estimates, lowermost plots- MLM estimates. Frequency is from 0 to 1.25 Hz.

CHAPTER 9

ESTIMATION OF WAVE DIRECTIONAL SPECTRUM: DISCUSSION AND CONCLUSION

This Chapter concludes the first part of this work and is an attempt at wrapping up the topic of directional spectrum estimation. Many different aspects of the topic have been discussed, existing methods have been examined and new ideas have been put forward. This Chapter will discuss general, as well as specific aspects of directional spectrum estimation in order to summarize the work presented so far in this dissertation.

9.1. DISCUSSION OF RESULTS

Numerous points have been discussed and argued so far and to summarize them all into a coherent body of text is far from being a simple task. General aspects will be firstly discussed before getting into more "methods-specific" aspects.

9.1.1. Wavestaff data: Direct vs. Pitch-Roll equivalent methods

It is probably safe to say that the most mind-boggling finding of this work so far is the failure of the Direct methods for wavestaff data to reach their full resolution potential. The results for the six-wavestaff array show a loss in resolution due to inconsistencies in the measured cross-power-spectral-density matrices. This is especially clear for the MLMC estimate

which yields a clearly bad estimate. As pointed out by Hashimoto et al.(1987), if the mathematical relationship between the directional spectrum and the cross-power spectra is destroyed in the multi-element measurements by errors contained in the estimates of the cross-power spectra, the method fails to find a correct estimate. The formulation of the corrected form of the MLM (MLMC) directly implies that a valid solution exists. However, even though the MLM formulation directly implies non-negativity of the solution, this by no mean implies that the solution to the MLMC formulation (Eq.7.28) will also be non-negative. In theory, if the relationship between the true directional spectrum and the estimated cross-power spectra is conserved, Eq.7.28 will yield a non-negative estimate of the directional spectrum which is fully consistent with the cross-power spectra estimates. In practice, it seems that some factor(s) induce inconsistencies within the estimated cross-power spectra, which will in turn reduce the resolution of methods to estimate the wave directional spectrum. The corrected form of the MLM (CMLM) has a more sensitive response to these inconsitencies than other methods. The system presented in Eq.7.28 is often badly conditioned and little changes in the estimated cross-spectra can produce a significant difference in the solution. Clearly, a solution satisfying Eq.7.28 will always be found since the system of N equations and N variables will never be exactly singular (because of errors), but the observed oscillations with negative values of the directional spectrum clearly indicate a wrong solution. The failure of the IMLM (in the first field data case) also indicates that no "smooth" (in the sense of "oscillation-free") estimate was consistent with the measured CPSD. Similarly to the MLMC method, nothing in the IMLM iterative scheme prevents it to converge toward a solution with negative values of energy. Such a solution would be consistent with the measured CPSD but is certainly wrong from a physical point of view. To avoid that, most algorithm would set the negative values equal to zero, which is in fact an

extraneous perturbation of the scheme, thus hindering convergence and producing oscillations. In many cases, such problems with the convergence of the IMLM may simply imply that, because of inconsistencies in the data, no smooth estimate consistent with the CPSD matrix exist.

At low wavenumbers, when the difference in water elevation between two wavestaffs becomes of the same order of magnitude as the quantization errors, the phase relationship between neighboring wavestaffs can be modified, thus introducing inconsistencies in the cross-spectra. The calculation of slope estimates from the wavestaff data produces good stable estimates, therefore indicating that the slope computation results in an efficient smoothing of the errors contained in the wavestaff data, thus effectively removing a lot of the noise. But this cannot explain the decrease in resolution at higher frequency. The main difference between wavestaff and pitch-roll analysis lies in the calculation of the wavenumber. For pitch-roll data, the wavenumber is implicitely defined from the cross-spectra (Eq.6.3) whereas for wavestaff data, is is taken directly from linear theory. This introduces an error significant enough in some cases(when the wavefield is not perfectly linear) to explain the resolution losses. Still, the fact that pitch-roll-heave equivalent methods give as good and even better estimates than direct methods is surprising. One could put in question the generality of those observations by casting doubts on the quality of the Lake Ontario data. However, the Lake Ontario dataset was acquired using high-quality instrumentation. Each wavestaff was calibrated before and after the data gathering period and showed little difference, indicating that the wavestaffs had a stable linear calibration for the entire observation period. Also, during the field observation period, the wavestaffs were cleaned almost every week to remove any impurities or algae that had accumulated on them (Tsanis and Donelan, 1989). Finally, for every run, the RMS spread of the

water elevation was compared for each wave staff and differences were always found to be less than 5%. Then, clearly, this indicates that the current methods are unable to take advantage of the added resolution potential given by the wavestaff array unless the wavenumber can be accurately calculated (the wavenumber calculated from the slopes is an apparent wavenumber which includes an error due to incorrect evaluation of the slopes, and then cannot be used directly for wavestaff data analysis). The direct MLM estimate will still be as good as the pitch-roll equivalent MLM estimate in many cases, and even better in some frequency bands (see Figure 8.30), but still, a method such as the MLMC which cannot be used as a direct method, will achieve in most cases a better resolution on a pitch-roll signal than any other method on the direct signal. Still, this should not be interpreted as meaning that the use of wavestaff arrays is not warranted, since this is certainly not the case, even if pitch-roll equivalent methods are used to reconstruct the wave directional spectrum. A buoy cannot physically detect any wave smaller than its diameter meaning that a 3 meters buoy will not see waves below at least 0.7 Hz, and more probably 0.5 Hz. Using wavestaff arrays with proper spacing should allow frequencies way above that (as was already discussed in Chapter 6). In effect, the slopes are not calculated in an optimum way for the Lake Ontario array as was shown in Figure 6.2. This was indicated by the fact that the Lake St.Clair array gave better high frequency slopes simply due to the fact that the slopes were not averaged over a large area, as done in Lake Ontario. In fact, since pitch-roll equivalent methods are superior to direct methods, particular attention should be given to the way slopes are evaluated. This would mean that wavestaffs further apart should be used for lower frequency waves (so as to minimize relative digitization errors) and more closely spaced wavestaffs should be used for higher frequency waves. This could easily be done for the Lake Ontario array, at the expense of requiring additional Fast Fourier Transform of time series.

From the test cases results, it was seen that any method using the heave-pitch-roll signal was unable to resolve bimodal distributions with similar magnitude peaks but unequal spreading. This stems from the fact that unless an infinite number of measurements is made, the number of directional spectra satisfying the CPSD matrix is also infinite. For such a bimodal distribution, all methods tend to return a bimodal estimate with modes having a more similar spread. This means that out of all the spectra satisfying the CPSD, the methods settle on the one with equal spread modes. In a sense, this is a good characteristic as if one was faced with a number of possible solutions, the best choice would probably be the simplest one which would probably also happens to be the most realistic one. Clearly, the reverse tendency (to return an estimate with modes having a very different spread when the input was not) would be very distressing. One should always keep in mind that in reconstructing wave directional spectra, the only available working tool is the cross-power spectral density matrix and that for each measured CPSD, multiple solutions do exist with no possible way of determining which is the good one in any particular case. In these conditions, one cannot reasonably expect to find an infallible method. From the tests cases, methods like the MLMC and the IMLM are seen to resolve accurately most cases of bimodal distributions and only fail in what could be considered "special cases" such as modes with markedly different spread. This is very likely a limitation of the pitch-roll measurement system and not a failure of directional spectrum estimation methods. In the case of the six-wavestaff array, the additional information is sufficient so that the method is able to make the distinction and return proper estimates in all of the test cases. However, examination of field data indicates that even if unusual spreading function such as the one presently discussed would be present in wavefields, the signal deterioration due to noise would hinder the wavestaff array direct methods to recognize them. Clearly then, the level of resolution

that can be obtained from a pitch-roll-buoy, compared to its maximum potential, is significantly better than the one for a six-wavestaff array which uses twice as many measurements.

9.1.2. Specific aspects

As it was shown from the test cases the CMLM method clearly improves the MLM estimates in only a few test cases. This is a direct consequence of basing the convolution on a constant window function, obtained using a function with a spreading parameter value of $\beta = 3$. The convolution will work out fine on functions with a similar spreading, but will have little effects with larger spreading

One of the problem of the NMLM method, as observed with field data, was the lack of consistency of the method from one frequency band to another, especially so with pitch-roll data. As shown in model tests, small variations in target spectra can result in huge variations in pitch-roll buoy NMLM estimates. This is the result of a lack of accuracy within the normalization scheme. This is less of a problem with wavestaff arrays where the normalization was found to be much more linear. It should be pointed out that a major flaw in the approach is that even if a very good scheme is established for a particular measurement system and/or computer routine, the system probably will not be exportable to another system. The method was originally thought of with unimodal distributions in mind, and this is where it would probably be most useful. However, it should be pointed out that the test cases were on symmetrical noiseless distributions, conditions never encountered in nature. Field data evidence points to the fact that for unimodal distributions, the MEM bimodal tendency and the MLMC peak flatness observed in test cases, are simply the result of using such symmetrical noiseless distributions. These tendencies were never observed for field data. This points out to the fact that the MLMC method might also be

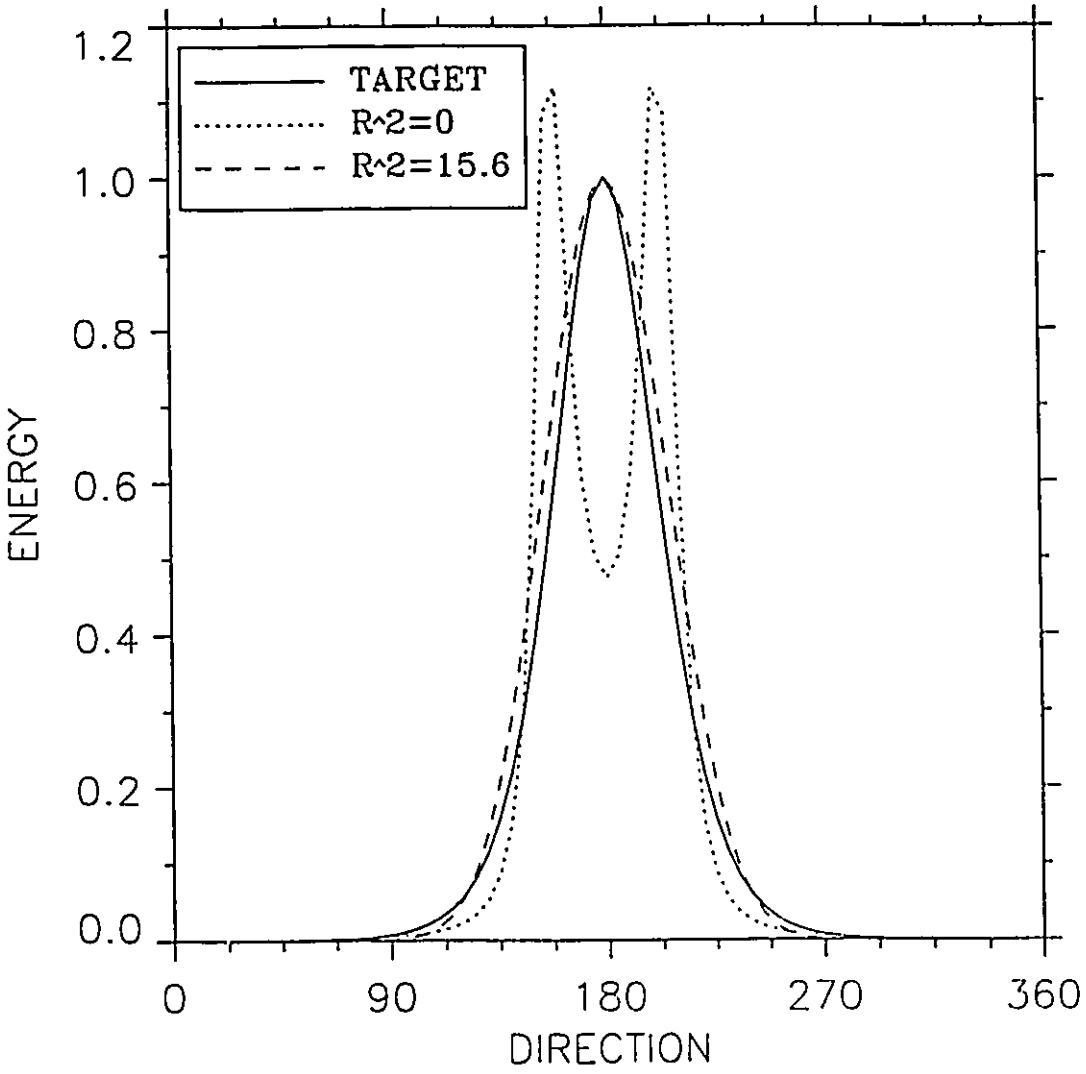

Fig.9.1 Directional spectrum estimate goodness of fit: Statistical vs. Engineering point of views.

the best performing method for unimodal distributions.

The ρ^2 statistics of Long (1980) has been discussed several times in the previous chapters. It was mentioned a number of times that an estimate can be wrong and still be perfectly consistent with the CPSD whereas another estimate can be acceptable from an engineering point of view while being rejected by the statistics as being inconsistent with the data. In order to illustrate such a statement, Figure 9.1 presents a $sech^2$ target spectra ($\beta = 2$) with the MEM estimate and a closely matching $\cos^2$ distribution. The MEM estimate, despite being perfectly consistent with the data ($\rho^2 = 0$), is not a very good representation of the model test. It means that the method returns a "true" estimate, that is one of the many possible solution to the CPSD matrix, which just happens to be the wrong one. On the other hand, the $\cos^2$ estimate is unacceptable as it is nowhere close to any possible solution of the CPSD. Nevertheless from an engineering viewpoint, very few people would argue that the MEM estimate is better. This is to say that the ρ^2 value should be interpreted accordingly, as an aid to evaluate directional spectra estimates, and not as an end.

9.1.3. Computing performance comparison

One aspect that has been largely neglected so far deals with the numerical aspect of efficiency. The computing time needed for the calculation of directional estimates is not a negligible point when dealing with daily routine analysis of large data sets. This section addresses the problem. Table 9.1 presents comparative data on the time and number of operations needed to calculate the different estimates. The term "flops" refers to the number of "floating points" operations. The results were obtained for typical field data using a 0.039 *Hz* bandwidth for frequencies up to 0.75 *Hz*. Computations were done on a Sun Sparcstation (speed

of about 1400 kflops/sec). Since the absolute time is dependent on the apparatus used, data is also presented in normalized form, using the Longuet-Higgins et al.(1963) method as a reference point. This allows for a quick relative comparison to be made in between different methods. Results presented in Table 9.1 indicate that direct methods are generally computationally more expensive than their pitch-roll-heave equivalent counterpart (except for the MLM and MLMC). Significant time differences exist between the different methods. Several points should be raised. The time and number of flops given in Table 9.1 take only in account the direct steps linked to the calculation of an estimate. This means for example that the numbers given for the IMLM do not include the time needed to compute the first MLM estimate. The same can be said for the INMLM. Theoretically, the time needed for computing an estimate should be closely linked to the number of flops. Practically, this is not so because the different routines are not equally efficient. An "efficiency" figure of merit is given by the last entry in Table 9.1 as the number of operations per unit of time, expressed in "kflops/sec". Roughly, the more vectorized an algorithm is, the more efficient it will be within the MATLAB platform. Loops and numerous calls to subroutines will necessarily decrease the algorithm performance, which explains why the 1400 kflops potential of the Sparcstation is never reached. All the routines were vectorized as far as possible and the different efficiency values are the result of intrinsic properties of the methods rather than differences within the computing schemes. The fact that the MLMC method was almost fully vectorized using Chapter 7 formulation explains why its speed is comparable to the other methods (for pitch-roll-heave equivalent methods) despite requiring at least 40 times more operations than any other methods. A method like the NMLM which is more or less the embryo of an expert system is condition based and thus is not very efficient. The low efficiency of the NMLM is also explained by the fitting algorithm developed in Chapter 7. The Nelder-Meade

TABLE 9.1. Performance Comparison

Lake Ontario Array					
Direct Methods					
Method	Flops Number	Flops Normalized	Time (seconds)	Time Normalized	Efficiency kflops/sec.
MLM	719913	24.2	3.5	22.1	204
IMLM	24101544	810.5	355.6	2222.5	68
MLMC	22737933	764.7	28.1	175.6	809
NMLM	6361997	214.0	1181.4	7383.8	5
INMLM	24111861	810.9	358.6	2241.0	67
Pitch-Roll-Heave Equivalent Methods					
Method	Flops Number	Flops Normalized	Time (seconds)	Time Normalized	Efficiency kflops/sec.
MLM	177262	6.0	3.80	23.8	46
PRB	29736	1.0	0.16	1.0	185
MEM	88338	3.0	2.21	13.8	39
IMLM	701117	23.6	9.52	59.5	73
EVMLM	165798	5.6	2.50	15.6	66
NMLM	2017232	67.8	262.59	1641.2	8
INMLM	702964	23.6	9.47	59.2	74
CMLM	217610	7.3	11.82	73.9	18
MLMC	18867998	634.5	19.62	122.6	962

Normalization is with respect to PRB method

simplex algorithm used to carry the four-free parameters least-square fit is very robust which is its main advantage (does not calculate any derivative) but can also be very slow which is the main problem of the method. In fact, about 65% of the NMLM computation time is devoted to the fitting procedure. If the distribution is unimodal the method is as fast as most methods, but if the energy spreading is a complex function, the algorithm convergence is painfully slow. A very crude scheme consisting of simply separating the energy on each side of a line proportionally located between the populations peaks was used in the early stage of the work with some success. The method was significantly faster but the results were not as good especially so for bimodal distributions with closely spaced peaks. As a result, rules for the normalization scheme were harder to obtain.

The computation of directional estimates is only part of the entire data processing process. The fact that some methods are slower than others might not be significant if the extra computing time is small compared to the rest of the analysis. As a comparative point, the time needed to transform a dataset from the time domain to the frequency domain and compute cross-spectral estimates was obtained. For a 31 minutes long segment from a six-wavestaff array, sampled at 20 *Hz* and windowed every 512 points with a 128 points overlap required 168 seconds (this included the calculation of cross-spectra for both the water elevation and reconstructed slopes). This value indicate that for pitch-roll-equivalent methods, the time to compute the directional estimates (except the NMLM) is slow enough as not to be a decision-making factor. The NMLM (and the INMLM) require extensive computing time, for all type of measurements and the time is long enough as to preclude the use of these methods for routine data analysis. Finally, it should be noted that the IMLM performance is adequate for Pitch-Roll data, but that the additional signals included in the wavestaff data significantly increase the number of

performed operations, making the method also very time-consuming.

9.2. RECOMMENDATIONS

Following a literature review, extensive testing and discussion of all available methods, a choice has to be made on which methods are best suited for data analysis. The recommendations are based on the need of reconstructing the entire angular distribution of energy, and not obtaining only a few directional parameters which can be obtained in a "model-free" fashion, using the first Fourier Coefficients of the directional distribution (see Kuik, Van Vledder and Holthuijsen, 1988).

9.2.1. Pitch-Roll-Heave Data

The results of the various test cases presented in the previous chapter indicate that for heave-pitch-roll data, two methods are clearly superior to the others: the Iterative Maximum Likelihood Method (IMLM) and the Maximum Likelihood Method Corrected form (MLMC). Solely based on the results presented in Chapter 8, the methods are essentially equivalent, except for the facts that the MLMC is more "elegant" (an arbitrary concept, at least from an engineering viewpoint, but certainly not from a mathematical point of view) and that it always returns an estimate fully consistent with the data (clear advantage from a physical point of view !). However, it should be kept in mind that for the particular applications linked to this work, we were able to fine-tune the use of the IMLM and determine exactly the number of iterations needed to reach an optimum estimate. The use of the IMLM method on another computer system, or within another computing routine would require the user to make several tests to redetermine the optimal characteristics of the method. This is highly impractical and even in the

best of cases, one can never be sure if the estimate will converge accurately (it will not in many cases even if the estimate might be close to target), and unless the ρ^2 statistics is computed, which can demonstrate the successful convergence of the scheme, results from the IMLM should always be interpreted carefully. The IMLM method remains a numerical technique, and unless it can be proven to be clearly superior (which is certainly not the case, the IMLM method with optimum conditions being at best comparable to the MLMC), another method should be preferred. Additionally, any method likely to give unpredictable results in some cases (like the IMLM in the always possible advent of very bad convergence) is not suited for at least, routine data analysis.

For these reasons, the Corrected form of the MLM (MLMC) developed in this work, is recommended, and will be used in the subsequent chapters dealing with the analysis of field data.

9.2.2. Wave-Staff Data

The field data results indicated that direct methods do not perform as well as their pitch-roll counterparts, probably due to small differences between the true wavenumbers and the linear theory approximations. This characteristic prevented the use of the MLMC method directly on the water elevation signals, and made the IMLM method very sensitive and very likely to produce oscillations, thus making heave-pitch-roll equivalent methods a better choice in most cases (unless the wavenumber inconsistency is resolved). Considering those results, one is faced with similar conclusions to the ones drawn in the previous section. The MLMC and IMLM now clearly stand out as being the favored methods. With the same arguments used in the previous section, the use of the MLMC is strongly recommended as being the best-performing method

9.3. CONCLUSIONS

In this first part of the work, theoretical foundations and testing procedures were established to evaluate and compare different methods of extracting the wave directional spectrum from a wave record. A number of methods were examined, their properties, characteristics and biases identified, and as a result, guidelines for the use of these methods were drawn. Extensive testing and comparison with field data showed that very good resolution directional spectrum estimates can be obtained with both pitch-roll buoys and wavestaff arrays. Specific conclusions having been drawn at the end of most chapters, the general conclusions of this first part of the dissertation can be stated as follows:

* All of the methods currently used for wave directional spectrum estimation have drawbacks. Out of the 5 methods reviewed, the MLM has the most stable characteristics and the IMLM the best resolution potential.

* Out of the three new methods proposed in this work, the Corrected form of the Maximum Likelihood (MLMC) estimate is the best choice, from both a theoretical and practical point of view. The MLMC method was shown to outperform all other estimates for both heave-pitch-roll and wavestaff data. As a consequence, the method will be used for the analysis of field data in the next part of the thesis.

* Comparison of all methods with field data indicated that the higher resolution potential of wavestaff arrays is not necessarily met, probably because of differences between true wavenumbers and the ones approximated using linear theory, and thus making the pitch-roll equivalent MLMC method a better choice for directional spectrum estimation.

CHAPTER 10

THE 1990 OCTOBER STORM IN THE SWADE EXPERIMENT: CASES OF TURNING WINDS

This Chapter and the following two are direct applications of the high-resolution methods of estimating the wave directional spectrum, and aim essentially at using the concepts previously developed, proving the validity of the claims based on synthetic test cases, and especially investigating the usefulness and advantages of the new methods developed in this work. As such, the following chapters are not in any way an "in depth" analysis of the evolution of wavefields in the SWADE experiment or in the Great Lakes (as such analysis represent formidable endeavors), but merely an effort at outlining the potential of high-resolution spectral methods in the analysis of directional seas.

10.1. THE SWADE EXPERIMENT

In a 1975 review of advances in the study of wind waves, Barnett and Kenyon (1975) noted that at the time Ursell (1956) reviewed the field of wind waves, field observations relevant to wave generation and dissipation in the ocean were nearly non-existent, and they were (in 1975) simply very scarce. Although not entirely true today, theoretical ideas still seem to be ahead of experimental testing. Donelan et al.(1985) pointed out that previous field experiments have been hampered by a lack of spatial resolution in both the wave and wind fields and

especially a lack of wave directional information.

Recognizing the above problems, the United States Navy's Office of Naval Research launched in 1988 an accelerated initiative whose central goal was to improve our understanding of the basic physics and dynamics of surface waves. It was realized that this goal would be better achieved through two separate but cooperative experiments: the Surface Wave Processes Program (SWAPP) and the Surface Wave Dynamics Experiment (SWADE). SWAPP was essentially concerned with local processes with an emphasis on wave breaking and energy dissipation whereas SWADE was focused on the generation and evolution of wave fields. An overview of the two ocean wave experiments can be found in Weller, Donelan, Briscoe and Huang (1991). The SWADE experiment was designed to provide spatial and temporal coverage on the east coast of the Atlantic Ocean. Figure 10.1 presents the cluster of buoys which was used during the experiment. The SWADE field observation period ran from October 1990 to March 1991 during which data gathered almost continually. SWADE data was made available to this research through the National Data Buoy Center (NDBC).

10.1.1. The Discus-N buoy

The cluster of buoys used during the SWADE experiment consisted of moored NDBC buoys which were already in location in addition to specific buoys which were put to sea specifically for the experiment. The centerpiece of the buoy cluster is the Discus-North buoy (NDBC 44001 in Figure 10.1) which is a 3-meters NDBC Discus Directional buoy onto which equipment was specifically added for the SWADE experiment. The Discus-N buoy is located (Figure 10.1) at $73°48.9'W$ longitude and $38°11.6'N$ latitude, at the edge of the continental shelf offshore of Virginia. All the data analyzed and presented in this Chapter comes from the

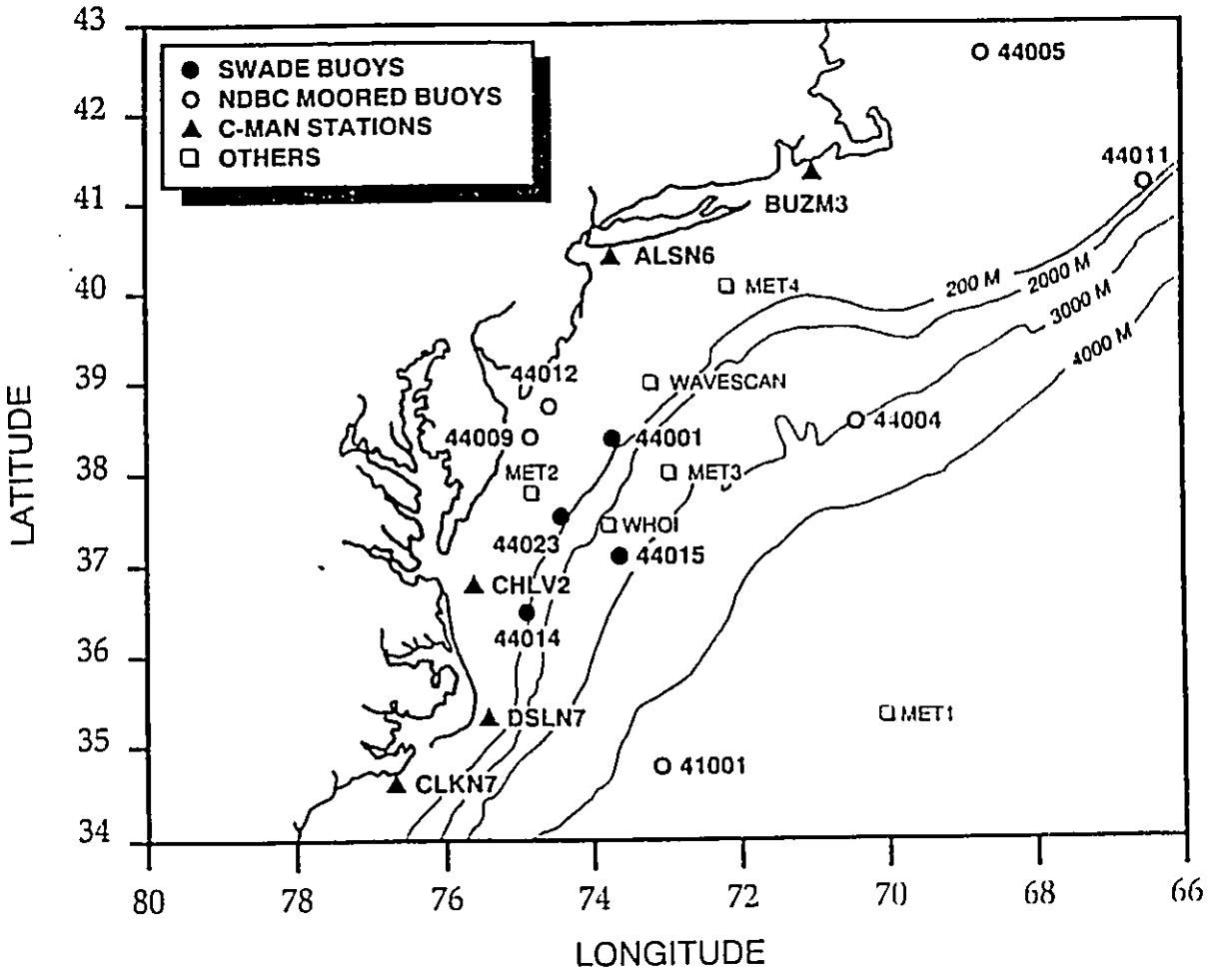

Fig.10.1 Geographic location of the SWADE experiment and location of various buoys (from Weller et al., 1991).

Discus-N buoy.

10.2. DATA CORRECTION

The Discus-N buoy is a NDBC directional buoy initially used specifically for the SWADE experiment. Discus-N data can be obtained via two channels: SWADE data in uncorrected form and via NDBC in the NDBC corrected format. As mentioned earlier, data needs to be corrected for many reasons, some of the main effects being caused by the fact that buoys are never perfect wave followers, they are free to drift and rotate around their axis and their response can be affected by their mooring line. The entire aspect of data acquisition, correction and verification is a complex task which should not be overlooked as it is fundamental to the obtainment of good, high-resolution wave directional spectra.

10.2.1. SWADE data

The complete procedure for the correction and analysis of "raw" SWADE data was done following the procedure presented in Anctil et al.(1992). The procedure to correct the data is herein only briefly outlined.

The buoy is free to rotate around its vertical axis so, in a first step the magnetometer data is used to calculate the position of the buoy in the $x-y$ horizontal plane. A mean direction (which corresponds to the wind direction) is then computed. The angles of Pitching and Rolling can then be transformed to the new coordinate system. The vertical acceleration is transformed to elevation (through a double integration in time). The accelerometer keeps its vertical orientation so that no correction for tilting is necessary. The signals are then transformed to the frequency domain through a Fast-Fourier-Transform (FFT) routine, and the cross-correlation between the

elevation and slopes signal can be computed (Cross Power Spectral Density CPSD matrix). Because the buoy is anchored and/or is not a perfect wave follower, it generally adopts a more or less permanent tilt which induces a phase lag between the three signals. Typically the co-spectra between elevation and slopes and the quad-spectrum between the slopes are found to be non-zero because of this induced phase lag. So in a final step, the signals are corrected to negate this phase lag.

10.2.2. SWADE data via NDBC

The files pertaining to directional buoys can be obtained through the National Oceanographic Data Center (NODC). The files contain time series meteorological and oceanographic data collected by moored buoys operated by the National Data Buoy Center (NDBC) of the National Oceanic and Atmospheric Administration (NOAA). Wave directional data comes into three different records. The first one contains the values of the cross-spectra between the pitch-roll-heave signals while the other two contain frequency dependent parameters related to the Fourier series of the spreading function. General information concerning the NDBC directional wave data can be obtained through the NODC Users Guide (1991).

Detailed information pertaining to directional-wave measurements with NDBC Discus Buoys, data acquisition, processing and transmitting can be found in Steele, Lau and Hsu (1985) and Steele et al. (1990). A preliminary directional analysis of the NDBC data using a truncated Fourier Series, following Longuet-Higgins et al. (1963), gave acceptable results (within the limits of the method) but higher resolution methods using the measured cross-power-spectral-density matrix failed due to a lack of consistency within the NDBC data. As suggested by Anctil et al. (1992), a simple test to detect any anomalies in the buoy wave-following capacities consists in

calculating the ratio $R(f)$ of the calculated wavenumber to the theoretical one (k_{th}) using linear theory, ratio which should be equal to 1:

$$R(f) = \frac{\left[\frac{C_{22} + C_{33}}{C_{11}}\right]^{\frac{1}{2}}}{k_{th}} = 1 \qquad (10.1)$$

In addition, in a linear wave field, phase shifts between the water elevation and surface slopes should be equal to $\frac{\pi}{2}$ leading to imaginary only cross-spectra (co-spectra = 0). Examination of the NDBC cross-spectral data showed significant departure from this behavior. Data was corrected for the artificial phase shifts. As pointed out by Anctil et al. (1992) a departure from this theoretical behavior does not necessarily mean that the buoy is not a good wave follower, but could also indicate that the wave field is non-linear or that Doppler shifting effects are significant. But, the impossibility of obtaining any spectra with either the MLM or MEM which are very sensitive non-linear estimators, without making the corrections, clearly indicates that the phase shifts are indeed essentially artificial.

After the NDBC data was corrected, a comparison between the methods outlined in sections 10.2.1. and 10.2.2. was done and showed that directional spectra obtained from both corrective schemes were virtually identical. Because of the equivalence of both approaches, NDBC data was corrected and used. This approach was chosen because CPSD matrices are directly available, and the time-consuming steps of handling large datasets and transforming them in the frequency domain could be avoided.

Cross-spectra for the heave, pitching and rolling signals are one hour averages given in frequency bands of 0.01 *Hz* (up to 0.35 *Hz*), giving spectral estimates with 72 degrees of freedom.

Wind speed and directions are 8.5 minutes averages taken at a height of 4 meters above the water surface.

10.3. THE 1990 OCTOBER STORM

10.3.1. General overview

During a period starting October 20 1990 and ending October 30 1990, three severe storms swept the SWADE location. Wind speed and wind direction for the entire duration of the events are shown in Figure 10.2. All three storm episodes had wind speed in excess of 12 m/sec and significant wave heights H_s of up to 6 m for the most severe storm. This succession of storms caused the loss of the SPAR buoy, one of the pivotal element of the SWADE array, which sank during these extreme environmental conditions. The SPAR buoy carried an array of six wavestaffs which was originally supposed to be the main focus of this work. This unfortunate turn of events prompted the need to establish the basis for selecting the best-performing method for heave-pitch-roll buoys, as such data would have to be used as a substitute for the SPAR data at the center of the SWADE array.

10.3.2. Cases of turning winds

The plot of the wind direction shown in Figure 10.2 indicates that many episodes of turning winds can be isolated during the 11 days period. In order to investigate more closely the directional spectrum response to turning winds, three cases were isolated from the 11 days period, and separately analyzed, using as a directional spectrum estimate, the corrected form of the Maximum Likelihood Method (MLMC) developed in this work. Table 10.1 gives

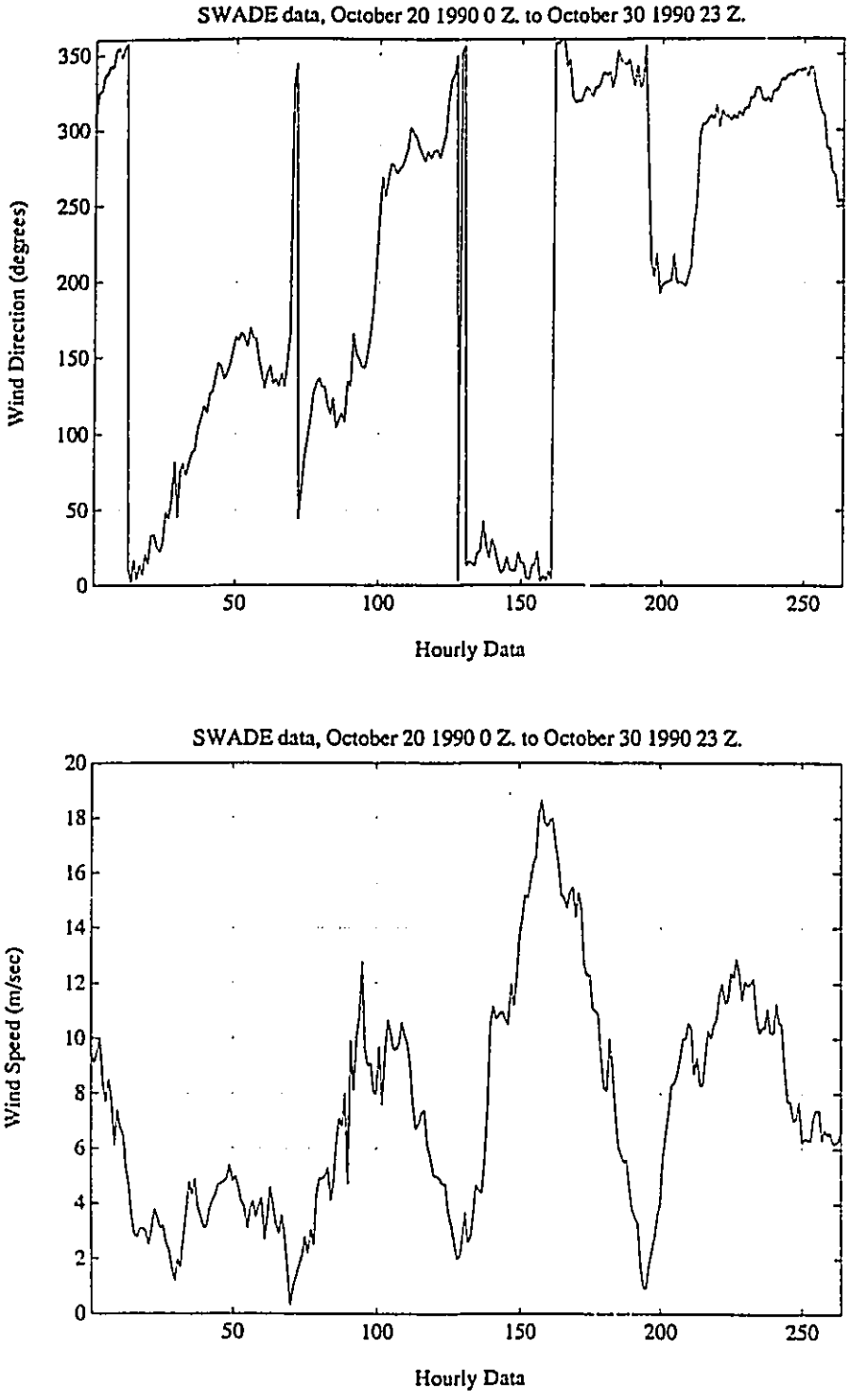

Fig.10.2 Time series of wind direction (top) and wind speed (bottom) during the October 20 to October 30 storm period. The wind speed data (taken at 4 meters) represent 8.5 minutes averages every hour.

TABLE 10.1. SWADE Cases selected

START (yymmddhh)	END (yymmddhh)	DUR. (hrs)	Missing Data #	mean $\lvert \partial \theta_w / \partial t \rvert$ (rad/sec)	($^o/hr$)	mean $\lvert \partial \bar{\theta} / \partial t \rvert$ (rad/sec)	($^o/hr$)
90102000	90102123	48	5-7-42-43	$2.8 \cdot 10^{-5}$	5.7	$3.1 \cdot 10^{-5}$	6.4
90102318	90102411	18	3-4-12-13-17	$4.7 \cdot 10^{-5}$	9.6	$3.7 \cdot 10^{-5}$	7.6
90102721	90102822	26	11-12-16-18-21	$5.9 \cdot 10^{-5}$	12.3	$6.7 \cdot 10^{-5}$	13.8

Start and end hours are GMT. Missing data refers to directional data only.
mean $\lvert \partial \bar{\theta} / \partial t \rvert$ is defined over the 0.1–0.35 *Hz* frequency range

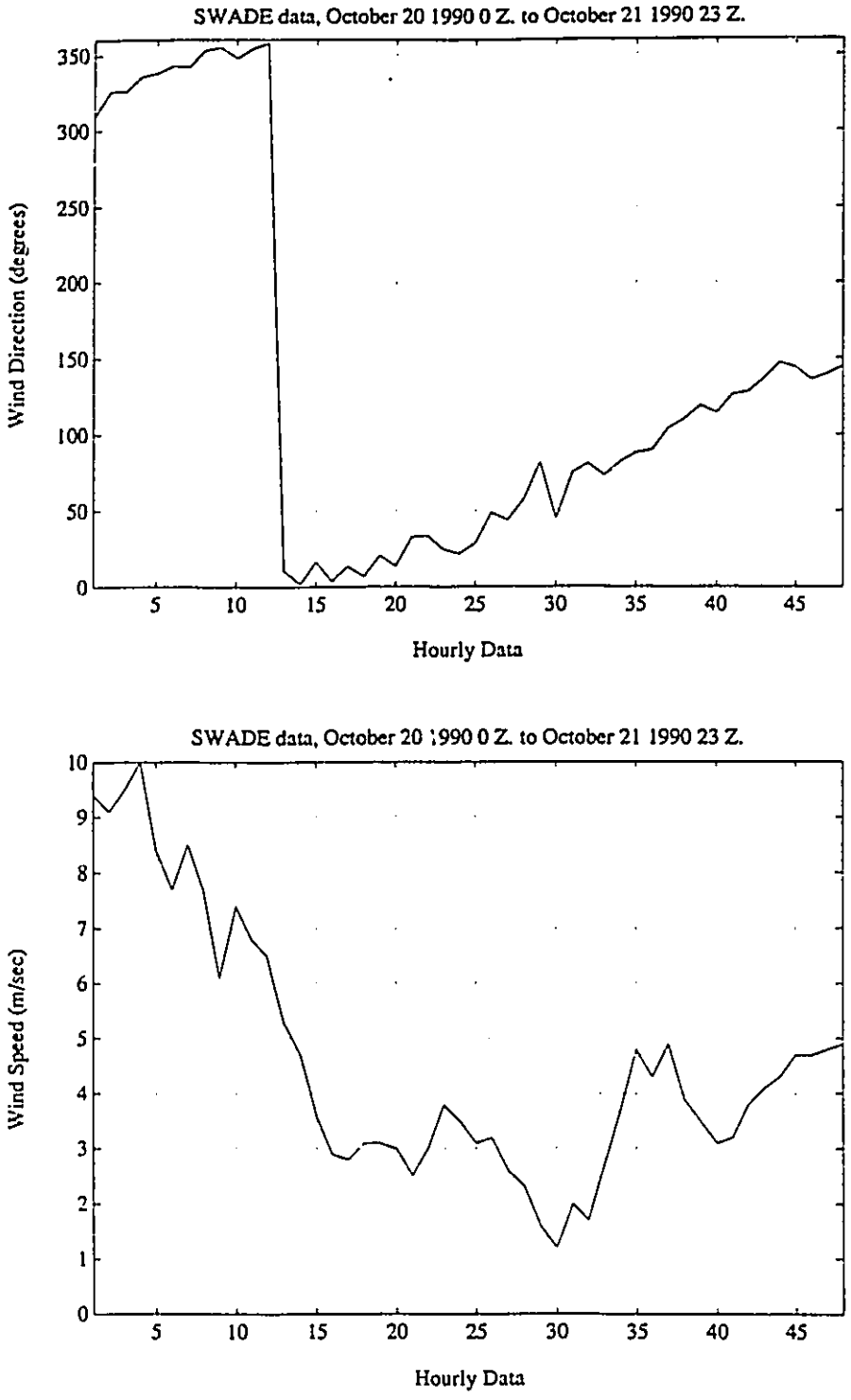

Fig.10.3 Time series of wind direction (top) and wind speed (bottom) for the first selected case of turning wind. The wind speed data (taken at 4 meters) represent 8.5 minutes averages every hour.

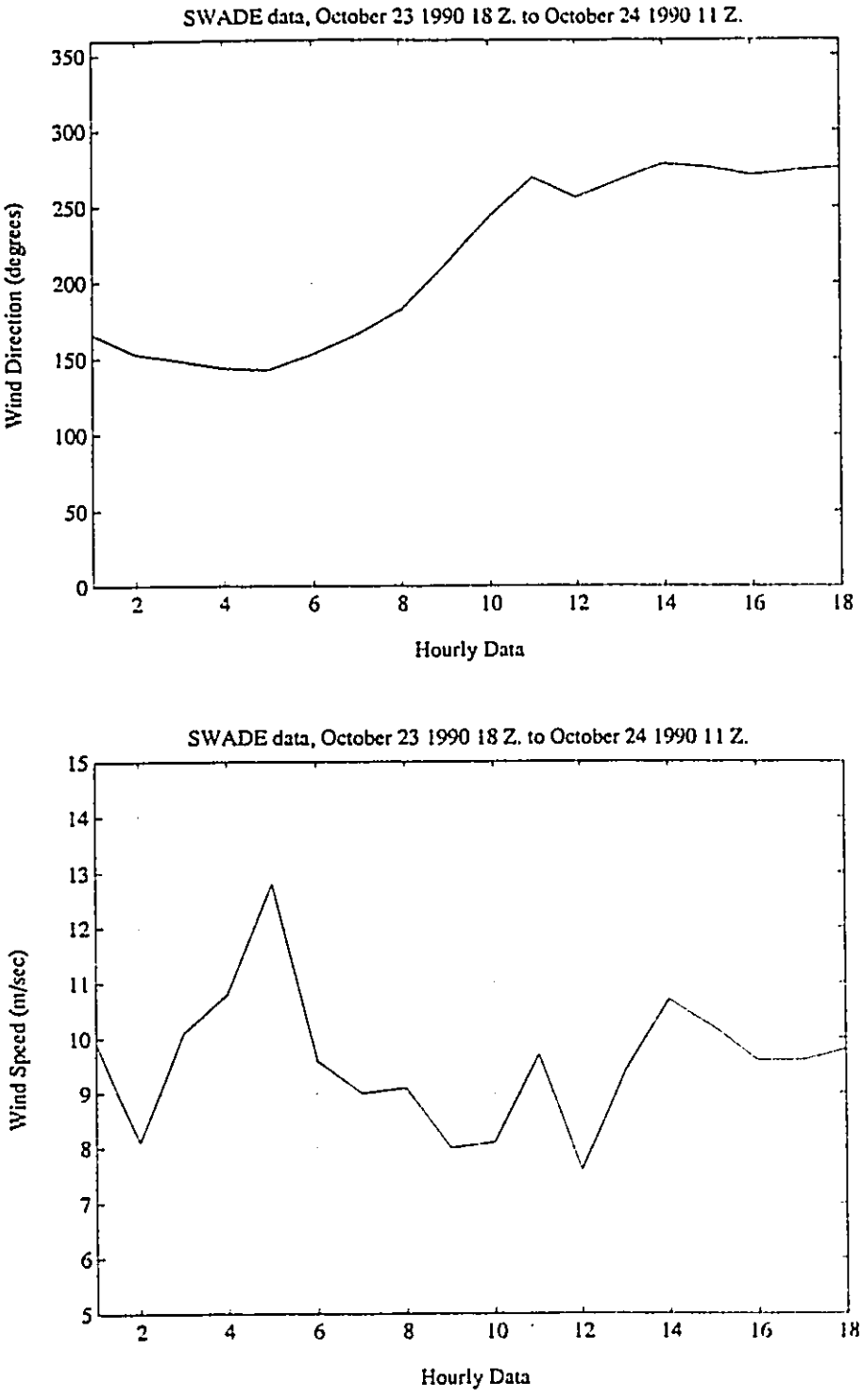

Fig.10.4 Time series of wind direction (top) and wind speed (bottom) for the second selected case of turning wind. The wind speed data (taken at 4 meters) represent 8.5 minutes averages every hour.

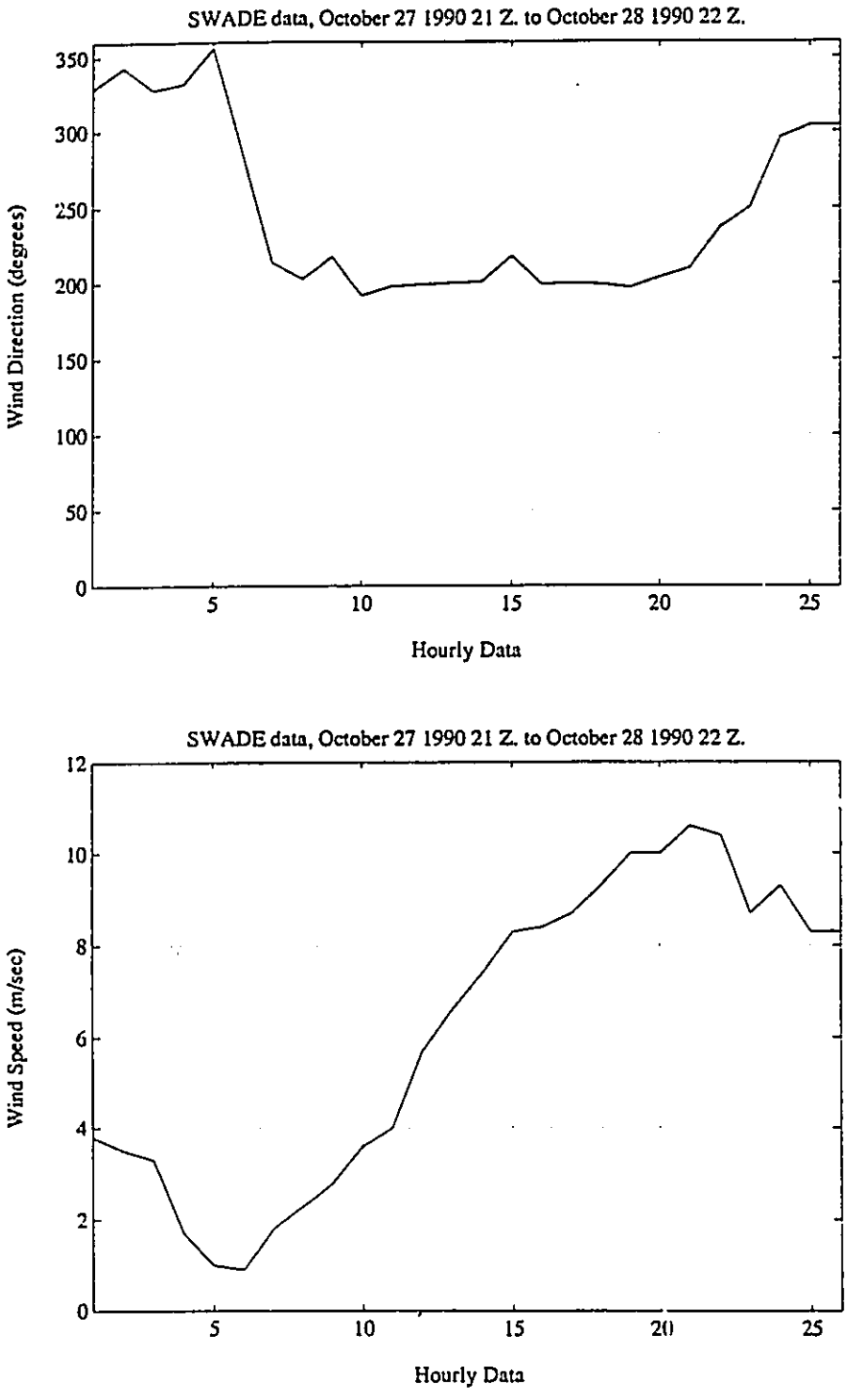

Fig.10.5 Time series of wind direction (top) and wind speed (bottom) for the third selected case of turning wind. The wind speed data (taken at 4 meters) represent 8.5 minutes averages every hour.

information on all three selected cases and Figures 10.3, 10.4 and 10.5 display the wind history for all three cases. These three cases were selected because they all presented different characteristics. The first case (C1) represents a wind turning over 200° at a roughly constant angular speed over the entire period of 48 hours. The second case (C2) depicts a wind turning by about 120° over an 8 hours period. Finally the third case (C3) represents a more complex situation with the wind rapidly shifting from 330° to 200° in less than three hours, build up momentum from that direction for about 13 hours and rapidly shifts again from 200° to 300°. The wind is roughly constant only for the second case. Missing data were interpolated in order to allow easy contouring of regularly spaced data.

10.3.2.a Case 1: General observations

Figure 10.6 presents a contour plot of the evolution of the frequency spectrum over the 48 hours period. The main feature of this case is the arrival of a swell in the area at around the 22 hours mark. The evolution of the directional spectrum at a frequency of 0.1 *Hz*, which is the frequency of the swell, is shown in Figure 10.7. The Figure shows that the swell, coming from about 130°, is largely unaffected by the relatively weak winds (3-4 m/sec). Nevertheless, the angular distribution of energy is observed to be slightly skewed toward the wind. A similar plot is presented in Figure 10.8 for a frequency of 0.15 *Hz*. The Figure presents the evolution of the directional spectrum normalized to unity, thus becoming a plot of the spreading function at this given frequency. The wind direction is presented by the superposed continuous solid line. It can be seen from this Figure that the wave direction essentially coincides with the wind direction until about 24 hours, at which time the swell, with energy in the same frequency band, creates a bimodality in the energy distribution. The wind sea energy still propagates with the wind until its

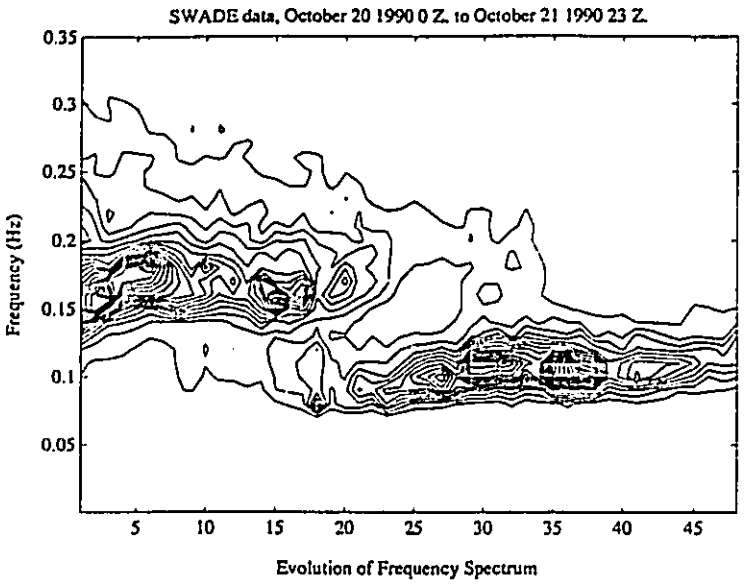

Fig.10.6 Evolution of the frequency spectrum over the October 20-21 period. Contours are equally spaced from maximum energy to zero energy.

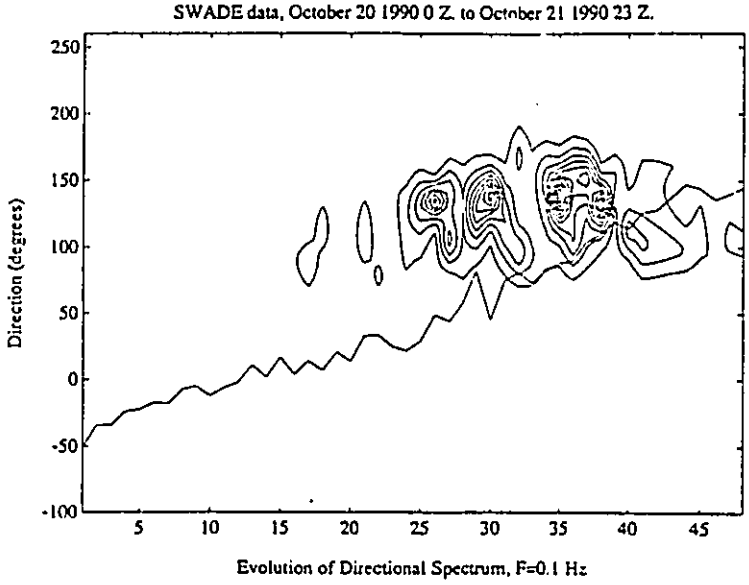

Fig.10.7 Evolution of the directional spectrum at $f = 0.1\ Hz$ over the October 20-21 period. Contours are equally spaced from maximum energy to zero energy. Solid line represents the wind direction.

direction coincides with the swell, at which point both systems coalesce. Figure 10.9 gives results for a frequency of 0.2 *Hz*. The wave direction in that frequency band coincides with the wind direction until the arrival of the swell (the swell has little or no energy in this frequency band), at which point the waves turn to be initially aligned perpendicular to the incoming swell. The same behavior is also expressed at higher frequencies, as shown in Figure 10.10, which presents the mean wave direction at discrete frequencies of 0.1, 0.15, 0.2, 0.25, 0.3 and 0.35 Hz, plotted with the wind direction. The mean direction θ_m is defined following Kuik, Van Vledder and Holthuijsen (1988) as the vectorial mean of the directional distribution which can also be expressed in terms of the first Fourier coefficients:

$$\theta_m(f) = atan\left[\frac{\int_0^{2\pi} \sin\theta\, D(\theta) d\theta}{\int_0^{2\pi} \cos\theta\, D(\theta) d\theta}\right] = atan\frac{b_1}{a_1} \qquad (10.2)$$

Figure 10.10 essentially summarizes all of the above results. During the first 25 hours, wave energy contained in frequency bands greater than about 1 *Hz*, follow the slowly turning wind. The energy distributions are unimodal as the sea smoothly adjusts to the turning wind. Immediately following the arrival of the swell, higher frequency waves turn away from the wind to align perpendicularly to the swell. From this point, they roughly keep a constant, frequency dependent angle to the wind direction. This angle tends to be smaller at higher frequencies.

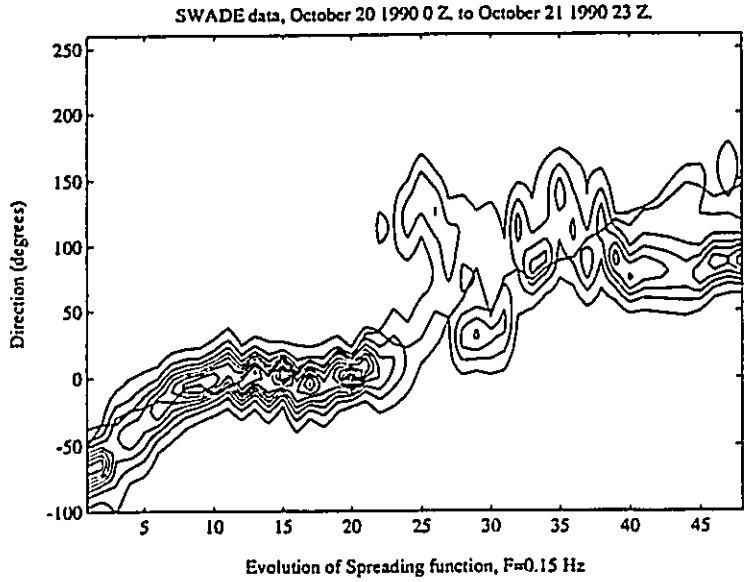

Fig.10.8 Evolution of the normalized directional spectrum (spreading function) at $f = 0.15\ Hz$ over the October 20-21 period. Contours are equally spaced from maximum energy to zero energy. Solid line represents the wind direction.

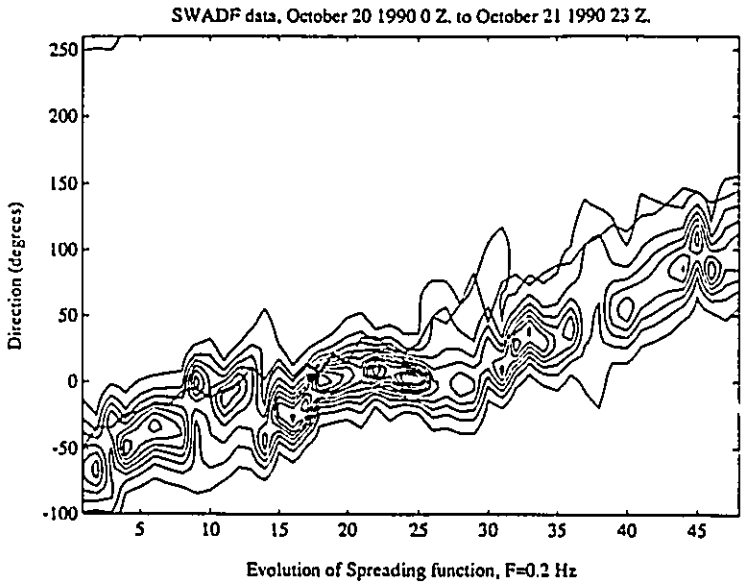

Fig.10.9 Evolution of the normalized directional spectrum (spreading function) at $f = 0.15\ Hz$ over the October 20-21 period. Contours are equally spaced from maximum energy to zero energy. Solid line represents the wind direction.

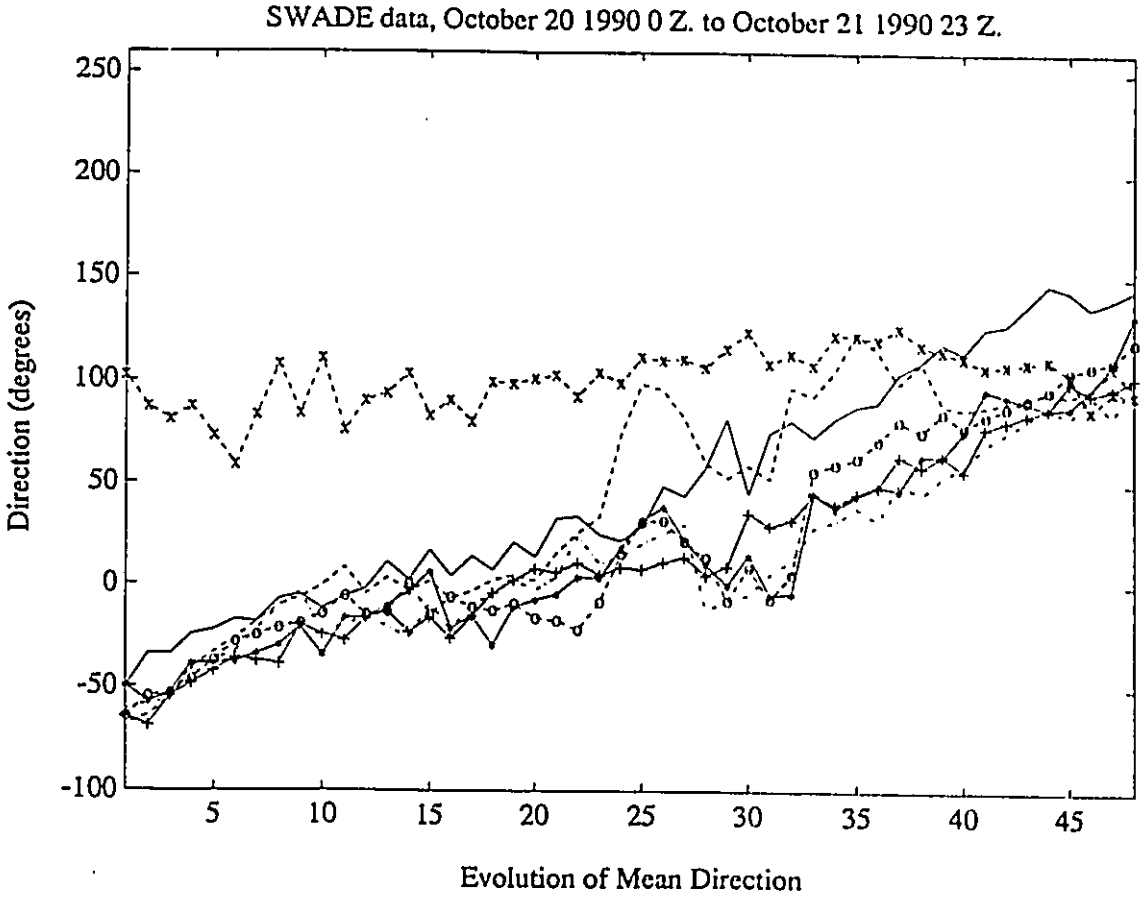

Fig.10.10 Evolution of the mean wave direction for various frequency bands, over the October 20-21 period. _____ Wind direction -x-x-x- 0.1 Hz - - - 0.15 Hz -+-+- 0.2 Hz _.-.-.- 0.25 Hz -*-*-*- 0.3 Hz -o-o-o- 0.35 Hz.

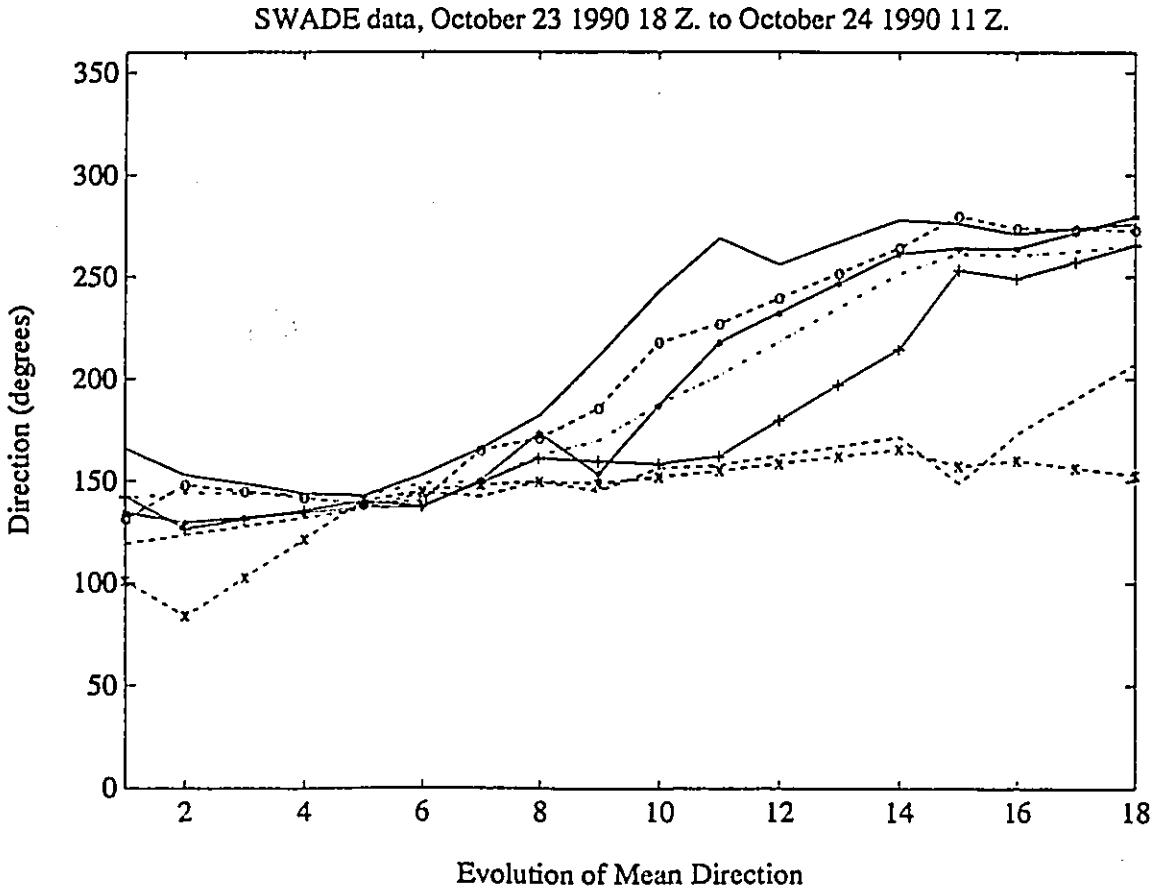

Fig.10.11 Evolution of the mean wave direction for various frequency bands, over the October 23-24 period. _____ Wind direction -x-x-x- 0.1 Hz - - - 0.15 Hz -+-+-+- 0.2 Hz _-_-_-_ 0.25 Hz -*-*-*- 0.3 Hz -o-o-o- 0.35 Hz.

10.3.2.b Case 2: General observations

In this second case presented, the wind shifts by about 120° in less than 6 hours, a wind shift gradient considerably higher than in the preceding case. Figure 10.11 presents a plot of the mean wave direction at 6 discrete frequencies, plotted with the wind direction. The plot clearly shows that the higher frequency components adjust quickly to the turning wind whereas the other lower frequency components progressively react slower. Figures 10.12 to 10.15 present the evolution of the wave energy spreading function at respective frequencies of 0.1, 0.15, 0.25 and 0.35 Hz. The 0.1 *Hz* frequency band initially turns very slightly into the wind (Figure 10.12) but then becomes completely decoupled from the wind and behaves separately. The next three frequency bands behave similarly despite the fact that their respective relaxation times are different. The interesting common feature of those higher frequency bands (Figs. 10.13, 10.14, 10.15) can be observed at about 10 hours when the wind shift gradient reaches its maximum. At this point, instead of turning slowly toward the wind as a whole, part of the spectrum energy becomes decoupled from the wind and dissipate on its own, while the rest of the energy turns toward the wind. This effect is more apparent at lower frequencies. Most of the spectrum energy stays coupled with the wind and only bimodal distributions with a smaller secondary peak are created.

10.3.2.c Case 3: General observations

The last case studied involves very high wind shift gradients with winds turning by as much as 150° in less than 3 hours (Fig. 10.5). Figure 10.16 presents a plot of the mean wave direction at 6 discrete frequencies, plotted with the wind direction. From this plot it can be seen that the behavior of the low and high frequency bands seems to be markedly different. The wave field is characterized by a 50° swell resulting from the previous storm (Fig. 10.2). The direction of the

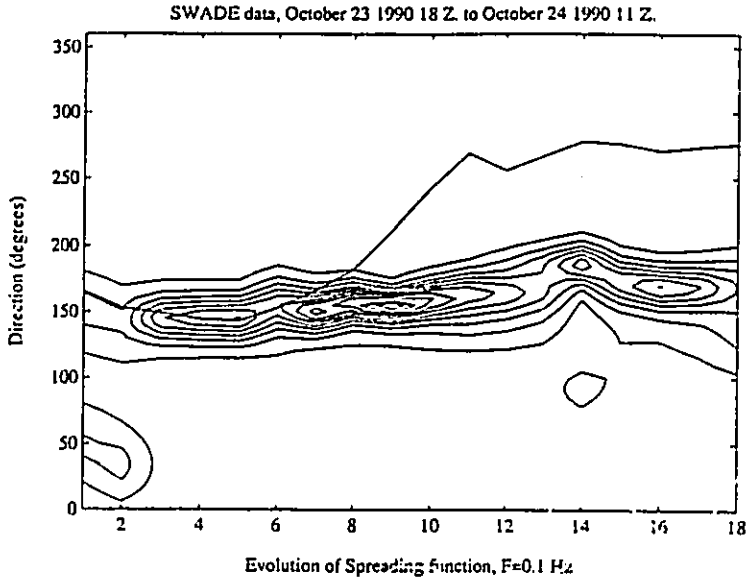

Fig.10.12 Evolution of the normalized directional spectrum (spreading function) at $f = 0.1\ Hz$ over the October 23-24 period. Contours are equally spaced from maximum energy to zero energy. Solid line represents the wind direction.

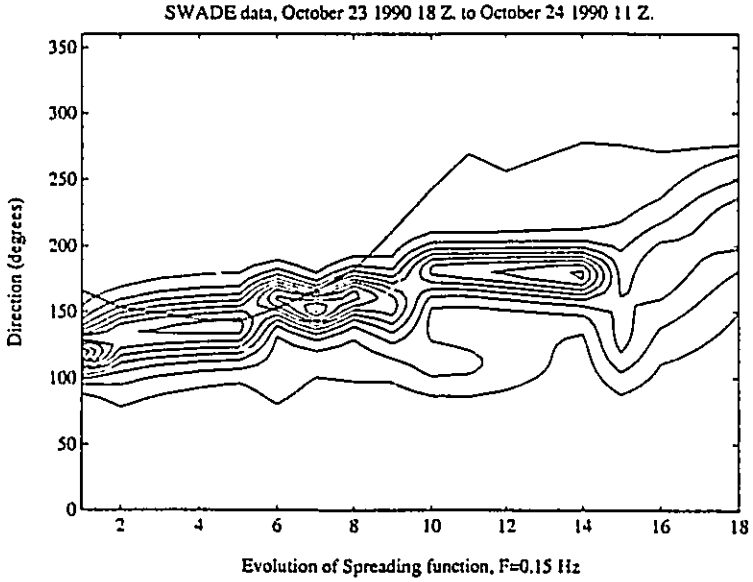

Fig.10.13 Evolution of the normalized directional spectrum (spreading function) at $f = 0.15\ Hz$ over the October 23-24 period. Contours are equally spaced from maximum energy to zero energy. Solid line represents the wind direction.

0.1 *Hz* band is essentially unaffected during the entire 26 hours period. Figures 10.17 to 10.20 present the evolution of the wave energy spreading function at respective frequencies of 0.15, 0.25, 0.3 and 0.35 Hz. Examination of the Figures indicate that the variations in the directional domain are markedly different than the one presented in the previous two cases. After the wind shifted rapidly, the preexisting spectra became essentially decoupled from the wind direction while a new spectrum is generated in the wind direction. The apparent different behavior of the low and high frequency bands observed in Figure 10.16 is simply the results of the incertitude linked to the calculation of a mean wave direction in cases of bimodal distributions. The observed decoupling associated with large wind shifts can create complex distributions of energy. Figures 10.21 and 10.22 give examples of the variation in the directional spectrum at different intervals. Figure 10.21 presents results at three successive hours at a frequency of 0.15 Hz, and clearly shows the old wind sea decaying while the new wind sea is being generated. Figure 10.22 presents similar results at a frequency of 0.35 Hz. Three different modes can be seen, the newly generated sea at 200°, the old sea at roughly 280°, and a third mode at about 60° which probably represents remnant energy from the strong storm that swept the area 30 hours before. In both cases it is clear that all modes behave individually with little or no interaction between them.

10.3.3. Observation of wave directional relaxation

The directional relaxation of waves in turning winds was investigated by Hasselman et al.(1980) with the JONSWAP data, using a simple model defined as:

$$\frac{\partial \theta_m(\omega)}{\partial t} = B\omega \sin(\theta_w - \theta_m(\omega)) \qquad (10.3)$$

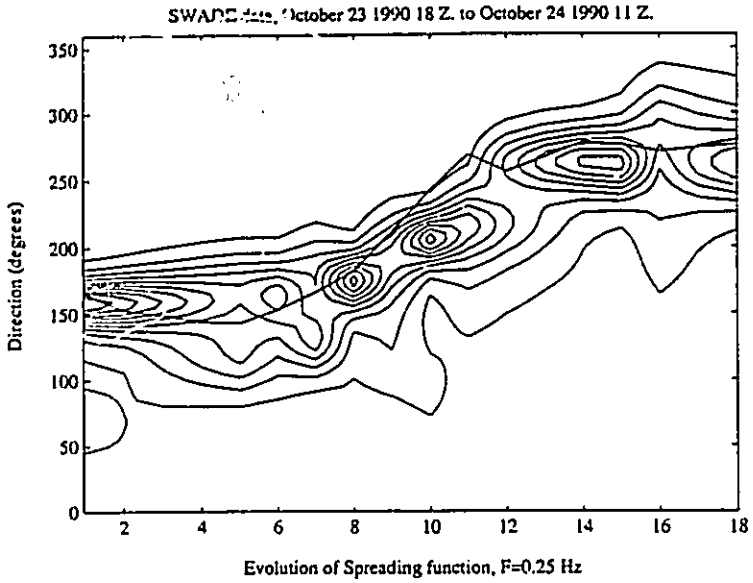

Fig.10.14 Evolution of the normalized directional spectrum (spreading function) at $f = 0.25\ Hz$ over the October 23-24 period. Contours are equally spaced from maximum energy to zero energy. Solid line represents the wind direction.

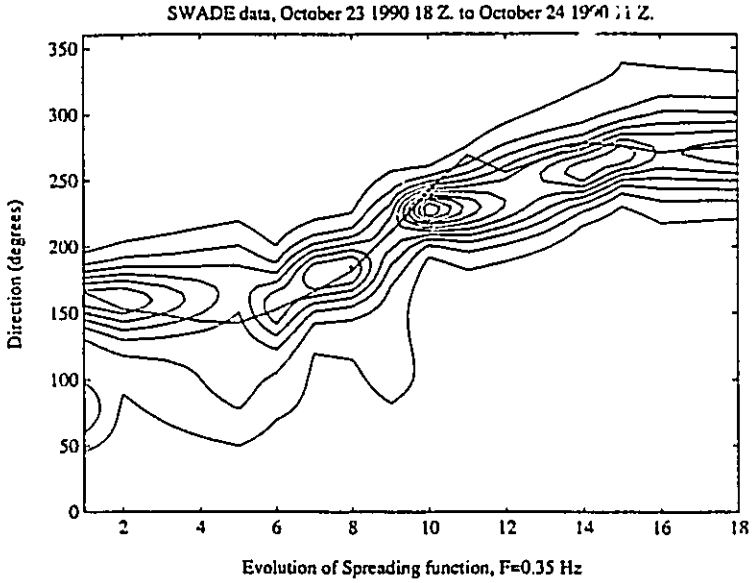

Fig.10.15 Evolution of the normalized directional spectrum (spreading function) at $f = 0.35\ Hz$ over the October 23-24 period. Contours are equally spaced from maximum energy to zero energy. Solid line represents the wind direction.

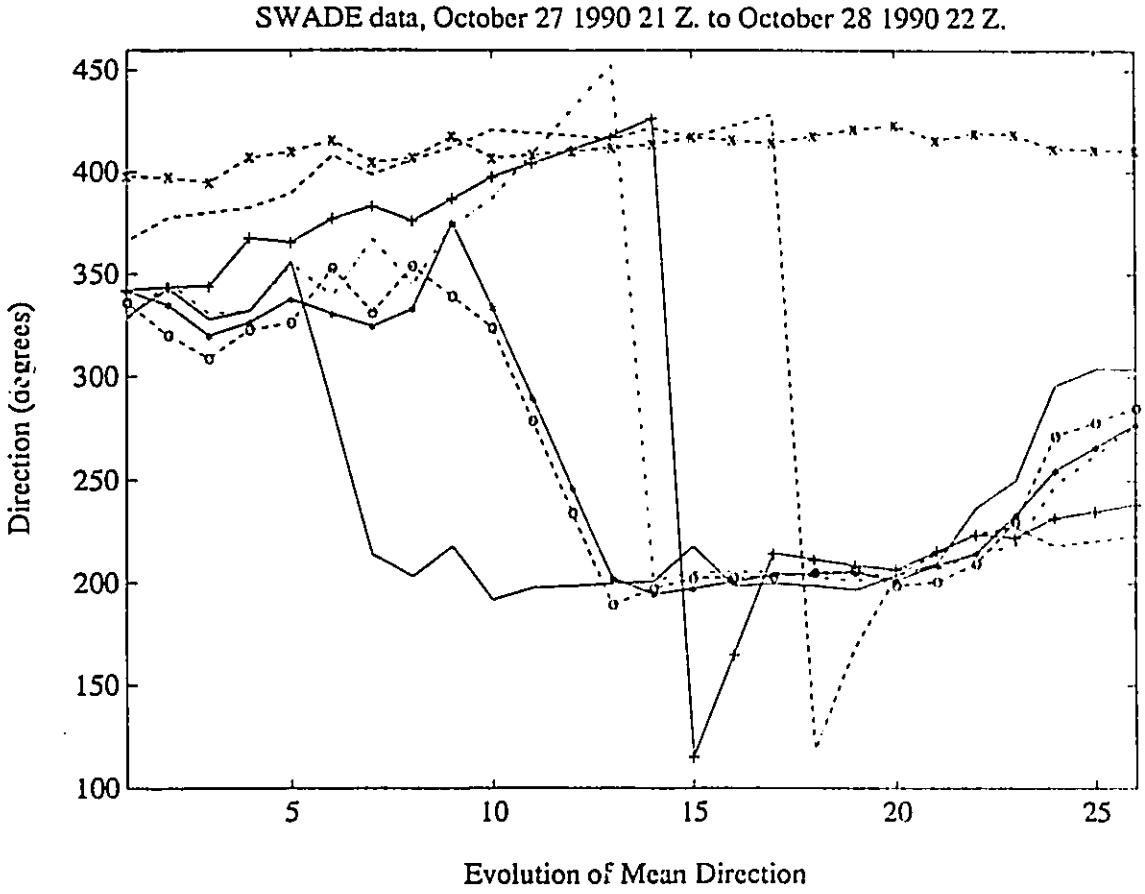

Fig.10.16 Evolution of the mean wave direction for various frequency bands, over the October 27-28 period. _____ Wind direction -x-x-x- 0.1 Hz - - - 0.15 Hz -+-+-+- 0.2 Hz _.-.-.- 0.25 Hz -*-*-*- 0.3 Hz -o-o-o- 0.35 Hz.

where $\theta_m(\omega)$ represent the mean wave direction of a given frequency band, θ_w is the wind direction and B is the relaxation parameter. Allender et al.(1983) slightly modified the form of Eq.(10.2) to include a dependency on the wind speed U_w (measured at 10 meters) such that:

$$\frac{\partial\theta_m(\omega)}{\partial t} = B'\left[\frac{U_w}{c(\omega)}\right]\omega\sin(\theta_w - \theta_m(\omega)) \tag{10.4}$$

with

$$B = B'\left[\frac{U_w}{c(\omega)}\right] \tag{10.5}$$

and the phase speed

$$c = \frac{g}{\omega} \tag{10.6}$$

In order to compute values of Eq. 10.3 and to allow comparison with previously published data, the wind measurements were transformed to their 10 meters value using a logarithmic velocity profile, Charnock's (1955) relationship and assuming neutral stability. To evaluate the derivative $\partial\theta_m(\omega)/\partial t$, a central difference scheme was used for all data excepts at the end points where forward and backward difference schemes were used.

The left $(\partial\theta_m(\omega)/\partial t)$ and right-hand $(\omega\sin(\theta_w - \theta_m(\omega)))$ sides of Eq.10.3 were computed for all frequency bands in all three cases, and correlation coefficients were calculated. Figures 10.23 and 10.24 present a plot of the correlation coefficient at each frequency for cases 1 and 3. Eq. 10.3 was modeled using both the mean and peak direction of the energy distribution. It can be seen that for both cases, correlation coefficients are close to zero and no frequency dependent trend can be observed. Negative correlation coefficients are also observed.

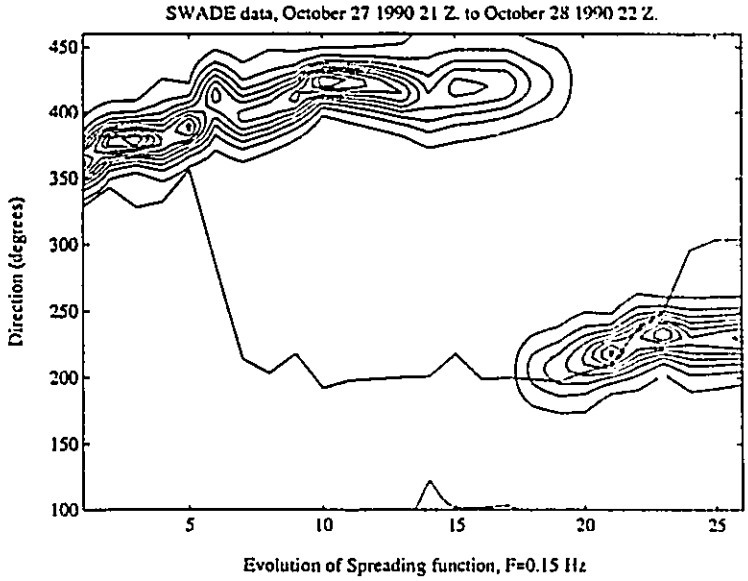

Fig.10.17 Evolution of the normalized directional spectrum (spreading function) at $f = 0.15\ Hz$ over the October 27-28 period. Contours are equally spaced from maximum energy to zero energy. Solid line represents the wind direction.

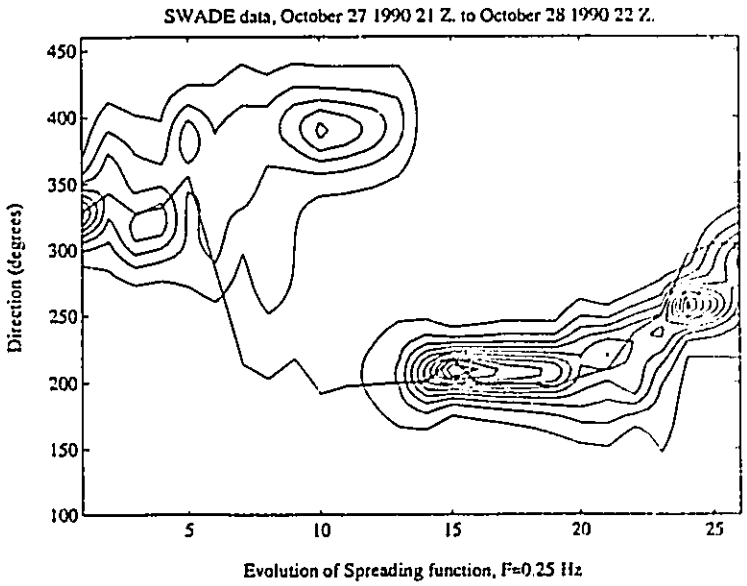

Fig.10.18 Evolution of the normalized directional spectrum (spreading function) at $f = 0.25\ Hz$ over the October 27-28 period. Contours are equally spaced from maximum energy to zero energy. Solid line represents the wind direction.

Figure 10.25 presents a similar plot for the second studied case. In this case, positive correlation coefficients are observed at all frequencies. The results can be seen to be significantly better when the mean direction is used as opposed to the peak direction. The correlation being significant, a one parameter regression was computed at each frequency in order to evaluate the relaxation parameter B (the proportionality coefficient). The results presented in Fig. 10.26 indicate that not only the regression gets better with frequency, the computed relaxation coefficient B gets larger with frequency, but seems to level off. In order to allow comparison with previously published data, results from case 2 were grouped in different U_w/c ranges. Table 2 presents a compilation of previous results and results presented in this chapter. The correlation coefficients obtained in this study are higher than all previous studies, especially for higher values of U_w/c.

10.4. DISCUSSION OF RESULTS

10.4.1. Case 1

This case illustrates that for sufficiently slowly turning winds, the directional spectrum adjusts very smoothly as to more or less follow the wind (Figure 10.10). The wind turns at a constant rate and in such a case, the wave energy adjustment does not display any frequency dependent trends (the relaxation rate is the same at all studied frequencies). The arrival of the swell illustrates the dramatic effect it can have on a wind sea. Low frequency swell components are little affected by the local wind whereas a definite interaction between swell and wind sea energy is observed.

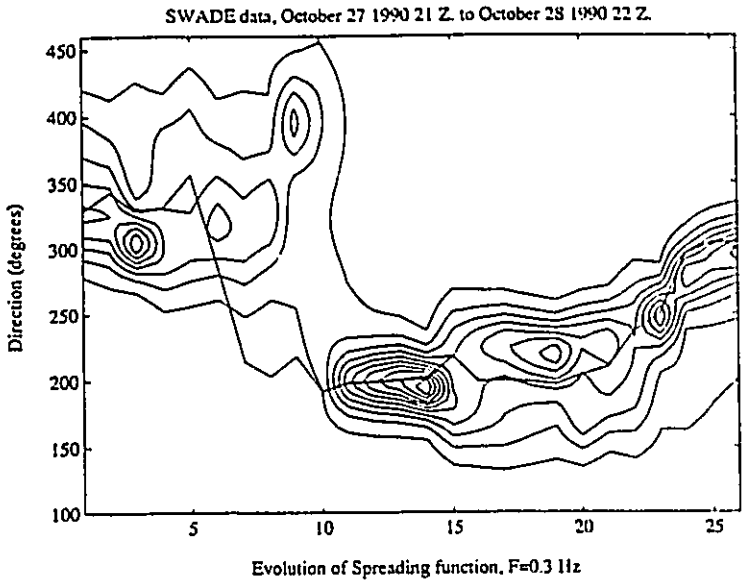

Fig.10.19 Evolution of the normalized directional spectrum (spreading function) at $f = 0.30\ Hz$ over the October 27-28 period. Contours are equally spaced from maximum energy to zero energy. Solid line represents the wind direction.

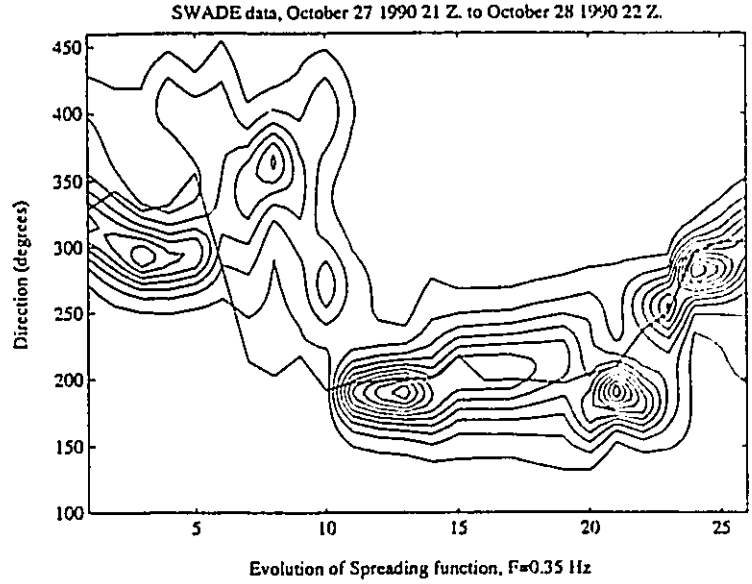

Fig.10.20 Evolution of the normalized directional spectrum (spreading function) at $f = 0.35\ Hz$ over the October 27-28 period. Contours are equally spaced from maximum energy to zero energy. Solid line represents the wind direction.

The tendency of higher frequency waves to align perpendicular to the swell in the early stage of its arrival is surprising. It is generally thought that interactions with a swell would have a tendency to align the wave field in the swell direction (Hasselman et al., 1980). The experimental evidence presented in this case seems to indicate that (for at least sufficiently different wind and swell directions) the wave generating component of the wind will tend to be perpendicularly aligned to the swell direction of propagation.

10.4.2. Case 2

This second case shows very nicely the difference in relaxation time for the various frequency bands. The most interesting feature of this case is clearly the decoupling of part of the spectrum when the wind starts to rapidly turn. Young et al.(1987) computationally examined the response of a wave spectrum to sudden changes in wind direction using two spectral energy balance models, the EXACT-NL model and the 3G-WAM model. Both models used the energy balance equation

$$\frac{\partial S(f,\theta,\vec{x},t)}{\partial t} + c_g \nabla S(f,\theta,\vec{x},t) = S_{in} + S_{nl} + S_{dis} \qquad (10.7)$$

where $S(f,\theta,\vec{x},t)$ is the directional spectrum, c_g the group velocity, and the three terms on the right are the source terms respectively representing the wind input, non-linear wave-wave interaction and dissipation. The two models differed only at the non-linear wave-wave interaction level, the EXACT-NL model using the exact representation of the non-linear transfer, whereas the 3G-WAM used a discrete approximation of the transfer. Both models gave similar results as they investigated sudden changes in the wind direction ranging from 30° to 180°. They found that for wind shifts smaller than 60°, the entire spectrum would adjust gradually to the new

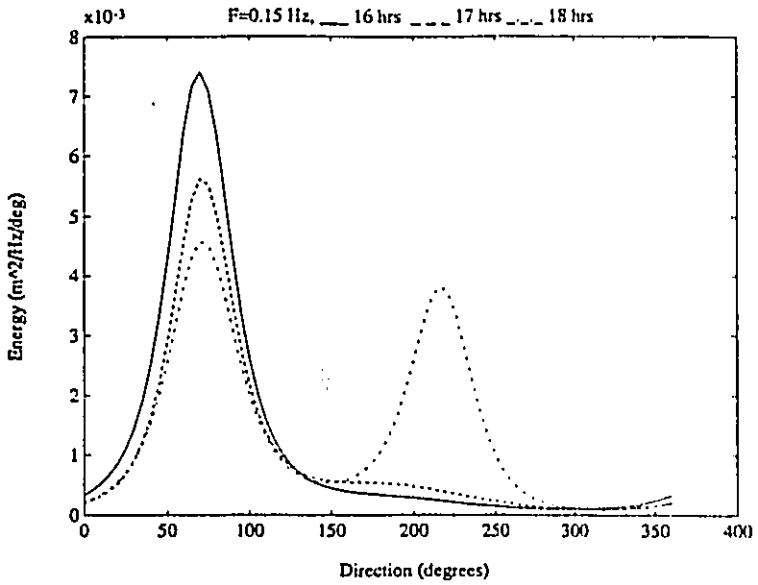

Fig.10.21 Directional spectrum estimate at a frequency of 0.15 Hz for three successive hours during the October 27-28 period.

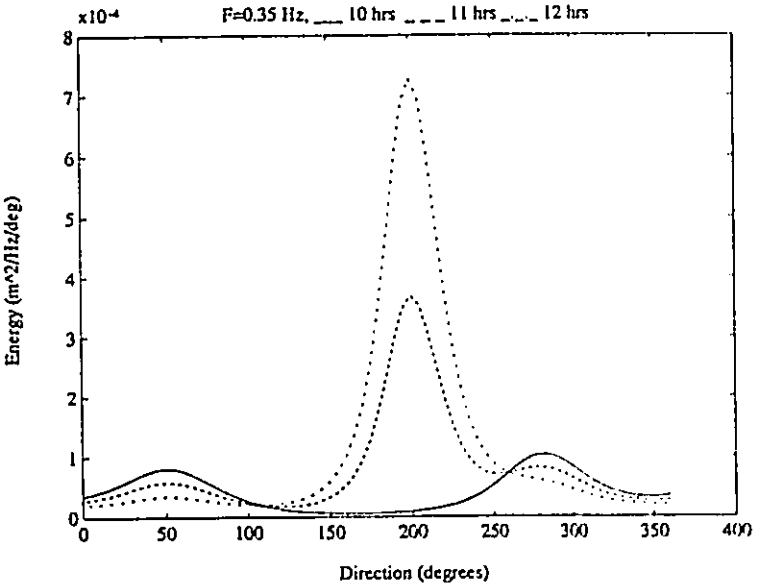

Fig.10.22 Directional spectrum estimate at a frequency of 0.35 Hz for three successive hours during the October 27-28 period.

wind direction, high frequency components first, then lower frequency components. For wind shifts higher than 60°, they found that a new wind sea was generated with the old sea gradually decaying into swell. To our knowledge, this has not been observed yet in field data. The minor decoupling observed in this second case might just be the representation of the onset of the phenomenon, the wind shift gradient being not quite large enough to initiate a full decoupling of the spectrum.

10.4.3. Case 3

This last case pushed the analysis undertaken in the preceding case one step further by looking at even higher turning wind gradients. Results from this directional analysis confirm for the first time the work of Young et al.(1987). For sufficiently high wind shift gradients, a new spectrum will be generated while the old wind sea will decay. This was observed at all frequencies in the 0.15 to 0.35 Hz range. As explained by Young et al.(1987), following an examination of the source terms within their simulations, if the wind shift does not exceed 60°, the non-linear wave-wave interactions prevent the growth of a high-frequency secondary peak aligned with the wind, by coupling the peak to the already existing more stable unimodal distribution. For higher wind shifts, the newly generated high-frequency peak is far away enough from the prevailing spectrum, so that the non-linear wave-wave interactions become too small to couple the new high frequency peak with the existing spectrum.

10.4.4. Wave directional relaxation

The simple relaxation model of Hasselman et al.(1980) presented in Eq. 10.3 was applied to all three cases of turning winds. Correlation coefficients were found to be essentially

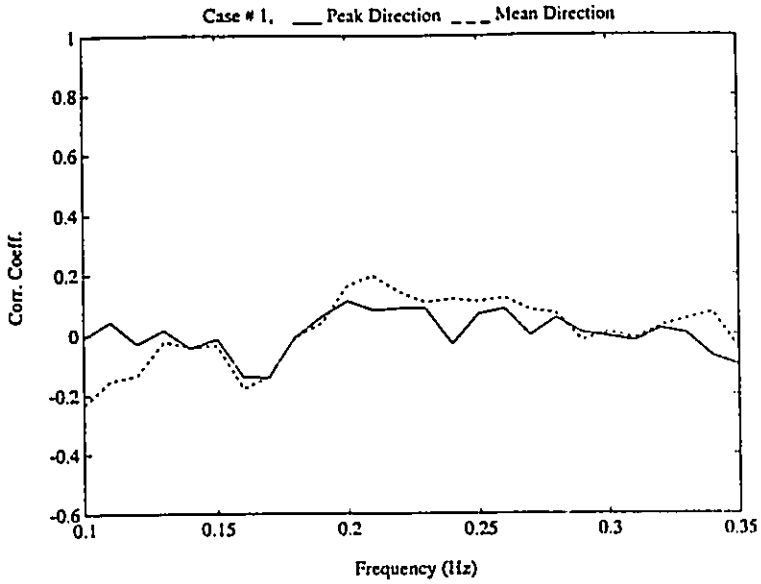

Fig.10.23 Correlation coefficient between the wave shifting gradient ($\partial\theta(\omega)/\partial t$) (for both peak wave and mean wave directions) and $\omega \sin(\theta_w - \theta(\omega))$ (Eq. 10.3), for the October 20-21 period.

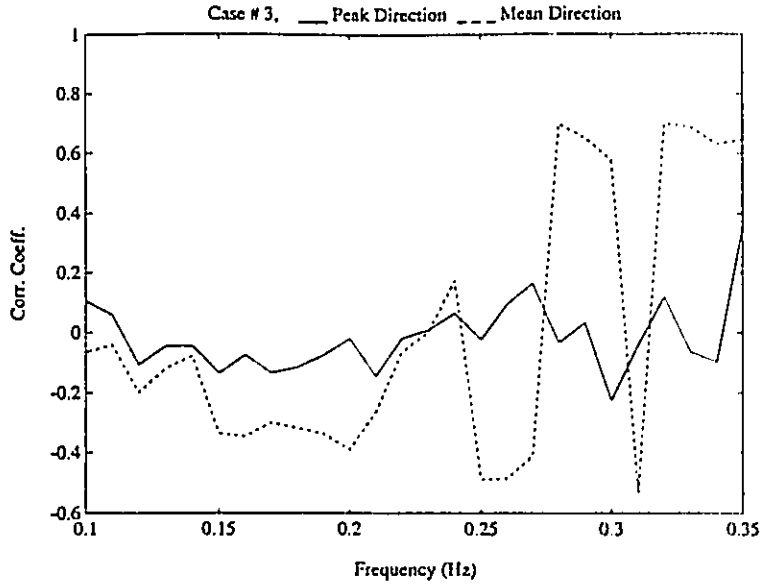

Fig.10.24 Correlation coefficient between the wave shifting gradient ($\partial\theta(\omega)/\partial t$) (for both peak wave and mean wave directions) and $\omega \sin(\theta_w - \theta(\omega))$ (Eq. 10.3), for the October 27-28 period.

zero for cases 1 and 3. This could indicate that the relaxation model is inadequate in explaining the observed response of the wave mean direction, but is probably due to other factors. The behavior of the directional spectrum in case 1 is controlled to a large extent by the arrival of the swell which actually forced the waves away from the wind. This effect probably masked all significant correlations that might have otherwise been measured in the absence of the swell. This points out to the importance of the interaction between swell and wind sea. Equation 10.3 also implicitly assumes that the spectrum reacts smoothly to a change in the wind direction. Thus, the spectral decoupling observed in case 3 is the expression of complex interactions that are beyond any simple relaxation model. The use of Eq. 10.3 to model such cases is not justifiable. Another factor that might blur the results is that in storm conditions such as the one present in late October 1990, the winds are very likely to change rapidly with distance and thus are likely to create waves coming from multi directions which can enter the area of concern and interact with locally generated waves. Finally, in both cases 1 and 3, the wind speed is changing, adding an extra variable to an already complicated picture. Of all the three cases, only case 2 was really fit for use with the relaxation model of Hasselman et al.(1980). It is essentially free of any swell influence (although a swell is present), the wind direction changes are smooth and the wind speed is essentially constant over the duration of the event.

The computational work of Young et al. (1987) predicted a wind dependence in the relaxation rate. This dependence is logically sound and simply implies that higher frequency bands will adjusts more rapidly to changing winds, and the higher the winds, the faster the adjustment. This relationship was never observed before the present study. Results from case 2 show a clear dependence with higher U_w/c values. The results also indicate that the relaxation coefficient B tends to reach a maximum value of roughly 6.3×10^{-5}.

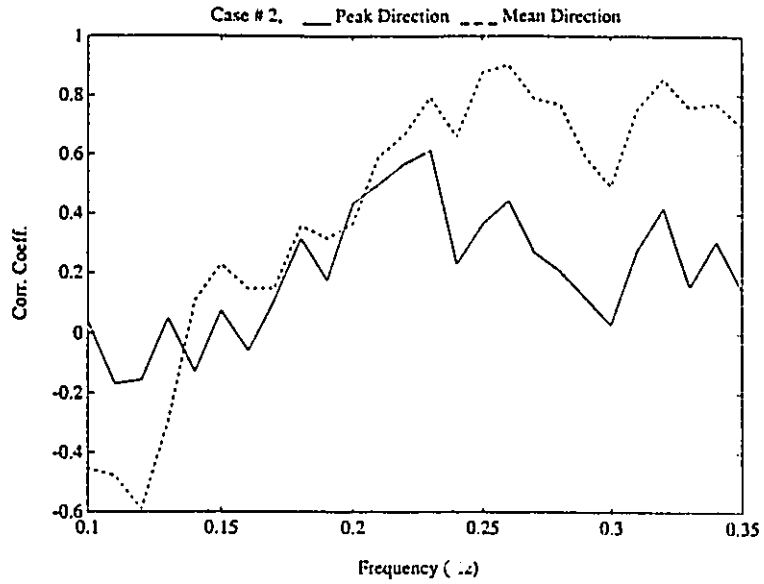

Fig.10.25 Correlation coefficient between the wave shifting gradient $(\partial\theta(\omega)/\partial t)$ (for both peak wave and mean wave directions) and $\omega \sin(\theta_w - \theta(\omega))$ (Eq. 10.3), for the October 23-24 period.

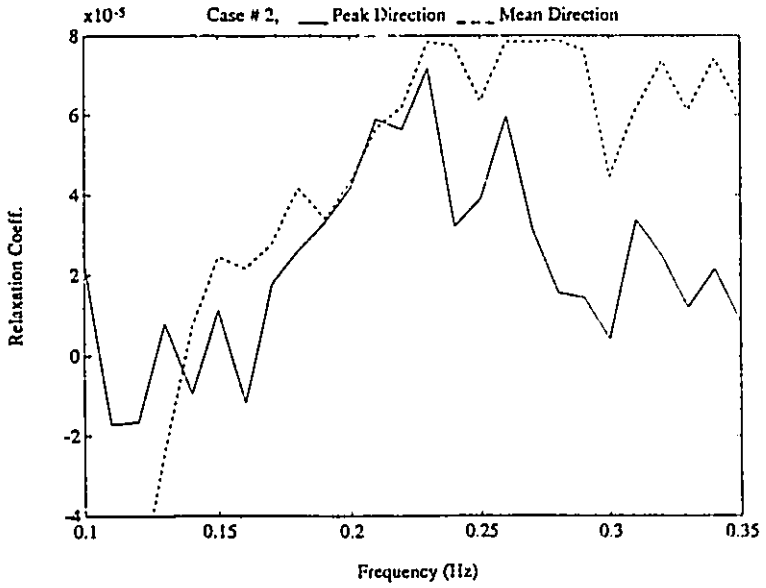

Fig.10.26 Values of relaxation parameter obtained for the October 23-24 period, as a function of frequency.

TABLE 10.2. Reported values of the relaxation parameter

U_w/c	Entries	$B(\times 10^5)$	r	Reference
1.0-1.2	152	2.3	0.40	Masson (1990)
1.2-1.6	256	3.8	0.56	
1.6-2.0	168	2.6	0.51	
1.0-2.0	576	3.1	0.55	
1.6	-	4.3	-	Young et al. (1987) **
2.18	-	11.0	-	
2.56	-	16.0	-	
1.0-1.8	-	4.0	-	
1.1	total	1.3	0.25	Allender et al. (1983)
1.4	of	1.7	0.25	
1.8	126	2.2	0.25	
1.0-1.2	150	1.6	0.29	Hasselman et al. (1980)
1.2-1.6	155	2.4	0.4	
1.6-2.0	126	2.0	0.3	
1.0-1.2	54	2.5	0.18	This Study
1.2-1.6	108	5.1	0.49	
1.6-2.0	126	6.8	0.69	
2.0-2.45	90	6.6	0.77	
1.0-1.8	216	5.2	0.47	
1.0-2.0	288	5.6	0.52	

** Experimental study with the EXACT-NL model with non-linear transfer exactly represented

The higher correlations obtained in this study can be the result of either a better data set or/and better estimation of the wave directional spectrum. Undoubtedly, the SWADE dataset is of high quality and case 2 represents nearly ideal conditions for the study of waves in turning winds but, other studies were also very careful in choosing close to ideal wave records from good datasets (Masson, 1990: CASP; Allender et al., 1983: NOAA data; Hasselman et al., 1980, JONSWAP). The methods of computing the mean wave direction differed. Allender et al.(1983) and Hasselman et al.(1980) (as well as this study) used the first Fourier coefficients obtained from a direct Fourier Transform in order to compute the mean wave direction. This approach, as pointed out by Borgman (1969) is equivalent to calculating the vectorial mean of the directional distribution $D(\theta)$ and is arguably better than treating the directional distribution as a linear one (as done by Masson, 1990), and calculating a mean wave direction which will be necessarily model-dependent, and thus introducing an additional variable in the system. Nevertheless, results from both methods should be similar except for highly skewed distributions, in which case the mean direction obtained by treating the directional distribution as a linear one, will be closer to the peak direction. However, if a good directional estimate is used, the choice of one method or the other to calculate the mean direction should not induce very significant changes in the observed correlations. Obviously, in both methods, the mean wave direction will not be very informative in cases of bimodal distributions. In such cases, there is a definite need to reconstruct the entire directional spectrum, and only high-resolution methods will give a true picture of the phenomena. Also, one should realize that the use of the first Fourier coefficients is justifiable for calculating the mean wave direction but certainly not to reconstruct the whole directional spectrum. Masson (1990) used the IMLM, a method with great resolution potential but subject to problems linked to the iterative scheme. Unless the ρ^2 statistics is computed,

which can demonstrate the successful convergence of the scheme, results from the IMLM should always be interpreted carefully. Even in ideal conditions, the performance of the IMLM is at best, similar to the MLMC (as shown in the previous chapters). Nevertheless, correlation coefficients obtained by Masson (1990) are significantly better than previous studies and comparable to the present study when the [1-2 Hz] range is considered. This is partly due to the fact that in this study, correlations in the low U_w/c range were very low, probably due to the 50° swell at these frequencies. No previous study was able to observe the U_w/c dependency predicted by Young et al.(1987) and seen in this work.

Values of the relaxation parameter B obtained in this study are generally slightly higher than previous studies but comparable especially for $U_w/c < 1.8$, in which case the calculated values agree with the ones obtained from the computational work of Young et al.(1987).

One last point to be raised concerns the effect of interpolated data on the correlation. In order to insure that the interpolation did not affect the correlations, these were recalculated with the missing points and results were found to be unchanged.

10.5. CONCLUSION

The directional spectrum response to turning winds was investigated for three cases of turning winds with various wind shift gradients. For small wind shifts, the spectrum was found to smoothly adjust to the wind changes. As the wind shift gradient increased, a portion of the spectrum energy was found to be decoupled from the wind while the bulk of the spectrum smoothly adjusted to the new wind direction. Finally, for even larger wind shift gradients, the preexisting spectrum was completely decoupled from the wind and decayed separately, as a new spectrum consistent with the wind direction was generated. These results confirm for the first

time the theoretical results of Young et al.(1987), obtained using a third generation wave model.

The relaxation of waves in turning winds was investigated using the model of Hasselman et al.(1980). Correlation coefficients obtained in this study are higher than previously published studies, and for the first time a definite relationship with the wind speed is established. The mean direction of the wavefield was found to be a better parameter than the peak direction to characterize turning waves.

The three cases studied clearly show that a simple relaxation model can only be used in ideal cases, the effect of swell being important in the evolution of wavefields and bimodal seas being very likely to be created in higher wind shift gradients.

The results presented in this Chapter clearly outline the potential of the newly developed corrected form of the Maximum Likelihood Method in studying an understanding the evolution of wavefields. The method even showed the ability to resolve three modes within a single frequency band.

CHAPTER 11

DIRECTIONAL SPECTRA STUDIES IN LAKE ONTARIO

The Canada Centre for Inland Waters (CCIW), in Burlington, Ontario, has operated a research platform on Lake Ontario since 1976. The platform was designed and used to allow air-water interaction research as part of the WAVES (Water Air Vertical Exchange Studies) project. During the 1985 to 1987 period, the "Deep Water Wave Breaking and Wave Turbulence Interaction" project was carried out on the Tower. During the three years period, several wave records were measured under various environmental conditions, using a six-wavestaff array. Following the investigation of SWADE data using a pitch-roll-heave signal, the 1985-1987 Lake Ontario dataset will allow wavestaff data to be used in order to calculate high-resolution wave directional spectrum estimates. The work presented in this Chapter is a brief overview of essentially two topics, the first one dealing with the wave direction of propagation versus the wind direction, and the second one dealing with the shape of the spreading functions. The goal of this overview is not to establish any new empirical relationships but merely an attempt to appraise the potential of high-resolution directional spectrum estimates in tackling the above topics.

11.1. EXPERIMENTAL ARRANGEMENTS

The CCIW Research Tower is seated in 12 meters of water, 1.1 kilometer off a beach at the west end of Lake Ontario near Hamilton (Figure 11.1). Since the Tower was designed with various limnological and air-water exchange process studies in mind, it is equipped with a great variety of instruments and sensors. Details on the instrumental, computational and data acquisition systems can be found in Tsanis and Donelan (1987) and Valdmanis et al.(1989). The wave-measuring instrument consist of six capacitance wavestaffs arranged in a pentagon with one wavestaff at the center (see Figure 6.1). The array spacing is 0.25 *m* and was designed with 0.6 to 8 seconds waves in mind (Tsanis and Donelan, 1989). The Tower position allows fetch lengths from 1.1 km in the west direction up to 300 km from the east.

11.2. FIELD DATA

For the purpose of this chapter three cases were picked and analyzed. Table 11.1 describes the three cases and different runs. The first case is about strong westerly winds, the second case is about slowly turning winds from the east to the north and finally, the last case is about strong winds coming from the east, followed by a rapid shift to strong south-westerly winds. These three cases were chosen to represent various wind conditions in Lake Ontario. Eighteen segments were analyzed for the first case, 21 for the second and 31 for the third case, giving a total of 70 runs.

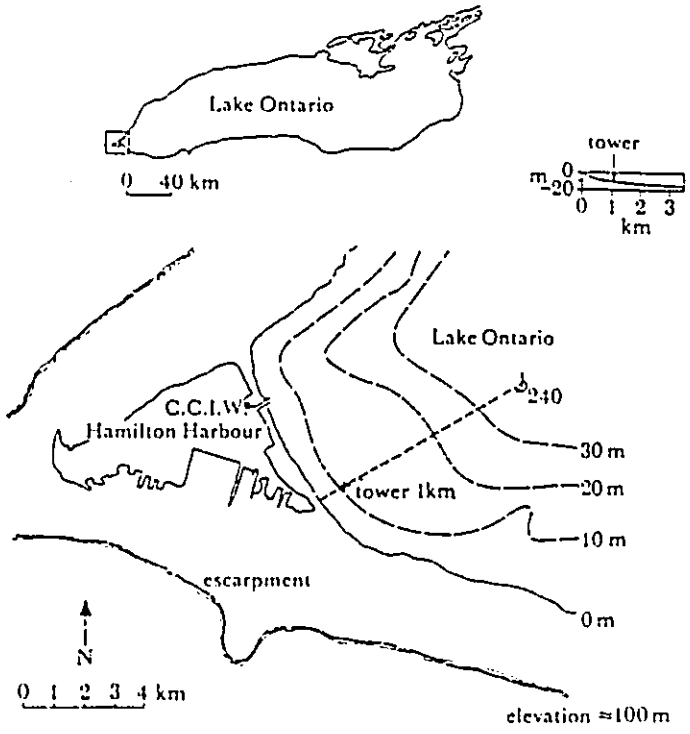

Fig.11.1 Geographic location of the CCIW Research Tower, at the west end of Lake Ontario (from Tsanis and Donelan, 1987).

TABLE 11.1. Lake Ontario Cases selected

Run	segment	Julian date	GMT time	length (min)	U_{12} (m/sec)	Wind dir (deg.)	Wave dir (deg.)
November 4-6 1987							
87016	a	308	21.50	33	6.4	250	241
87017	a,b,c	308	22.54	95	7.0	263	308
87018	a,b,c	309	00.48	95	5.7	248	273
87019	-	309	17.27	10	8.0	274	-
87020	a	309	18.50	21*	10.8	300	328
87021	a,b,c	309	20.27	95	12.0	288	309
87022	a,b,c	309	22.41	95	9.8	301	325
87023	a,b,c	310	01.48	95	11.0	302	316
87024	a	310	04.14	31	6.2	324	328
November 15-16 1987							
87053	a	319	17.40	28*	4.1	67	73
87054	a	319	18.12	32	4.1	63	71
87055	a	319	18.46	40	4.3	51	73
87056	a,b,c	319	20.21	95	4.4	42	67
87057	a	319	22.26	39	3.4	45	67
87058	a,b	319	23.11	58	3.8	46	67
87059	a,b	320	02.58	60	4.0	24	71
87060	a	320	03.59	40	4.0	11	62
87061	a,b,c	320	05.51	95	2.1	15	43
87062	a,b,c	320	07.51	95	2.7	356	45
87063	a	320	11.01	33	1.7	337	43
87064	a,b	320	11.42	58	1.5	350	42
December 15-16 1987							
87185	a,b,c	349	11.54	93.0	14.4	84	73
87186	a	349	13.31	29.0*	15.8	83	67
87187	a,b	349	14.02	48.5	15.7	89	66
87188	a,b	349	14.53	66.0	14.6	82	67
87189	a,b,c	349	16.01	84.0	14.1	84	67
87190	a	349	20.18	35.0	9.5	240	59
87191	a to h	349	20.56	250.0	8.8	233	61
87192	a	350	02.18	38.5	12.5	210	198
87193	a to j	350	04.31	320.0	11.0	219	208

*All segments are 31 min. long (exc. *) giving at least 100 d.o.f*
U_{12} - wind speed at 12 m, Wave direction is mean direction at the peak frequency of segment "a" of each run

11.2.1. Wave Directional Spectrum Estimation

Following the results obtained in the previous chapters, the directional spectrum estimates were computed using heave-pitch-roll equivalent methods. The radial R (in meters) and angular A (degrees) coordinates of the six wave staffs Lake Ontario array are given by:

$$R = [\,0.25 \;\; 0.25 \;\; 0 \;\; 0.25 \;\; 0.25 \;\; 0.25\,] \qquad A = [\,0 \;\; 72 \;\; 0 \;\; 288 \;\; 144 \;\; 216\,] \tag{11.1}$$

The heave pitch and roll signals are calculated using:

$$\eta(t,\vec{x}) = \eta_3 \tag{11.2a}$$

$$\frac{\partial \eta(t,\vec{x})}{\partial x} = 0.5 \left[\frac{\eta_1 - \eta_3}{0.25} + \frac{2\eta_3 - (\eta_5 + \eta_6)}{2 * 0.2023} \right] \tag{11.2b}$$

$$\frac{\partial \eta(t,\vec{x})}{\partial y} = 0.5 \left[\frac{\eta_2 - \eta_4}{2 * 0.2378} + \frac{\eta_5 - \eta_6}{2 * 0.1469} \right] \tag{11.2c}$$

For all runs, IMLM and MLMC estimates were computed and were found to give very similar results except at lower frequencies (typically below about 0.12 Hz) where the MLMC solution started to break down due to errors in the approximated slope signals. This could probably be avoided if, as discussed in Chapter 9, slopes were calculated in a frequency-dependent manner. However, since the IMLM gave similar results and since there is usually little wave energy in Lake Ontario at these frequencies, the scheme presented in Eq.11.2 was used and the IMLM estimate was used in the few cases of low frequency instabilities of the MLMC. For all runs, data was sampled at 20 *Hz*, and 31 minutes long segments (except where indicated in Table 11.1) were used and FFT averaged to a 0.039 *Hz* bandwidth, giving spectral estimates with in excess of 100 degrees of freedom.

11.3. WAVE VS. WIND DIRECTION

It has been shown (Hasselman et al., 1980; Donelan et al., 1985) that the wave direction around the spectral peak will not necessarily coincide with the wind direction in non-stationary or fetch-limited conditions. Based on similarity considerations, Donelan (1980) showed that the waves can be biased toward the longer fetch if the fetch-gradient is large enough to compensate for the smaller generating force of the wind.

The CCIW Research Tower location at the extreme west of Lake Ontario causes very large fetch gradients from various directions. As a result, the mean wave direction is very likely to differ from the wind direction in many cases. As a result, it is necessary to establish the wind/wave direction relationship due to the fetch gradient. In order to do so, the procedure outlined in Bishop and Donelan (1989) was followed (detailed in Chapter 12). The wind vs. wave direction theoretical relationship based on is shown in Fig. 11.2 for the CCIW Research Tower. It can be seen that significant differences between wind and wave directions can be expected for northerly and south-easterly winds, that is when the fetch gradient about the wind direction is large.

11.3.1. Results and discussion

The plots displayed in Figure 11.3 present the wind vs. wave direction relationship for all 70 runs of Table 11.1. The plots present the data with the wave direction at the peak frequency given by its mean, as calculated using Eq.10.2, and using the peak of the angular distribution of energy. The peak frequency was always used to construct these plots, except in 9 runs of case # 2 where the frequency spectrum peak was clearly propagating as a swell. In these cases, since there was no clear demarcation between swell and sea, an arbitrary frequency of 0.3

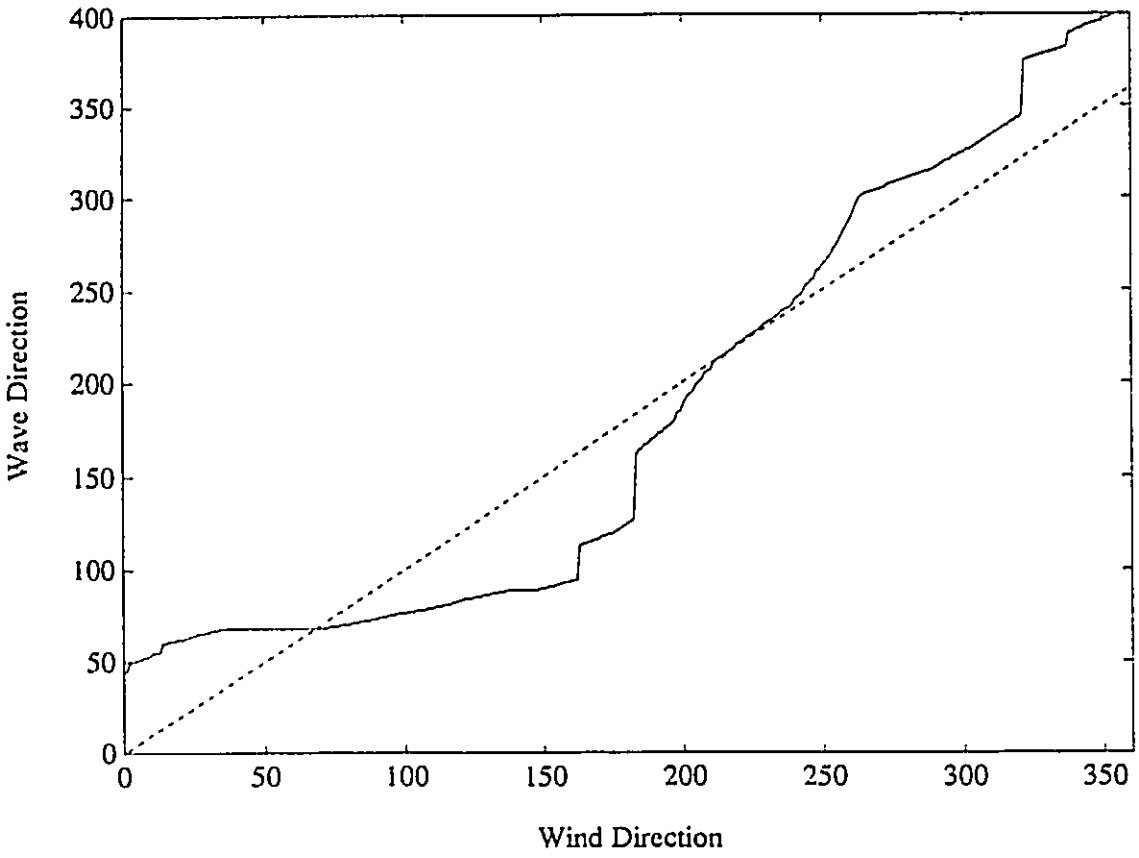

Fig.11.2 Wave vs. Wind direction relationship calculated at the CCIW Research Tower location. The solid line is based on the work of Donelan (1980) and takes into account fetch-gradient effect, whereas the dashed line is the line of perfect agreement.

Hz was used as being more representative of the wind conditions (following a visual inspection of those runs). It can be seen from the plots that both representations of the wave direction of propagation are in good agreement with the similarity-based fetch relationship of Donelan (1980). The mean wave direction representation is seen to produce less scatter than the peak wave representation.

Those results confirm the results obtained for Lake Ontario by Donelan et al.(1985). The agreement is good for all cases, even for all runs of the November 15-16 period, some of which which are not fetch-limited. The reduced scatter obtained using the mean wave direction (compared to the peak wave direction), coupled with results from the previous chapter, indicate that the mean wave direction of propagation better represents the wavefield than the peak wave direction.

In an attempt to further look at the relationship between wind and wave direction, the mean wave direction at the peak frequency for the December 15-16 case was plotted with the wind direction in Fig 11.4. When the wind blows from about 80°, the waves are coming from the longer fetch direction, but consistently 5 to 10 degrees off the theoretically preferred direction. When the wind abruptly switches direction from 80° to about 230°, the swell aligns itself with the preferred direction. This seems to indicate that the wind has an effect in forcing the waves and the resulting effect is a non-symmetrical energy distribution still coming from the longer fetch but slightly skewed toward the wind.

In order to further examine this effect, runs from the November 4-6 period were selected and examined for skewed and bimodal distributions around the spectral peak. The November 4-6 period was chosen because of the strong winds and shorter fetch lengths which probably allowed for greater variability of the directional spectrum. Most runs from that case

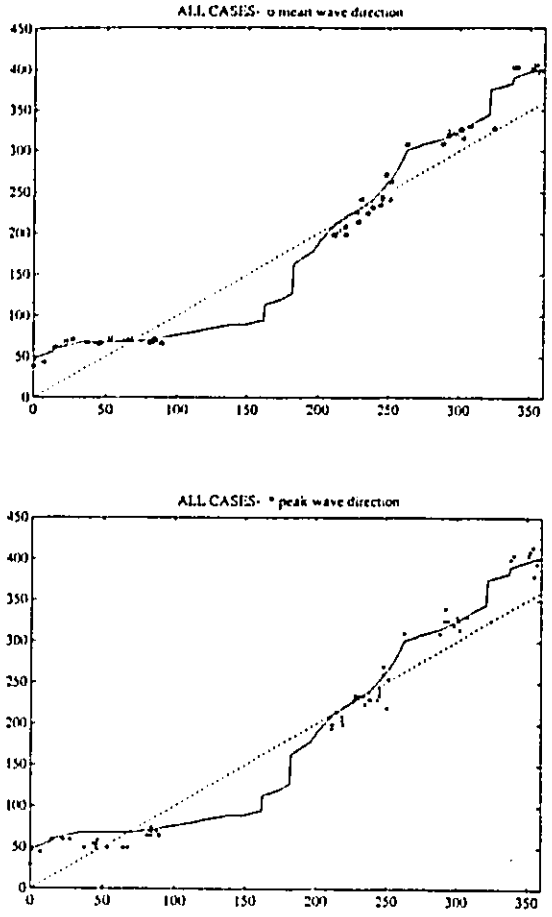

Fig.11.3 Top: Observed mean wave direction (at $f = f_p$) plotted against wind direction for the 70 runs listed in Table 11.1. Bottom: Observed peak wave direction (at $f = f_p$) plotted against wind direction for the 70 runs listed in Table 11.1. The wind direction is given in the horizontal axis and the wave direction in the vertical axis.

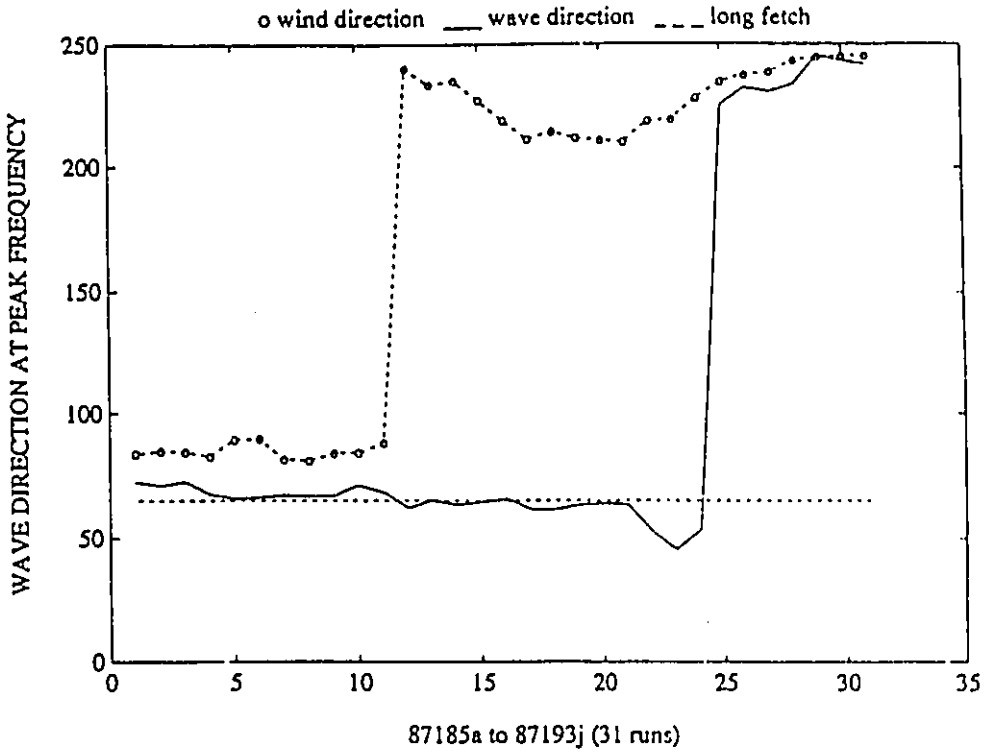

Fig.11.4 Observed mean wave direction (at $f = f_p$) for runs 87185A to 87193J. The solid line is the mean wave direction and the straight dashed line represents the longer fetch preferred direction for easterly winds.

were found to be significantly skewed, although very few were truly bimodal around the spectral peak. For the two runs presented in Table 11.2 (87021B and 87023C), up to two $sech^2$ spreading functions were fitted to the observed energy distribution at four different frequency bands, starting from the band centered at the peak frequency. Results are presented in Table 11.2 as well as in graphical form in Figures 11.5a and 11.5b. In both cases, it can be seen that the energy distribution at the spectral peak is essentially unimodal, and gets more and more skewed as one looks at frequency bands away from the peak frequency. At all frequency bands, the fitted $sech^2$ spreading function reproduce accurately the observed energy distributions, as can be seen from the dashed lines in Figures 11.5a and 11.5b. As seen from the data in Table 11.2, the position of the fitted spreading functions is approximately constant and only the ratio of energy varies. The position of the two fitted functions seems to correspond to the wind direction and the longer fetch direction. This indicates that at the peak frequency, the mean wave direction of propagation is closely approximated by the fetch-relationship of Donelan (1980), but as the frequency increases, more and more energy comes from the wind direction. The only difference between the two presented runs lies in the fact that a larger amount of energy comes from the wind direction in run 87021B, which can be hypothesized to be the result of higher wind forcing compared to run 87023C. If this is the case, then potentially, the partitioning of energy between wind and long-fetch direction could be parametrized. However not all the studied runs displayed the trend observed in Figures 11.5a and 11.5b and clearly, more cases should be analyzed and more work done before definite conclusions can be made.

TABLE 11.2. Energy as a Function of Wind and Fetch

Run 87021B f_p = 0.43 *Hz* U_{12} = 9.8 *m/sec*				
Wind direction = 298° Long fetch direction = 323°				
f	energy percent wind	energy percent long fetch	θ_w	θ_f
0.43	0	100	-	320
0.47	22	88	275	324
0.51	36	64	288	334
0.55	65	35	295	345
Run 87023C f_p = 0.51 *Hz* U_{12} = 7.7 *m/sec*				
Wind direction = 294° Long fetch direction = 320°				
f	energy percent wind	energy percent long fetch	θ_w	θ_f
0.51	0	100	-	325
0.55	6	94	280	325
0.59	12	88	273	325
0.63	14	86	263	325

θ_w and θ_f *respectively refer to the mean direction of the modes linked to the wind and longer fetch directions*

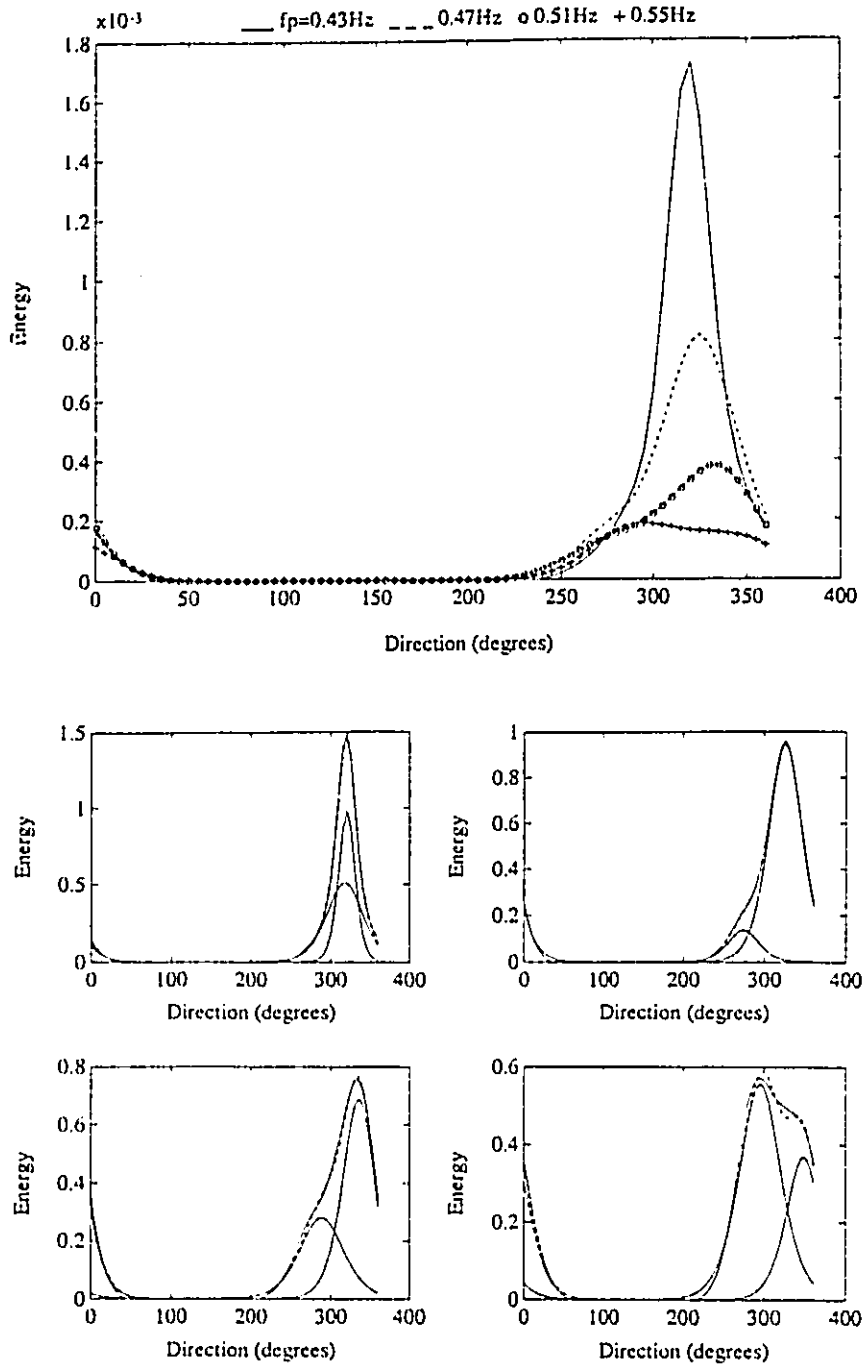

Fig.11.5a Bimodal energy distribution around the spectral peak for run 87021B. Top figure: directional spectrum for all four frequency bands. Bottom figures: separation of energy distribution into unimodal components. The dashed line is the distribution obtained by adding up the two unimodal components.

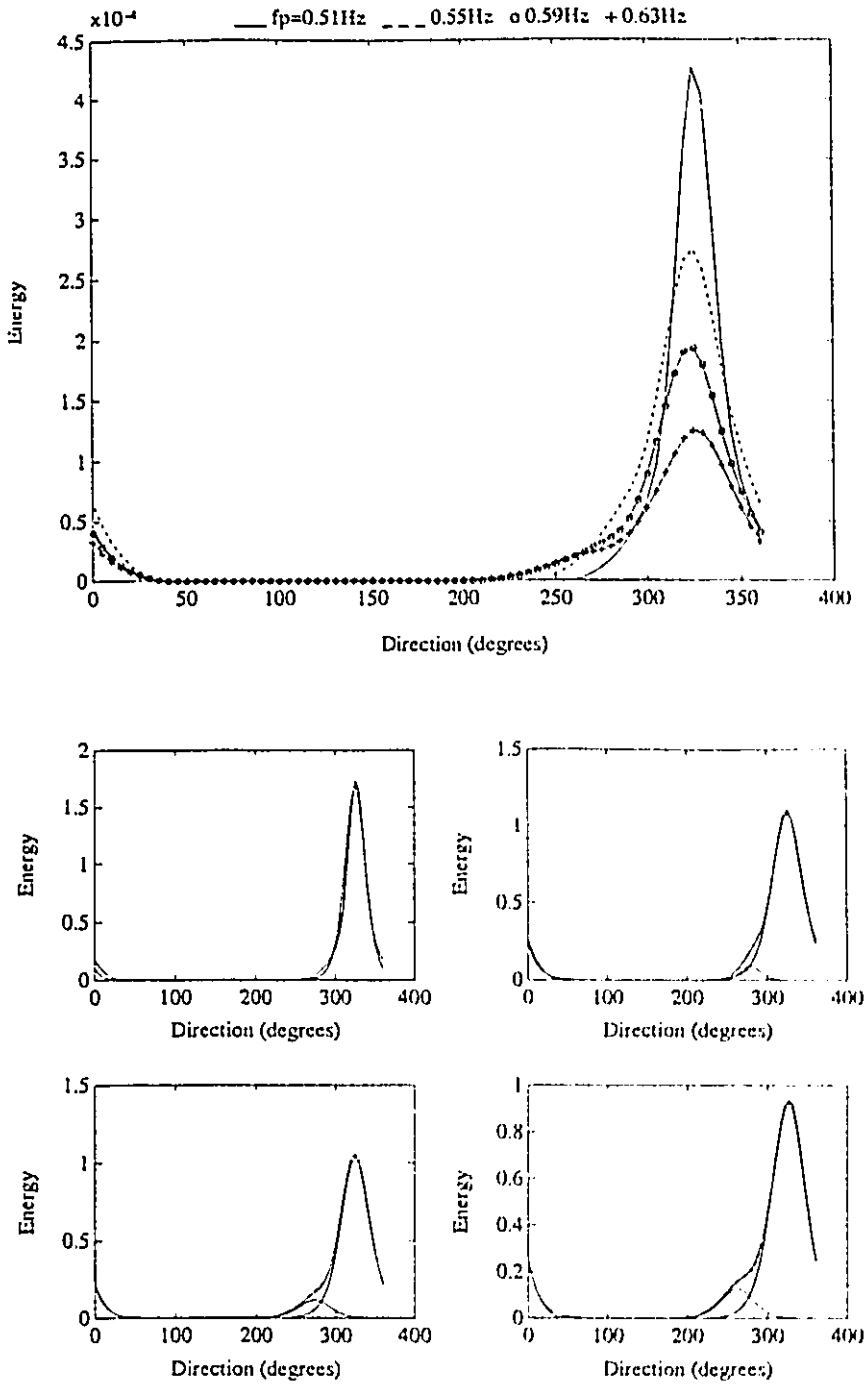

Fig.11.5b Bimodal energy distribution around the spectral peak for run 87023C. Top figure: directional spectrum for all four frequency bands. Bottom figures: separation of energy distribution into unimodal components. The dashed line is the distribution obtained by adding up the two unimodal components.

11.4. VALUES OF THE SPREADING PARAMETER

Few studies have looked at the behavior of the wave directional spectrum. One of the main area of interest consists in finding the best possible form for the spreading function and to establish relationships for the spread of the function for various windfields. A study by Mitsuyatsu et al.(1975) used the $\cos^{2s}$ function to establish empirical relationships for the value of the spreading parameter "s" based on the non-dimensional frequency $\bar{f} = 2\pi f U_{10}/g = U_{10}/C$. Subsequent work by Hasselman et al.(1980) did not support the Mitsuyatsu parametrization and proposed a parametrization in which the peak frequency f_p is the relevant scaling parameter. They still observed an additional dependency on U_{10}/C_p, where C_p is the wave celerity at the peak frequency. Donelan et al.(1985) showed that the dependency on the wind strength and a lot of the scatter could be removed by matching the spreading function to the half-height width of the spectrum. They explained this by arguing that the half-height width was in the energy containing region and thus, less likely to be affected by the noisier part of the spectrum. They also hypothesized that the tails of the directional spread were more influenced by changes in U_{10}/C_p than the peak was. They also found that a $sech^2$ spreading function, based on the work of Hui and Hamilton (1979) and Hui (1980) predicted the peak of the spreading function with more accuracy than the $\cos^{2s}$ spreading function. It should be noted that the 1975 and 1980 studies used the first 2 Fourier coefficients obtained following Longuet-Higgins et al.(1963) in order to obtain values of the spreading parameter "s". The method suffers from several inadequacies and was shown earlier to perform badly for narrow spreading functions. Donelan et al. (1985) recognizing the problem, fitted their estimate to the half-power width of the spectrum, an approach which does not take into account the general form of the spectrum. Therefore, we propose to look at the spreading function using a different approach. Using the IMLM or MLMC

estimates, $sech^2$ spreading functions will be fitted to the observed angular distribution of energy at all energy containing frequency bands. The fitting procedure of up to 2 functions will follow the scheme outlined in Chapter 7. The main advantage is to provide a true best fit based on the entire energy spread and not only on a few parameters. The main disadvantage is that the fit is likely to be influenced by energy tails. This is nevertheless not thought to be a problem and will be further discussed later.

11.4.1. Results

Fifteen runs were selected from each of the three cases presented in Table 11.1. The 15 runs were selected so as to give a wide range of wind speed, direction and peak frequency. The only constraint was that the frequency spectrum be unimodal. The 15 runs are presented in Table 11.3, as well as with runs from the SWADE dataset which will be presented later for comparison purposes. In cases where a well defined swell (in bimodal frequency spectrum) was present, only the wind sea was selected. Figure 11.6 presents the results for all three Lake Ontario cases, and Figure 11.7 presents the same results for all three individual cases. The solid line represents the Donelan et al.(1985) parametrization. Despite the considerable amount of scattering, the general trend is seen to be similar to the Donelan et al. (1985) representation, except that the values of the spreading parameter β are systematically larger and that the β values on the front face of the spectrum fall off much more rapidly with little sign of leveling off. Figure 11.8 presents the β values for all three Lake Ontario cases plotted against the dimensionless frequency U_{10}/C_i, where C_i is the wave celerity at any given frequency. Although the high values of β are only found at low U_{10}/C_i, the scatter is large and no particular trend can be observed from that particular data. In an attempt to isolate other factors controlling the spread of

TABLE 11.3. Cases Selected for Spreading Function Analysis

Run	Julian date	U_{10} (m/sec)	Wind dir (deg.)	f_p (Hz)
November 4-6 1987				
87018a	309	5.6	248	0.78
87018c	309	5.6	244	0.89
87020a	309	10.6	300	0.43
87021c	309	11.5	292	0.47
87023a	310	8.4	302	0.40
November 15-16 1987				
87056a	319	4.3	38	0.23
87056b	319	4.3	46	0.23
87057a	319	3.3	46	0.20
87060a	320	3.9	15	0.20
87061a	320	2.1	7	0.20
December 15-16 1987				
87185a	349	14.2	84	0.20
87189c	349	12.9	88	0.16
87193d	349	10.8	235	0.51
87193f	349	10.8	239	0.51
87193i	350	10.8	245	0.59
SWADE data October 1990				
102119	294	4.6	147	0.11
102121	294	5.1	136	0.12
102123	294	5.3	145	0.12
102206	295	3.32	170	0.11
102212	295	2.89	140	0.12
102601	299	11.5	11	0.16
102606	299	15.8	15	0.14
102612	299	20.1	2	0.11
102621	299	16.7	342	0.09
102701	300	15.9	320	0.08
102707	300	12.2	329	0.08
102721	300	4.1	329	0.08
102906	302	11.2	309	0.15
103006	303	7.6	339	0.14
103012	303	6.8	341	0.08

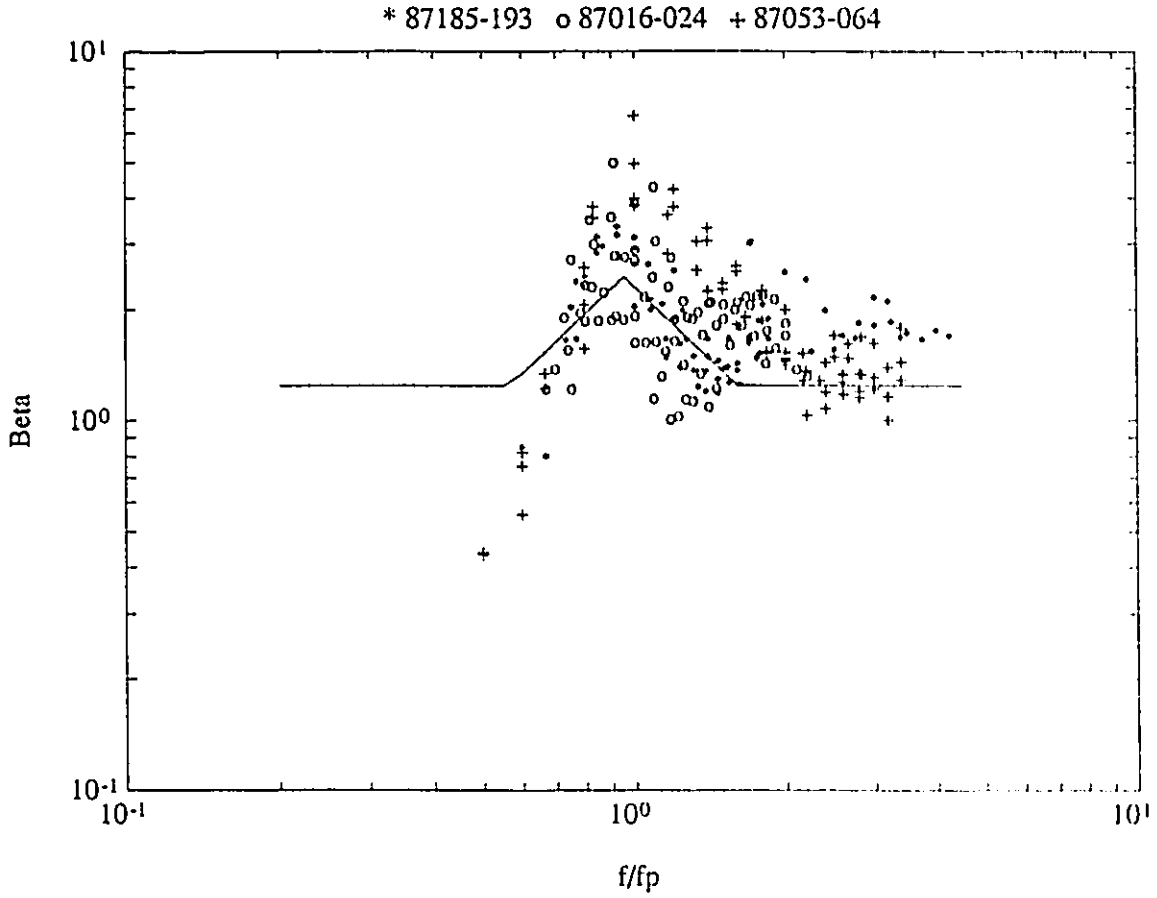

Fig.11.6 Spreading parameter (β) values obtained from fitting $sech^2$ spreading functions to observed energy distribution, for Lake Ontario runs listed in Table 11.3, as a function of relative frequency f/f_p.

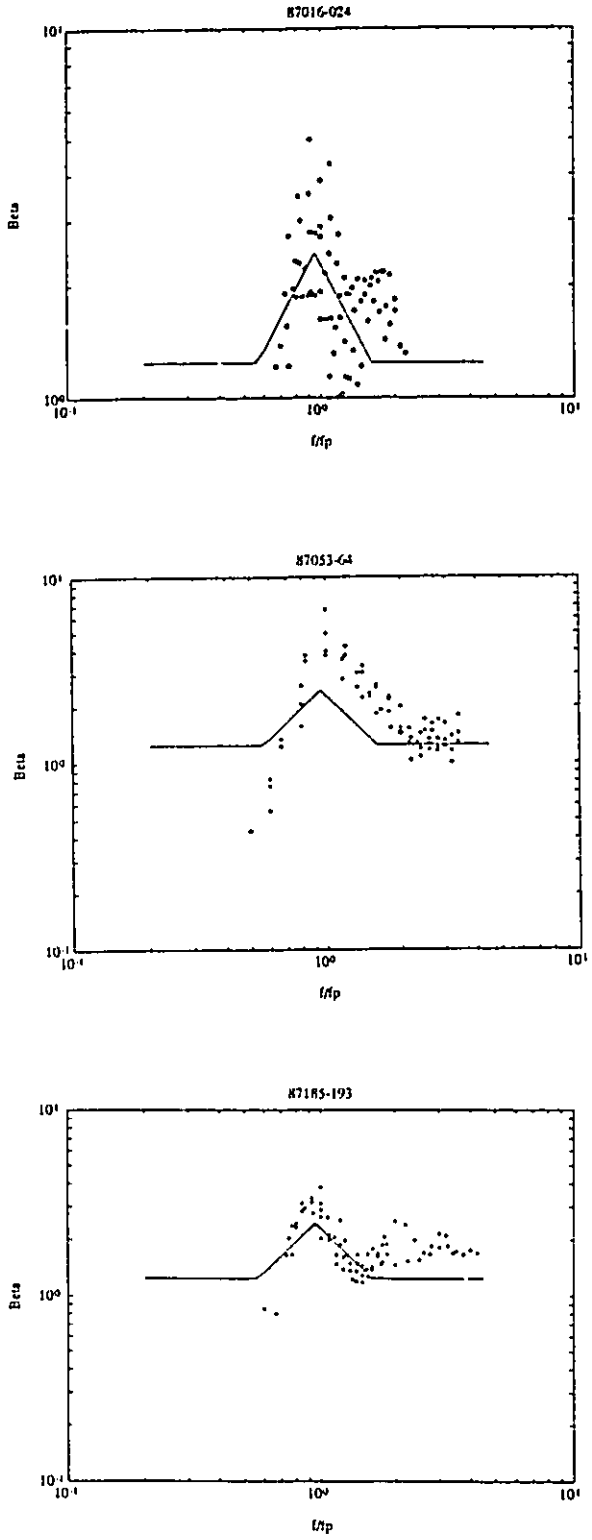

Fig.11.7 Spreading parameter (β) values obtained from fitting $sech^2$ spreading functions to observed energy distribution, for Lake Ontario runs listed in Table 11.3, as a function of relative frequency f/f_p. Top: Case1, Middle: Case2, Bottom: Case3.

energy, the β values at the peak frequency were plotted as a function of their frequency for all 15 runs in Figure 11.9. Despite the few datapoints, a definite linear trend is observed indicating that the energy spread at the peak frequency is likely to be wider at higher frequencies. To further pursue this idea, β values for all 15 runs were normalized to the value at their peak frequency β_p. Results are presented in Figure 11.10 which shows both the direct and normalized schemes. It can be seen that the scatter (although still large) is reduced when data is normalized to β_p. This is especially true in the 1 to 2 (f/f_p) range. Finally, for comparison purposes, a similar analysis was performed for 15 runs of the SWADE experiment. Data was taken from the October storm period discussed in the previous chapter. The 15 selected runs are listed in Table 11.3. Figure 11.11 presents plots for both the SWADE and Lake Ontario data (for comparison purposes). The general trend observed in the SWADE data is similar to what is seen in the Lake Ontario data, in that the observed β values are higher than the Donelan et al.(1985) representation. For the SWADE data, the scatter is larger, β values slightly larger than for Lake Ontario, and the values of β for the front face of the spectrum fall off in a manner more consistent with the Donelan et al.(1985) representation.

11.4.2. Discussion

One of the main feature of the previous plots is the large amount of scatter. As mentioned by Hasselman et al.(1980), the scatter is larger that can be explained by sampling error at over 100 degrees of freedom, and so other parameters must enter into play. Probably, part of the scatter is due to the fitting procedure. Even though the goodness of the fit can be evaluated by simply looking at the error squared or at the magnitude of the residuals, no attempt was made to select "best-fit cases" which would have reduced the scatter, at the expense of

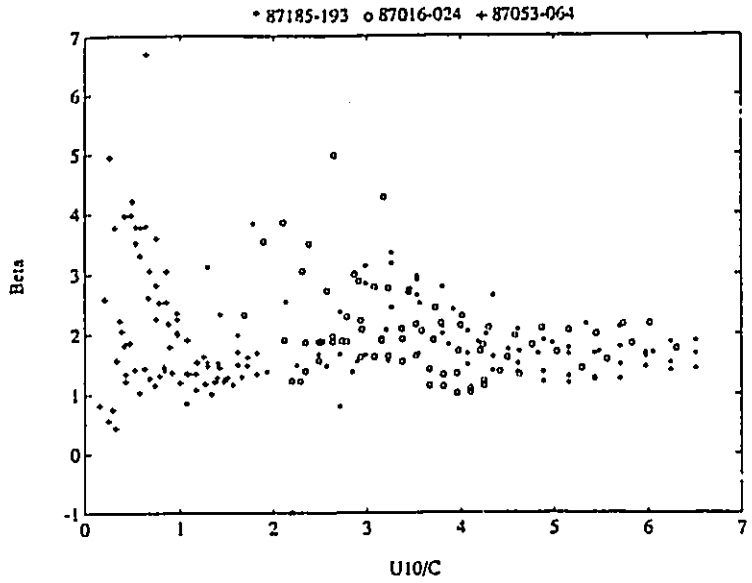

Fig.11.8 Spreading parameter (β) values obtained from fitting $sech^2$ spreading functions to observed energy distribution, for Lake Ontario runs listed in Table 11.3, as a function of U_{10}/C.

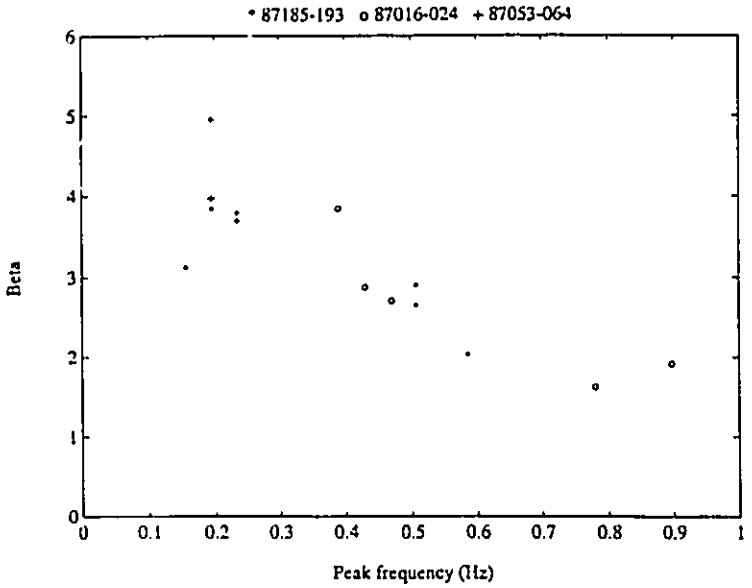

Fig.11.9 Spreading parameter (β) values obtained from fitting $sech^2$ spreading functions to observed energy distribution at the spectral peak f_p, for Lake Ontario runs listed in Table 11.3, as a function of frequency at the spectral peak.

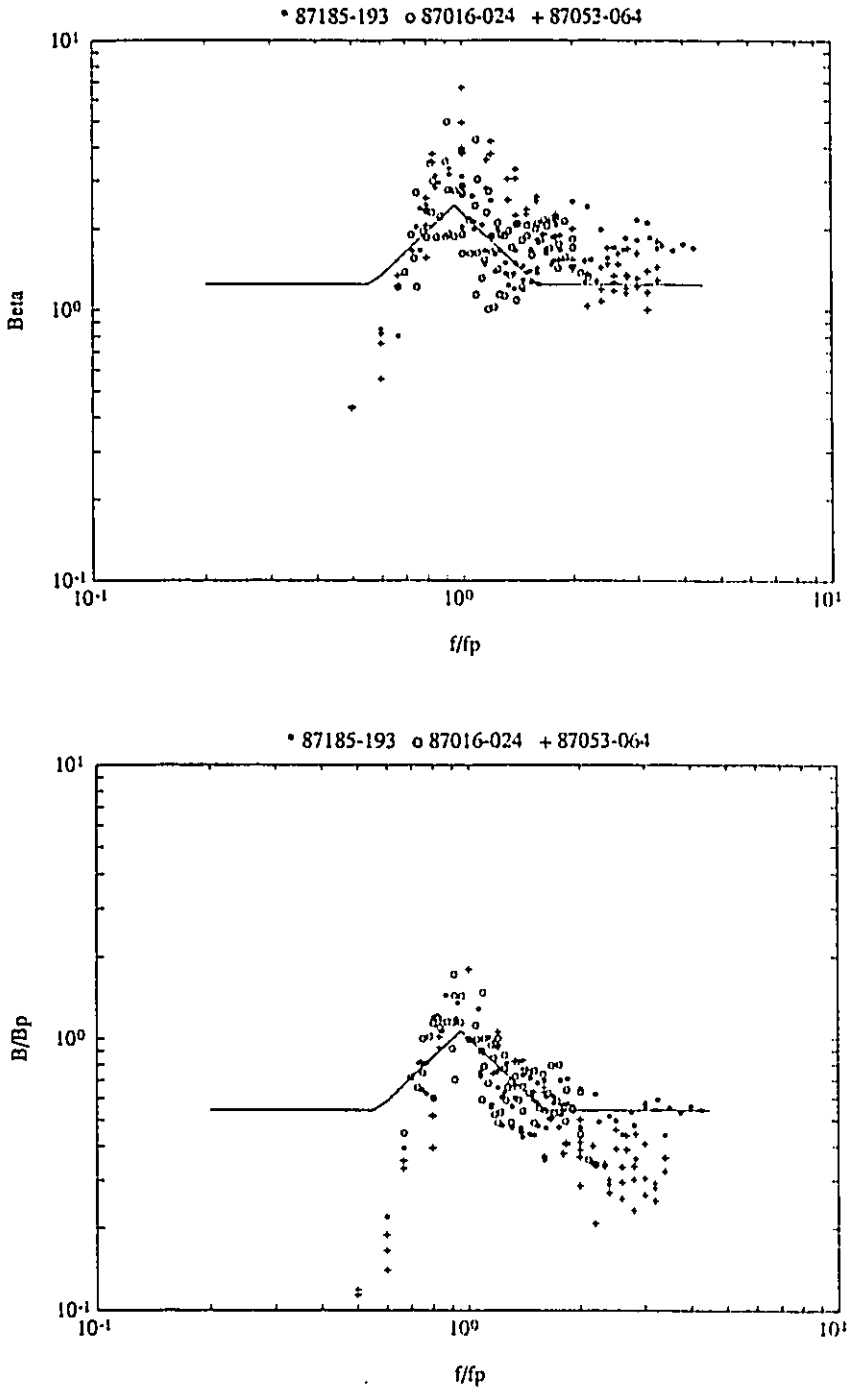

Fig.11.10 Top: Spreading parameter (β) values obtained from fitting $sech^2$ spreading functions to observed energy distribution, for Lake Ontario runs listed in Table 11.3, as a function of relative frequency f/f_p. Bottom: relative value of the spreading parameter β/β_p for Lake Ontario runs listed in Table 11.3, as a function of relative frequency f/f_p.

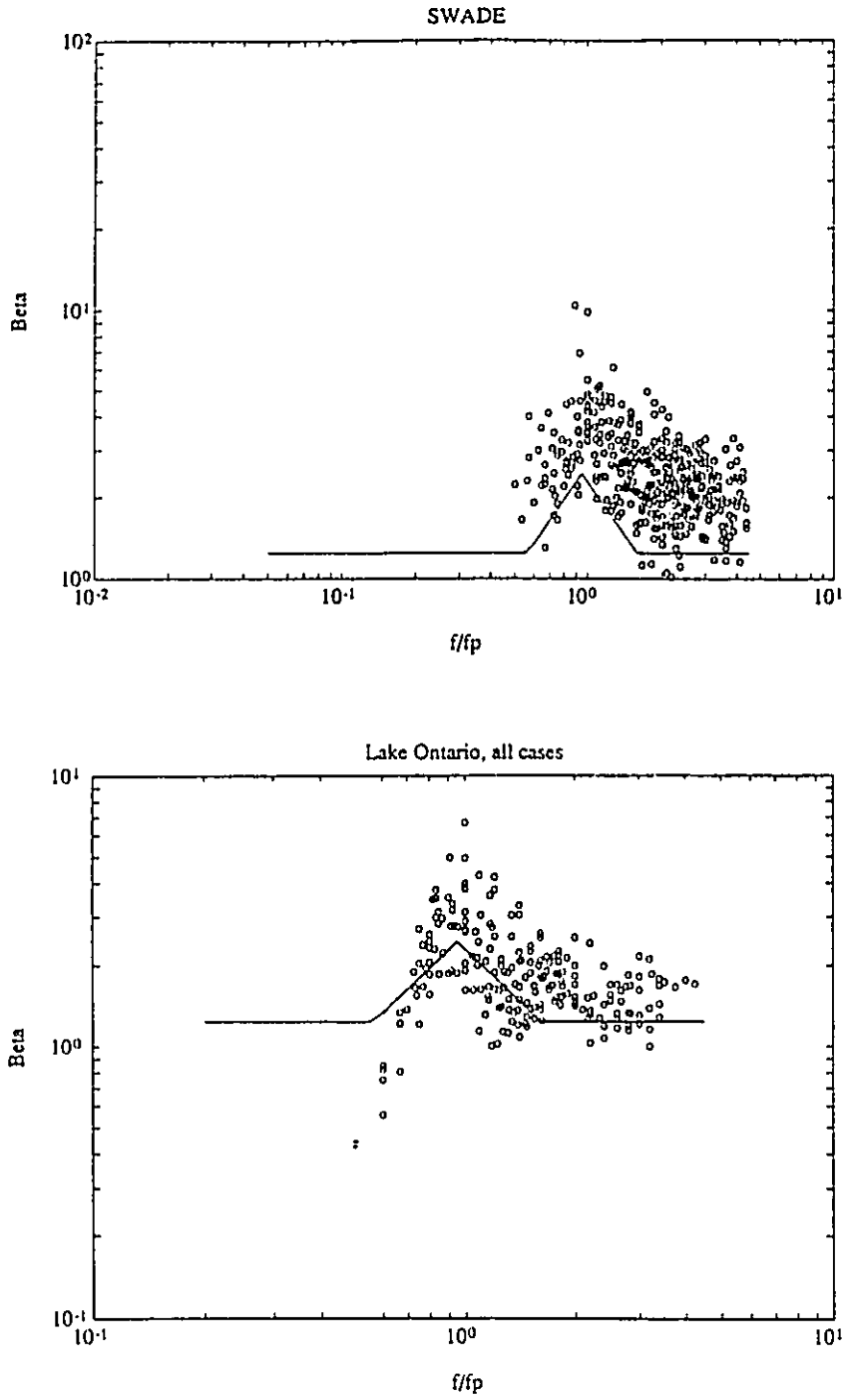

Fig.11.11 Top: Spreading parameter (β) values obtained from fitting $sech^2$ spreading functions to observed energy distribution, for SWADE runs listed in Table 11.3, as a function of relative frequency f/f_p. Bottom: same for Lake Ontario runs.

diminishing the generality of the results. Least-square fitting techniques such as the one used are very likely to be affected by the tails at the ends of the energy spread. However, in most cases, two distributions were fitted to the distribution, the main distribution approximating the energy containing region and the second (generally significantly smaller) comprising most of the tails. All the plots presented used only the main fitted distribution, thus effectively removing most of the spread due to the tails. The effect of fitting the entire energy spread (including the tails) to one distribution would be to reduce the value of the spreading parameter, compared to when fitting to the half-height width. Also, no particular effort was made to select ideal cases of fully developed seas which would have surely diminish the scatter. In fact, the runs were especially chosen as to include various environmental conditions. Runs from the November 15-16 case, despite all showing a unimodal frequency spectrum (Figure 11.12) all have a peak frequency behaving as a swell in the weak winds and the definition between swell and sea is hard to make in these runs. The same can be said for the SWADE data. The SWADE data used was from the October 1990 11-days storm period, where the winds were strong and changing rapidly, and the SWADE area was swell-infested. Clearly, despite trying to choose "near-stationary conditions" for the used runs, this was not the ideal data for such an undertaking. Nevertheless, the aim of the investigation was to get a general idea of the results that could be obtained in a careful study using higher resolution methods of estimating the wave directional spectrum, and as such, various points can be raised. The function defining the value of the spreading parameter β as a function of the dimensionless frequency f/f_p follows the general shape defined by Donelan et al. (1985), but two differences need to be discussed. First, for Lake Ontario data, the front face of the spectrum falls off much more rapidly. This is more than likely due to the way the slope signals are evaluated. As discussed in Chapter 9, at these low frequencies, the slopes, as calculated in

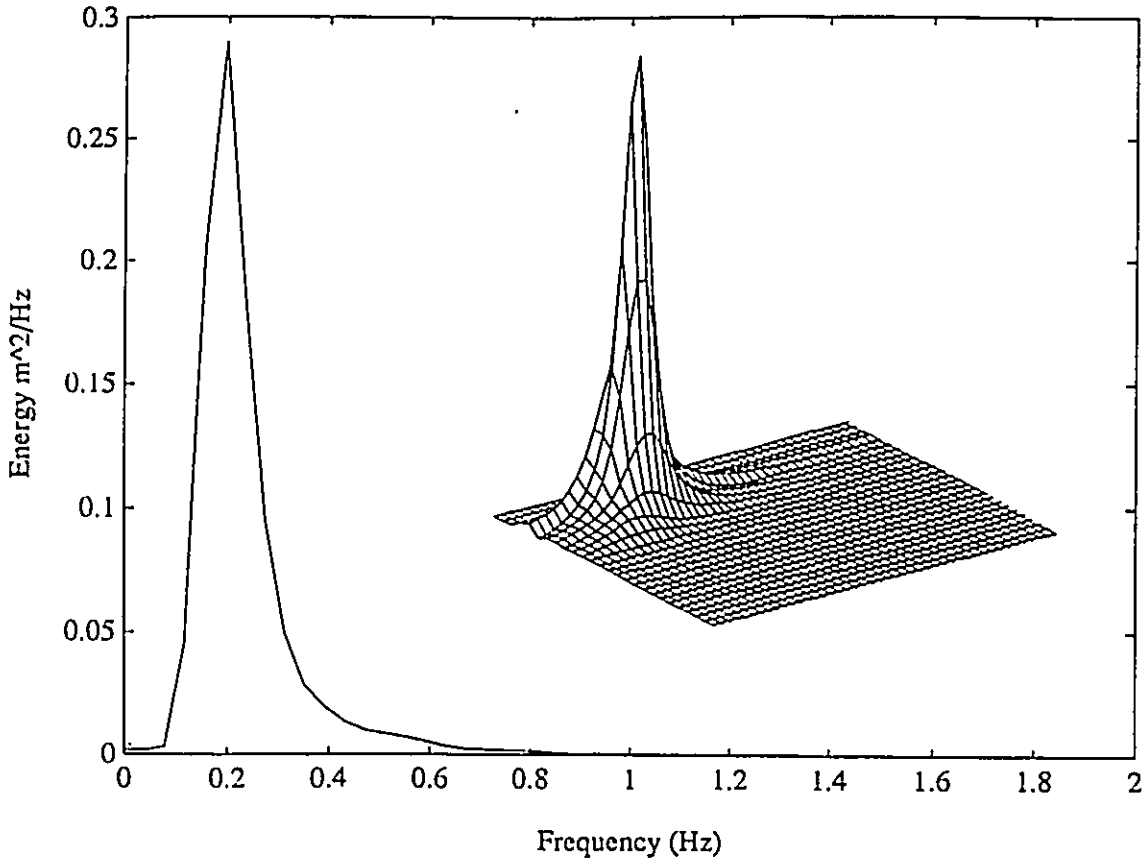

Fig.11.12 Typical frequency and directional spectrum for runs during the November 15-16 (run 87061C) period. For directional spectrum: frequency is from 0 to 1 Hz and direction from 0 to 200°.

11.2 are not accurate anymore. The problem is more critical as one moves away from the peak, as less and less energy is present. As a result, the methods tend to return a flatter estimate. The SWADE data, which uses a true pitch-roll-heave signal does not show that tendency. Potentially, the problem could be solved for Lake Ontario by using a frequency dependent slope calculation scheme, as discussed in Chapter 9. The other difference is that despite showing a similar trend as the function defined by Donelan et al.(1985), the values of the spreading parameter β are systematically higher over the entire range of f/f_p studied, and especially so around the spectral peak. This is probably the result of using higher resolution methods which should give better estimates of the spread of energy. Lesser resolution methods were shown to give smeared estimates and this could easily account for the observed difference. This outlines the importance of carefully choosing a method of estimating the wave directional spectrum, as the results are very likely to be "method-dependent". As discussed earlier, the SWADE data gave values of β higher than the Donelan et al.(1985) function but also higher than the Lake Ontario data. The difference is not easily explained as the same procedure was used for both cases. The difference could be due to various geophysical parameters. As an example, it is hypothesized that winds are less likely to vary on the ocean as much as they would in inland waters. Clearly, more work needs to be done to establish without a doubt any potential difference between the patterns of energy spread in the Atlantic Ocean and Lake Ontario. Finally, a word should be said about the peak-frequency dependence shown in Figure 11.9. In a sense, this dependency (although based on only a few data points) is understandable since variations in the wind field are far more likely to influence the spread of the spectrum at higher frequencies, where there is far less energy. More specifically, for similar U_{10}/C_p values, the spectrum with a lower peak frequency f_p should be less influenced by wind fluctuations, as the time scale needed for a significant build-up

of energy at low frequencies is probably order of magnitudes larger than the wind fluctuation time scale.

11.5. HIGH-FREQUENCY BIMODAL DISTRIBUTIONS

An interesting feature that was not discussed in the previous section can be seen in Figure 11.7. It can be seen on all three plots (although more clearly on the third one) that as the relative frequency f/f_p reaches a value of about 1.5 to 2, there is a sudden decrease in the value of the spreading parameter β, followed by a small rise at which point the β parameter reaches a more or less constant value. This observed feature seems to be the result of the passage from a unimodal directional spectrum around the peak frequency, to a bimodal directional spectrum at higher frequencies, away from the peak. The transition between unimodal and bimodal spectra gives rise to a broader spectrum explaining the lower β values in that region. A careful survey of all analyzed Lake Ontario cases indicated that the transition from unimodal to bimodal directional spectra was common to almost all of the analyzed runs. The only runs where the feature was absent where cases of weak winds. Figures 11.13 and 11.14 illustrate two such cases. In Figure 11.13, the directional spectrum multiplied by the frequency to the fourth power (in order to emphasize high frequency features) is shown for runs 87055A and 87064A. In the first run the wind blows from 51° at 4.28 m/sec and the transition to a bimodal spectrum is clearly seen, whereas in the second case, as the wind is only blowing at 1.54 m/sec (from 350°), the spectrum is unimodal. Figure 11.14 presents similar plots for runs 87189C and 87190A. In the three hours that separated those two runs, the wind abruptly shifted from 85° to 240° changing the sea of 87189C into a swell. As far as can be seen (since the sea in 87190A hides high frequency results), the transition from sea to swell removed the higher frequency bimodality

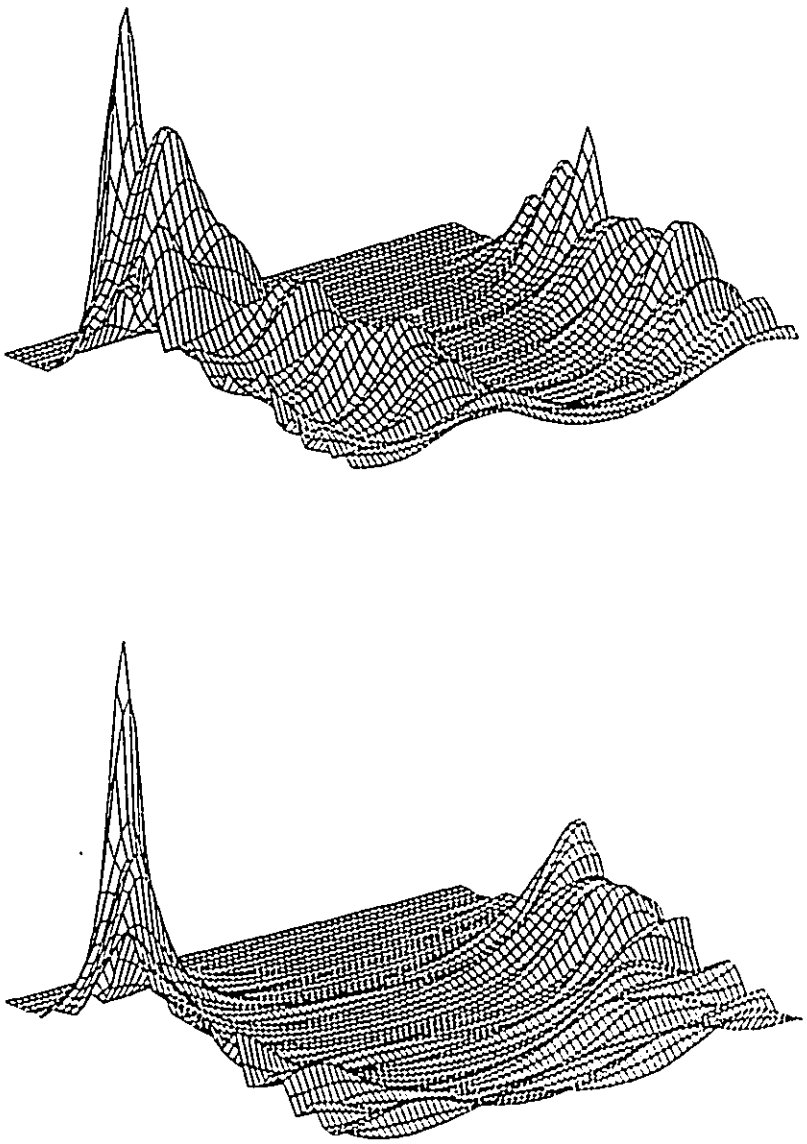

Fig.11.13 Directional spectrum multiplied by f^4 to outline high-frequency features. Frequencies range from 0 to 2.5 Hz and direction from 0 to 360°. Top: run 87055A, $U_{12} = 4.3\ m/sec$. Bottom: run 87064A, $U_{12} = 1.5\ m/sec$.

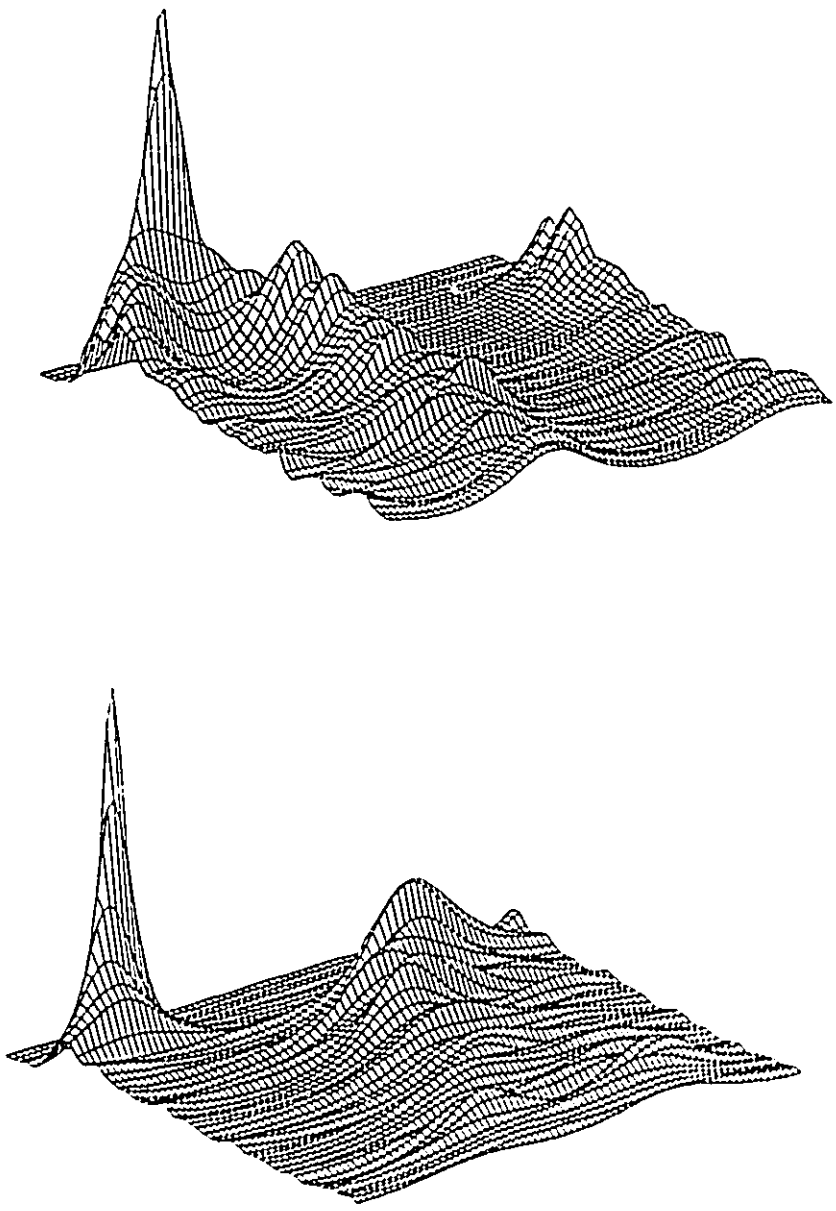

Fig.11.14 Directional spectrum multiplied by f^4 to outline high-frequency features. Frequencies range from 0 to 2.5 Hz and direction from 0 to 360°. Top: run 87189C, U_{12} = 13.1 *m/sec*, wind direction = 85°, Bottom: run 87190A, U_{12} = 9.5 *m/sec*, wind direction = 240°.

observed in 87189C.

From these results, it would seem that the transition from a unimodal to a bimodal directional spectrum is wind-induced. As soon as the wind input is removed, the spectrum returns to a unimodal form over most of the observed frequency range. The feature is more than likely not a method artifact, since it was detected on both the wavestaff data and reconstructed slope signals. As to why such a spectrum would form is an impossible question to answer at this point, and at best we can hypothesize that the feature is somehow linked to wave breaking at a given frequency, which would in turn affect the development of higher frequency waves. In such a case, correlations should be observed between wind speed and the transition frequency between unimodal and bimodal directional spectra. Clearly, more work needs to be done on this particular aspect before a clearer picture emerges.

As far as the author knows, such a feature has never been reported elsewhere. Even if this is a common feature in wavefields, the absence of such reports can still be explained to a certain extent. First and foremost, most of the wave directional spectrum measurements have been made in the ocean using heave-pitch-roll buoys. Typically, waves with a frequency larger than about 0.4 Hz can't be resolved in such cases and this could be too small in many instances. Secondly, most of the attention is generally devoted to the energy containing region, where such bimodalities are generally absent (consider that it was necessary to multiply the spectrum by f^4 to reveal such a feature). Finally, many if not most of the applications still use the Longuet-Higgins et al.(1963) method of reconstructing the spectrum, method which is incapable of resolving such a feature.

11.6. CONCLUSION

Following this overview of various aspects linked to the angular spreading of energy in Lake Ontario wavefields, the following points can be stressed:

1.- The wave directions of propagation (defined as the mean wave direction) in various wind conditions are in good agreement with the similarity-based fetch relationship of Donelan (1980). This confirms the results obtained for Lake Ontario by Donelan et al.(1985).

2.- Results from the Lake Ontario data, as well as data from the previous chapter indicate that the mean wave direction of propagation better represents the wavefield than the peak wave direction.

3.- An investigation of the values of the spreading parameter β indicate that the trend is consistent with the work of Donelan et al.(1985), but that despite the considerable scatter, the values are consistently higher, especially so for the Atlantic Ocean SWADE data. Additionally, a dependence of β on the peak frequency f_p was observed, but none on the non-dimensional frequency U/C, which supports the observations of Donelan et al.(1985) which first contradicted the study of Mitsuyatsu et al.(1975) and Hasselman et al.(1980).

4.- Finally, higher frequency results indicate that bimodal distributions of energy away from the peak frequency, are commonly observed in the Lake Ontario dataset.

The results presented in this Chapter indicate that the use of high-resolution methods of directional spectrum estimation can potentially significantly improve our ability to accurately look at wavefields. Careful studies in controlled conditions should now be undertaken, using these methods, in order to better understand the factors that determine the angular spread of energy in wavefields.

CHAPTER 12

WAVE-CURRENT INTERACTION IN LAKE ST. CLAIR

The last application deals with wave data from Lake St.Clair. The first application of the concepts developed in the first part of this work dealt with SWADE data in the Atlantic Ocean. Then, Lake Ontario data was used. By finally using data from Lake St.Clair, applications of the study of wave directional spectra were shown at three different scales spanning more than two orders of magnitude.

Analysis of wave data collected during a 1985 field study on Lake St.Clair (Venkatesh et al., 1987) revealed important differences in certain cases between the wind and wave directions. In cases of westerly winds, peak waves were found to propagate at an angle of up to 60° to the wind direction. Work presented in this Chapter makes use of high-resolution methods of estimating the wave directional spectrum, in order to gain some more insights into the nature of the phenomenon.

12.1. INTRODUCTION

Lake St.Clair (Figure 12.1), located between Lake Huron and Lake Erie, has a surface area of 1200 km^2 and is characterized by its shallowness, its maximum depth being just about 6 m, and its average depth of 4 m. The St.Clair River carries an outflow of about 6000 m^3 from the upper three Great Lakes into Lake St.Clair. This high volume combined with the shallowness

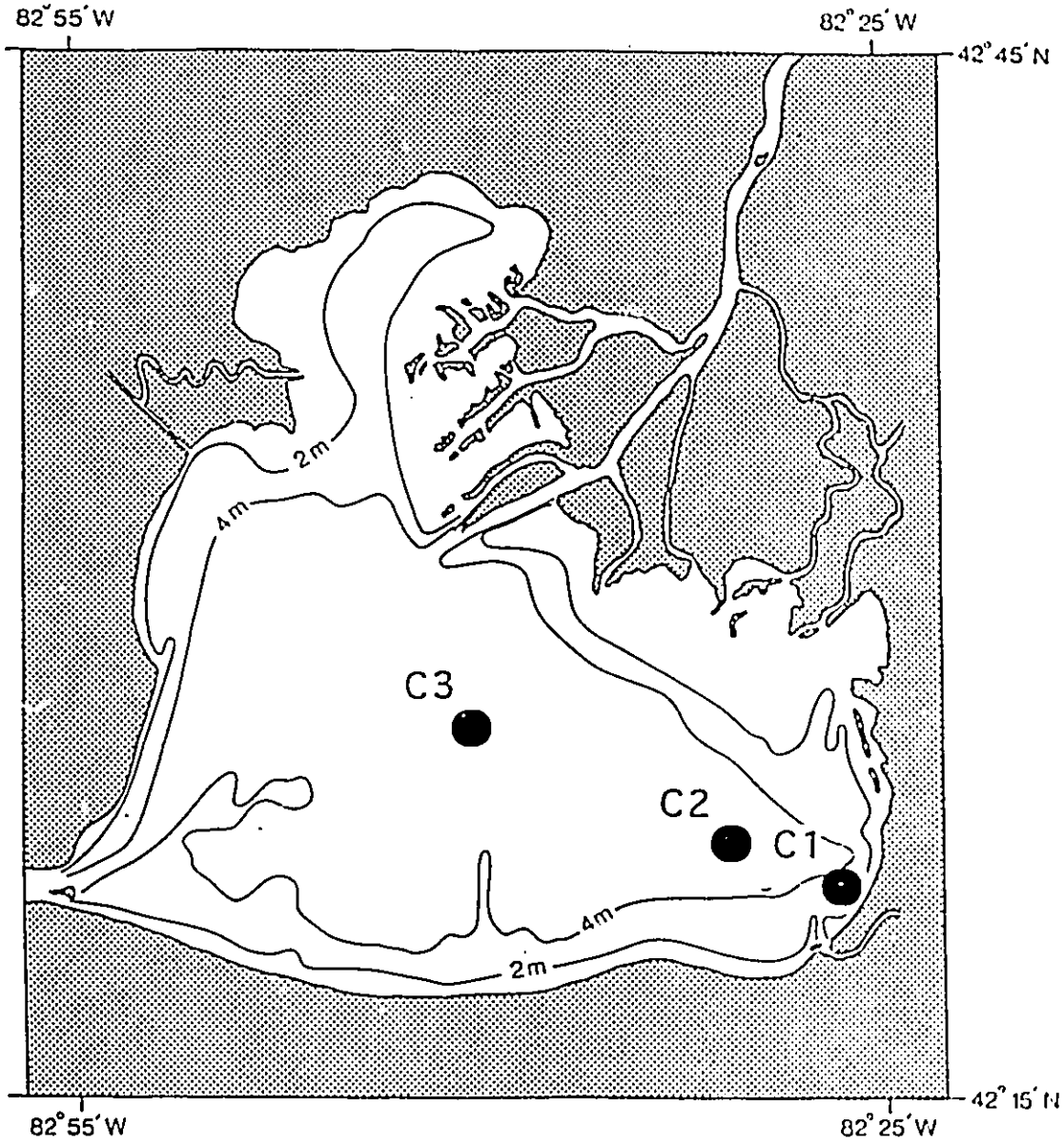

Fig.12.1 Geographic location of CCIW wavestaff arrays in Lake St.Clair (from Venkatesh et al., 1987).

of Lake St.Clair (residence time of 9 days) indicate that hydraulic and wind-driven circulation are likely to form strong currents (Schwab et al., 1989).

During the fall of 1985, an experiment conducted by the National Water Research Institute (NWRI) and the National Oceanic and Atmospheric Administration (NOAA) Great Lakes Environmental Research Laboratory (GLERL), allowed data to be gathered during a two and a half months period at different locations on Lake St.Clair (Venkatesh et al., 1987). The experiment, which aimed at studying the growth rate of wind-generated waves, allowed directional information to be obtained at three locations on the lake. The initial investigation used the Direct Fourier Transform method of Longuet-Higgins et al. (1963) (presented in section 3.1) to obtain parameters of the angular distribution of energy such as the mean direction of propagation and the RMS spread. Figure 12.2 presents a plot of the peak wave direction compared to the wind direction at the central location on the lake (C3). The plot shows systematic deviations from the wind direction that are in excess of those that would be expected due to the gradient in fetch with direction (Donelan, 1980). The general pattern of the deviations seems compatible with the presence of a strong hydraulic current aligned roughly north to south which would tend to deflect the waves toward the south (Figure 12.3). Nevertheless, there are data that are not consistent with this simple idea, so that, in addition to a detailed analysis of the current structure, high resolution directional estimates are warranted to establish the exact nature of the wavefield.

12.2. DIRECTIONAL SPECTRUM ESTIMATION

In order to obtain wave directional information during the 1985 experiment, arrays of wave staffs were mounted on three towers, C1, C2 and C3 (see Figure 1). The three identical

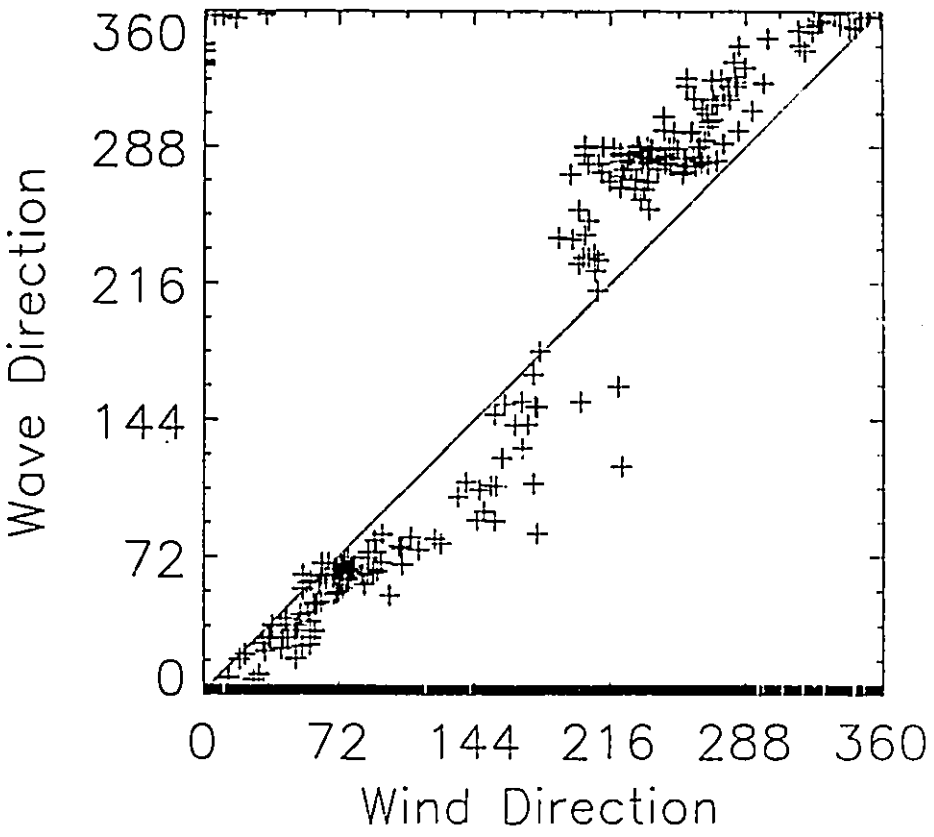

Fig.12.2 Observed mean wave direction at the spectral peak as a function of wind direction.

arrays consisted of three wave staffs each arranged in the vertices of an isosceles (0.25 m) right triangle (Figure 12.4). Water surface elevation was sampled at 4 *Hz* for 17 minutes every two hours. Samples were FFT averaged to a frequency bandwidth of 0.03 *Hz*, giving spectral estimates with 64 degrees of freedom. Cross-Power-Spectral-Density (CPSD) matrices were computed using the water elevations at each wave staff (η) but also on the heave (η), pitch ($\partial\eta/\partial x$) and roll ($\partial\eta/\partial y$) signals using:

$$\eta = \eta_2 \tag{12.1a}$$

$$\frac{\partial \eta}{\partial x} = 4\,(\eta_1 - \eta_2) \tag{12.1b}$$

$$\frac{\partial \eta}{\partial y} = 4\,(\eta_2 - \eta_3) \tag{12.1c}$$

where the subscripts refer to a particular wavestaff. Using both CPSD matrices allows the use of all the methods developed in the first part of this work. Since the wavestaff arrays used on Lake St.Clair each had three wavestaffs, it follows that the use of pitch-roll-heave-equivalent methods should in theory give the same resolution as direct methods (see Chapter 6), as long as the slopes calculated with Eq. 12.1 are accurate. Work presented in section 6.1.2. showed that the reconstructed heave-pitch-roll signals are accurate at frequencies up to 1.25 Hz.

12.2.1. Fetch-gradient effects

It has been shown (Hasselman et al., 1980; Donelan et al., 1985) that the wave direction around the spectral peak will not necessarily coincide with the wind direction in non-stationary or fetch-limited conditions. Donelan (1980) showed that the waves can be biased toward the longer fetch if the fetch-gradient is large enough to compensate for the smaller

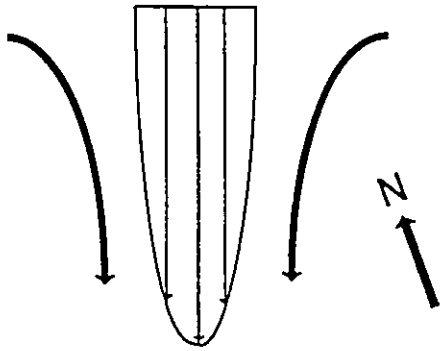

Fig.12.3 Schematic representation of wave refraction pattern due to a shear current.

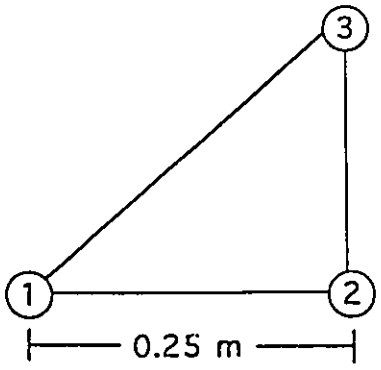

Fig.12.4 Geometry of three-wavestaff array used in Lake St.Clair.

generating force of the wind. Differences of up to 50° between wind and wave direction have been measured in Lake Ontario (Donelan et al., 1985).

As a result, before investigating possible wave-current interaction, it is necessary to establish how much of the variation observed in the data presented in Figure 12.2 is in fact due to a fetch-gradient effect. In order to do so, the procedure outlined in Bishop and Donelan (1989) was followed, which consists in maximizing the following expression for a given location:

$$F^{0.426}\cos(\theta_{wind}-\theta_{wave}) \tag{12.2}$$

where F is the fetch length. The maximization was done by setting up a computer routine which calculated the fetch length at Tower C3, for every degree (averaged over $\pm 15^{\circ}$), using a schematic map of Lake St.Clair with digitized values of the circumference of the Lake (Figure 12.5). Using the calculated fetch directions, Eq. 12.2 was maximized at every wind direction using a $1^{\circ} step$. The wind vs. wave direction relationship for Tower C3 is shown in Fig. 12.6 with the data presented in Fig. 12.2. It can be seen that although part of the discrepancies can be explained by a fetch effect, most of the differences between wind and wave direction remain unaccounted for. This was predictable to a certain extent considering that the general shape of Lake St.Clair, combined with the central location of Tower C3 gave limited fetch gradients in all directions.

12.3. HYDRODYNAMIC MODEL OF LAKE ST.CLAIR

In order to further investigate the possibility of wave-current interaction in Lake St.Clair, the water current structure needs to be established. A two-dimensional nearly-horizontal flow model (Tsanis and Wu, 1990) is used to simulate the hydraulic and wind-induced

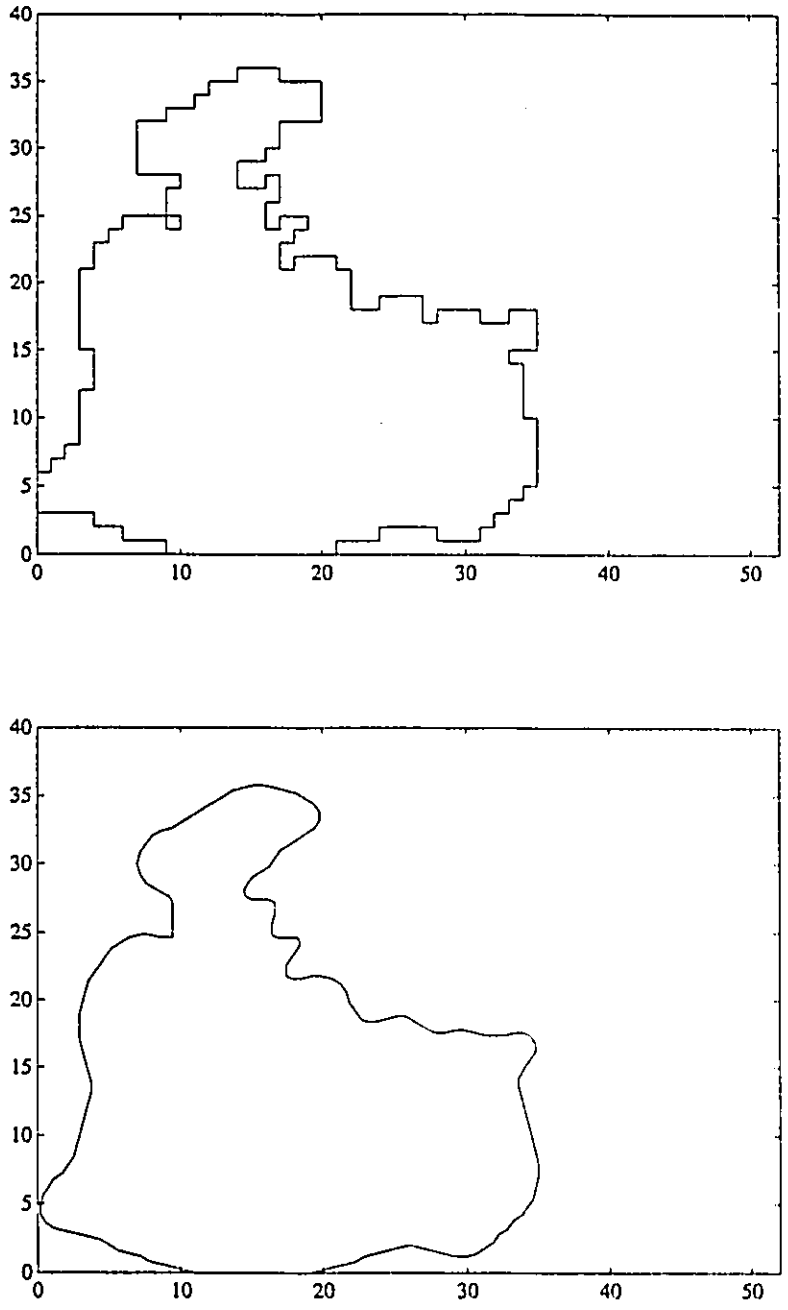

Fig.12.5 Grid map of Lake St.Clair (top) and resulting smoothed contour plot (bottom) used in calculating fetch lengths.

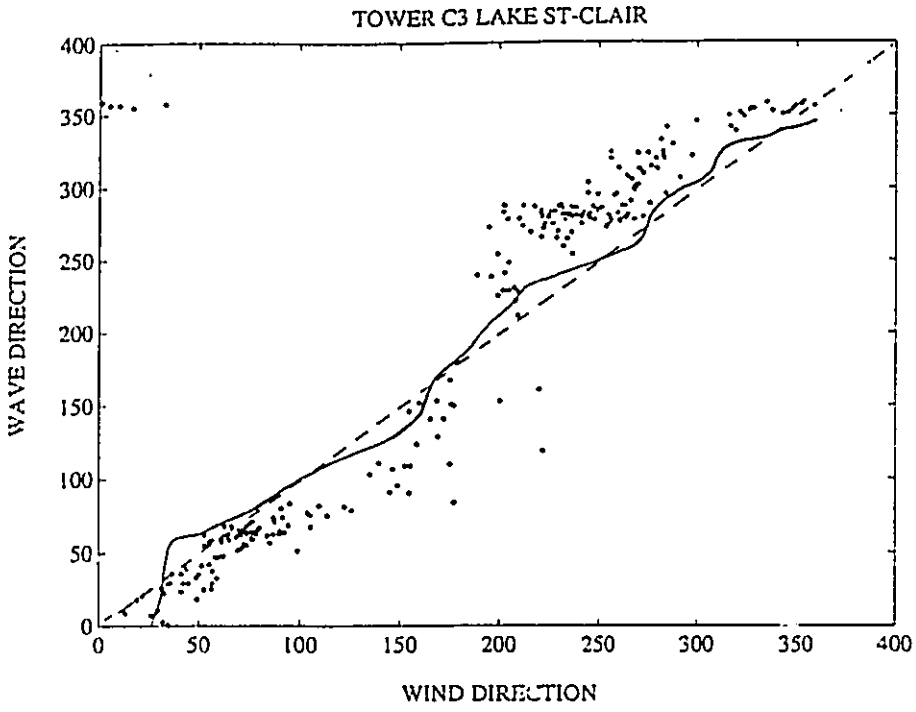

Fig.12.6 Observed mean wave direction (at $f = f_p$) plotted against wind direction . The solid line is based on the work of Donelan (1980) and takes into account fetch-gradient effect, whereas the dashed line is the line of perfect agreement.

circulation in Lake St.Clair. Using standard assumptions for a two-dimensional approximation (Blaisdell et al., 1991), the equations of motion in the x and y direction and the continuity equation can be reduced to:

$$\frac{\partial U}{\partial t} + U\frac{\partial U}{\partial x} + V\frac{\partial U}{\partial y} = -g\frac{\partial \eta}{\partial x} + 2V\Omega\sin\phi + \frac{k}{h}|W|W_x - \frac{C_b}{h}U\sqrt{U^2+V^2} \tag{12.3}$$

$$\frac{\partial V}{\partial t} + U\frac{\partial V}{\partial x} + V\frac{\partial V}{\partial y} = -g\frac{\partial \eta}{\partial y} + 2U\Omega\sin\phi + \frac{k}{h}|W|W_y - \frac{C_b}{h}V\sqrt{U^2+V^2} \tag{12.4}$$

$$\frac{\partial \eta}{\partial t} + \frac{\partial Uh}{\partial x} + \frac{\partial Vh}{\partial y} = q \tag{12.5}$$

where U and V are the depth-averaged velocities in the x and y directions respectively, g is the gravitational acceleration, η the water free surface elevation relative to the still water level, d is the water depth, Ω the angular rotation of the earth, ϕ the latitude, h the total water depth ($h = d + \eta$), W the wind speed at a 10 meter elevation, q the specific discharge of a source or a sink, k a surface friction coefficient and C_b is a dimensionless bottom friction coefficient defined as:

$$C_b = \frac{n^2 g}{h^{1/3}} \tag{12.6}$$

where n is the Manning coefficient. Eqs. 12.3 to 12.5 are solved numerically using an explicit finite difference scheme. The above model was applied to Lake St.Clair (Tsanis and Wu, 1990). A quasi three-dimensional model used by Wu and Tsanis (1991), applied to Lake St.Clair, was successfully tested against field data and gave similar results to the 2-D model. Details on the hydrodynamic model and numerical scheme can be found in Blaisdell et al. (1991).

12.4. RESULTS

12.4.1. Hydraulic and Wind-induced circulation

The water circulation in any body of water is dependent on the wind direction as well as the wind speed. But in Lake St.Clair case, an essential feature of the circulation pattern is always present, independently of the wind speed or direction (Figure 12.7). The circulation pattern is characterized by a strong (velocities of up to 1 m/sec at the inlet/outlet) hydraulic current with a NNE-SSW main axis, or more specifically, coming on average from about 20–25°. The main axis of the current will slightly rotate depending on the wind conditions, but it is always present. The strong current and its presence in all wind conditions is the result of the shallowness of Lake St.Clair combined with the relatively high volume of the St.Clair-Detroit river system.

12.4.2. Directional spectrum estimates

In a first step, directional estimates will be calculated for a few directions in order to look at the behavior of the directional spectra for different wind inputs. This approach will help identify the general characteristics of the wave directional spectra in Lake St.Clair and help focus more in-depth studies. Unless otherwise stated, all directional estimates were obtained using the corrected form of the MLM (MLMC).

12.4.2.a Preliminary investigation

As shown in Table 12.1, four different cases will be briefly discussed. The chosen cases illustrate some of the characteristics of wave directional spectra in Lake St.Clair for various wind

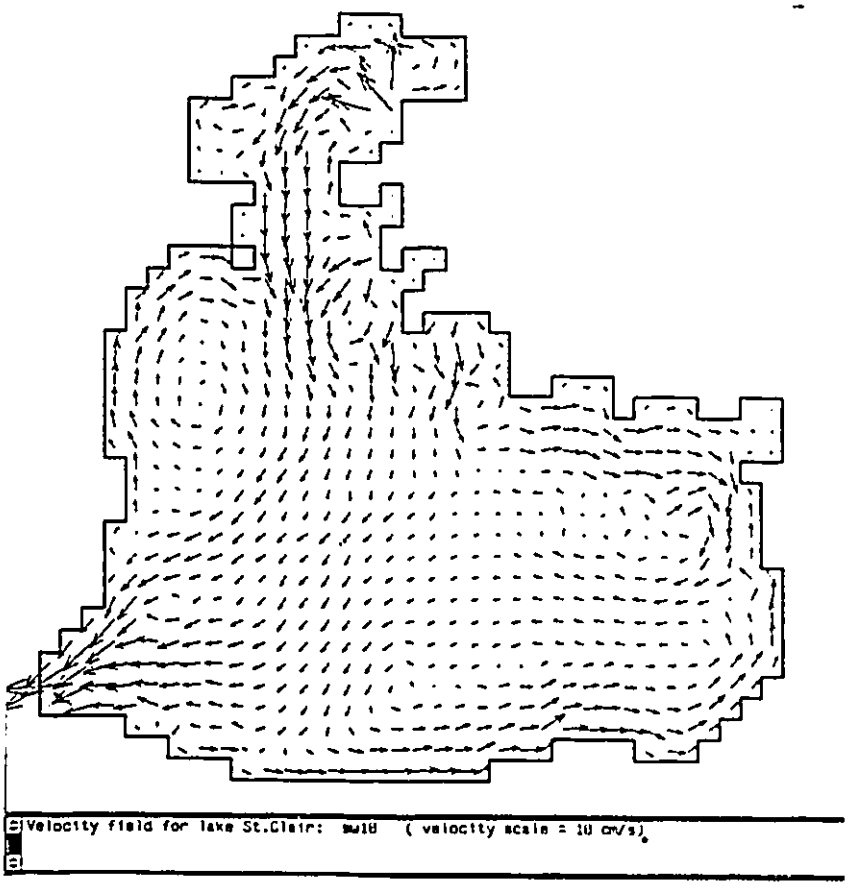

Fig.12.7 Typical hydraulic/wind-induced circulation in Lake St.Clair.

TABLE 12.1. Field Data

RUN #	Julian Day	Wind Dir. (degrees)	Wind Sp. (m/sec)	Wave Dir. (degrees)	$f_p(Hz)$
85270.22	270	326	4.5	353	0.32
85311.20	311	275	11.2	324	0.31
85320.06	320	87	12.3	63	0.28
85321.08	321	230	9.3	287	0.27

f_p is the frequency at the spectral peak. Wave direction is for peak wave as obtained following Longuet-Higgins et al.(1963).

directions.

Figure 12.8a is a contour plot of the directional spectrum for case 85270.22 with the wind blowing from 326°. Figures 12.8b and 12.8c respectively present the hydraulic and wind-induced circulation for this case and a plot of the mean wave direction in each frequency band. It can be seen that the lower frequency bands tend to be more consistent with a north direction whereas higher frequency bands tend to propagate with the wind (Figure 12.8c). This idea is consistent with refraction process of the wavefield by the roughly north-south current.

Figures 12.9a and 12.9b present similar plots for run 85311.20, which is a case of a strong westerly blowing wind. The spectrum is complex and harder to interpret. The peak frequency comes from a 320° direction. This direction is biased toward both a longer fetch direction and the hydraulic/wind-induced current. A secondary mode is also observed at about 255° which is also a longer fetch direction (see Figure 12.6). It is hypothesized here that most of the energy distribution is controlled by the current, while part of it is more consistent with the wind direction. At frequencies higher than about 1 Hz, the spectrum is again unimodal and the mean wave direction becomes more consistent with the wind.

The next plots (Figures 12.10a and 12.10b) are for run 85320.06, a case of a strong easterly blowing wind. Figures 12.10a is a contour plot of the directional spectrum and Figure 12.10b presents the hydraulic/wind-induced circulation for that case. The circulation plot indicates that in response to the strong easterly wind, a roughly east-west current develops in the eastern part of the lake. The directional spectrum is again observed to be bimodal, one mode coming from about 50° and one other coming from the wind direction (85°). Similarly to the previous case, part of the spectrum is partly decoupled from the wind and seems to be controlled to some extent by the current. At higher frequencies (> 1.1 Hz) the spectrum is unimodal and

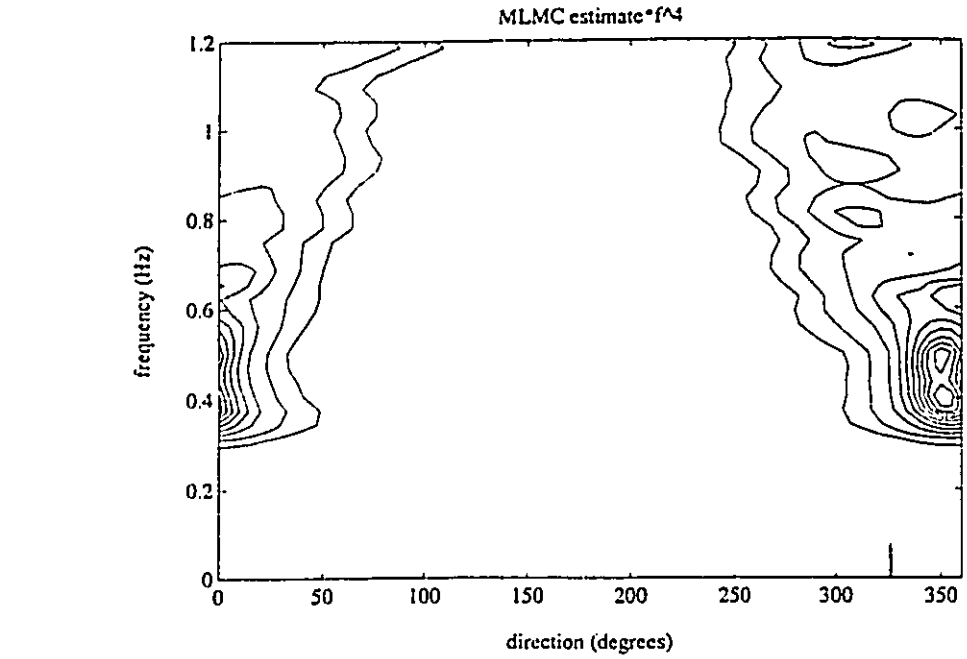

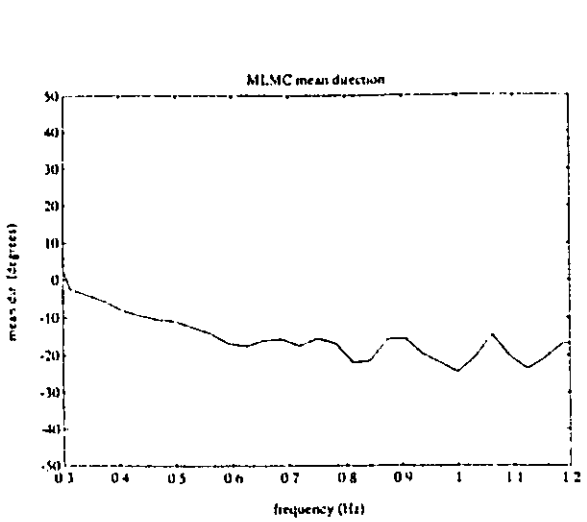

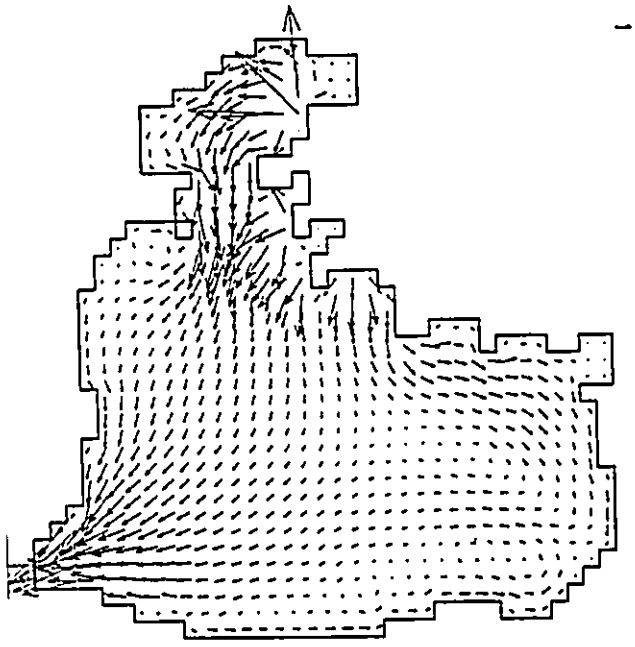

Fig.12.8 Top: Directional spectrum estimate (multiplied by f^4) for case 85272.22 with the wind blowing from 326°. Contours are equally spaced from maximum energy to zero energy. The wind direction is indicated by the solid line at the bottom of the plot. Bottom right: mean hydraulic/wind-induced circulation for case 85272.22. Velocity scale is 10 cm/sec. Bottom left: Mean wave direction as a function of frequency for case 85272.22. Negative values should be added up to 360 (ie: -10 = 350).

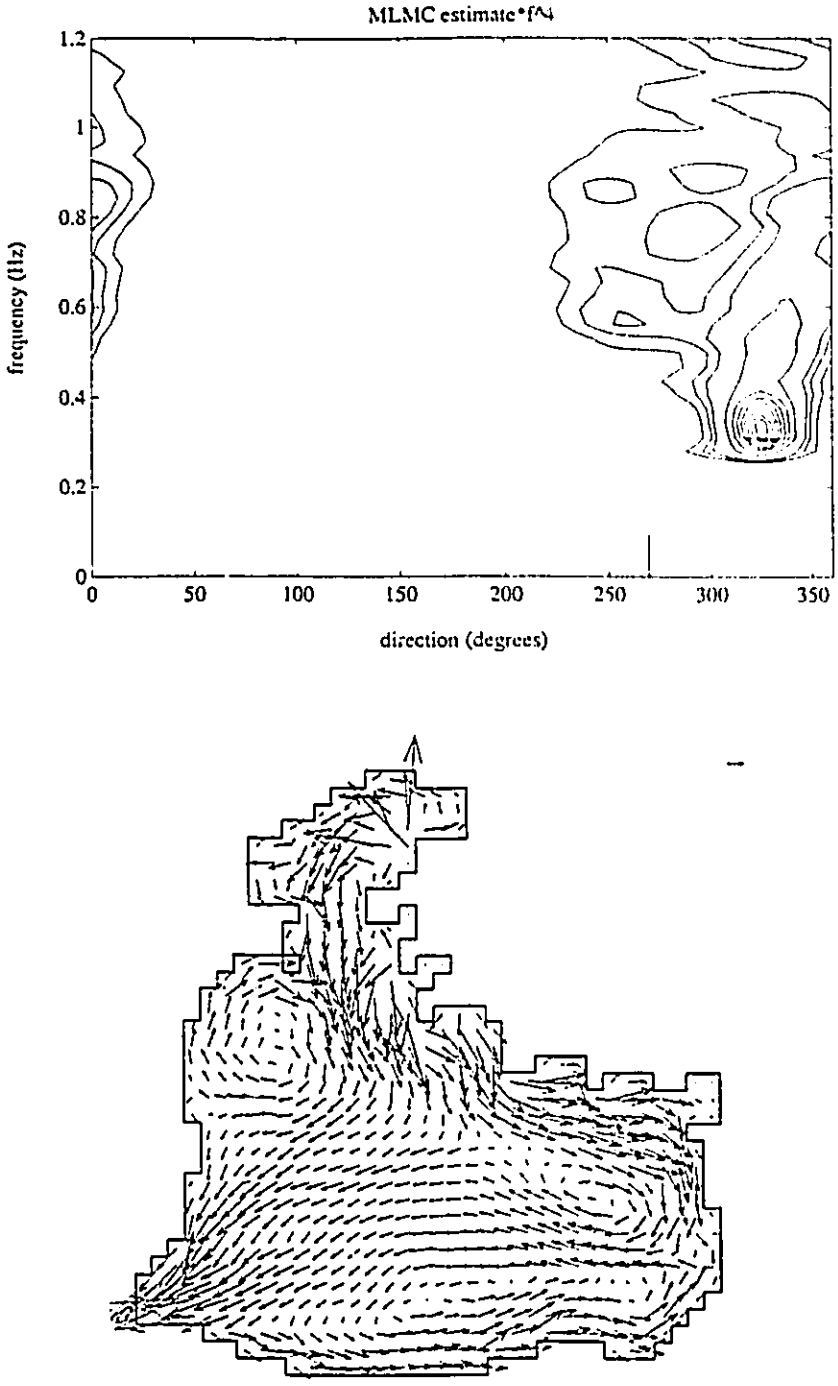

Fig.12.9 Top: Directional spectrum estimate (multiplied by f^4) for case 85311.20 for a strong westerly wind. Contours are equally spaced from maximum energy to zero energy. The wind direction is indicated by the solid line at the bottom of the plot. Bottom right: mean hydraulic/wind-induced circulation for case 85311.20. Velocity scale is 10 cm/sec.

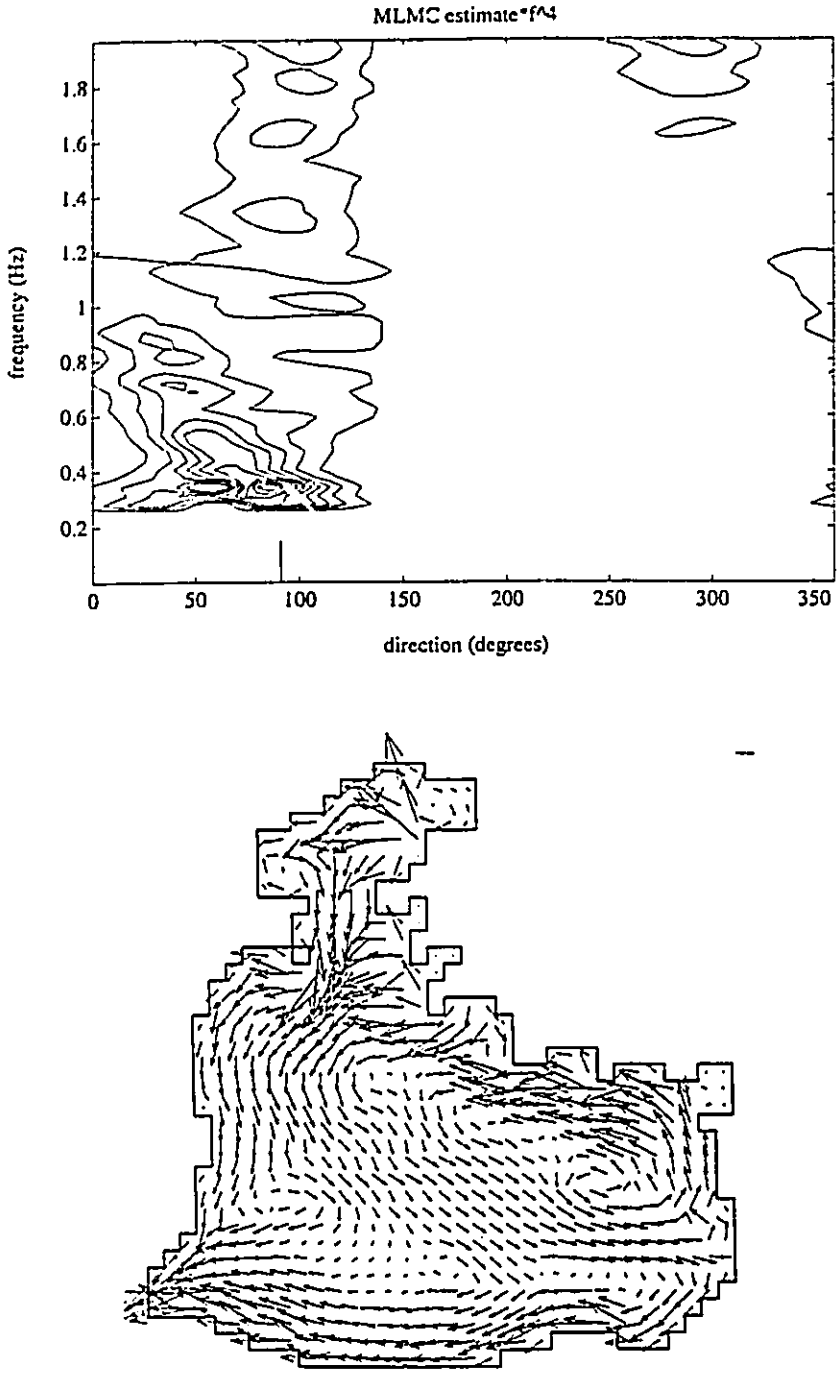

Fig.12.10 Top: Directional spectrum estimate (multiplied by f^4) for case 85320.06 for a strong easterly wind. Contours are equally spaced from maximum energy to zero energy. The wind direction is indicated by the solid line at the bottom of the plot. Bottom right: mean hydraulic/wind-induced circulation for case 85320.06. Velocity scale is 10 cm/sec.

consistent with the wind.

The last case is for a 230° wind, which is essentially opposite to the NE-SW current as shown in the circulation plot of Fig. 12.11b. A contour plot of the directional spectrum is also presented in Figure 12.11a. The spectrum is again bimodal, but surprisingly, neither modes are traveling with the wind, one coming from around 290° and the other from about 185°. These results essentially indicate that the wave energy is partitioned on each side on the current.

These results indicate that the most anomalous behavior of the directional spectrum occurs in cases of south to south-westerly winds, when the wind blows opposite to the main hydraulic current created by the St.Clair-Detroit river system.

12.4.2.b South to South-Westerly winds

The results presented in Figure 12.2 and in the previous section indicate that maximum discrepancy between observed wind and wave direction is obtained for SSW winds. To assess the observed difference, three cases of turning winds were analyzed, as presented in Table 12.2. In all these cases, the wind shifts from a south-easterly to westerly direction. Figures 12.12 to 12.17 present plots of the wind history and of the evolution of the wave directional spectrum, for the three cases presented in Table 12.2. The corrected form of the MLM (MLMC) was used in the first case whereas the normalized form of the MLM (NMLM) was used for the next two. Spectral features were the same for both estimates. The three cases are similar as they all present the same characteristics. From the work presented in Chapter 10, it is seen that the wind shift gradient ($2.5\times10^{-5} rad/sec$ on average) is small enough that the spectrum should adjust smoothly to the change in wind direction. What is observed in these cases though is totally different. Essentially, as the wind slowly shifts from one side of the main hydraulic current to the other, the

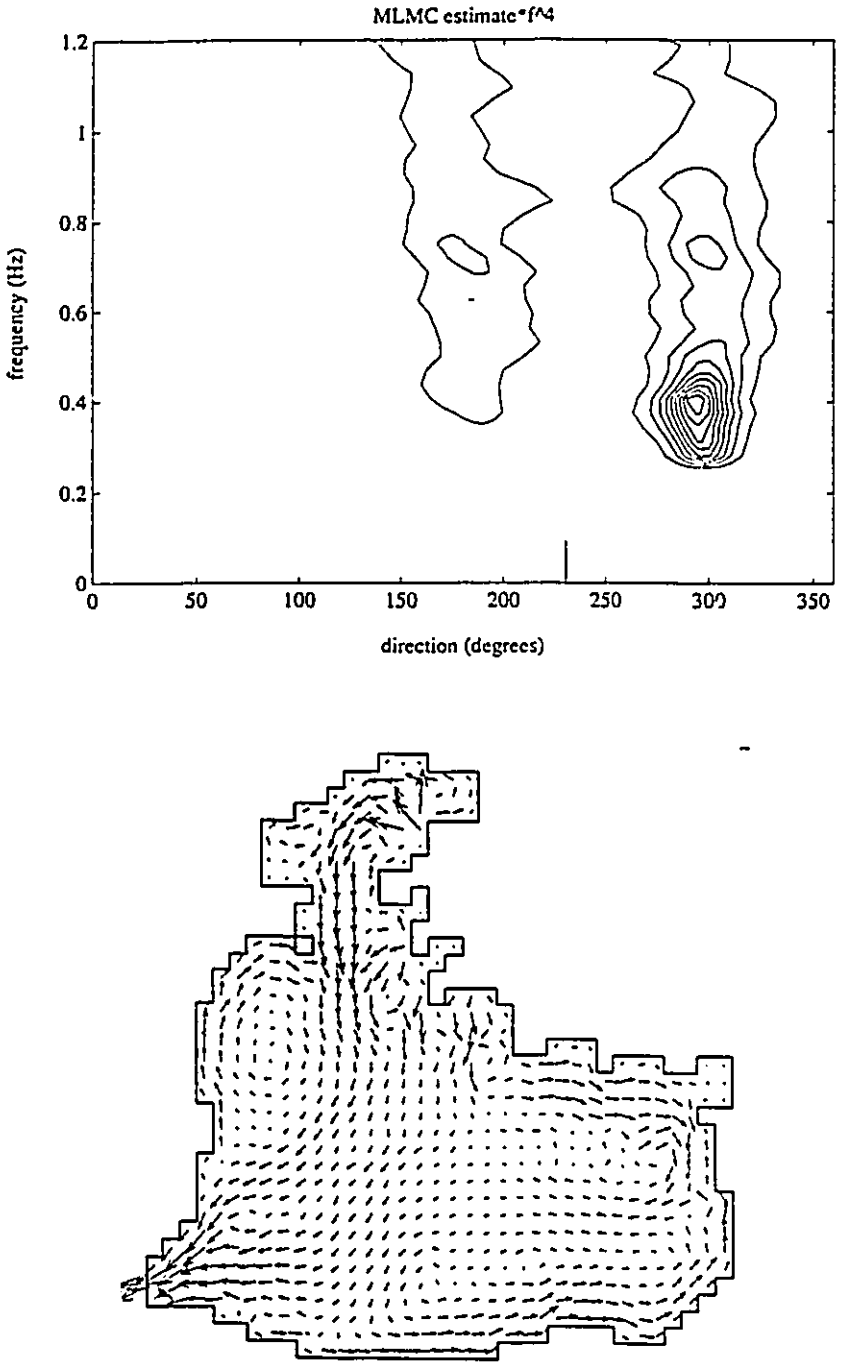

Fig.12.11 Top: Directional spectrum estimate (multiplied by f^4) for case 85321.08 with the wind blowing from 230°. Contours are equally spaced from maximum energy to zero energy. The wind direction is indicated by the solid line at the bottom of the plot. Bottom right: mean hydraulic/wind-induced circulation for case 85321.08. Velocity scale is 10 cm/sec.

TABLE 12.2. South-Westerly Turning Wind Cases

RUN #	Julian Day	Duration Hours	Wind Dir (degrees)	$\bar{U}_{10}$ (m/sec)
85266.00 to 85267.10	266-267	35	145 to 270	6.9
85324.00 to 85324.23	324	24	140 to 260	11.2
85335.12 to 85336.19	335-336	32	90 to 270	14.0

$\bar{U}_{10}$ is the average wind speed at 10 meters over the event duration

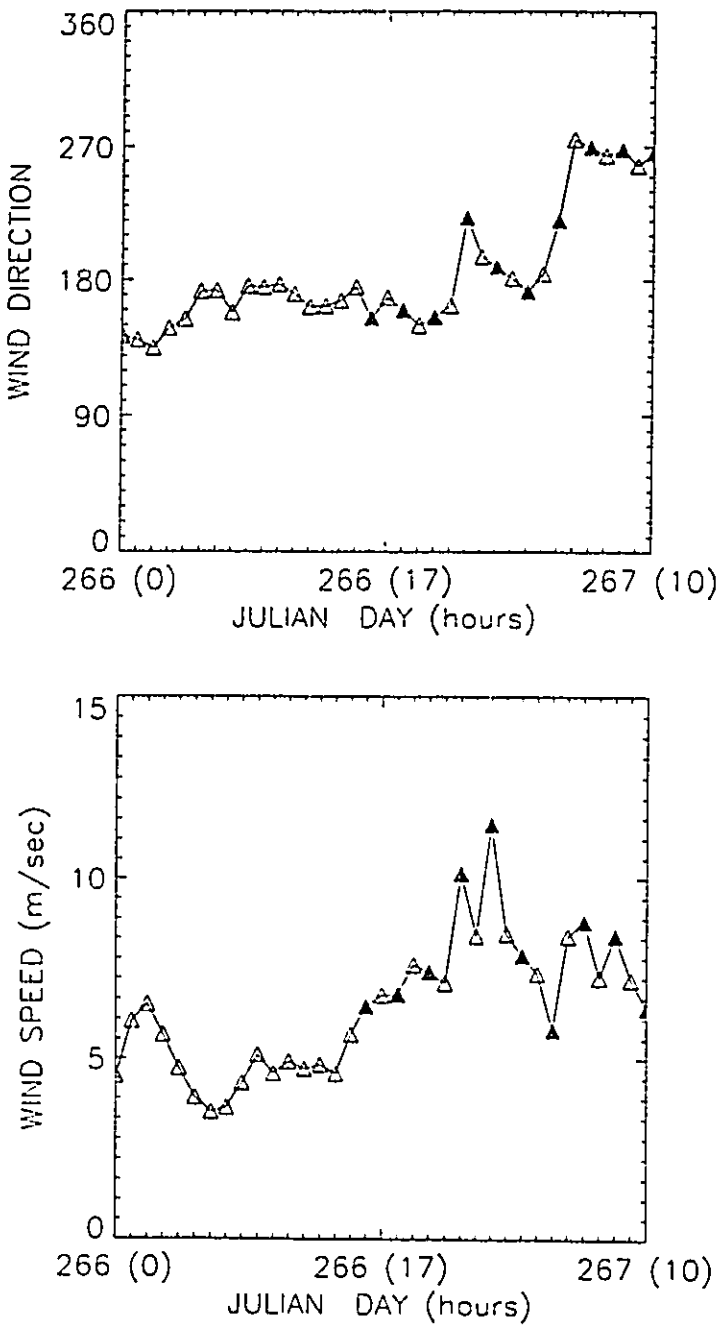

Fig.12.12 Wind direction and wind speed history for the first selected case of westerly turning winds.

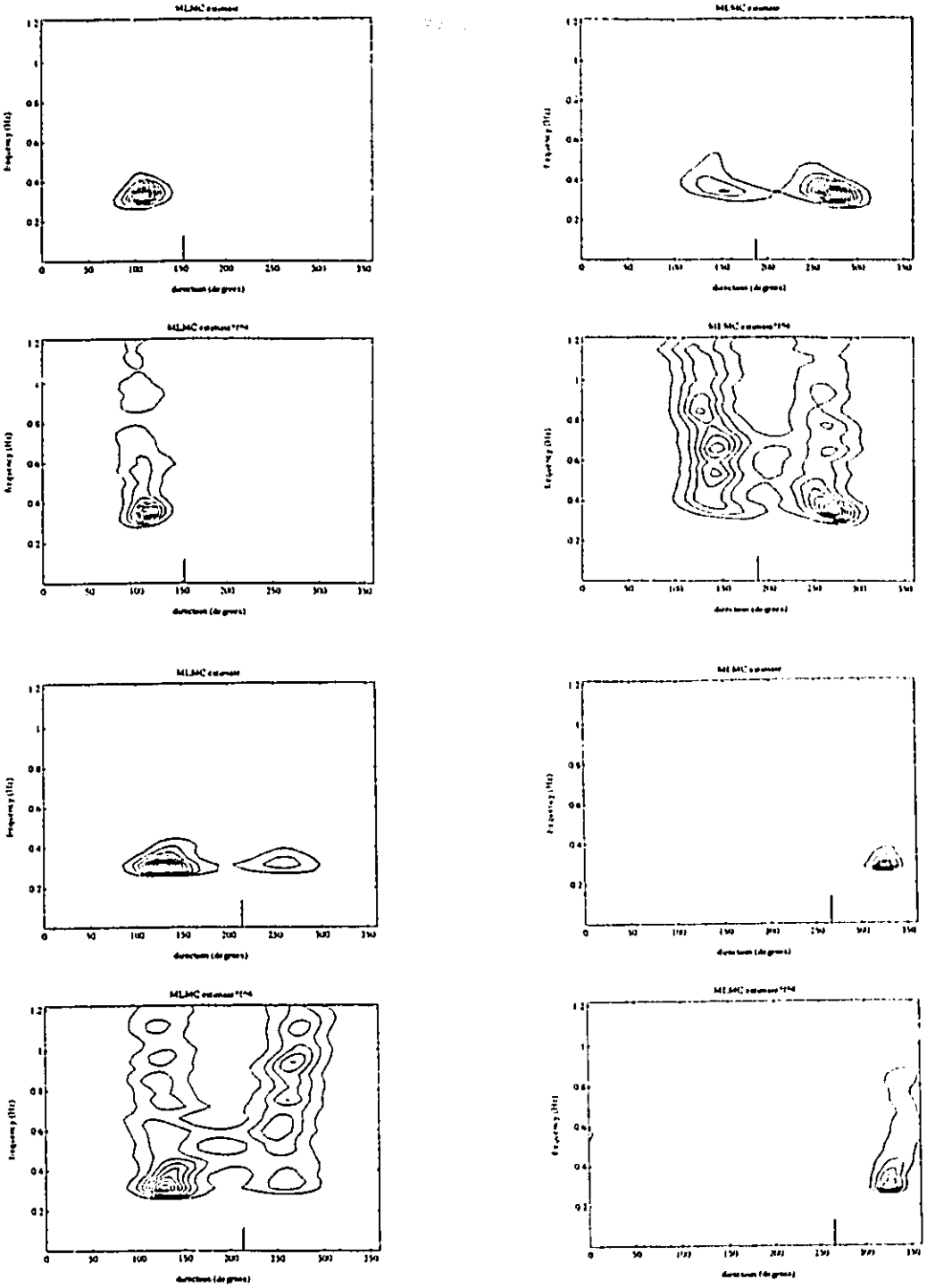

Fig.12.13 Directional spectrum estimate and directional spectrum estimate multiplied by f^4. Contours are equally spaced from maximum energy to zero energy. The wind direction is indicated by the solid line at the bottom of each plot. Top left 2 plots: 85266.20, top right: 85267.00, bottom left: 85267.04, bottom right: 85267.06.

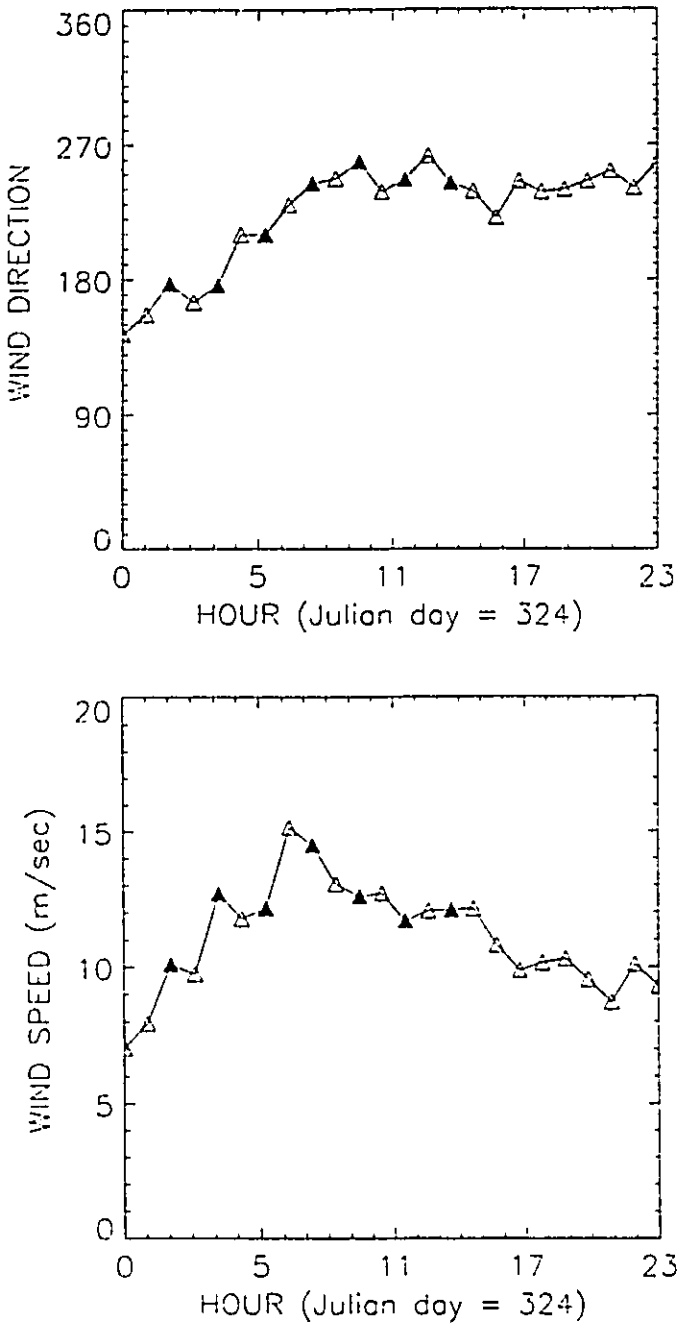

Fig.12.14 Wind direction and wind speed history for the second selected case of westerly turning winds.

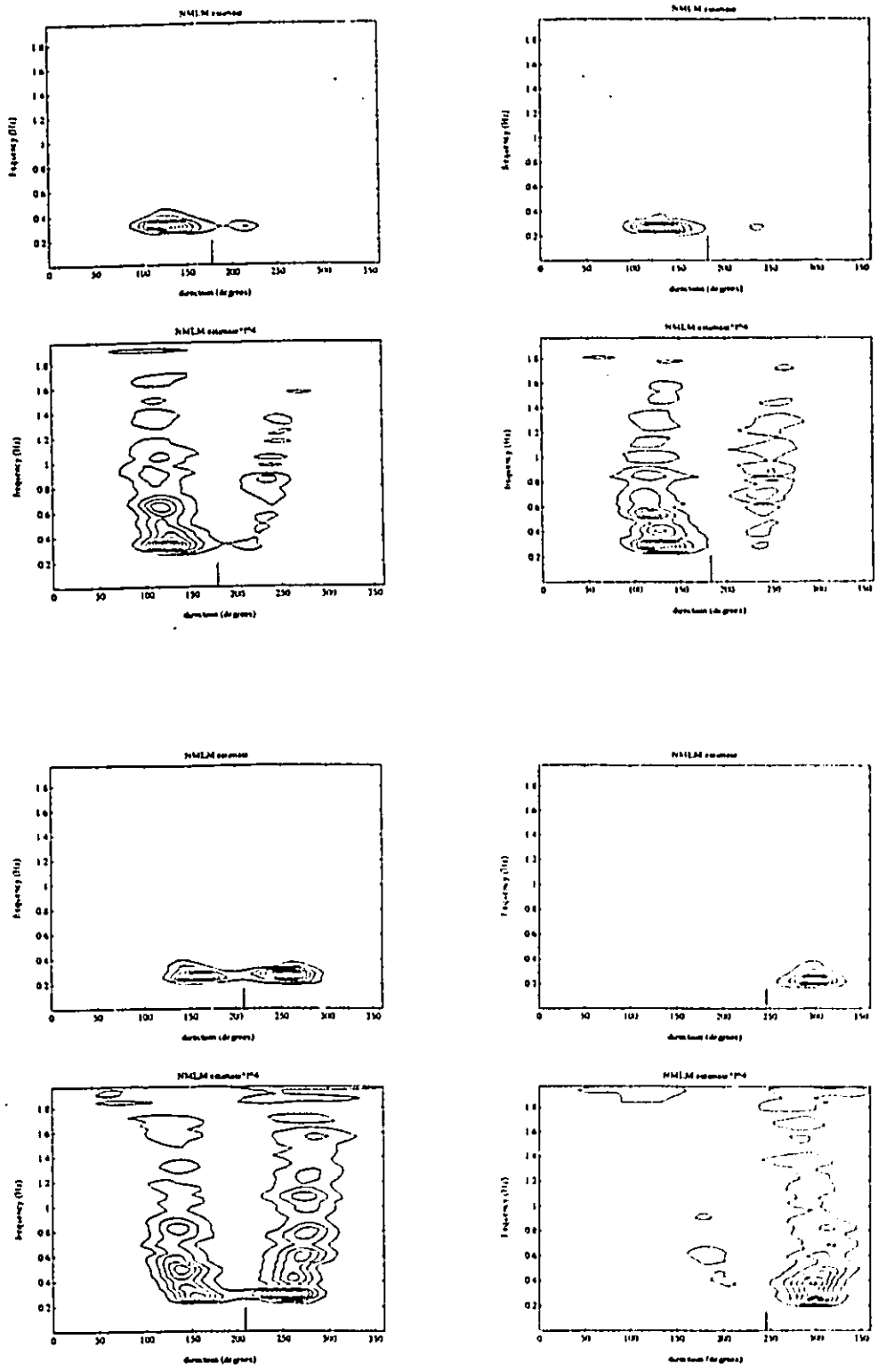

Fig.12.15 Directional spectrum estimate and directional spectrum estimate multiplied by f^4. Contours are equally spaced from maximum energy to zero energy. The wind direction is indicated by the solid line at the bottom of each plot. Top left 2 plots: 85324.02, top right: 85324.04, bottom left: 85324.06, bottom right: 85324.08.

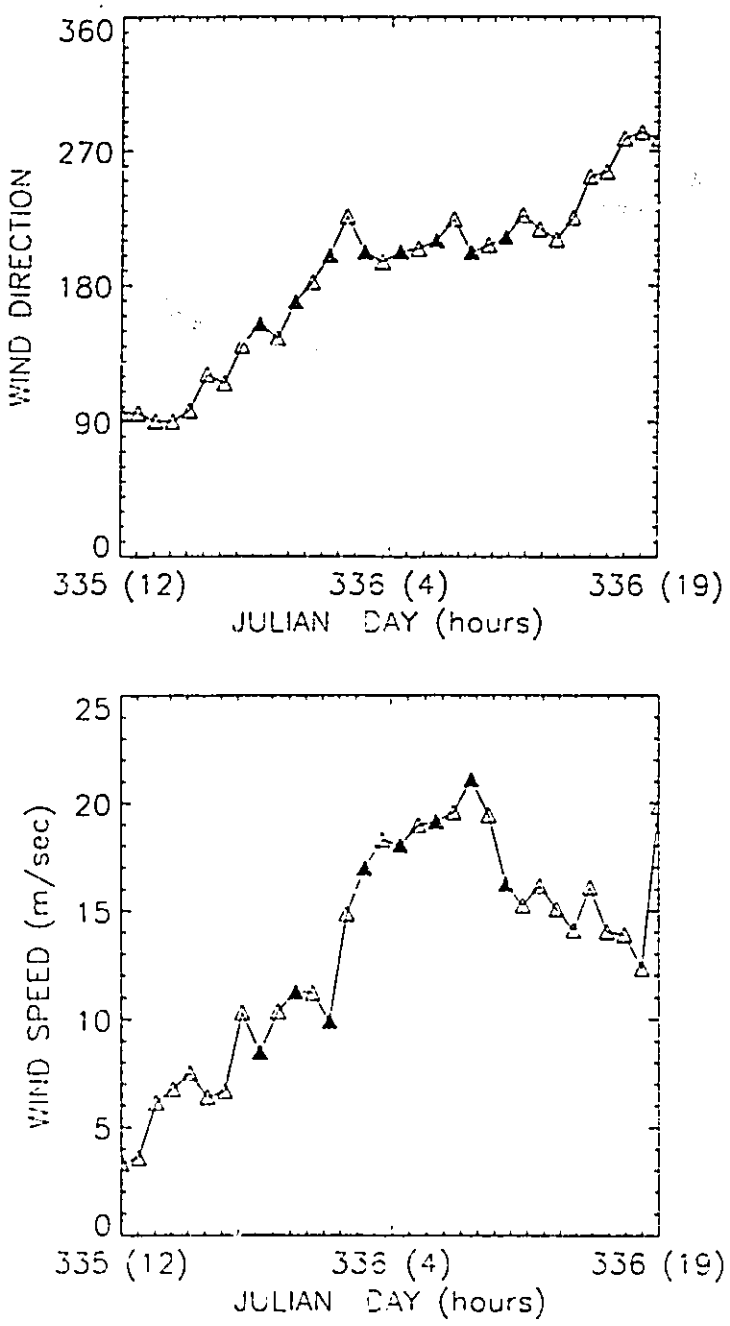

Fig.12.16 Wind direction and wind speed history for the third selected case of westerly turning winds.

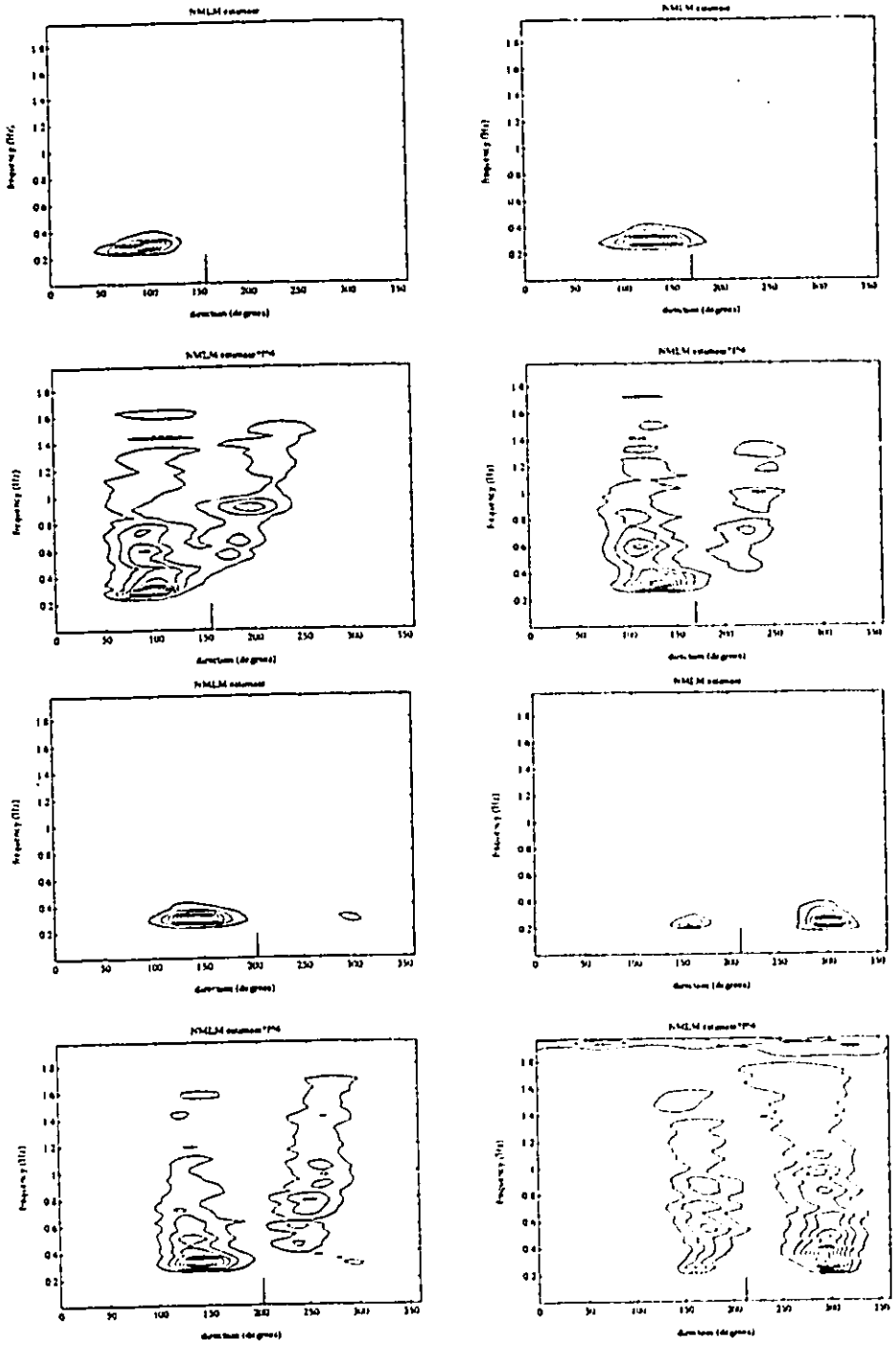

Fig.12.17 Directional spectrum estimate and directional spectrum estimate multiplied by f^4. Contours are equally spaced from maximum energy to zero energy. The wind direction is indicated by the solid line at the bottom of each plot. Top left 2 plots: 85335.20, top right: 85335.22, bottom left: 85336.00, bottom right: 85336.02.

generation of a new sea is observed on the west side of the current, as the old sea (on the eastern side) decays on its own. At any time, there seems to be little (if any) energy propagating against the current. As the wind moves about the current main axis, wind energy is transmitted into wave generation on either side of the current, but not against it.

12.5. DISCUSSION

Figure 12.18 shows the theoretical wavenumber response of the Lake St.Clair array, as computed in Chapter 4 (using the MLMC estimate as a target), plotted with the measured response. It can be seen that the measured response differs from the theoretical one at both low and high frequencies. At low frequencies, this is probably an indication that digitization errors become of the same order of magnitude as the difference in water elevation between adjacent wavestaffs. It should also be noted that there is little wave energy in Lake St.Clair at frequencies lower than about 0.25 Hz. At higher frequencies the discrepancies are more difficult to explain. For the case presented in Figure 12.18, a given wavenumber is associated with a higher frequency than predicted by theory. This is consistent with Doppler shifting of the waves by the strong currents. For a current velocity U (where U is positive in the wave direction) and a wavenumber k, the Doppler shifted frequency $\omega^{\bullet}$ is given as a function of ω by:

$$\omega^{\bullet} = \omega + k\,U \tag{12.7}$$

Figure 12.19 shows the wavenumber-frequency relationship for positive currents of various velocity. This idea was tested against several St.Clair cases but wasn't found to be conclusive. The measured k–f curve was almost always found to lie below the theoretical one, even when the waves were propagating against the current. The fact that the waves do not follow the simple relationship expressed in 12.7 might not be surprising after all. Wave-current interaction has not

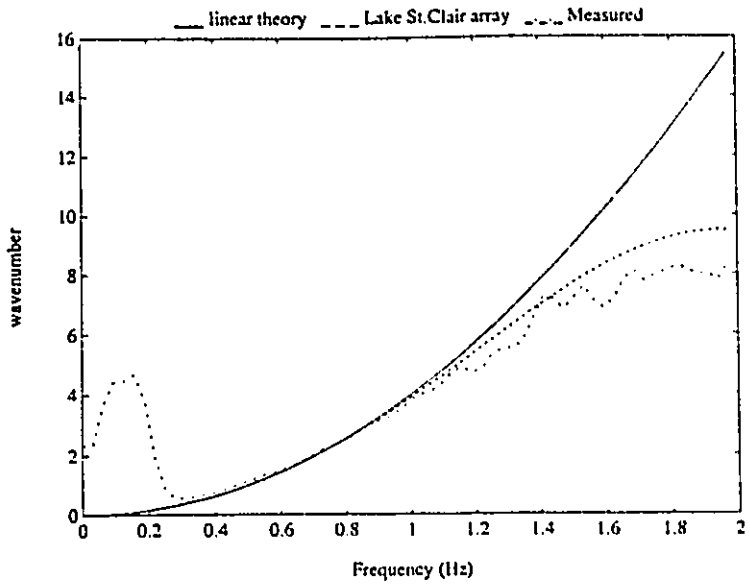

Fig.12.18 Theoretical and measured response of wavestaff array with respect to calculation of water surface slopes. Solid line is linear theory, dashed line is theoretical response and dash-dotted line is the measured response.

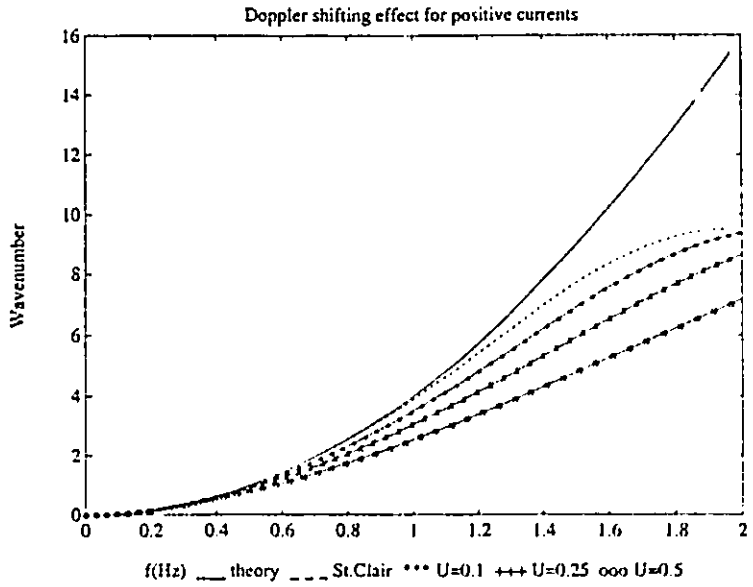

Fig.12.19 Doppler shifting effect for waves traveling in the direction of a current.

been extensively studied and is very complicated. The simplest case is that of deep-water waves on a uniform current. In Lake St.Clair, the uniform current hypothesis cannot be accepted since there are considerable velocity gradients in both the vertical and horizontal directions. In cases of high winds, both the surface current velocity and direction can vary with depth (Wu and Tsanis, 1991). In addition to that, in situations of non-uniform currents, wave energy is not conserved since there is an exchange of energy with the mean current (Peregrine, 1976). Also, the presence of waves affects the mean current profile, due to the additional mass transport (Stokes drift) caused by the waves (Srokosz, 1986). Experimental evidence also points out the fact that the wave profile is affected in the presence of currents (Kemp and Simons, 1982).

Considering the effect of all those factors, it becomes extremely difficult to try to express the field observations within the framework of a wave-current model. This would require considerable work which would be well beyond the aim of the present investigation. Nevertheless, some of the observed features in Lake St.Clair can be relevant in understanding some aspects of the complex interaction between waves and currents.

The cases studied indicate that wave refraction due to the hydraulic current is important in Lake St.Clair. The preliminary results presented above indicate that only the lower frequency components are affected, the higher frequency components tending to be aligned with the wind direction. Results also indicate that bimodal distributions due to refraction processes are very likely to be observed if the wind direction is sufficiently different than the wind direction (runs 85311.20 and 85320.06). In such cases, one mode seems to be consistent with the wind direction, the other with the refracted wave field. In cases where the wind direction is closer to the current direction (run 85270.22), the spectrum stays unimodal.

The cases of winds blowing against a current are more complex. The currents are relatively strong but are nevertheless relatively small when compared to the celerity of the larger waves. For large enough currents, waves will not be able to propagate (Peregrine, 1976). Then, assuming the current is strong enough to suppress the formation of short waves, this would in turn inhibit the formation of longer waves which feed and grow upon the shorter ones. Still, this argument is not very intuitively sound as we know that waves form on rivers with current velocities significantly larger than the one measured in Lake St.Clair. Similarly to the argument put up by Donelan (1980) in examining fetch-gradient effects, one could argue that in areas with significant current-velocity gradients, the waves will use a path of less resistance if the gain in momentum is sufficient enough to compensate for the smaller generating force of the wind. In order to supplement the previous assertion, the theoretical wind-wave direction relationship due to fetch-gradient was recalculated under the assumption that the hydraulic current would inhibit wave formation, thus effectively acting as a boundary. The results, shown in Figure 12.20 indicate that a significant part of the observed discrepancies between wind and wave directions is now accounted for. As a result, the remainder of the difference between wind and wave directions can now be more easily attributed to wave refraction processes. A far better understanding of the exact process would have been reached if continuous data had been available. The 20 minutes dataset every 2 hours yielded good directional information, but the fine details of the directional relaxation of the spectrum are left unknown. It is still not clear if at some point wave energy propagates directly against the current, or if the energy shifts from one peak to the other (on each side of the current) without any interaction.

To our knowledge, nothing similar has ever been observed anywhere. This can be partly explained by the fact that Lake St.Clair is characterized by an unusually low residence

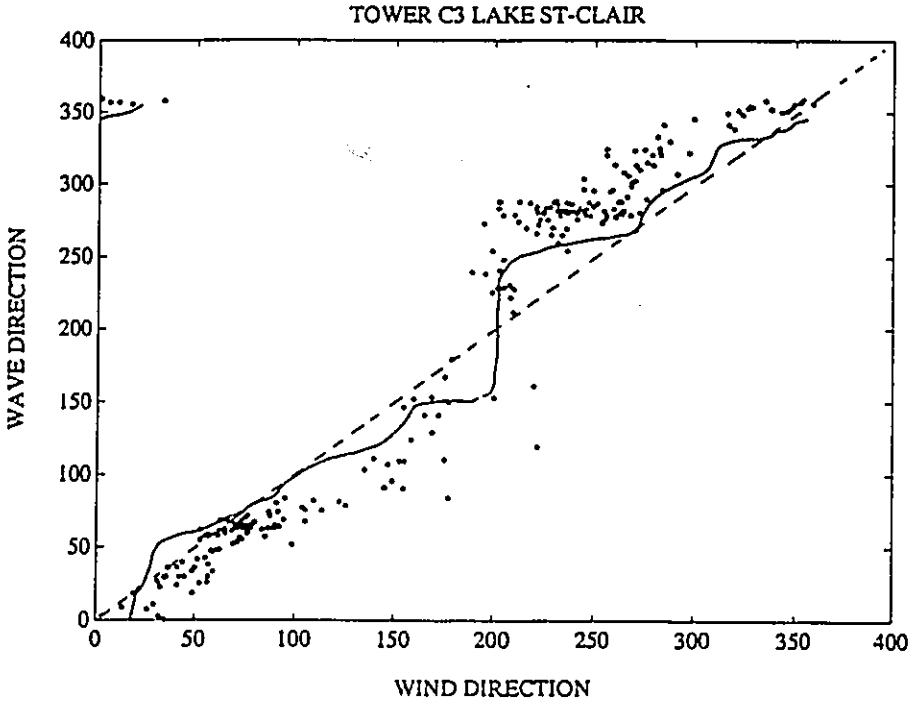

Fig.12.20 Observed mean wave direction (at $f = f_p$) plotted against wind direction . The solid line is based on the work of Donelan (1980) and takes into account fetch-gradient effect and uses the shear current as a solid boundary, whereas the dashed line is the line of perfect agreement.

time, causing strong currents and especially steep horizontal velocity gradients. These conditions are not likely to be met in the open ocean where most of the directional information is obtained. Even if other similar lakes are studied, the complex wave energy structure might not have been observed without the use of high-resolution directional spectrum estimates.

Finally, it should be pointed out that the original directional results that prompted this investigation, were obtained using the Direct Fourier Transform method of Longuet-Higgins et al.(1963), a method which was shown to produce inaccurate results, especially in the case of bimodal seas. Part of the observed discrepancies between wind and wave directions is also probably due to the use of that method to calculate the mean wave direction.

12.6. CONCLUSION

The results from this study clearly indicate that the wavefield structure of lakes as small as Lake St.Clair can be very complicated and display significant directional effects. Indeed, bimodal spectra in Lake St.Clair seem to be the norm for a wide range of frequency bands. Many of the observed features seem to be consistent with the idea of complex wave-current interaction in the shallow lake. Some of the findings indicate that bimodal spectra can be the result of refraction of the wavefield by spatially varying currents, and that the wave direction of propagation might be biased toward directions where the component of the current against the wave might be reduced.

The Lake St.Clair study clearly outlines the need for using high resolution directional spectrum estimates to resolve the fine details of the energy distribution, and help to better understand the behavior of wavefields in various environmental conditions.

CHAPTER 13

GENERAL CONCLUSION AND FUTURE RESEARCH

Because conclusions on various specific aspects of the work have already been presented at the end of the first part of this dissertation and in the previous three Chapters, this final conclusion will focus on the achievements of this work and suggestions for future studies.

13.1. ACHIEVEMENTS OF PRESENT STUDY

13.1.1. Wave directional spectrum estimation

On the topic of wave directional spectrum estimation, which was the main focus of this dissertation, the following points should be stressed:

* A review of existing methods of estimating the wave directional spectrum was achieved.
* A comparison of existing estimates was made on the basis of various model tests and field data, for both pitch-roll and wavestaff data.
* All existing methods were evaluated and all were found to have shortcomings.
* As a result, new methods of estimating the wave directional spectrum were developed and subsequently tested against existing methods, using both unimodal and bimodal model test cases.

* The corrected form of the Maximum Likelihood Method (MLMC) developed in this work was found to achieve better resolution than all other methods, for both pitch-roll-heave data and wavestaff data.

* Comparison of all methods with field data indicated that the higher resolution potential of wavestaff arrays may be lost due to inconsistencies present in the cross-spectra, probably due to the assumption of a perfectly linear wavefield, and thus making pitch-roll-equivalent methods (such as the MLMC) a better choice in many cases.

On slightly different but related topics:

* An integrated software for the analysis of directional seas was developed by linking various routines under the MATLAB platform. The routines are complete, versatile and allow most aspects of wavefields to be investigated using both heave-pitch-roll and wavestaff data.

* The two main methods of generating directional sets of water elevation data were investigated and found to have shortcomings, at least from the viewpoint of testing directional spectrum estimates.

* A procedure to test the theoretical slope response (when slopes are evaluated from wavestaff arrays) of wavestaff arrays was developed, procedure which could help improve array designs.

* A routine was developed to fit two spreading functions to a unimodal distribution. The procedure involves a least-square minimization of a function with four independent parameters. The routine was subsequently used in many aspects of this work.

13.1.2. Field study

The analysis of field data, although merely an attempt at demonstrating the potential of higher resolution directional spectrum methods, nevertheless yielded interesting information. Specifically:

* Completely decoupled spectra were observed for the first time in rapidly turning winds, thus confirming the computational work of Young et al.(1987).

* Correlations obtained between $\partial\theta_m(\omega)/\partial t$ and $\omega \sin(\theta_w - \theta_m(\omega))$ were significantly higher than all previous studies.

* For the first time a clear dependency between the wave relaxation parameter and the frequency was observed.

* Various aspects of the relationship between wind and wave direction were investigated in Lake Ontario.

* Directional spreading parameters (β) values were found to be higher than the established values in previous studies, for both Lake Ontario and Atlantic Ocean data. In addition, the Atlantic Ocean directional spectra were found to be narrower than their Lake Ontario counterpart.

* High frequency bimodal distributions were found to be very common in Lake Ontario, and, in a preliminary investigation, were linked to the wind speed.

* Work with Lake St.Clair data showed that the structure of directional spectra can be very complicated, even in Lakes as small as Lake St.Clair.

* The strong hydraulic/wind-induced current caused by the St-Clair/Detroit river systems was found to have a significant effect on the wave directional spectrum. The shear current, besides causing refraction of the incoming wavefields was found to inhibit the generation of waves propagating directly against it.

13.2. FUTURE WORK

13.2.1. Evolution of wave fields

In this work, theoretical foundations and testing procedures were established to evaluate and compare different methods of extracting the wave directional spectrum from a wave record. A number of methods were examined, their properties, characteristics and biases identified, and as a result, guidelines for the use of these methods were drawn. Extensive testing and comparison with field data showed that very good resolution directional spectrum estimates can be obtained with both pitch-roll buoys and wave-staff arrays. Now that the fundamental ground work has been cleared, the main objective should now focus on the study of the evolution of wave fields. Results presented in the second part of this work, although interesting, were obtained from a preliminary and basic investigation. Using high-resolution directional spectrum estimates, much more could be accomplished.

The SWADE dataset is extensive. Extensive analysis of the data using the exact form of the MLM developed in this work could provide valuable information on the generation, attenuation and relaxation of wave fields. Such information is already available in the frequency domain but little has been done in the directional domain as well. As an example, a study oriented toward the relaxation of wavefields in turning winds could make use of the entire

SWADE dataset in order to select a few ideal cases of turning winds with little or no swell influence and constant wind speed. In addition to looking at the mean direction response of various frequency bands, the variation in the shape of the spectrum (as reflected by higher-order statistics, RMS spread and spreading parameter values) should also be looked at.

On the same note, the shape of the angular distribution of energy should be investigated on a wider basis than the studies done in Chapter 11. Special care should be taken in selecting "ideal cases" of fully developed spectrum so as to reduce the observed scatter. By doing so for both Lake Ontario and the Atlantic Ocean, one could resolve the problem addressed in Chapter 11 in which the Atlantic Ocean directional spectra were found to be narrower on average. Work in Lake Ontario should make use of better slope estimates as discussed in Chapter 9. Also, high frequency bimodal spectra should be given more attention as they constitute an interesting problem. As far as possible, confirmation of the observations from another body of water would be useful. As a possible starting point, an attempt should be made to correlate the onset of the phenomenon with various wave parameters such as the relative or dimensionless frequency. The angle formed by the bimodal distributions whose spacing increases with frequency, should be measured.

13.2.2. Wave directional spectrum estimation

Even if it is thought that the focus of future work be put on the analysis of field data, this should not mean in any way that the work on methods of estimating the wave directional spectrum should stop. Directional spectrum estimation from heave-pitch-roll buoys has come a long way and the exact form of the MLM might have reached what could be potentially considered "an optimum resolution method" for a three signals device but, that does not mean

that other methods yet to be implemented, could perform as well and be used with arrays of wavestaffs. As stated earlier, it would seem that the level of resolution that can be obtained from a pitch-roll-buoy, compared to its maximum potential, is significantly better than the one for a 6 wavestaffs array which uses twice as many measurements. Areas of research specifically linked to this work should be specifically focused on wavestaff arrays where the most potential resolution gain is to be made. Essentially, work should be done on how to accurately and easily calculate the wavenumber, since the assumption of a perfectly linear wavefield can induce inconsistencies (even for very slightly non-linear wavefields) that will reduce the directional spectrum resolution. As discussed earlier, the use of wavestaffs to calculate slopes and subsequently the wavenumber, is not a solution unless the slopes can be shown to be accurately approximated. Otherwise the true slopes (and hence the true wavenumber) are masked by a weighting function characteristic of the array. More work could be done on the NMLM and CMLM methods. More specifically, spreading-dependent windowing schemes could be used with the CMLM and refinements could be made on the NMLM normalizing scheme so as to make it more "expert-system" like. Or an approximate version of the MLMC could be implemented by forcing the system to be positive. However, since these methods are ultimately based on the MLM estimate, it does not take care of the fundamental problem of noise effects. It is therefore recommended that the most urgent work deals with:

1- Investigating the effect of noise on cross-spectra between various water surface elevation signals. As there is no method we are aware of to correctly simulate noise directly at the CPSD level, the only other way to go is to add noise directly at the wavestaff level. But, in order to add random digitization errors at that level requires the capability of accurately simulating water surface elevation of directional seas, a problem which is not simple, as previously discussed in

Chater 4. A better understanding of the effect of noise on CPSD could potentially lead to methods of effectively filtering or removing most of the noise, thus allowing the use of the MLMC method, which was shown to have great potential in resolving all cases of mixed seas.

2- A search for new methods of estimating wave directional spectra should be continued with emphasis on methods dealing with signals contaminated with noise. Literature in the fields of data processing and acoustics should be reviewed as they constantly have to deal with such problems.

13.2.3. Wave-Current Interaction in Lake St.Clair

Arguably, the most puzzling results of this work were obtained in Lake St.Clair. Clearly, there is a need for experimental data to confirm the findings. Experimental work with wind generated waves against a shear current in the middle of a large basin could go a long way in helping to understand the phenomena. Possibly, remote sensing data could yield more information by studying, for example, whitecaps in cases of south-westerly winds. Additional observations of the phenomenon (from the water surface or not) would considerably strengthen the arguments. Supplementing the actual data set with continuous recording in cases of turning winds (and not only 20 minutes every 2 hours) could provide invaluable information. Finally, from a theoretical viewpoint, a wave-current model could be applied to Lake St-Clair. The current structure is already known and would need to be coupled with a wave model. This is not by any means simple because, as pointed out by Peregrine (1976), wave energy is not conserved, as there is a net exchange of energy between the current and the waves. Work done by Tolman (1990) addresses some points on how to tackle the problem.

REFERENCES

Allender, J.H., Albrecht, J., and Hamilton, G., 1983: Observations of directional relaxation of wind sea spectra. *J. Phys. Oceanogr.* , 13, 1519-1525.

Anctil, F., Donelan, M.A., Forristal, G.Z., Steele, K.E., and Ouellet, Y., 1992: Deep water field evaluation of NDBC-SWADE 3 meter discus directional buoy. *J. of Atmos. and Ocean. Tech.* , (to appear).

Barnett, T.P., and Kenyon, K.E., 1975: Recent advances in the study of wind waves. *Rep. Prog. Phys.* , v.38, 667-729.

Bishop, C.T., and Donelan, M.A., 1988: Waves and wave forecasting. *Civil Engineering practice 3- Geotechnical/Ocean engineering.* , Chap 20, 653-695.

Blaisdell, M.A., Tsanis, I.K., and Krestinitis, Y., 1991: Modelling the steady-stage circulation in a distorted physical model of the Windemere basin. *Can. J. Civ. Eng.*, 18, 756-764.

Borgman, L.E., 1969: Directional spectra models for design use. *Offsh. Tech. Conf.* , Houston, Amer. Inst. Mining Metallurg. Petrol. Eng. and others, 721-746.

Burg, J.P., 1967: Maximum entropy spectral analysis. *Proc. 37th Int. Soc. Explor. Geophys.* , Oklahoma city.

Capon, J., 1969: High-resolution frequency-wavenumber spectrum analysis. *Proc. IEEE* , 57, 1408-1418.

Cartwright, D.E., and Smith, N.D., 1964: Buoy techniques for obtaining directional wave spectra. *Buoy Technology, Washington* , D.C., Marine Tech. Soc., 112-121.

Charnock, H., 1955: Wind stress on a water surface. *Quart. J. Roy. Meteor. Soc.* , 81, 639-640.

Davis, R.E., and Regier, L.A., 1977: Methods for estimating directional wave spectra from multi-element arrays. *Jour. Mar. Res.* , 35, 453-477.

Dean, R.G., and Dalrymple, R.A., 1984: Water wave mechanics for engineers and scientists. *Prentice-Hall* , 353p.

Donelan, M.A., 1980: Similarity theory applied to forecasting of wave heights, periods and directions. *Proc. Canadian. Coastal Conf.*, 47-61.

Donelan, M.A., Hamilton, J., and Hui, W.H., 1985: Directional spectra of wind-generated waves. *Phil. Trans. R. Soc. Lond.*, A-315, 509-562.

Gottfried, B.S., and Weisman,J., 1973: Introduction to optimization theory. *Prentice-Hall Inc.* , 571 p.

Harris, F.J., 1978: On the use of windows for harmonic analysis with the discrete fourier transform. *IEEE Proc.* , 66, 51-83.

Hashimoto, N., Kobune, K., and Kameyama, Y., 1987: Estimation of directional wave spectrum using the bayesian approach, and its application to field data analysis. *Rep. of the Port and Harb. Res. Inst.* , 57-99.

Hasselman, D.E., Dunckell, M., and Ewing, J.A., 1980: Directional wave spectra observed during JONSWAP 1973. *J. Phys. Oceanogr.* , 10, 1264-1280.

Herbers, T.H.C., and Guza, R.T., 1990: Estimation of directional wave spectra from multi-components observations. *J. Phys. Oceanogr.* , 20, 1703-1724.

Hui, W.H., 1980: Three dimensional nonlinear evolution of water waves. *in: Nonlinear partial differential equations in engineering and applied sciences* , Marcel Dekker Inc., New-York, 167-187.

Hui, W.H., and Hamilton, J., 1979: Exact solutions of a three-dimensional nonlinear Schrodinger equation applied to gravity waves. *Jour. Fluid Mech.* , 93, 117-133..sp

IAHR, International Association for Hydraulic Research, 1987: List of sea state parameters. *in: Wave analysis and generation in laboratory basins* . XXII Congress, Lausanne, Suisse, 11-74.

Isobe, M., Kondo, K., and Horikawa, K., 1984: Extension of the MLM for estimating directional wave spectrum. *Symp. on Desc. and Model. of Direc. Seas* , Tech. University, Denmark, A-6, 1-15.

Jefferys, E.R., 1986: Comparison of three methods for calculation of directional spectra. *Proc. 5th Int. Off. Mech. and Artic Eng. Symp.* , Tokyo, Japan, 45-50.

Jefferys, E.R., Wateham, G.T., Ramsden, M.A., and Platts, M.J., 1981: Measuring directional spectra with the MLM. *Proc. Directional Wave Spectra App. Conf., University of California* , Berkeley, California, 203-219.

Kemp, P.H., and Simons, R.R., 1982: The interaction between waves and a turbulent current: waves propagating with the current. *Jour. Fluid Mech.* , 116, 227-250.

Kinsman, B., 1965: Wind waves, their generation and propagation on the ocean surface. *Prentice-Hall* , 679p.

Kobune, K., and Hashimoto, N., 1986: Estimation of directional spectra from the maximum entropy principle. *Proc. 5th Int. Off. Mech. and Artic Eng. Symp.* , Tokyo, Japan, 80-85.

Krogstad, H.E., Gordon, R.L., and Miller, M.C., 1988: High-resolution directional wave spectra from horizontally mounted acoustic doppler current meters. *Jour. Atmos. Oceanic Tech.* , 5, 340-352.

Kuik, A.J., VanVledder, G.P., and Holthuijsen, L.H., 1988: A method for the routine analysis of pitch and roll buoy wave data. *J. of Phys. Oceanogr.* , 18, 1020-1034.

Lacoss, P., 1971: Data adaptive spectral analysis methods. *Geophys.* , 36(4), 661-675.

Lawson, L.M., and Long, R.B., 1983: Multimodal properties of the surface wave field observed with pitch-roll buoys during GATE. *J. of Phys. Oceanogr.* , 13, 474-486.

Lighthill, J.G, 1978: Waves in fluids. *Cambridge University Press* , 504p.

Long, R.B., 1980: The statistical evaluation of directional spectrum estimates derived from pitch/roll buoy data. *J. of Phys. Oceanogr.* , 10, 944-952.

Long, R.B., and Hasselmann, K., 1979: A variational technique for extracting directional spectra from multi-component wave data. *J. of Phys. Oceanogr.* , 9, 373-381.

Longuet-Higgins, M.S., Cartwright, D.E., and Smith, N.D., 1963: Observations of the directional spectrum of sea waves using the motions of a floating buoy. in *Ocean Wave Spectra* , Prentice-Hall, New-Jersey, 111-132.

Lygre, A., and Krogstad, H.E., 1986: Maximum entropy estimation of the directional distribution in ocean wave spectra. *J. Phys. Oceanogr.* , 16, 2052-2060.

Marsden, R.F., and Juszko, B.-A., 1987: An eigenvector method for the calculation of directional spectra from heave, pitch and roll buoy data. *J. Phys. Oceanogr.* , 17, 2157-2167.

Masson, D., 1990: Observations of the response of sea waves to veering winds. *Jour. Phys. Oceanogr.*, v20, 1876-1885.

Miles, M.D., 1989: A note on directional random wave synthesis by the single summation method. *Proc. of the 23rd IAHR Congress*, Ottawa, Canada, C, 243-250.

Miles, M.D., and Funke, E.R., 1987: A comparison of methods for synthesis of directional seas. *Proc. 6th Int. Off. Mech. and Artic Eng. Symp.*, Houston, Texas, 247-255.

Mitsuyasu, H., Tasai, F., Sabara, T., Mizuno, S., Okusu, M., Honda, T., and Rikiishi, K.,1975): Observation of the wave directional spectrum of ocean waves using a clover-leaf buoy. *Jour. Phys. Oceanogr.*, v5, 750-760.

NODC Users Guide, 1991: Key to Oceanographic Records Documentation No. 14., *National Oceanographic Data Center*, Washington, DC, US Department of Commerce.

Nwogu, O., 1989: Maximum entropy estimation of directional wave spectra from an array of wave probes. *App. Ocean Res.*, 176-182.

Nwogu, O.U., Mansard, E.P.D., Miles, M.D., and Isaacson, M., 1987: Estimation of directional wave spectra by the maximum entropy method. *Proc. 6th Int. Off. Mech. and Artic Eng. Symp.*, IAHR Seminar on wave generation and analysis in laboratory wave basins, Lausanne, Switzerland, 363-376.

Oakley, O.H., and Lozow, J.B., 1977: Directional spectra measurements by small arrays. *Proc. Offsh. Tech. Conf.*, Houston, 155-166.

Oltman-Shay, J., and Guza, R.T., 1984: A data adaptive ocean wave directional spectrum estimator for pitch/roll type measurements. *J. Phys. Oceanogr.*, 14, 1800-1810.

Pawka, S.S., 1983: Island shadows in wave directional spectra. *J. Geophys. Res.*, 88, 2579-2591.

Peregrine, 1976: Interaction of water waves and currents. *Adv. Appl. Mech.*, 16, 9-117.

Phillips, O.M., 1977: Dynamics of the upper ocean. *Cambridge University Press*, 2nd edition, 336p.

Press, W.H., Flannery, B.P., Teukolsky, S.A, and Vetterling, W.T., 1986: Numerical recipes, the art of scientific computing. *Cambridge University Press*, 818p.

Schwab, D.J., Clites, A.H., Murthy, C.R., Sandall J.E., Meadows, L.A., and Meadows, G.A., 1989: The effect of wind on transport and circulation in Lake St.Clair. *Jour. Geophys. Res.*, 94 (C4), 4947-4958.

Shore Protection Manual, 1984: U.S. Army Corps of Engineers, Coastal Engineering Research Center, Vicksburg, Mississipi. v.I,II.

Srokosz, M.A., 1987: Models of wave-currert interaction. *Advances in Underwater Technology, Ocean Science and Offshore Engineering* , 12, 313-325.

Steele, K.E., Wang, D.W., Teng, C.C, and Lang, N.C., 1990: Directional Wave measurements with NDBC 3-meter Discus Buoys. *U.S. Department of Commerce, NOAA, NDBC, Stennis Space Center* , #1804-01.05, 1-35.

Steele, K.E., Lau, J.C., and Hsu, Y.L., 1985: Theory and application of calibration techniques for an NDBC directional wave measurements buoy. *IEEE J. Oceanic Eng.* , OE-10 (4), 382-396.

Tolman, H.L., 1990: Wind wave propagation in tidal seas. *Communications on hydraulic and geotechnical engineering* , Delft University of Technology, report nr. 90-1. 170p.

Tsanis, I.K., and Brissette, F.P., 1992: Wave directional spectra studies in Lake Ontario. *J. Great Lakes Res.* , 18 (3), 489-506.

Tsanis, I.K., and Brissette, F.P., 1991: A wave directional spectra program for wave gauge arrays. *Env. Soft.* , 6 (3), 151-160.

Tsanis, I.K., and Wu, J.J., 1990: Hydrodynamic Modelling of Lake St.Clair. *Atmospheric Environment Service (AES) report.*

Tsanis, I.K., and Donelan, M.A., 1989: Wave directional spectra in mixed seas. *Proc. 2nd Int. Workshop on Wave Hind. and Fore.* , 387-396.

Tsanis, I.K., and Donelan, M.A., 1987: The WAVES Program on the CCIW Research Tower. *National Water Research Institute (NWRI) Report No.87-65* , Reasearch and Applications Branch, Canada Centre for Inland Waters.

Ulrych, T.J., and Bishop, T.N., 1975: Maximum entropy spectral analysis and autoregressive decomposition. *Rev. Geophys. Space Phys.* , 13, 183-200.

Ursell, F., 1956: Wave generation by wind. *in Surveys in Mechanics., London, Cambridge University Press* , 216-249.

VanVledder, G.P., and Holthuijsen, L.H., 1988: Waves in turning windfields. *Proc. 21st Coastal Eng. Conf.*, ASCE, Malaga, Spain, 602-611.

Venkatesh, S., Donelan, M.A., Graber, H., Liu, P., Schwab, D., and Skafel, M., 1987: Finite depth wind waves - A preliminary analysis of data from a field study on Lake St.Clair. *Am. Meteorol. Soc. Ann. Meeting*, Santa-Barbara. (NWRI Contribution 87-153)

Valdmanis, J., Tsanis, I.K., Donelan, M.A., and Desrosiers, R.J., 1989: The "WAVES" platform and research towers, buoys and instruments, Lake Ontario, *23rd IAHR Conf.*, Ottawa, Canada.

Weller, R.A., Donelan, M.A., Briscoe, M.G., and Huang, N.E., 1991: Riding the crest: A tale of two wave experiments. *B. of Amer. Meteorol. Soc.*, 72(2), 163-183.

Wu, J.J., and Tsanis, I.K., 1991: Quasi three-dimensional circulation modelling for Lake St.Clair. *Proc. 10th Can. Hydrotech. Conf.*, I, 26-35.

Young, I.R., Hasselmann, S., and Hasselmann, K., 1987: Computations of the response of a wave spectrum to a sudden change in wind direction. *J. Phys. Oceanogr.*, 17, 1317-1338.

APPENDIX 1

A simple analogy to the constraint problem of the MLM

In Chapter 3, a derivation of the Maximum Likelihood Method of estimating the wave directional spectrum was presented, using optimization of a function through the constraint that a monochromatic wave without noise be passed with unit gain. The constraint presented in eq. 3.44 can also be derived using a simple example which can help provide a better understanding of the process leading to the MLM estimate.

For any measured property of a physical system, we can say that the measured output M is the result of the summation of an input signal I plus noise N through a filtering process

$$I + N \rightarrow FILTER \rightarrow M \tag{A1.1}$$

At a given time, for a monochromatic wave propagating in direction θ_d, the water surface elevation (Y_j) at sensor j is given by the sum of the signal (see also eq. 2.10) and a noise component ε_j such that

$$Y_j = a\, e^{i(\vec{k}\cdot\vec{r}_j)} + \varepsilon_j \tag{A1.2}$$

with $\vec{k} = (|\vec{k}|\cos\theta_d, |\vec{k}|\sin\theta_d)$ and $\vec{r}_j$ are the (x,y) coordinates of the jth sensor. Through the filtering process, the measured output M_j is given by a convolution equation

$$M_j = \sum_{n=1}^{N} (A_n Y_{j+n-1}) \tag{A1.3}$$

where N is the number of wave sensors and the A's satisfy the condition that a pure signal without noise be passed without change, that is

$$a\, e^{i(\vec{k}\cdot\vec{r}_1)} = \sum_{n=1}^{N} A_n\, a\, e^{i(\vec{k}\cdot\vec{r}_{1,n-1})} \tag{A1.4}$$

dividing both sides by the left-hand-side of eq. A1.4 we find

$$1 = \sum_{n=1}^{N} A_n\, e^{i(\vec{k}\cdot\vec{r}_{n-1})} \tag{A1.5}$$

or

$$1 = A_1 e^{i\vec{k}\cdot\vec{r}_1} + A_2 e^{i\vec{k}\cdot\vec{r}_2} + \ldots\ldots + A_N e^{i\vec{k}\cdot\vec{r}_N} \tag{A1.6}$$

or, in matrix form

$$1 = A^T X = X^T A \tag{A1.7}$$

which is equivalent to Eq.3.44.

APPENDIX 2

Lagrange Multiplier Theory: Unconstrained Optimization

In Chapter 3, it was stated that the unconstrained optimization of the Lagrangian function (eq. 3.45) is in fact equivalent to the optimization of the original function with a constraint. Here we briefly show the equivalence of both approaches, following a similar treatment by Gottfried and Weisman (1973, p.43-45).

We have to optimize the function $F(x,y)$ under the constraint $G(x,y) = c$ where c is a constant. We have to find a minimum of $F(x,y)$,

$$dF = \frac{\partial F}{\partial x}dx + \frac{\partial F}{\partial y}dy = 0 \tag{A2.1}$$

which also satisfies

$$dG = \frac{\partial G}{\partial x}dx + \frac{\partial G}{\partial y}dy = 0 \tag{A2.2}$$

since G is constant over the constraint path. From A1.1 and A1.2 we have:

$$\frac{dx}{dy} = \frac{\partial F/\partial y}{\partial F/\partial x} \quad \text{and} \quad \frac{dx}{dy} = \frac{\partial G/\partial y}{\partial G/\partial x} \tag{A2.3}$$

which can be rewritten as:

$$\frac{\partial F}{\partial y}\frac{\partial G}{\partial x} - \frac{\partial G}{\partial y}\frac{\partial F}{\partial x} = 0 \tag{A2.4}$$

Eq. A2.4 is the necessary condition for $F(x,y)$ to have a minimum under the constraint $G(x,y)$. Now taking the unconstrained function

$$L(x,y,\mu) = F(x,y) + \mu(G(x,y) - c) \tag{A2.5}$$

The necessary conditions for $L(x,y,\mu)$ to have a minimum are given by:

$$\frac{\partial L}{\partial x} = \frac{\partial F}{\partial x} + \mu\frac{\partial G}{\partial x} = 0 \tag{A2.6}$$

$$\frac{\partial L}{\partial y} = \frac{\partial F}{\partial y} + \mu\frac{\partial G}{\partial y} = 0 \tag{A2.7}$$

$$\frac{\partial L}{\partial \mu} = G = c \tag{A2.8}$$

Eliminating μ form A2.6 and A2.7, we find that the necessary condition for the unconstrained optimization is given by

$$\frac{\partial F}{\partial y}\frac{\partial G}{\partial x} - \frac{\partial G}{\partial y}\frac{\partial F}{\partial x} = 0 \tag{A2.9}$$

which is the same as the constrained problem as expressed in A2.4.

APPENDIX 3

The ρ^2 statistics

The statistical test has its origin in Long (1980) and aims at establishing the statistical validity and variability of directional spectrum estimates. The original paper dealt specifically with the parametric approach presented in 3.1, whereas the following is more general in scope (although it is still based on pitch-roll-heave data) and follows Marsden and Juzsko (1987). The estimate $\hat{C}$ of the true Cross-Power-Spectral-Density matrix C is subject to many errors and can be expressed as:

$$C = \hat{C} - \delta\hat{C} \tag{A3.1}$$

such that:

$$\delta\hat{C} = \hat{C} - C \tag{A3.2}$$

and, following Eq. 3.36, we have:

$$\delta\hat{C} = \hat{C} - \int_0^{2\pi} \Xi\, \Xi^H S(\theta) d\theta \tag{A3.3}$$

where $S(\theta)$ is the directional spectrum at a given frequency. Assuming that the estimate of the directional spectrum $\hat{S}(\theta)$ is in fact the true value of the spectrum, then, $\delta\hat{C}$ must be the result of random variability in $\hat{C}$. Using this formulation, we can rewrite Eq. A3.1 as:

$$\delta\hat{C} = \begin{bmatrix} \hat{C}_{11} \\ \hat{C}_{12} \\ \hat{Q}_{12} \\ \hat{C}_{13} \\ \hat{Q}_{13} \\ \hat{C}_{22} \\ \hat{C}_{23} \\ \hat{Q}_{23} \\ \hat{C}_{33} \end{bmatrix} - \hat{C}_{11} \begin{bmatrix} 1 \\ 0 \\ \int_0^{2\pi} k\cos\theta\hat{S}(\theta)d\theta \\ 0 \\ \int_0^{2\pi} k\sin\theta\hat{S}(\theta)d\theta \\ \int_0^{2\pi} k^2\cos^2\theta\hat{S}(\theta)d\theta \\ \int_0^{2\pi} k^2\sin\theta\cos\theta\hat{S}(\theta)d\theta \\ 0 \\ \int_0^{2\pi} k^2\sin^2\theta\hat{S}(\theta)d\theta \end{bmatrix} \qquad \text{(A3.4)}$$

with

$$k = \left[\frac{\hat{C}_{22} + \hat{C}_{33}}{\hat{C}_{11}} \right]^{0.5} \qquad \text{(A3.5)}$$

An estimate of the error of $\delta\hat{C}$ can be obtained as:

$$\rho^2 = \delta\hat{C}^H V^{-1} \delta\hat{C} \qquad \text{(A3.6)}$$

where V^{-1} is the matrix of covariances between the elements of A3.4 (Long and Hasselman, 1979). The elements of V can be calculated using equation 11 of Long (1980) directly from A3.4 and knowing the number of degrees of freedom d_f of the spectral estimates:

$$d_f = 2\,\delta f\; t_r \qquad \text{(A3.7)}$$

where δf is the width of a spectral band and t_r the length of the wave record in seconds. For small errors of $\delta\hat{C}$, ρ^2 follows a χ^2_n distribution where n is the number of elements in the system defined in A3.4 (9 in this case). The normalization of the energy of the directional spectrum to a unit value, as well as the use of A3.5 reduces the value of "n" to 7. Then, at the 80% significance level, any directional spectrum with a value of ρ^2 smaller than 9.8 should be accepted as having an acceptable level of error. As pointed out by Long (1980), statistical validity of an estimate should be accepted as a necessary but not sufficient condition for its acceptance. For example, the Maximum Entropy Method always fits the data exactly ($\rho^2 = 0$) whether or not the estimate is close or not to the real underlying true directional spectrum. In that sense, the statistic is more likely to indicate if we have a bad spectrum than if we have a good one.

APPENDIX 4

Simulation of heave-pitch-roll spectra from wave-staff data

Following equation 3.36, the true cross-power-spectral density (CPSD) matrix that should be measured for a given frequency or frequency band ω_k is:

$$C_{jl}(\omega_k) = \sum_{i=1}^{N} X_j(\theta_i,\omega_k)\, X_l^H(\theta_i,\omega_k)\, S(\theta_i,\omega_k) \tag{A4.1}$$

where, from equation 3.37:

$$X_j(\theta_i,\omega_k) = e^{ik(\cos\theta_i r_{xj}+\sin\theta_i r_{yj})} = e^{i\vec{k}\cdot\vec{r_j}} \tag{A4.2}$$

where $\vec{r_j}=(r_{xj},r_{yj})$ are the x,y coordinates of the jth sensor.

So using (A4.1) with a known directional spectrum $S(\theta_i,\omega_k)$, it is possible to compute the theoretical cross-power-spectral-density matrix. The problem is then to obtain the Heave-Pitch-Roll cross-spectra using this data. The first step is to decide how to calculate the slopes from the wave staff array geometry. The following will use as an example the lake St.Clair and Lake Ontario arrays but can be applied to any array geometry. The radial R (in meters) and angular A (degrees) coordinates of the Lake St.Clair three wave staffs array are given by:

$$R = [\,0.25 \quad 0 \quad 0.25\,] \qquad A = [\,180 \quad 0 \quad 90\,] \tag{A4.3}$$

Denoting the water elevations at each wave staff at any given time by $\eta_1 \quad \eta_2 \quad \eta_3$ we adopt the following convention for the calculations of the heave pitch and roll signals.

$$\eta(t,\vec{x}) = \eta_2 \tag{A4.4a}$$

$$\frac{\partial \eta(t,\vec{x})}{\partial x} = (\eta_1 - \eta_2)/0.25 \tag{A4.4b}$$

$$\frac{\partial \eta(t,\vec{x})}{\partial y} = (\eta_2 - \eta_3)/0.25 \tag{A4.4c}$$

The Fourier transform is a linear transform. Using the following notation for the Fourier coefficients of each wave staffs at each frequency (a_1,b_1) (a_2,b_2) (a_3,b_3) and using the linearity property, we have the following Fourier coefficients for the heave, pitch and roll signals:

$$\eta \rightarrow (a_2,b_2) \tag{A4.5a}$$

$$\frac{\partial \eta(t,\vec{x})}{\partial x} \rightarrow (a_1-a_2,b_1-b_2)/0.25 \tag{A4.5b}$$

$$\frac{\partial \eta(t,\vec{x})}{\partial y} \rightarrow (a_2-a_3,b_2-b_3)/0.25 \tag{A4.5c}$$

As an example, to calculate the cross spectra between the heave and pitch signal, one simply multiplies the heave Fourier coefficients by the conjugate of the pitch Fourier coefficients giving:

$$\frac{1}{0.25}\left[\left[(a_1-a_2)\,a_2 + (b_1-b_2)\,b_2\right] + i\,\left[(a_1-a_2)\,b_2 + (b_2-b_1)\,a_2\right]\right] \tag{A4.6}$$

which can be rearranged to:

$$\frac{1}{0.25}\left[\left[a_1a_2 + b_1b_2 + i(a_1b_2 - b_1a_2)\right] - (a_2^2 - b_2^2)\right] \tag{A4.7}$$

which by definition is equal to $(C_{21} - C_{22})/0.25$. Similarly, taking η, x, y as the subscripts for the heave, pitching and rolling signals, it can be shown that the heave-pitch-roll cross-spectra are given by the following:

$$C_{\eta\eta} = C_{11} \tag{A4.8a}$$

$$C_{xx} = (C_{11} + C_{22} - 2real(C_{12})) /0.25 /0.25 \tag{A4.8b}$$

$$C_{yy} = (C_{22} + C_{33} - 2real(C_{23})) /0.25 /0.25 \tag{A4.8c}$$

$$C_{\eta x} = (C_{21} - C_{22}) /0.25 \tag{A4.8d}$$

$$C_{\eta y} = (C_{32} - C_{22}) /0.25 \tag{A4.8e}$$

$$C_{xy} = (C_{12} + C_{23} - C_{22} - C_{13}) \, 0.25/0.25 \tag{A4.8f}$$

In the case of Lake Ontario, The radial R (in meters) and angular A (degrees) coordinates of the six wave staffs array are given by:

$$R = [\,0.25 \;\; 0.25 \;\; 0 \;\; 0.25 \;\; 0.25 \;\; 0.25\,] \qquad A = [\,0 \;\; 72 \;\; 0 \;\; 288 \;\; 144 \;\; 216\,] \tag{A4.9}$$

The heave pitch and roll signals are calculated using:

$$\eta(t,\vec{x}) = \eta_3 \tag{A4.10a}$$

$$\frac{\partial \eta(t,\vec{x})}{\partial x} = 0.5 \left[\frac{\eta_1 - \eta_3}{0.25} + \frac{2\eta_3 - (\eta_5 + \eta_6)}{2 * 0.2023} \right] \tag{A4.10b}$$

$$\frac{\partial \eta(t,\vec{x})}{\partial y} = 0.5 \left[\frac{\eta_2 - \eta_4}{2 * 0.2378} + \frac{\eta_5 - \eta_6}{2 * 0.1469} \right] \tag{A4.10c}$$

Using the same steps as before, we find that the heave-pitch-roll cross-spectra are given by the following:

$$C_{\eta\eta} = C_{33} \tag{A4.11a}$$

$$C_{xx} = 0.25\, real \left\{ \frac{C_{11} + C_{33} - 2C_{13}}{J^2} + \frac{4C_{33} + C_{55} + C_{66} - 4C_{35} - 4C_{36} + 2C_{56}}{K^2} + \frac{4C_{13} - 4C_{33} + 2C_{35} + 2C_{36} - 2C_{15} - 2C_{16}}{J*K} \right\} \tag{A4.11b}$$

$$C_{yy} = 0.25\, real \left\{ \frac{C_{22} + C_{44} - 2C_{24}}{H^2} + \frac{C_{55} + C_{66} - 2C_{56}}{I^2} + \frac{2C_{25} + 2C_{46} - 2C_{26} - 2C_{45}}{H*I} \right\} \tag{A4.11c}$$

$$C_{\eta x} = 0.5\left[\frac{C_{31}-C_{33}}{J}+\frac{2C_{33}-C_{35}-C_{36}}{K}\right] \tag{A4.11d}$$

$$C_{\eta y} = 0.5\left[\frac{C_{32}-C_{34}}{H}-\frac{(C_{35}+C_{36})}{I}\right] \tag{A4.11e}$$

$$C_{xy} = 0.25\left[\frac{C_{12}-C_{14}-C_{32}+C_{34}}{J*H}+\frac{C_{15}-C_{16}-C_{35}+C_{36}}{J*I}+\frac{2C_{32}-2C_{34}-C_{52}+C_{54}-C_{62}+C_{64}}{K*H}+\frac{2C_{35}-2C_{36}-C_{55}+C_{56}-C_{65}+C_{66}}{K*I}\right] \tag{A4.11f}$$

with:

$$J = 0.25 \qquad K = 0.4046 \qquad H = 0.4756 \qquad I = 0.2938 \tag{A4.12}$$

Using the above two examples, simple rules can be devised and applied to easily calculate the cross-spectra between any quantity obtained from a linear combination of point measurements. Using an array of N wave-staffs and using the fact that the water elevation from one wave staff will be used as the heave signal and that the slopes will be evaluated from a linear combination of all (or a number) the water elevations, we can write:

$$\eta(t,\vec{x}) = \eta_i \tag{A4.13a}$$

$$\frac{\partial\eta(t,\vec{x})}{\partial x} = \alpha_1\eta_1 + \alpha_2\eta_2 + \alpha_3\eta_3 + \ldots\ldots + \alpha_N\eta_N \tag{A4.13b}$$

$$\frac{\partial\eta(t,\vec{x})}{\partial y} = \beta_1\eta_1 + \beta_2\eta_2 + \beta_3\eta_3 + \ldots\ldots + \beta_N\eta_N \tag{A4.13c}$$

from which we can find that the heave, pitch and roll cross-spectra are given by:

$$C_{\eta\eta} = C_{ii} \tag{A4.14a}$$

$$C_{xx} = \sum_{i=1}^{N}\alpha_i^2 C_{ii} + 2\sum_{i=1}^{N}\sum_{j=i+1}^{N}\alpha_i\alpha_j C_{ij} \tag{A4.14b}$$

$$C_{yy} = \sum_{i=1}^{N}\beta_i^2 C_{ii} + 2\sum_{i=1}^{N}\sum_{j=i+1}^{N}\beta_i\beta_j C_{ij} \tag{A4.14c}$$

$$C_{\eta x} = \sum_{j=1}^{N} \alpha_j C_{ij} \tag{A4.14d}$$

$$C_{\eta y} = \sum_{j=1}^{N} \beta_j C_{ij} \tag{A4.14e}$$

$$C_{xy} = \sum_{i=1}^{N} \sum_{j=1}^{N} \alpha_i \beta_j C_{ij} \tag{A4.14f}$$

APPENDIX 5

Unimodal Distributions Test cases: Target Spectra

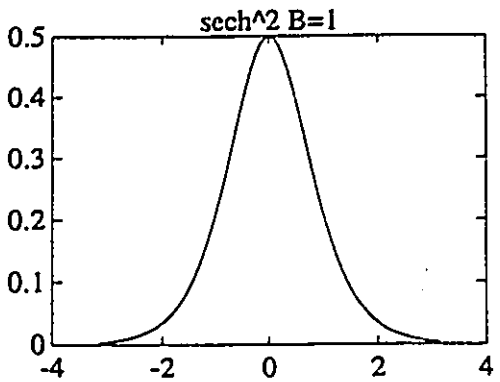
sech^2 B=1
0.5
0.4
0.3
0.2
0.1
0
-4
-2
0
2
4

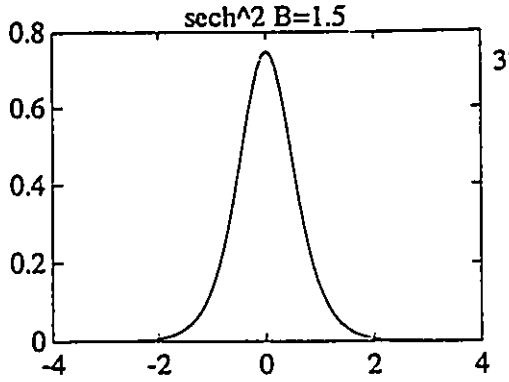
sech^2 B=1.5
0.8
0.6
0.4
0.2
0
-4
-2
0
2
4

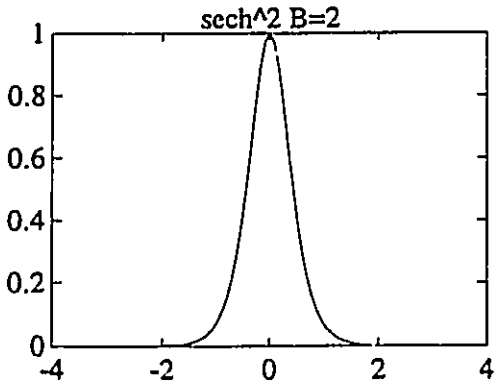
sech^2 B=2
1
0.8
0.6
0.4
0.2
0
-4
-2
0
2
4

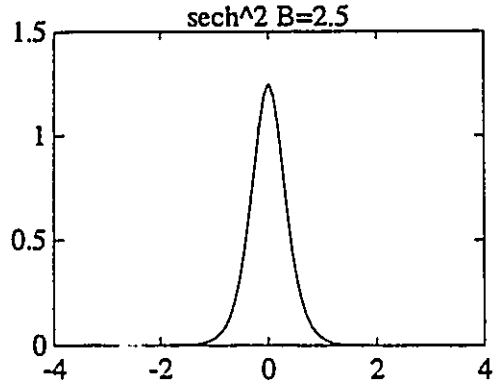
sech^2 B=2.5
1.5
1
0.5
0
-4
-2
0
2
4

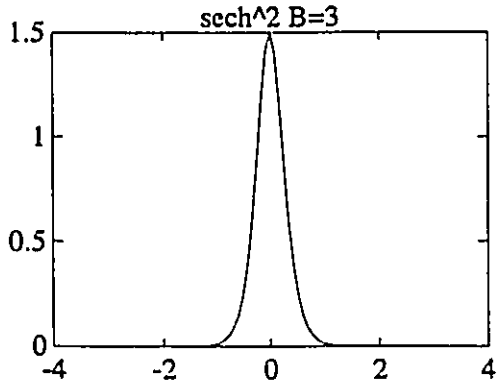
sech^2 B=3
1.5
1
0.5
0
-4
-2
0
2
4

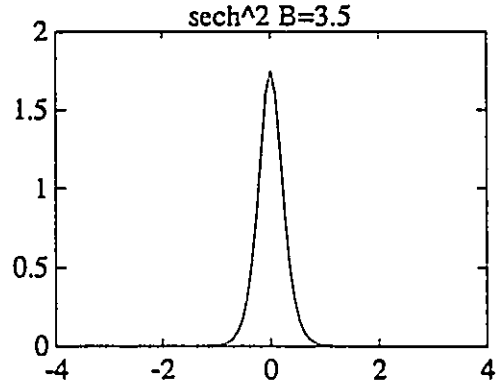
sech^2 B=3.5
2
1.5
1
0.5
0
-4
-2
0
2
4

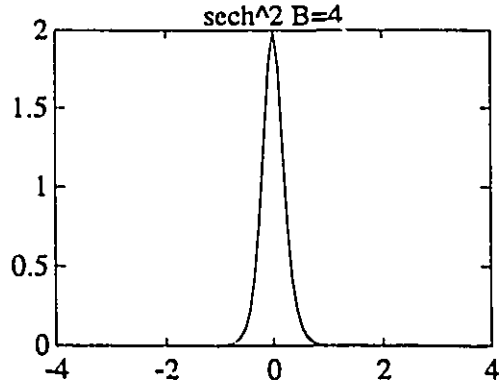
sech^2 B=4
2
1.5
1
0.5
0
-4
-2
0
2
4

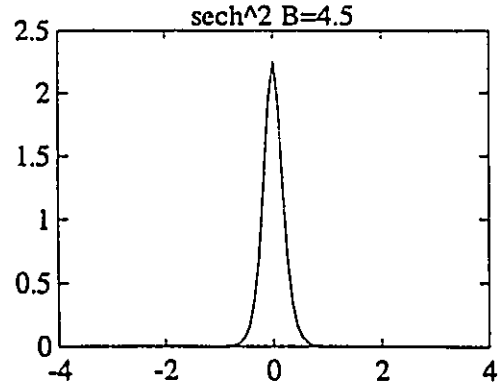
sech^2 B=4.5
2.5
2
1.5
1
0.5
0
-4
-2
0
2
4

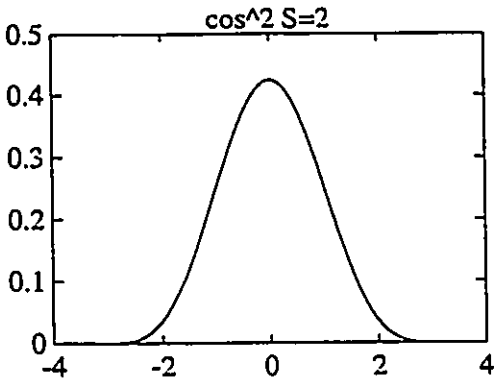
cos^2 S=2
0.5
0.4
0.3
0.2
0.1
0
-4
-2
0
2
4

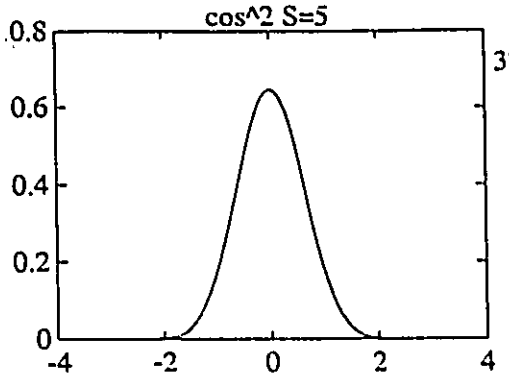
cos^2 S=5
0.8
0.6
0.4
0.2
0
-4
-2
0
2
4

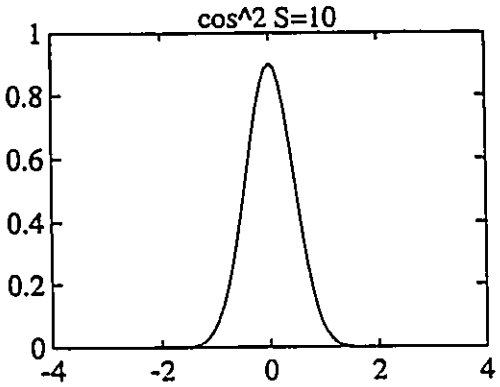
cos^2 S=10
1
0.8
0.6
0.4
0.2
0
-4
-2
0
2
4

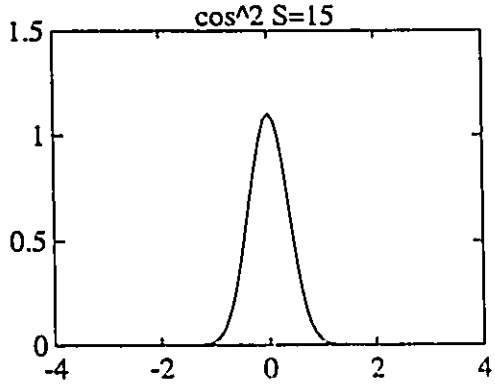
cos^2 S=15
1.5
1
0.5
0
-4
-2
0
2
4

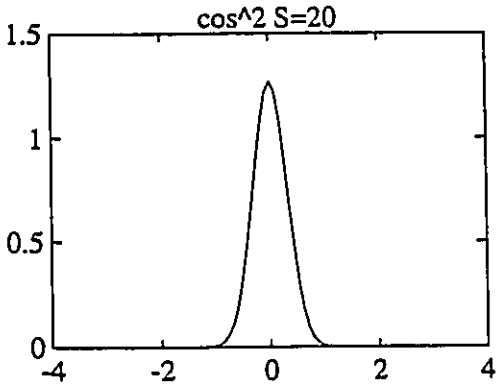
cos^2 S=20
1.5
1
0.5
0
-4
-2
0
2
4

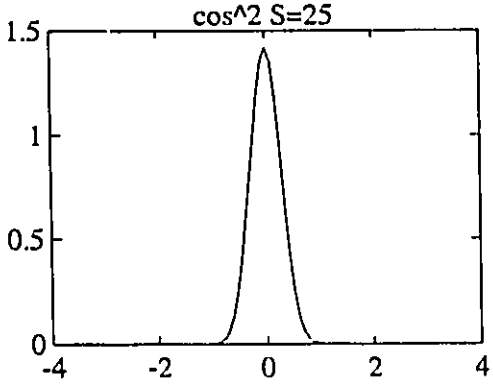
cos^2 S=25
1.5
1
0.5
0
-4
-2
0
2
4

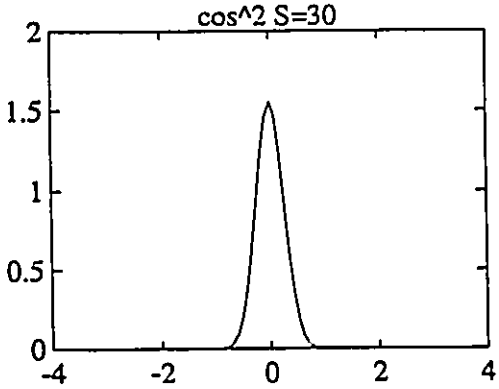
cos^2 S=30
2
1.5
1
0.5
0
-4
-2
0
2
4

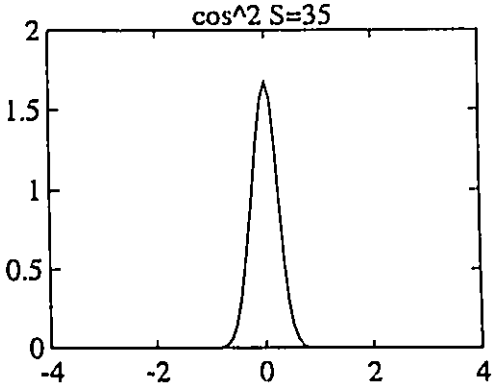
cos^2 S=35
2
1.5
1
0.5
0
-4
-2
0
2
4

APPENDIX 6

Bimodal Distributions Test cases: Target Spectra

Each plot display the same distributions and spacing but with different energy ratios varying from 1 (equal energy of distributions) to 4. A total of 72 bimodal distributions are shown in 18 plots. The first two numbers on top of each plot refer to the values of the spreading parameter β and the third number to the spacing between both $sech^2$ distributions in degrees.

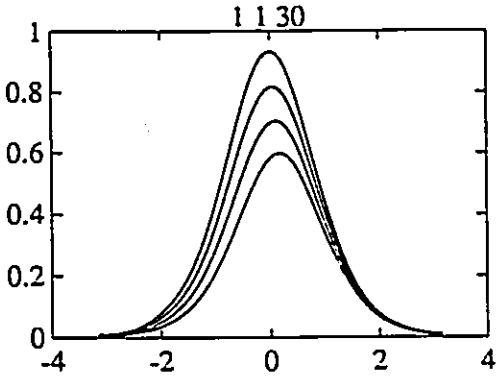
1 1 30

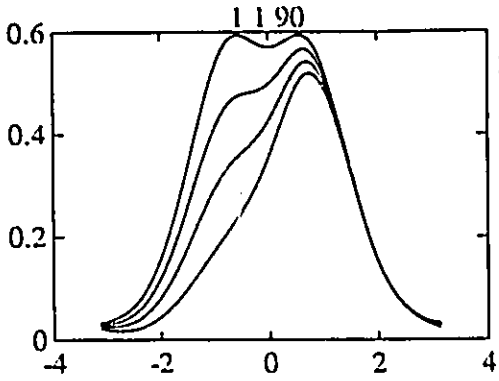
1 1 90

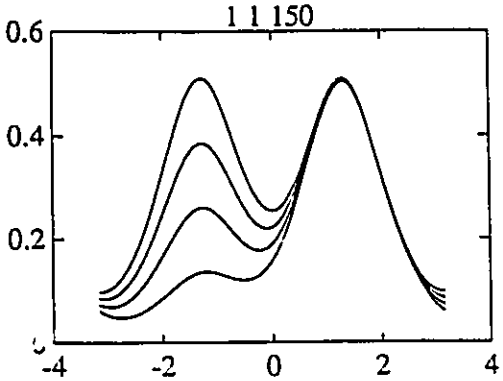
1 1 150

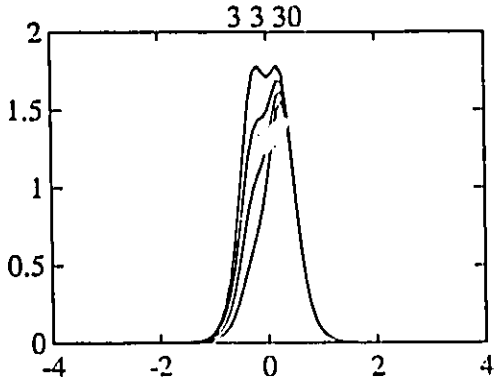
3 3 30

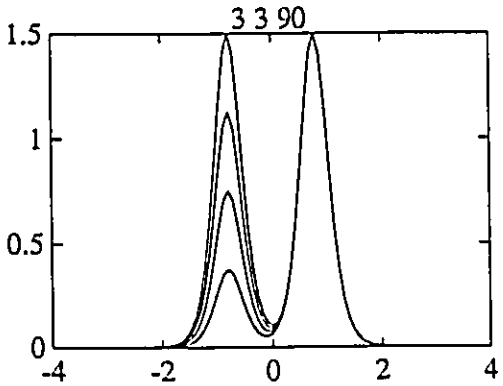
3 3 90

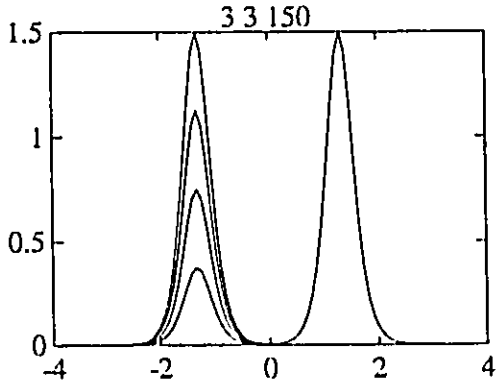
3 3 150

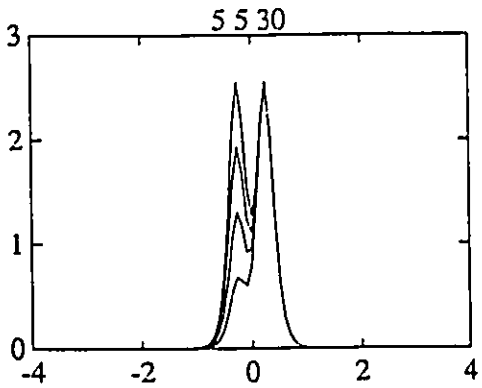
5 5 30

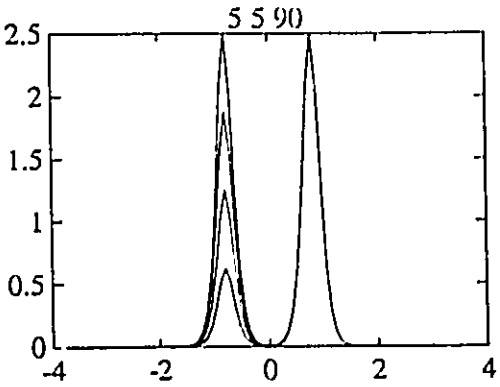
5 5 90

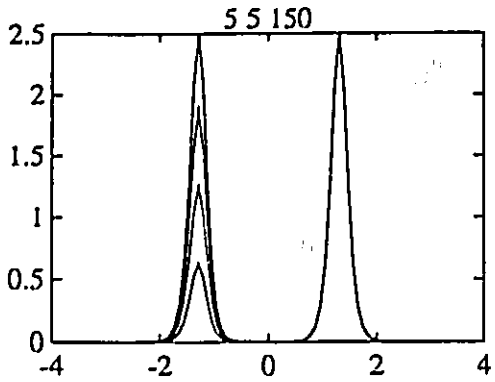
5 5 150

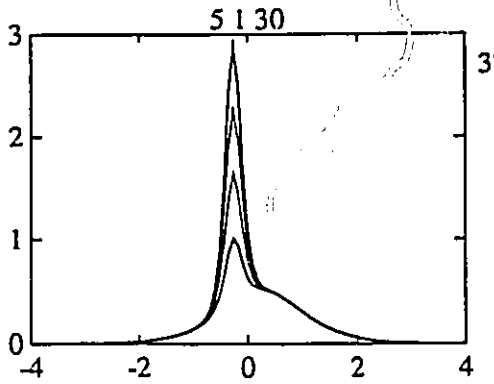
5 1 30

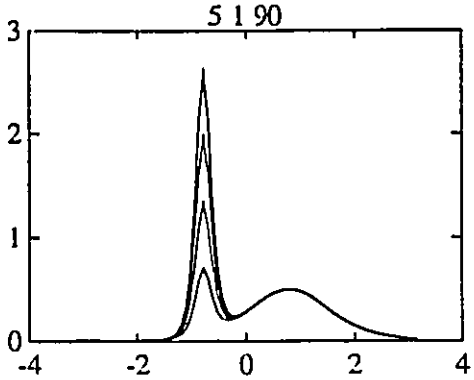
5 1 90

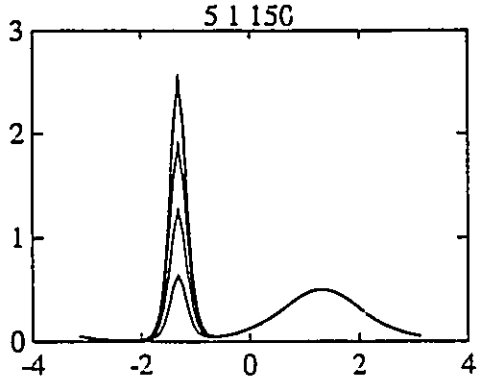
5 1 150

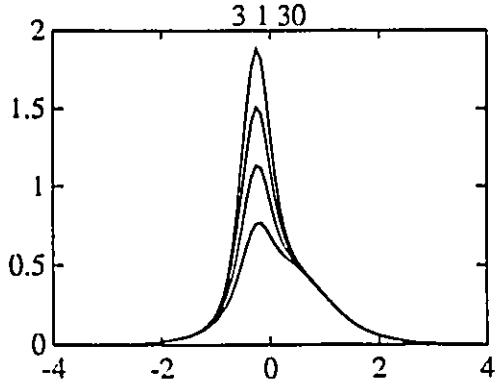
3 1 30

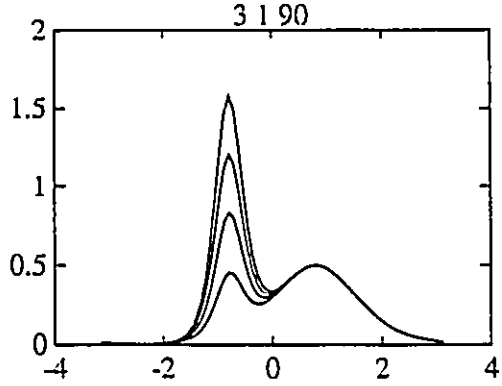
3 1 90

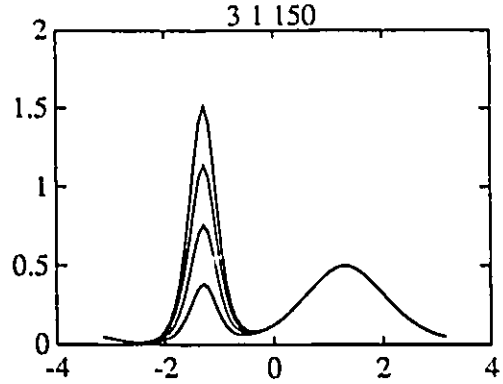
3 1 150

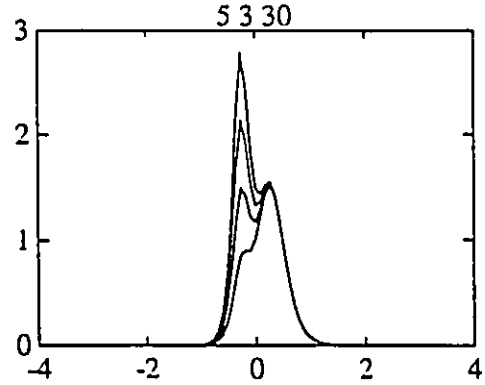
5 3 30

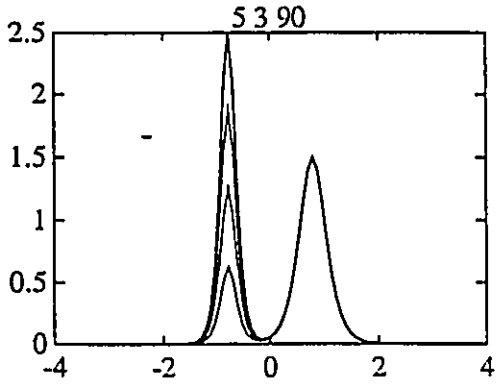
5 3 90
2.5
2
1.5
1
0.5
0
-4
-2
0
2
4

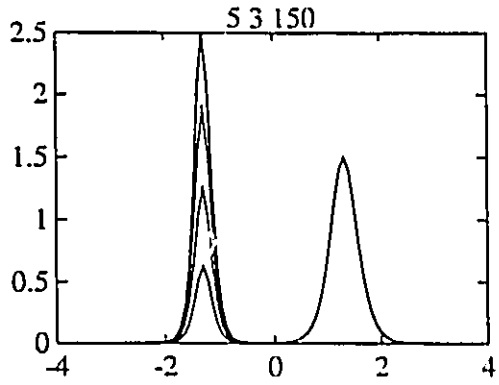
5 3 150
2.5
2
1.5
1
0.5
0
-4
-2
0
2
4

APPENDIX 7

NMLM normalization scheme for bimodal distributions

In Chapter 7, it was found possible to establish correcting rules based on only two measured values of the MLM fitted populations: The spreading parameter β of the population containing the most energy, and the peak ratio between both populations. The normalization curves presented in Figures 7.11 and 7.12 were derived using distributions with various spreading, spacing and energy ratios. The only constraint used was that in all cases, both populations had equal spreading. In these conditions, since the maximum peak of each distribution is given by

$$\frac{\phi_i \beta_i}{2} \tag{A7.1}$$

it can be seen that the peak ratio (PR) between the distributions is also equal to the energy ratio. Following a least square fit of two distributions to the MLM estimate, we can define values of the scaling parameters, ϕ_1 and ϕ_2, spreading parameters β_1 and β_2, and angular spacing between both distributions, where the subscript 1 refers to the population containing the most energy. The normalization scheme is based on the correlation of some parameters with the energy ratio between both fitted populations. In a first step, the β ratio (BR), defined as:

$$BR = \frac{\beta(fitted)}{\beta(input)} \tag{A7.2}$$

was calculated for the distribution containing the most energy. From Figure 7.11, we have:

$$BR = -0.0017 \cdot PR^2 + 0.0313 \cdot PR + 0.7283 \tag{A7.3}$$

From which the true value of the spreading parameter β_1' for the first distribution can be calculated as:

$$\beta_1' = \frac{\beta_1}{BR} \tag{A7.4}$$

In order to normalize the second distribution, correlations were made between the measured peak ratio (PR) and the true peak ratio (TPR). With the TPR value, and using Eq. A7.1, it can be approximated that the true value of the spreading parameter for the second distribution β_2' is given by

$$\beta_2' = \frac{\phi_1 \beta_1'}{\phi_2 TPR} \tag{A7.5}$$

Using correlations in Figure 12, we find:

$$\begin{aligned} TPR &= 1.0625 \cdot PR && spacing = 150^\circ \\ TPR &= (PR-1)\cdot((\beta_1' \cdot -0.2)+1.73)+1 && spacing = 90^\circ \\ TPR &= (PR-1)\cdot((\beta_1' \cdot -0.25)+2.36)+1 && spacing = 60^\circ \end{aligned} \tag{A7.6}$$

For intermediate values of the spacing, linear interpolation was used. A very similar normalization scheme was used for pitch-roll-heave data, the only difference being that the initial beta ratio was computed on the second distribution, the correlation being better than for the first one. In such a case we find:

$$\beta_2' = \frac{\beta_2}{BR} \tag{A7.7}$$

with

$$BR = 0.0149 \cdot PR^2 - 0.1681 \cdot PR + 0.6414 \tag{A7.8}$$

and

$$\beta_1' = \frac{TPR \cdot \phi_2 \beta_2'}{\phi_1} \tag{A7.9}$$

with the values of TPR given by:

$$\begin{aligned} TPR &= (PR-1)\cdot((\beta_2'\cdot-0.27)+1.94)+1 \qquad spacing=150^\circ \\ TPR &= (PR-1)\cdot((\beta_2'\cdot-0.54)+3.89)+1 \qquad spacing=90^\circ \\ TPR &= 2.58\cdot PR-1.58 \qquad spacing=60^\circ \end{aligned} \tag{A7.10}$$

It should be noted that in the heave-pitch-roll case, the correlations were not nearly as good as in the case of the six-wavestaff array previously discussed.

APPENDIX 8

Thesis-related publications

(1) Peer Reviewed

journal articles

Tsanis, I.K., **Brissette, F.P.** , 1992, Wave Directional Spectra Measurements by Small Arrays in Lake Ontario. Journal of Great Lakes Research. v.18 (3) p.489-506.

Tsanis, I.K., and **Brissette, F.P.**, 1991, A Wave Directional Spectra Program for Wave Cage Arrays. Environmental Software, v.6 (3), p.151-160.

proceedings of meetings

Brissette, F.P. and Tsanis, I.K., 1992, Maximum Likelihood Method Techniques for Directional Analysis of Heave-Pitch-Roll data. 3rd International Workshop on Wave Hindcasting and Forecasting, Montreal, Quebec, 1992. p.1-11.

Brissette, F.P. and Wu, J.J., 1992, Wave Directional Spectra and Current Interaction in Lake St.Clair, 3rd International Workshop on Wave Hindcasting and Forecasting, Montreal, Quebec, 1992. p.12-23.

Brissette, F.P. and Tsanis, I.K., 1992, An Integrated Software for the Analysis of Directional Seas. in: Computer Techniques in Environmental Studies IV, ed. P.Zannetti., Elsevier, Fourth Int. Conf. ENVIROSOFT, Southampton, England, p.359-369.

Tsanis, I.K. and **Brissette, F.P.** , 1992, Methods for Directional Spectra Measurements by Small Arrays. 3rd International Workshop on Wave Hindcasting and Forecasting, Montreal, Quebec, 1992. p.24-31.

Brissette, F.P. and Tsanis, I.K., 1991, Wave Directional Spectra in Lake Ontario and Lake St.Clair. International Association for Great Lakes Research annual meeting, Buffalo, June 2-6, IAGLR Program and Abstracts, v.34.

(2) Submitted for Publication

Brissette, F.P. and Tsanis, I.K., 1992, Estimation of Wave Directional Spectra from Pitch-Roll Buoy Data. Journal of Waterway Port Coastal and Ocean Engineering (ASCE).

Brissette, F.P. and Tsanis, I.K., 1992, Estimation of Directional Wave Spectra using an exact form of the Maximum Likelihood Method. Journal of Atmospheric and Oceanic Technology.

Brissette, F.P. and Tsanis, I.K., 1992, Observations of the Directional Spectrum Relaxation of Wavefields in Slowly and Rapidly Turning Winds. Journal of Physical Oceanography.

Brissette, F.P., Tsanis, I.K. and Wu J., 1992, Wave Directional Spectra and Wave-Current Interaction in ake St.Clair. Journal of Great Lakes Research.

(3) In Preparation

Brissette, F.P. and Tsanis, I.K., 1993, Directional Spectrum Estimation from Small Wave Gauge Arrays. to be submitted to the Journal of Geophysical Research.

(4) Not Peer Reviewed

contributed seminars

Brissette, F.P., On the Estimation of Wave Directional Spectra with Applications to Lake St.Clair, Great Lakes Environmental Research Laboratory, National Oceanic and Atmospheric Administration, Ann Arbor, Michigan, May 5, 1992

Brissette, F.P., Numerical simulation of directional seas and implications for directional spectra estimators, W.A.V.E.S. Seminar Series, Research and Application Branch, National Water Research Institute, Canada centre for Inland Waters, Burlington, February 6, 1991

Brissette, F.P., The SWADE project in the Atlantic Ocean, Fluid Mechanics Seminar Series, Faculty of Engineering, McMaster University, Hamilton, March 30, 1990

others

Tsanis, I.K., and Brissette, F.P., 1992, Observation of Directional Wave Spectra: Pullen Island West, Beaufort Sea. Report prepared for the Department of Fisheries and Oceans, Contract # NRC92-164, December 1993.

Tsanis, I.K., and Brissette, F.P., 1992, Directional Wave Spectra during the Surface Wave Dynamics Experiment (SWADE). Report prepared for the Department of Fisheries and Oceans, Contract # NRC91-164, Supply and Services Canada, Science Branch, Hull, Quebec, February 1992.

Tsanis, I.K., and Brissette, F.P., 1991, Directional Wave Spectra during the Surface Wave Dynamics Experiment (SWADE). Report prepared for the Department of Fisheries and Oceans, Contract # FP802-0-2500/01-SS, Supply and Services Canada, Science Branch, Hull, Quebec, March 1991.

December 21, 1992.